

Diss. ETH No. 12795

On the Applicability of
Relaxed Eddy Accumulation and Common Methods
for Measuring Trace Gas Surface Fluxes

A dissertation submitted to the
SWISS FEDERAL INSTITUTE OF TECHNOLOGY ZURICH

for the degree of
DOCTOR OF NATURAL SCIENCES

presented by
CHRISTOF AMMANN
dipl. natw. ETH
born 22 December 1965
citizen of Kirchberg SG

accepted on the recommendation of

Prof. Dr. A. Ohmura, examiner
Dr. R. L. Desjardins, co-examiner
Dr. F. X. Meixner, co-examiner
Dr. M. Rotach, co-examiner

Zürich, 1998

Leer - Vide - Empty

Summary

The accurate measurement of the trace gas exchange at the Earth's surface is very important for understanding various problems in current environmental research such as the greenhouse effect, atmospheric chemistry, aerosol and cloud formation, and nutrient cycling. Several techniques have been developed for measuring trace gas exchange at natural surfaces, among which the 'eddy correlation' technique is regarded as the most direct and reliable one. However, it requires trace gas measurements at a high temporal resolution, which are currently not available for most species. In order to overcome this problem, Desjardins (1972) proposed a modification of the eddy correlation technique called 'eddy accumulation', in a somewhat simplified form known as 'relaxed eddy accumulation' (Businger and Oncley, 1990). For this method, the fast response trace gas sensor is replaced by fast response sampling valves combined with accumulative or slow analysis techniques available for many trace gases.

In the present study, the relaxed eddy accumulation technique (REA) was investigated with respect to theoretical, methodological, environmental and instrumental requirements and limitations. For that purpose, a relaxed eddy accumulation system was built and tested during an extended field campaign in direct comparison with common flux measurement techniques, namely the eddy correlation and aerodynamic profile methods. The field experiment was performed in June/July 1995 over a senescent cereal field near Bellheim, Southern Germany. The eddy correlation dataset obtained for the fluxes of four different scalar quantities (temperature, CO₂, H₂O, O₃) allowed comprehensive simulation studies of the REA method for a wide range of environmental conditions. The REA b-factor as well as other REA related quantities in the inertial sublayer were described in a concise way within the framework of the Monin-Obukhov-similarity-theory, i.e. as a function of the dimensionless stability z/L . In good agreement with previous publications, a constant value of about 0.57 was obtained for unstable and near-neutral conditions. For stable conditions, however, a significant increase with stability was observed which could be well described by a logarithmic functional relationship between b and z/L . The systematic variation of the REA b-factor was examined and interpreted in relation to the bivariate joint frequency distribution of the vertical windspeed and the scalar quantity. Additional simulation studies concerning the influence of a deadband and several systematic error effects were also performed. They complement the findings of recent publications which are mostly based on a small sample size and limited to unstable daytime conditions as well as homogenous terrain.

The evaluation of the REA field measurements revealed several practical problems of the setup applied (after Baker et al., 1992). The most crucial effect turned out to be the non-constant sampling flow due to pressure fluctuations in the sampling system. It can be avoided in future experiments by a modification of the system design. The systematic errors were partly compensated by the estimation of effective b-factors based on the temperature data. This procedure yielded satisfying REA results (compared to the reference eddy correlation values) for the CO₂ uptake under unstable daytime conditions. A direct comparison with the profile method under favourable and limited fetch conditions (inhomogenous source areas) was made. In the latter case, the REA tended to give the same flux results like the eddy correlation, whereas the profile method often yielded unrepresentative or even physically implausible values.

Together with the findings of other publications, the results of the present study show that the relaxed eddy accumulation represents a self-standing theoretical concept relying only little on empirical assumptions. The REA method has substantial advantages in theory and practice compared to the profile techniques. It thus represents a useful alternative for the flux measurement of trace gases, for which no fast response sensors but accurate slow response or accumulative analysis techniques are available.

Zusammenfassung

Eine möglichst genaue Bestimmung des Spurengasaustausches an der Erdoberfläche ist sehr wichtig für das Verständnis vieler aktueller Probleme der modernen Umweltforschung wie z.B. Treibhauseffekt, Atmosphärenchemie, Aerosol- und Wolkenbildung oder globale Nährstoff-Kreisläufe. Die direkteste und deshalb vertrauenswürdigste Methode zur Flussmessung, die bisher eingesetzt wurde, ist die sogenannte 'Eddy-Korrelation'. Allerdings benötigt sie sehr schnelle Spurengas-Sensoren, die bisher nur für einige wenige Stoffe zur Verfügung stehen. Um dieses Problem zu umgehen, schlug Desjardins (1972) eine Modifizierung der Eddy-Korrelation vor, die später als 'Eddy-Akkumulation' und in einer vereinfachten Version als 'Relaxed-Eddy-Akkumulation' (REA) bekannt wurde. Bei diesen Methoden kann der schnelle Spurengassensor durch schnell reagierende Ventile ersetzt werden, welche den Probeluft-Strom modulieren und so eine langsame Analyse oder akkumulative Sammlung des Spurengases erlauben.

In der vorliegenden Arbeit wurde die REA unter theoretischen wie auch methodologischen Aspekten untersucht und bezüglich ihrer Vorteile und Limitierungen analysiert. Zu diesem Zweck wurde ein REA-System zur Messung des CO₂- und Wasserdampf-Flusses aufgebaut und in einer intensiven Feldmesskampagne getestet, in direktem Vergleich zu herkömmlichen Techniken wie der Eddy-Korrelation und der aerodynamischen Profilmethode. Das Feldexperiment wurde im Juni/Juli 1995 über einem seneszenten Triticale-Feld in der Nähe von Bellheim (Süddeutschland) durchgeführt. Die zeitlich hochaufgelösten Messdaten des Eddy-Korrelations-Systems (für Temperatur, CO₂, H₂O und O₃) erlaubten umfassende Simulationsstudien der REA-Methode für verschiedene Umweltbedingungen. Für die REA-Methode wichtige Größen wie z.B. der Proportionalitätsfaktor b konnten im Rahmen der Monin-Obukhov-Ähnlichkeitstheorie als Funktion des Stabilitätsparameters z/L beschrieben werden. Für instabile und nahe-neutrale Verhältnisse wurde, in Übereinstimmung mit Literaturwerten, ein konstanter b -Faktor von ca. 0.57 gefunden. Im stabilen Bereich wurde dagegen ein signifikanter Anstieg beobachtet, der sich durch eine logarithmische Beziehung zwischen b und z/L beschreiben lässt. Die systematische Variation des b -Faktors konnte durch eine Analyse der bivariaten Verteilung von Vertikalwind und transportierter skalarer Größe erklärt werden. Weitere Simulationsstudien untersuchten den Einfluss eines Schwellenwertes für den Vertikalwind ('deadband') sowie verschiedener systematischer Fehlerfaktoren. Die gewonnenen Ergebnisse ergänzen die bisher veröffentlichten Resultate anderer Autoren, die meist auf kleinen Datensätzen beruhen und auf instabile Verhältnisse beschränkt sind.

Die Auswertung der REA-Feldmessungen deckte einige praktische Probleme des verwendeten Messsystems (nach Baker et al., 1992) auf. Dabei stellte der variierende Probeluftstrom, der durch Druckschwankungen im System verursacht wurde, die grösste Fehlerquelle dar. Es konnte jedoch eine Lösung für dieses Problem aufgezeigt werden, die in einer Modifikation des Messaufbaus besteht. Der systematische Fehler in den REA-Messungen konnte teilweise kompensiert werden durch die Berechnung effektiver b -Faktoren aus den Temperaturdaten des Eddy-Korrelations-Systems. Dieses Vorgehen lieferte befriedigende Resultate für die CO₂-Aufnahme unter instabilen Bedingungen. Ein direkter Vergleich mit der Profilmethode zeigte, dass die REA insbesondere für inhomogene Oberflächenbedingungen eine deutlich bessere Übereinstimmung mit den Ergebnissen der Eddy-Korrelation erzielte.

Die vorliegende Untersuchung zeigt, zusammen mit den Resultaten anderer Studien, dass der REA-Methode ein eigenständiges und wohl definiertes Konzept zugrunde liegt, das nur zu einem geringen Grad auf empirischen Annahmen beruht. Im Vergleich zur Profilmethode zeigt die REA erhebliche theoretische wie auch praktische Vorteile. Sie stellt deshalb eine nützliche Alternative zur Flussmessung vieler Spurengase dar, für die keine schnellen Sensoren jedoch langsame Analyseverfahren mit ausreichender Genauigkeit zur Verfügung stehen.

Acknowledgements

I gratefully acknowledge the contribution of many people who gave advice and support in the course of the present study.

I would like to thank my 'doctorfather' Prof. Atsumu Ohmura for accepting to be examiner of this thesis. He originally raised my interest in micrometeorology through his lecture courses.

I am especially indebted to Prof. Franz Meixner who initiated and supervised this work. He offered me the opportunity to work in a interdisciplinary environment with a high degree of independence. I much appreciate his enthusiasm, encouragement and friendship.

The co-examiners Dr. Raymond L. Desjardins and Dr. Mathias Rotach spent great efforts in reviewing the manuscript. I am very grateful for their valuable comments and suggestions which led to significant improvements of the thesis.

The present study was carried out at the Biogeochemistry Department of the Max Planck Institute for Chemistry in Mainz. I would like to thank all my colleges who created a friendly and stimulating atmosphere at the institute. Among these I want to mention my room mates Franz Nathaus and Michael Welling as well as Detlev Sprung, Tae Siek Rhee, Uwe Kuhn and Jörg Ludwig. They gave advice and support and they shared countless discussions on scientific and non-scientific problems. Some of them also helped to review and copy the manuscript.

My thanks also go to all the people who contributed to the realisation of the Bellheim'95 field experiment. The farmer Paul Gärtner generously allowed to use the field site and electric power. Joachim Busch performed the time consuming porometry measurements. Dr. Frank Helleis created the data acquisition and control program for the eddy correlation and relaxed eddy accumulation measurements. Dr. Hans Güsten provided his fast response ozone sensor. The staff of the electronic and mechanical workshops of the Max Planck Institute built several important parts of the equipment.

Last but not least I thank my parents for their continuous support throughout my academic education and for the opportunity to relax from the sometimes stressful work.

Leer - Vide - Empty

Table of Contents

1	INTRODUCTION	1
2	THEORY	4
2.1	Trace Gas Exchange Between Biosphere and Atmosphere.....	4
2.1.1	Exchange Processes at the Surface.....	5
2.1.2	Turbulent Transport in the Atmospheric Boundary Layer.....	6
2.1.3	Quantitative Description and Resistance Models.....	8
2.1.4	Surface Energy Budget.....	11
2.2	Measurement Principles for Trace Gas Exchange.....	12
2.2.1	Basic Considerations.....	12
2.2.2	Enclosure Techniques.....	13
2.2.3	Micrometeorological Concepts.....	15
2.3	Eddy Correlation Method.....	18
2.3.1	Ergodicity and Taylor Hypothesis.....	18
2.3.2	Turbulence Spectra.....	19
2.3.3	Statistical Description of Turbulence.....	21
2.3.4	Application of the Eddy Correlation Method.....	23
2.4	Semi-empirical Relationships for Turbulent Fluxes.....	24
2.4.1	Dimensional Analysis and Similarity-Theory for the Surface Layer.....	25
2.4.2	Flux-Profile-Relationships.....	27
2.4.3	Displacement Height and Roughness Length.....	30
2.4.4	Variance Similarity.....	32
2.4.5	Limitations of Monin-Obukhov-similarity.....	35
2.5	Eddy Accumulation Method.....	36
2.5.1	Motivation and Theory.....	36
2.5.2	Realisation of the Proportional Eddy Accumulation Technique.....	38
2.5.3	Relaxed Eddy Accumulation Concept.....	41
2.5.4	Application of the REA Technique.....	44
2.6	Spatial Representativeness of Flux Measurements.....	45
2.6.1	Source Areas of Micrometeorological Methods.....	45
2.6.2	Comparison and Interpretation of Different Methods.....	47
3	MEASUREMENTS	50
3.1	General Description of Field Experiment.....	50
3.1.1	Measurement Site and Period.....	50
3.1.2	Characterisation of the Triticale Canopy.....	51
3.1.3	Overview of Measured Quantities and Instrumentation.....	53
3.1.4	Tower Setup and Operation Periods.....	55
3.2	Profile Systems.....	56
3.2.1	Setup and Components.....	56
3.2.2	Trace Gas Analysers.....	59
3.2.3	Sensors for Meteorological Quantities.....	60

3.3	Eddy Correlation Systems	61
3.3.1	Setup and Components	61
3.3.2	Sonic Anemometer-Thermometer	63
3.3.3	Closed Path Infra-Red-Gas-Analyser	67
3.3.4	Fast Response Ozone Detector	71
3.4	Relaxed Eddy Accumulation System	72
3.4.1	Setup and Components	72
3.4.2	Trace Gas Analysis	73
3.4.3	Conditional Sampling Valves	74
3.5	Determination of Non-turbulent Energy Fluxes	76
3.5.1	Radiation Budget	76
3.5.2	Energy Storage in the Canopy	77
3.5.3	Soil Heat Flux	78
4	EVALUATION OF COMMON METHODS	80
4.1	Eddy Correlation Calculations	80
4.1.1	Delay Time of Trace Gas Measurements	81
4.1.2	Detrending and Covariance Calculation	84
4.1.3	Coordinate Rotation of the Wind Vector	86
4.1.4	Calibration and Correction for Correlated Density Effects	90
4.1.5	Correction for High Frequency Attenuation	94
4.1.6	Spectral and Integral Similarity Relationships	97
4.2	Aerodynamic Flux-Profile Calculations	103
4.2.1	Determination of z_0 and d	104
4.2.2	Numerical Calculation of Turbulence Parameters	106
4.2.3	Flux Calculation and Correction	108
4.3	Data Rejection and Error Estimation	109
4.3.1	Rejection Criteria and Final Datasets	109
4.3.2	Theoretical Uncertainty of Finite Turbulence Measurements	111
4.3.3	Instrumental Noise and Measurement Resolution	113
4.3.4	Systematic Error Sources	114
4.4	Environmental Conditions and Flux Results	115
4.4.1	General Weather Conditions	115
4.4.2	Source Area and Fetch Conditions	117
4.4.3	Senescence Development of the Triticale Field	120
4.4.4	Diurnal Variation of Fluxes and Concentrations	123
5	EVALUATION OF REA METHOD	126
5.1	Simulation of Ideal REA System	126
5.1.1	Simulation Procedure and Conditioning of Time Series	126
5.1.2	b-Factors for Different Scalar Quantities	128
5.1.3	Relation between b-Factor and Bivariate Distribution	131
5.1.4	Effect of a Deadband	135
5.2	Simulation of Non-Ideal REA Systems	137
5.2.1	Measurement Errors in the Vertical Windspeed	137
5.2.2	Delay Time of Conditional Sampling	140
5.2.3	Non-Constant Conditional Sampling Flow	144

5.3	Evaluation of Measured REA Fluxes	146
5.3.1	Calculations and Corrections.....	146
5.3.2	Data Rejection	148
5.3.3	Error Estimation	149
6	DISCUSSION	151
6.1	Comparison and Verification of Measured Fluxes.....	151
6.1.1	General Considerations	151
6.1.2	Closure of the Surface Energy Budget	152
6.1.3	Comparison with Enclosure Measurements.....	156
6.1.4	General Comparison of Micrometeorological Methods.....	158
6.1.5	Selected Diurnal Cycles of CO ₂ Flux.....	162
6.2	General Validity of the REA Concept.....	166
6.2.1	Ideal b-Factor	166
6.2.2	Deadband Effect	169
6.2.3	Dependence on Joint Frequency Distribution.....	171
6.2.4	Applicability Outside the Inertial Sublayer	172
6.3	Analyser Resolution Requirements	174
6.3.1	Comparison of Different Methods for Bellheim Field Conditions.....	174
6.3.2	Requirements of REA Method for Specific Trace Gases	177
6.4	Design of Conditional Sampling Systems	180
6.4.1	Sampling Flow System for Online Analysis	180
6.4.2	Alternative Accumulation and Analysing Methods.....	182
6.4.3	Windspeed Measurement and Valve Control.....	184
7	CONCLUSIONS	187
7.1	Major Findings of the Present Study.....	187
7.2	Recommendations and Outlook	189
	APPENDICES	191
	Appendix A: Spectral Analysis of Turbulence Time Series	191
	A.1 Harmonic Fourier Decomposition	191
	A.2 Unresolvable High and Low Frequencies	192
	A.3 Calculation of Spectral Amplitudes.....	193
	A.4 Variance and Covariance Spectra	194
	A.5 Spectral Averaging and Statistical Significance.....	196
	A.6 Semi-empirical Form of Turbulence Spectra.....	197
	A.7 Spectral Response of Turbulence Measurement Systems.....	199
	A.8 Spectral Attenuation of Covariance Measurements.....	203
	Appendix B: Compilation of Flux Results	207
	Appendix C: Symbols and Abbreviations	214
	REFERENCES	217

1 INTRODUCTION

Besides the main constituents, oxygen, nitrogen, argon, and water vapour, the Earth's atmosphere contains a large number of trace gases with concentrations well below one percent. Only in the last few decades it has been fully recognised how strongly the properties of the atmosphere are influenced by these trace gases. Many of them contribute to the radiation balance of the Earth (Houghton et al., 1990) or have a critical role in regional and global atmospheric chemistry (Thompson, 1992; Graedel and Crutzen, 1993; Kley, 1997). Some compounds like carbon dioxide, ozone, and nitrogen oxides have direct impact on plants, animals, and ecosystems (Heck et al., 1982; Wellburn, 1990; Field et al., 1992; Ceulemans and Mousseau, 1993).

The past and present change in the composition of the atmosphere is well documented by atmospheric measurements at a number of monitoring stations around the world for the last 25 years (e.g. Rasmussen and Khalil, 1986) and by the record provided through the analysis of air bubbles trapped in glacial ice (Neftel et al., 1985; Raynaud et al., 1988). They indicate that the present increase observed for CO_2 ($+0.5\% \text{ y}^{-1}$), CH_4 ($+0.6\% \text{ y}^{-1}$), N_2O ($+0.25\% \text{ y}^{-1}$), and other important trace gases is greater than any atmospheric perturbation experienced over the last hundreds of thousands of years (Matson and Harriss, 1995). The direct anthropogenic release of trace gases from industry, traffic, and domestic heating can be estimated usually with satisfying accuracy through economic, technical, and demographic investigations (Baumbach, 1996). On the other hand, there is relatively poor knowledge about the biogenic (natural and agricultural) emission and uptake of trace gases and the processes controlling them. They are part of a complex interacting system and show variations across different temporal and spatial scales (Ehleringer and Field, 1993; see also Sections 2.1 and 2.6). Although the local biogenic exchange rates are relatively small and difficult to quantify, the mass exchanges can get significant when integrated over large scale natural or agricultural ecosystems.

Determination of Trace Gas Exchange

For an appropriate quantification and modelling of trace gas exchange at the Earth's surface, accurate and representative measurements are necessary. Laboratory studies provide some information on the biological mechanisms involved in trace gas exchange (Conrad, 1995; Kesselmeier et al., 1997a), the physics of air motion (Raupach et al., 1986), and the chemical characteristics of trace gases (Moortgat et al., 1989; Neeb, 1995). Yet, measurements under natural field conditions will never be replaceable, because a vegetated surface is of such complexity that it cannot be replicated in the laboratory with all relevant processes. The exchange characteristics have to be studied under representative and undisturbed environmental conditions with typical diurnal and seasonal cycles.

Several techniques have been developed for measuring trace gas exchange in the field, but the so-called 'eddy correlation' technique is regarded as the most direct and reliable for that purpose (Delany, 1993; Lenschow, 1995). With ground-based measurements at only one location and with a minimum disturbance of the environmental conditions, it allows determination of the net vertical exchange integrated over a surface area with a length-scale of 10^1 to 10^3 metres. Although it has some requirements and limitations concerning the surface homogeneity or the atmospheric conditions, they are generally less restrictive compared to alternative methods (see Sections 2.2 and 2.4).

With the eddy correlation method, the mean vertical flux of a trace gas is measured in the air layer above the surface of interest. The airflow near the surface is usually turbulent leading to instantaneous fluctuations of the vertical windspeed and to an effective vertical transport (mixing) of the trace gases. The net vertical exchange can be determined by measuring and computing the covariance of the vertical wind velocity and the trace gas concentration over a suitable averaging period (for details see Section 2.3). Since the turbulent transport happens over a wide range of temporal and spatial scales down to very small and short-lived motions, the eddy correlation technique requires windspeed and trace gas measurements at a high temporal resolution and thus sensors with a response time faster than about one second. Such instruments have been developed up to now only for few compounds like water vapour, ozone, carbon dioxide, methane, or nitrous oxide. They are usually research type or prototype instruments, which are quite expensive and need intensive maintenance. For the majority of trace gases, no sensors with a time resolution below one minute are available. The gases have to be scrubbed from the air and accumulated over several minutes or hours before they can be analysed with sophisticated chromatographic, spectrometric, or wet chemical methods.

In order to overcome this problem, Desjardins (1977) proposed a modification of the eddy correlation technique called 'eddy accumulation'. For this method, the required fast response trace gas sensor can be replaced by fast response sampling valves combined with slow analysis techniques. A somewhat simplified form known as 'relaxed eddy accumulation' (Businger and Oncley, 1990) seems to be a promising alternative to common methods using slow sensors like gradient or enclosure techniques. However, only few experimental studies with the relaxed eddy accumulation method have been performed so far, and there are still theoretical as well as practical uncertainties and problems. Further investigations are necessary to validate the general applicability for different trace compounds under various environmental conditions. Also, the theoretical foundation has to be improved and completed.

Objectives and Experimental Activities

The main objective of this study is a comprehensive investigation of the relaxed eddy accumulation method including the examination of theoretical, methodological, environmental and instrumental requirements and limitations. For that purpose, a relaxed eddy accumulation system was built up and tested during an intensive field campaign under a wide range of environmental conditions. For validation and comparison purposes, it was designed for the measurement of water vapour and carbon dioxide fluxes, which could be measured as well by other (more common) techniques. The relaxed eddy accumulation system was operated side by side with eddy correlation and aerodynamic profile systems. In addition to the direct validation of the relaxed eddy accumulation system, the eddy correlation datasets were also used for detailed simulation studies addressing the following aspects:

- the validity of the relaxed eddy accumulation concept
- general requirements and limitations of the relaxed eddy accumulation concerning imperfect sensors and environmental conditions
- specific instrumental and setup problems of relaxed eddy accumulation systems and possible solutions
- necessity and applicability of online and post-processing corrections

The investigations are expected to demonstrate the advantages and disadvantages of the relaxed eddy accumulation compared to common flux measurement techniques. They will help to decide, under which circumstances the relaxed eddy accumulation can be a promising alternative for the flux measurement of

specific trace gases. Moreover, the findings should lead to an optimised setup and operation of relaxed eddy accumulation systems.

Structure and Content of the Present Study

In order to facilitate the explanation and discussion of the measurements and simulations in the present study, a survey of the fundamental theory is given in Chapter 2. It presents the relevant processes for the biosphere-atmosphere exchange of trace gases and the available flux measurement concepts and techniques. Especially the theory of the turbulent transport and the related micrometeorological methods need a relatively detailed explanation. In Chapter 3, the field measurement campaign is described with a presentation of the site, the experimental setup and instrumentation, and the measurement periods. The evaluation of the measured data set is presented in Chapters 4 and 5, separately for the common methods (eddy correlation and profile technique) and for the novel relaxed eddy accumulation method. The evaluation of the common methods is based on established calculation and correction procedures, whereas the relaxed eddy accumulation needs a detailed analysis and discussion of the necessary and optimal corrections. Chapter 4 also includes a presentation of the environmental conditions and an overview of the observed trace gas exchange during the field campaign. Finally, the results of the evaluations are discussed and compared to literature values in Chapter 6. Besides the verification and comparison of the different methods, the applicability of the relaxed eddy accumulation technique is discussed under various theoretical and practical aspects.

The appendices include some information on the spectral analysis of atmospheric turbulence, which is important especially for the evaluation of the eddy correlation measurements, a compilation of all flux results displayed as synchronous time series, and a table of the symbols and abbreviations used.

2 THEORY

2.1 Trace Gas Exchange Between Biosphere and Atmosphere

The net exchange rate of trace gases between an ecosystem and the atmosphere is usually a result of many interacting processes. For an adequate understanding and modelling, one has to identify (and to separate) the relevant sub-processes within the complex system of the soil-vegetation-atmosphere-interface. Different uptake and release processes can occur simultaneously on and within several parts of the vegetation canopy and the soil. A simplified schematic illustration is given in Fig. 2.1.

The sources and sinks are linked to each other and to the atmospheric environment through various transport mechanisms. These mechanisms control (and limit) the transport efficiency of trace gases away from sources and towards sinks. They are particularly important, because most of the exchange processes are very sensitive to the actual trace gas concentration in the ambient air. In the atmosphere, trace gases are transported relatively fast over long distances by the mean horizontal air motion, but for the exchange with the surface and between different air layers, turbulence is the main relevant process. It ensures an effective mixing of the air and, therefore, has a permanent tendency to compensate local surplus or deficits in the trace gas distribution.

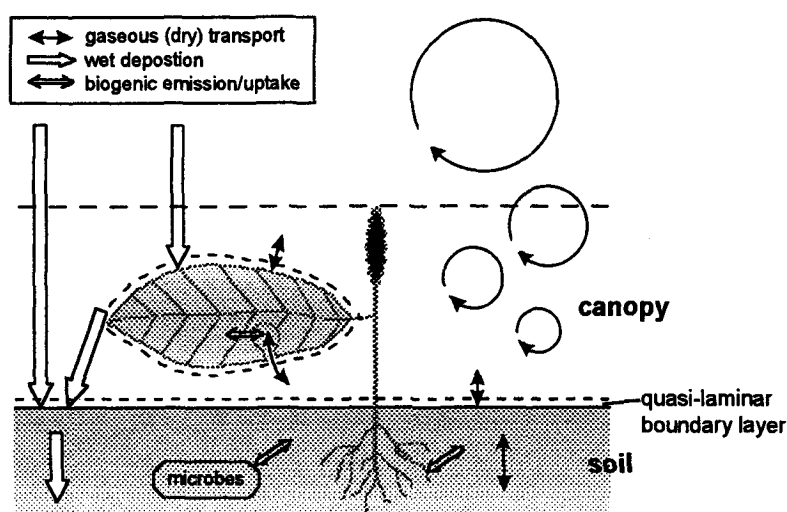


Fig. 2.1: Schematic overview of the relevant transfer mechanisms for trace gases at a vegetated surface.

For certain trace compounds the interactions between the gaseous form and aerosols as well as water droplets (dissolved form) has to be considered (Gallagher et al., 1997). For budget studies of the surface exchange, a distinction is usually made according to the state of aggregation, in which a certain substance is deposited to the surface. 'Dry deposition' in gaseous and particulate form is often a continuous process, whereas 'wet deposition' in dissolved form is connected to rain or fog events (see Fig. 2.1). The present study is focused on *gaseous exchange* of trace compounds between the biosphere and the atmosphere, and the other processes will not be considered. However, many models and methods discussed here are also applicable for the exchange of solid particles and droplets (cf. Duyzer, 1985; Fairall, 1984; Vong and Kowalsky, 1995).

In the following two sections, the relevant processes for the trace gas exchange directly at the surface and the turbulent transport in the air are discussed mainly in a qualitative way. A possibility for a simple quantitative description and comparison of all the different processes is provided by resistance models (Section 2.1.3). They are used, despite their limitations, in various scientific domains such as micrometeorology, soil sciences, hydrology, plant physiology, ecology, and engineering sciences. Another helpful method for the determination and understanding of trace gas exchange is the study of the energy budget at the surface, which is discussed in Section 2.1.4.

The basic theory of turbulence and other micrometeorological processes presented in this chapter, is taken (if not stated otherwise) from the textbooks of Panofsky and Dutton (1984), Stull (1988), Garratt (1992), and Kaimal and Finnigan (1994). They will be referenced in the following in an abbreviated form as PD84, St88, Ga92, and KF94 together with the corresponding page number.

2.1.1 Exchange Processes at the Surface

Exchange with and in the soil

The production and destruction of trace gases in the soil can be either due to physico-chemical deposition and emission to/from dead soil material and soil water or due to metabolic uptake/release by soil organisms like microbes, fungi and plant roots (Rosswall et al., 1989, Kesselmeier et al., 1997). The transport of gases between the soil surface and deeper layers is maintained by molecular diffusion through the air-filled soil pores. The available pore space, which controls the diffusivity, depends on the composition and structure of the soil and on the water content (cf. Hillel, 1980: 272; last number signifying the page). If a large part of the pore space is filled with water, the gas diffusion can be considerably restricted or even blocked. Under special conditions (e.g. very porous soil or cracks/fissures, strong temperature gradients, pressure fluctuations), convective transport may also occur in the uppermost soil layer and lead to an enhanced gas exchange (Hillel, 1980: 269; Rudolph, 1994).

Exchange with plants

The trace gas exchange with plants can be connected to the active metabolism (Kesselmeier et al., 1997) or just a passive physico-chemical adsorption and desorption on the plants surfaces (van Hove et al., 1989). The metabolic release and uptake by higher plants occur mainly through the stomates, although some transfer via the cuticle cannot be excluded (Kesselmeier, 1991). The transfer through the stoma openings and the movement in the sub-stomatal cavity is purely diffusive (Leuning, 1983). Once inside, gas molecules may enter and react with intercellular fluids or be transported across cell membranes. Through the regulation of the stomatal aperture, the plants are able to control their transpiration as well as the exchange of CO₂ and other trace gases. This mechanism is strongly influenced by external factors such as light intensity, leaf temperature, relative humidity, and soil water content. Similar to these properties, the stomatal exchange shows significant temporal variations especially on the diurnal and seasonal scale. Reactive gases like ozone or acids may be absorbed at the outer plant surface. In this case, the wetting effect of rain or dewfall becomes very important (Bieder et al., 1992). The physical and chemical characteristics of the surface change and, in particular, the affinity for water soluble species is drastically increased. Dissolved compounds on the plant surface can be released again when the film of water evaporates, or they can be washed off to the ground.

Quasi-laminar boundary layer

Turbulence represents the main transport and mixing mechanism for trace gases in the air near the surface (see next section). However, turbulent air motion alone is not able to transfer trace gas mole-

cules from/to solid and liquid surfaces. Due to the strong friction effects, the airflow is mainly laminar within a few millimetres above the surface (cf. St88:252). Trace gases can pass this thin 'quasi-laminar boundary layer' only by molecular diffusion, which is much less effective than turbulent mixing. With increasing distance from the surface, the effect of turbulence grows more and more, and the effect of molecular diffusion becomes negligible. All plant and soil surfaces are considered to be surrounded by a quasi-laminar boundary layer (cf. Fig. 2.1), where molecular diffusion limits the exchange processes.

2.1.2 Turbulent Transport in the Atmospheric Boundary Layer

Persisting atmospheric turbulence mainly occurs near the ground, because the surface provides the principal forcing effects for turbulent motion. The first driving force is shear stress in the mean horizontal air motion that is produced by friction at the surface. The strength of this mechanical turbulence production or 'forced convection' depends on the windspeed and on the surface roughness, and it is associated with the mean vertical gradient in the windspeed profile ($\overline{\partial u/\partial z}$). The overbar signifies a temporal average over a suitable interval, which is discussed later in Section 2.3.3. The second driving force for turbulence is buoyancy effects due to air density variations with height. It occurs mainly during daytime, when the surface, together with the lowest air layers, is heated by solar radiation. The warmer air at the ground is less dense than the layers above and rises inducing a turbulent turnover. This process is called thermal turbulence production or 'free convection'. The buoyancy of an air parcel is not only dependent on its temperature T , but also on the pressure p and the humidity conditions. Over land surfaces, the influence of humidity is usually small and is, therefore, often ignored (KF94:7). Following this practice, the buoyancy can be quantified by the 'potential temperature' θ referring to a standard pressure $p_0 = 1000$ hPa:

$$\theta = T \cdot \left(\frac{p_0}{p} \right)^{0.286} \quad (2.1)$$

If significant moisture effects are involved, θ has to be replaced by the virtual potential temperature (cf. St88:7). The mean vertical gradient of the potential temperature ($\overline{\partial \theta/\partial z}$) determines the static stability of an air layer. Thermal turbulence production occurs only if the gradient is negative (unstable stratification). A zero gradient indicates neutral and a positive gradient stable stratification. In the latter case, with dense cold air at the ground and warmer layers above, the negative buoyancy force moderates or even inhibits vertical turbulent mixing. According to the relative strength of shear and buoyancy forces, different turbulent regimes develop in the atmosphere near the surface. Figure 2.2 gives a rough classification of the possible turbulent states (dynamic stability states). For a quantitative characterisation of the dynamic stability, the Gradient Richardson Number Ri represents an appropriate parameter:

$$Ri = \frac{g/\overline{\theta} \cdot (\overline{\partial \theta/\partial z})}{(\overline{\partial u/\partial z})^2} \quad (2.2)$$

Ri is dimensionless and represents the ratio of the buoyancy (thermal) effect to the wind shear (mechanical) effect on turbulence (Richardson, 1938). The buoyancy force is represented by the gravity acceleration g and the vertical gradient of the potential temperature, which determines the sign of Ri . The denominator with the squared vertical gradient of horizontal windspeed is always positive. Richardson Numbers close to zero indicate predominant forced convection, large negative values indicate free convection. Both forms of convection often appear simultaneously creating 'mixed convection' at Ri

values around -1 . A Richardson Number larger than $+1$ signifies that the mechanical driving force is totally counterbalanced by the thermal damping and no turbulence can occur. The flow remains laminar and dynamically stable. But already at lower values, a critical point $Ri_{crit} \approx 0.2$ can be found, above which the turbulence is often interrupted and cannot fully develop. This state is called intermittent.

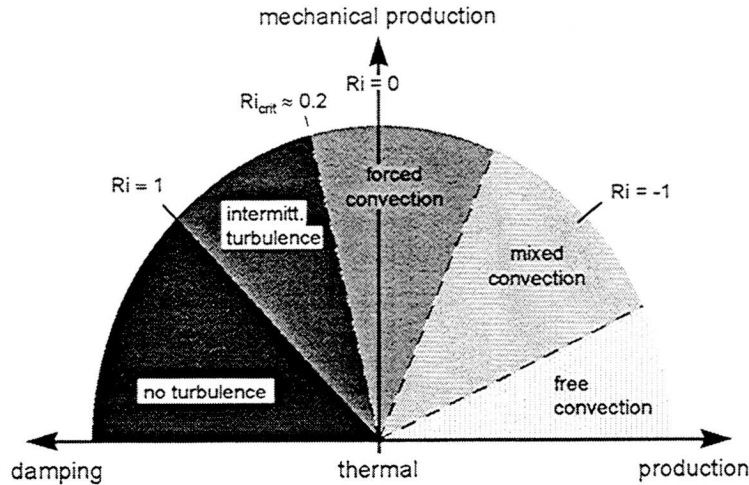


Fig. 2.2: Different turbulence regimes dependent on the strength of the production and/or damping mechanisms (after Stull, 1988: 158).

Because of the irregular fluctuating structure of turbulent air motion, a direct calculation of the flow field based on deterministic physical theory can not be realised in a suitable way. For a quantitative characterisation, statistical moments like average, variance or covariance have to be used. In a qualitative way, turbulence may be idealised as consisting of different-size swirls or eddies that are moving with the mean flow. The forcing mechanisms mentioned above are able to produce eddies up to length-scales of 10^2 to 10^3 metres. These large eddies contain the largest part of the turbulent kinetic energy, but they 'break up' and pass their energy in a cascade to smaller and smaller scale eddies. At very small scales (below ca. 10^{-2} metres) the turbulence is damped by viscous forces (molecular friction) and the turbulent kinetic energy is converted into heat. This process is called dissipation and it has the consequence that turbulence is not a self-preserving phenomenon but needs a continuous energy input from the producing forces.

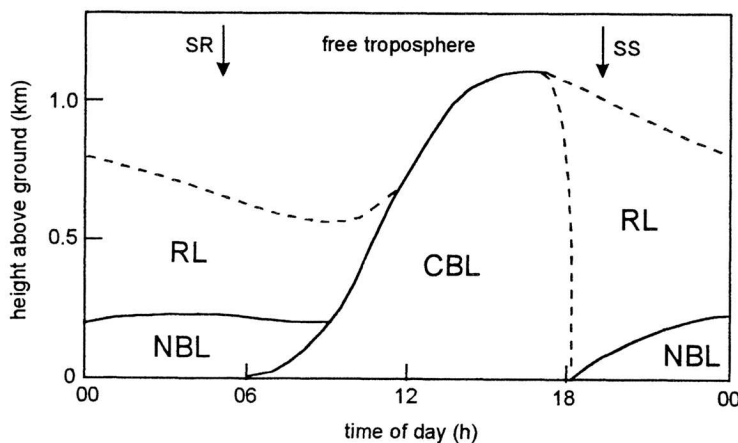


Fig. 2.3: Idealised diurnal course of boundary layer structure under clear sky conditions (after Oke, 1987); SR: sunrise, SS: sunset, CBL: convective boundary layer, NBL: nocturnal boundary layer, RL: residual layer.

The type and strength of turbulence controls its vertical extent and is, therefore, important for the trace gas exchange between surface and atmosphere. It determines how effective compounds emitted at the surface can be diluted in the atmosphere, or from which heights gases can reach the surface to be deposited. The part of the atmosphere that is in direct contact (in the time scale of one hour or less) with the surface through turbulent mixing is described as Planetary Boundary Layer (PBL). The depth of the PBL is strongly varying depending on surface structure, windspeed, and especially warming and cooling processes (see also Section 2.1.4).

An idealised diurnal course of the boundary layer structure is displayed in Figure 2.3. During daytime, with the help of thermal convection, the PBL reaches its largest extent up to a height of 1-2 km. This state is called Convective Boundary Layer (CBL); all properties show a generally well-mixed distribution with only small gradients. In the evening the surface begins to cool down by thermal radiation and creates a stable air stratification from below. Thus, thermal convection in the CBL decays and only mechanical turbulence persists near the ground. The Nocturnal Boundary Layer (NBL) is much thinner than the CBL (about 50-500 m) because the influence of roughness-generated turbulence decreases with height and is additionally damped by negative buoyancy effects. Above the NBL, a part of the daytime CBL remains as Residual Layer (RL). It is near-neutrally stratified and hardly turbulent. In weak wind conditions during night, it is possible that only intermittent turbulence occurs even at the surface and no clear boundary layer structure can be defined. After sunrise in the morning, the surface is again continuously heated by solar radiation creating thermal convection. Thus, a new CBL develops from the ground. After it has 'filled up' the nocturnal inversion, it grows rapidly to its full height. Although the CBL is normally limited at the top by a thermal inversion, the strong turbulence underneath leads to entrainment (local exchange) of air from the free atmosphere above.

2.1.3 Quantitative Description and Resistance Models

For the measurement and quantitative description of exchange processes, a corresponding physical measure (quantity) has to be defined. Trace gas exchange across a given surface or plane can be described in a suitable way as a scalar flux density, which is defined as transferred amount of matter (or mass) per unit time and per unit area.

$$\text{flux density} \equiv \frac{\text{transferred amount of matter}}{\text{time} \times \text{area}} \quad ; \quad F_c \equiv \frac{M_c}{\Delta t \cdot A} \quad (2.3)$$

In accordance with the common practice in literature, the terms 'flux' or 'exchange rate' are generally used here for the flux density. The amount of matter is given in the standard units *mol* resulting in flux units $mol\ m^{-2}\ s^{-1}$. These units are not very popular in micrometeorology, where mass fluxes ($kg\ m^{-2}\ s^{-1}$) are commonly used, but they lead to a considerable simplification of the formulas and calculations, especially if different trace gases are studied simultaneously. The physical foundation of trace gas fluxes depends on the underlying process. If a trace gas flux is created by passive transport with a directed air flow through the reference surface, it can be related to the local trace gas density ρ_c and the flow velocity component v_n normal to the reference plane:

$$F_c = v_n \cdot \rho_c \quad (2.4)$$

However, most transfer processes mentioned in Section 2.1.1 can not be described in this way, because they are not connected to the mean air flow but rather have a diffusive characteristic. A useful but

simplifying approach for the description of such processes is the so-called 'resistance analogy' (Thom, 1975; Oke, 1987: 70). The trace gas flux between two points is expressed in terms of the respective concentration difference $\Delta\rho_c$ and a resistance R , which restricts the exchange (equalisation) of the trace compound:

$$\text{flux} = -\frac{\text{concentration difference}}{\text{resistance}} \quad ; \quad F_c = -\frac{1}{R} \cdot \Delta\rho_c \quad . \quad (2.5)$$

The negative sign indicates that the direction of the flux is towards the lower concentration and thus opposite to the concentration gradient. Equation 2.5 is analogous to Ohm's Law that describes the electrical current as ratio of voltage (potential difference) and electrical resistance. With the flux and the concentration difference given in compatible units ($\text{mol m}^{-2} \text{s}^{-1}$ and mol m^{-3} respectively) the resistance R results in units s m^{-1} . Thus the reciprocal R^{-1} has the units of a velocity (m s^{-1}). In plant physiology it is called 'conductance' (Jones 1994: 52), whereas in certain micrometeorological studies (e.g. Müller et al., 1993) it is termed 'transfer velocity' v_{tr} :

$$F_c = -v_{tr} \cdot \Delta\rho_c \quad . \quad (2.6)$$

In analogy to electrical circuits, resistances can be combined in series ($R_{tot} = R_1 + R_2$) and in parallel ($R_{tot}^{-1} = R_1^{-1} + R_2^{-1}$). Accordingly, gas exchange systems can be displayed as resistance network diagrams. Figure 2.4a shows the schematic resistance network for the trace gas exchange of a vegetated surface after Hicks et al. (1987) and Erisman et al. (1994). The resistance formulation is useful only if the respective concentrations at the end points are defined (and can be determined). The air concentration $\rho_{c,air}$ in a certain height z is in general easily accessible, whereas the representative concentrations for plants ($\rho_{c,int}$ and $\rho_{c,ext}$) and for the soil ($\rho_{c,soil}$) imply some theoretical and practical problems. In the most simple case (e.g. for ozone, SO_2 , HNO_3), the concentrations in plants and soil can be set to zero, indicating that the compartments always act as a sink for the respective trace gases and that the deposition is irreversible (absolute). Hence, the proposed resistance network in Figure 2.4a is 'enclosed' between two defined concentration points and can be simplified significantly (Fig. 2.4b).

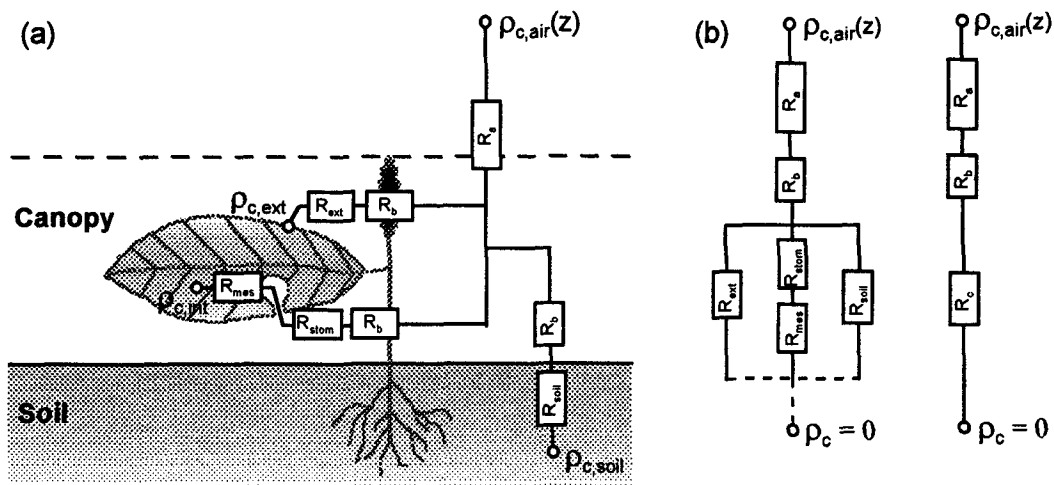


Fig. 2.4: (a) Resistance system for the trace gas exchange of a vegetated surface for dry deposition as proposed by Hicks et al. (1987) and Erisman et al. (1994). R_a : aerodynamic (turbulent) resistance, R_b : (quasi-laminar or viscous) boundary layer resistance, R_{stom} : stomatal resistance, R_{mes} : mesophyll resistance, R_{ext} : external leaf surface resistance, R_{soil} : soil resistance; (b) simplified resistance system for absolute deposition.

The different R_b values are assumed to be of similar size and are therefore unified. In addition, the parallel resistances for plant and soil exchange are often combined to form a single 'canopy resistance' R_c . It represents the effective surface resistance of the whole plant-soil-system. In this simple deposition model, the inverse of the total resistance (i.e. the total transfer velocity) is called 'deposition velocity' v_d (Hicks et al., 1987):

$$v_d(z) = \frac{1}{R_{\text{tot}}(z)} = \frac{1}{R_a(z) + R_b + R_c} = -\frac{F_c}{\rho_{c,\text{air}}(z)} \quad (2.7)$$

The deposition velocity (in contrast to the transfer velocity) has a simple and obvious physical meaning. It represents the mean vertical velocity of the trace gas molecules *towards* the surface caused by the deposition process. This quantity is equal to the (negative) ratio of flux and concentration, which is an important parameter not only for deposition but for trace gas exchange measurements in general, as will be seen later. For normalisation purposes, v_d is often given for the standard height $z = 1$ m.

The reverse case to absolute deposition, a general gas emission due to a defined non-zero reference concentration in the plant, is represented by the stomatal transpiration. Because the mesophyll walls are always wet, the relative air humidity in the sub-stomatal cavity is assumed to be 100%. The water vapour concentration, that can be calculated with the help of the actual leaf temperature, is usually higher than in the ambient air. For water soluble substances (acids, ammonia), the reference concentration in the plant or wet soil substrate may be set equivalent to the saturation vapour pressure, i.e. the equilibrium concentration according to Henry's law (Sutton et al., 1995; Gabriel et al., 1996; Nefel et al., 1997). Hence, an exchange in both directions is possible depending on whether the ambient air concentration is larger or smaller than the equilibrium concentration. Such a bidirectional behaviour as a function of the ambient concentration is also observed for many other compounds with more complex exchange processes, for example simultaneous production and consumption of NO, NO₂, COS and other compounds by different soil microbes (Conrad, 1994; 1995). The equilibrium concentration, at which the net flux is zero, is called 'compensation point'. It can be determined experimentally through measurements of the exchange rate at (naturally or artificially) varying ambient concentrations.

Resistances as well as compensation points are generally not constant in time and space but vary with environmental and physiological conditions. For use in models, corresponding parameterisation schemes of all resistances and the important compounds are proposed in the literature (see reviews by Wesely, 1989; Erisman et al., 1994). The turbulent and quasi-laminar boundary layer resistance are mainly a function of windspeed and surface roughness, whereas the stomatal resistance depends on plant type and growing state, light intensity, leaf temperature and water status (Jones, 1994: 145f.). While the turbulent resistance R_a is assumed to be equal for all trace gases (see later, Section 2.4), the other resistances depend more or less on the molecular structure (molecular diffusion coefficient) and chemical characteristics of the trace gas.

The resistance model in Fig. 2.4a is, in a strict sense, only valid for a single leaf (or leaf layer), because the environmental factors controlling the resistances can vary strongly within the canopy. In order to overcome this problem, multilayer models have been applied with a detailed treatment of leaf area, light, temperature and wind distribution inside the canopy (e.g. Baldocchi, 1988; Kondo and Watanabe, 1992). But it has been shown (Raupach et al., 1986; Raupach, 1989; Denmead, 1995), that this approach often fails to give an appropriate simulation of the turbulent exchange within the canopy. In any form, resistance models are simplifying reality and need many assumptions. Therefore, they have clear limitations for the physical description and determination of trace gas exchange. Nevertheless, such

models can be a useful tool to estimate and compare the importance of the different processes involved. Often, they represent the only practical method for parameterising the boundary conditions for complex air chemistry/transport models.

2.1.4 Surface Energy Budget

Similar to trace gases, energy in different forms is absorbed and emitted at the surface. The energy exchange is of special importance for the understanding and determination of the trace gas fluxes for several reasons. First, it determines the microclimatic state of a vegetated surface (e.g. radiation, humidity, leaf and soil temperature) and the overlying air layers (thermal turbulence production, stability) and thus influences the exchange processes decisively. Secondly, the transport of mass related (sensible and latent) energy in the air is supposed to be analogous to the transport of trace compounds. This analogy can be very helpful for the determination of exchange characteristics (e.g. resistances), because the energy content of the air can usually be measured easier and more accurately than trace gas concentrations. Moreover, there are independent methods for the determination and verification of energy fluxes, that do not exist for trace compounds.

In contrast to trace gases, energy can be transported in several different forms. The most obvious form is the radiative transfer that is usually divided into shortwave and longwave transfer with a threshold wavelength of 4000 nm. Shortwave radiation from the sun is the main external controlling factor for the surface energy budget and creates a characteristic diurnal variation. The incoming solar radiation is partly reflected and partly transformed to other energy forms: mainly sensible heat (enthalpie, appearing as temperature change) and latent heat (evaporation of water). The sensible heat is either stored and conducted inside the solid/liquid phase (vegetation, water, soil) or it is transferred to the adjacent air, where it undergoes the turbulent mixing processes similar to the trace gases. The latter way is also taken by the latent heat represented by water vapour. Both energy forms may also be transferred in the reversed way, what mainly happens during night time when no solar radiation is coming in. The Earth's surface also emits thermal radiation in the longwave range according to its temperature and absorption/emission coefficient. At the same time, it absorbs longwave radiation emitted by the atmosphere and the clouds.

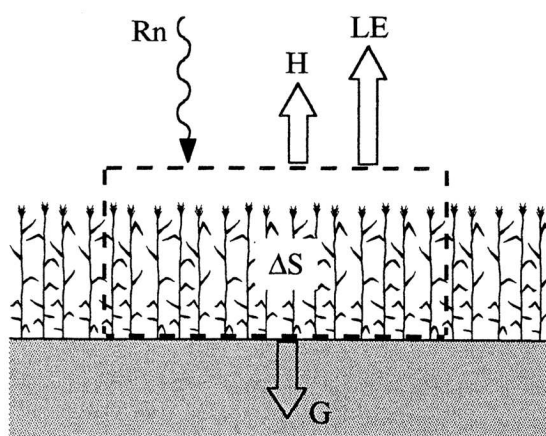


Fig. 2.5: Components of the surface energy budget after Oke (1987). The directions of the arrows indicate positive fluxes. R_n : net radiation flux, H : sensible heat flux, LE : latent heat flux, G : soil heat flux, ΔS : energy storage change in the canopy layer.

For an ideal homogeneous surface, the energy exchange can be simplified to a one-dimensional problem in the vertical direction. According to the energy conservation law, the increase of energy in a certain reference volume is equal to the sum of fluxes into the volume. For convenience, the reference volume is usually chosen to contain just the canopy layer (see Fig. 2.5). Thus, the energy conservation law can be written as:

$$\Delta S = R_n - G - H - LE \quad (2.8)$$

ΔS describes the energy storage change within the canopy and the other terms represent the vertical energy fluxes through the top and bottom limits of the vegetation layer. All components are usually given in analogy to the definition of trace gas fluxes (Eq. 2.3) in units of energy per time and area ($J m^{-2} s^{-1} = W m^{-2}$). G stands for the conductive heat flux into the soil, H and LE for the turbulent transport of sensible and latent heat with the air through the top of the canopy and R_n for the net radiative energy flux into the canopy. The positive direction of the different fluxes is defined by convention as indicated by the arrows in Fig. 2.6 (cf. Oke, 1987: 111). In some cases, especially for low vegetation, the storage term is so small compared to the others that it may be ignored (Thom, 1975: 97). In the context of turbulent flux measurements, Eq. 2.8 is usually rearranged by grouping the turbulent and the non-turbulent energy fluxes:

$$H + LE = R_n - G - \Delta S \quad (2.9)$$

The sum of the non-turbulent fluxes on the right hand side is sometimes called 'available energy', indicating that it is available for turbulent transport to the atmosphere. Whether it is transported mainly as sensible or as latent heat strongly depends on the vegetation type and activity as well as on the availability of water. The Bowen-ratio $\beta = H/LE$ (Bowen, 1926) representing the ratio of both turbulent fluxes is, therefore, an often used quantity for characterising vegetated surfaces. The closure of the energy budget, i.e. the validity of Eq. 2.9, can be used to test the quality of flux measurements if all components are determined individually. Alternatively, one unknown energy flux can be calculated as residual of Eq. 2.9.

2.2 Measurement Principles for Trace Gas Exchange

2.2.1 Basic Considerations

For the determination of trace gas exchange between the plant-soil-system and the air, one of the three quantitative relationships 2.3, 2.4, or 2.5 has to be applied. In the first concept (Eq. 2.3), the corresponding mass change in one of the two compartments (biosphere or atmosphere) has to be measured. The surface (canopy and soil) may appear more appropriate at first sight, because it is easily accessible and has a limited vertical extension. However, most trace compounds are chemically converted when absorbed or released at the surface and thus are difficult to identify in the solid or liquid phase of plants and soil. Moreover, the relative mass change is so small, that it can hardly be detected except for special compounds and situations. Among the gaseous atmospheric compounds, only water vapour is exchanged in such amounts, that a mass change of the liquid phase at the surface can be resolved in the time scale of days or hours with the help of lysimeters or dew balances (cf. Brutsaert, 1982: 248). Over several days or weeks, a significant mass change of organic carbon in growing vegetation (assimilated and respired exclusively as CO_2) may also be detected. For ionic species like sulphate deposited on

external leaf surfaces, the 'throughfall' and 'stemflow' methods sometimes provide valuable results (Lindberg et al., 1986; Lovett and Lindberg, 1993). They make use of the washing effect due to precipitation water, which is collected above and below the canopy layer. The difference in ionic concentrations is a measure for dry deposition to the washed surfaces between two precipitation events.

In the atmosphere (gas phase), the detection of even small trace gas concentrations is comparatively easy and accurate. Exchange measurement methods in the air compartment are usually based on the mass conservation law:

$$V \frac{\partial \langle \rho_c \rangle_v}{\partial t} = \sum_{i=0}^m A_i \cdot F_{c,i} \quad (2.10)$$

The mass change (increase) in a reference volume V is equal to the net inward flux through its boundary areas A_i (see Fig. 2.6). The triangular brackets around the trace gas concentration signify a spatial average over V . For a reference volume directly above the surface, relationship 2.10 can be rearranged for the surface exchange flux $F_{c,\text{surf}}$, which is defined upward by convention (i.e. the flux into the volume V through the bottom area A_0):

$$F_{c,\text{surf}} \equiv F_{c,0} = \frac{1}{A_0} \left(V \frac{\partial \langle \rho_c \rangle_v}{\partial t} - \sum_{i=1}^m A_i \cdot F_{c,i} \right) \quad (2.11)$$

For practical purposes, the reference volume should be chosen in such a way, that as many terms as possible on the right hand side of Eq. 2.11 vanish (are equal to zero). This can be realised either by the application of artificial enclosures (Section 2.2.2) or by taking advantage of suitable natural environmental conditions (Section 2.2.3).

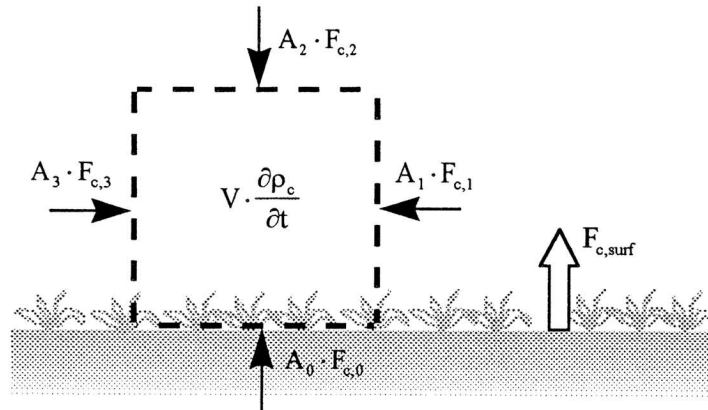


Fig. 2.6: Illustration of the mass conservation of a trace gas with density ρ_c within a reference volume V directly above the surface (Eq. 2.11); $F_{c,\text{surf}}$: surface exchange flux, $F_{c,i}$: fluxes through volume boundary areas A_i .

2.2.2 Enclosure Techniques

The most simple application of Equation 2.11 is represented by the so-called static chamber method (see Livingston and Hutchinson, 1995). The chamber is placed on the investigated surface and is closed against the surrounding air (see Fig. 2.7a). Thus the surface exchange is proportional to the concentration change with time inside the enclosed volume. In order to create reproducible conditions and to

facilitate the trace gas measurements, the enclosed air volume should be well mixed leading to an almost uniform concentration distribution. For an enclosure of height h_{encl} , a basal surface A_{encl} , the adaption of Equation 2.11 leads to:

$$F_{c,\text{surf}} = \frac{V}{A_{\text{encl}}} \cdot \frac{\partial \langle \rho_c \rangle_v}{\partial t} = h_{\text{encl}} \cdot \frac{\partial \langle \rho_c \rangle_v}{\partial t} \quad (2.12)$$

In the alternative approach, the dynamic chamber method, the temporal derivative in Eq. 2.11 is set to zero by creating stationary conditions inside the enclosure. This is obtained by a continuous flushing of the chamber at an appropriate rate, replacing the air volume typically one or more times per minute (cf. Ludwig, 1994; Kuhn et al., 1997). The airflow in and out of the enclosure can be guided through tubes, where the volume flowrate Q and the trace gas concentrations ρ_c can be easily measured (see Fig. 2.7b). The surface exchange is then given by:

$$F_{c,\text{surf}} = \frac{1}{A_{\text{encl}}} (Q_{\text{out}} \rho_{c,\text{out}} - Q_{\text{in}} \rho_{c,\text{in}}) \quad (2.13)$$

Even if the chamber is totally closed except for inlet and outlet, the two air volume flowrates Q_{in} and Q_{out} are in general not strictly equal. Through exchange processes inside the chamber, the mass of the sweep air (by addition of water vapour) as well as its density (by changes in temperature) can be modified. However, in many cases these effects can be neglected or the concentrations can be normalised to standard conditions. Hence Equation 2.13 reduces to:

$$F_{c,\text{surf}} = \frac{Q}{A_{\text{encl}}} (\rho_{c,\text{out}} - \rho_{c,\text{in}}) \quad (2.14)$$

In order to create conditions as representative as possible, the dynamic chamber should be flushed with ambient air. In the past, a lot of experiments were made with zero sweep air (free of the investigated trace gas). However, this procedure can result in big deviations (even an opposite sign) from the flux values under natural conditions (Castro and Galloway, 1991). Like in the static case, the air inside the dynamic chamber should be well mixed to assure defined conditions. Enclosure techniques may not only be applied to surface areas but also to individual plant parts (branches or single leaves). This is often the only possible procedure for higher vegetation like forest or high crops (e.g. maize). Moreover, special plant parts can be studied as separated from the rest of the canopy. The size of cuvette systems can range from small (1 cm^2) single-leaf chambers for portable porometers to large ($>10 \text{ m}^2$) chambers that can enclose bigger plants or canopy areas (Jones, 1994: 177).

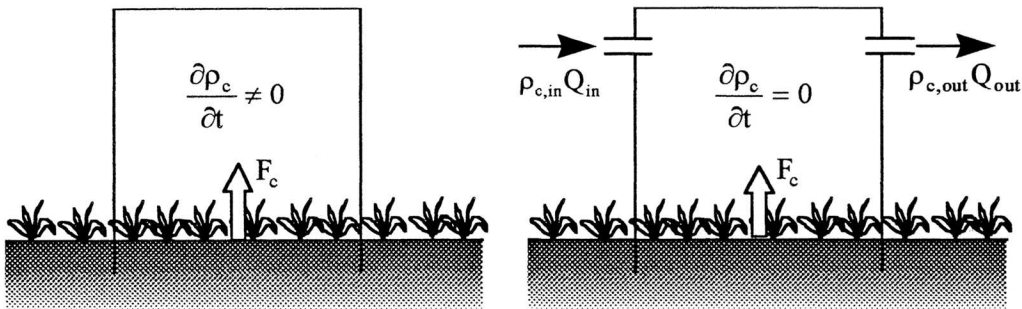


Fig. 2.7: Schematic enclosure systems for measuring trace gas surface exchange: (a) static system, (b) dynamic system; F_c : trace gas surface flux, ρ_c : trace gas density; Q : air volume flowrate.

Every chamber creates its own special microclimate and trace gas concentration and is therefore not able to measure fully representative exchange rates. The differences to the ambient conditions depend on setup characteristics like the transparency of the box material and on the flushing rate. Concerning the latter effect, the static chambers show the largest deviations. For dynamic chambers, the flushing rate may only be set as high as the concentration difference between in- and outlet can be resolved. Another negative characteristic is the potential occurrence of chemical reactions in the enclosed volume and on the artificial surfaces (chamber material). Therefore an empty chamber ('blind box') is frequently operated simultaneously to the probing chamber, in order to estimate this effects (Ludwig, 1994; Meixner et al., 1997). Nevertheless, special care must be taken in the choice and test of the used materials.

2.2.3 Micrometeorological Concepts

Similar measurement principles as for the enclosure methods can also be applied in the undisturbed atmospheric environment, if certain 'ideal' conditions are met. The most important requirement is the local horizontal homogeneity of the surface and thus of the trace gas exchange. It implies, that horizontal exchange processes can be neglected and only vertical transport has to be considered. Thus the problem becomes merely one-dimensional and allows spatially representative flux measurements at one location. The effective extension of the required horizontal homogeneity is discussed in Section 2.6.

In addition to trace gas concentrations, micrometeorological methods need information about physical properties like the temperature or the wind vector in order to determine the dynamic state of the air. For convenience, the coordinate system in micrometeorology is not chosen fixed but always aligned to the mean wind vector as shown in Figure 2.8. Two axes of the right-handed rectangular system are parallel to the surface, the first one (x) points in the direction of the mean wind flow. The third axis (z) is set perpendicular to the previous two and thus gives the height above the surface. The instantaneous wind vector, that fluctuates around the mean vector due to turbulent motion, is given by the corresponding components (u , v , w).

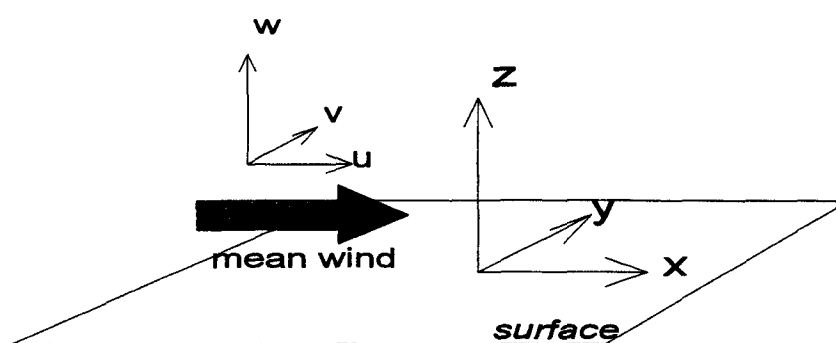


Fig. 2.8: Micrometeorological coordinate system (x,y,z) and wind components (u,v,w).

Boundary Layer Budget

The trace gas exchange at the Earth's surface creates local concentration surplus or deficit in the adjacent air layers. Usually, these effects are distributed very fast (in the timescale of minutes to hours) throughout the whole PBL by turbulent mixing. An idealised PBL thus represents a well-mixed closed chamber and the surface flux can be described according to Equation 2.12. However, in real conditions (especially during daytime), it has to be considered, that the PBL is not constant in height (cf. Fig. 2.3)

and continuously mixes with overlying air layers while growing. Additionally, horizontal advection cannot be neglected in general. For taking into account these effects, the PBL has to be investigated intensively in three dimensions by aircraft measurements (cf. Betts et al., 1992; Gallagher et al., 1994). During nighttime, however, the boundary layer height h_{PBL} and its temporal variations are comparatively small. Due to usually low windspeeds, advection effects as well as turbulent transfer at the top of the nocturnal boundary layer may often be neglected. In that case, the surface flux can be determined in analogy to the static chamber from the concentration change in the turbulent layer. Since the concentration generally varies with height z , the concentration profile has to be integrated (averaged) over z :

$$F_{c,\text{surf}} = \frac{\partial}{\partial t} \int_0^{h_{\text{PBL}}} \rho_c(z) \cdot dz = h_{\text{PBL}} \frac{\partial \langle \rho_c \rangle_z}{\partial t} \quad (2.15)$$

This method requires information about the temporal development of the trace gas profile up to a height of a few tens to a few hundreds of meters. They are obtained for example with sensors carried by a tethered balloon (Choularton et al., 1995; Colbeck and Harrison, 1985; Mihalopoulos et al., 1989; Sprung, 1993). Such measurements are difficult to perform for most trace gases and are hardly possible on an operational basis. It has to be considered that a measured boundary layer profile is representative for the underlying surface only if the exchange flux is relatively homogeneous over a large region, which is often difficult to find, especially in populated areas. Moreover, Equation 2.15 is only valid, if the respective trace compound is not subjected to any conversion process (i.e. chemical or photochemical reactions).

'Constant flux layer'

If not the whole PBL can be measured or if a horizontally limited surface area has to be investigated, the surface exchange has to be determined from measurements close to the ground. For that purpose, it has to be known, how the vertical turbulent flux varies in the boundary layer. Typically, the vertical fluxes are largest at the surface, where trace gases are emitted or deposited and decrease in magnitude towards the top of the PBL (Wyngaard, 1973). In experimental studies, an approximately linear decrease with height is often observed e.g. for sensible heat, water vapour, or ozone (St88; Beier and Weber, 1992). Based on this idealised behaviour illustrated in Fig. 2.9, the concept of the 'surface layer' (SL) was developed as the lowest 10% of the PBL (PD84:113).

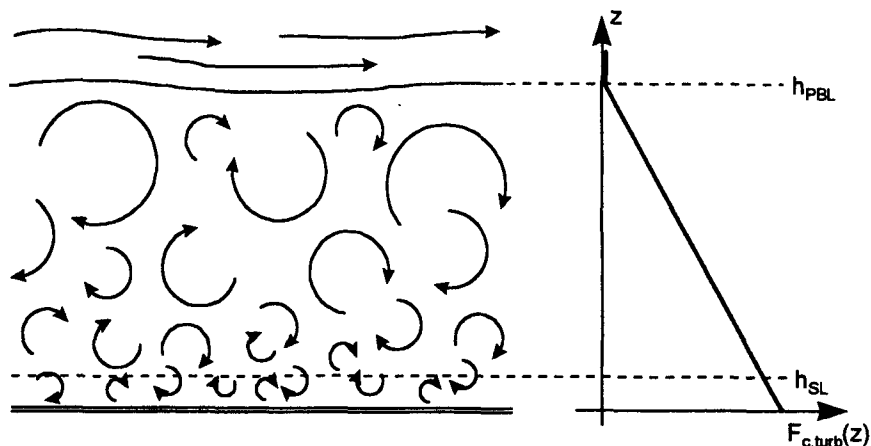


Fig. 2.9: Idealised height dependency of vertical turbulent trace gas fluxes in the atmospheric boundary layer. The surface layer (of height h_{SL}) is defined as the lowest 10% of the planetary boundary layer (of height h_{PBL}) and includes flux variations of only about 10%.

The variability of the vertical fluxes in the SL is assumed to be only 10% or less, which is usually below detectability and may be ignored for many purposes. Corresponding experimental studies are reported for example by Haugen et al. (1971) or Dyer and Hicks (1972) (for a review, see Sprung, 1993). Thus the fluxes in the surface layer are treated as roughly constant with height, and the SL is also called 'constant flux layer'. For unstable daytime conditions, the surface layer definition and the constant flux assumption are usually not problematic. A typical CBL height of 1 km results in a surface layer height of 100 m. During nighttime, a more careful and restrictive view is required. Under strongly stable conditions, the flux is likely to decrease with height faster than linearly (KF94:26), because the intensity of turbulent mixing also diminishes with height. In this case, an alternative definition of the surface layer based on stability (see Section 2.4) may be more appropriate.

Another problem, that must be considered, is the lower limit of the constant flux layer. Even a homogeneous vegetated surface consists of single canopy elements (trees, plants, plant rows) that create characteristic concentration and windfield patterns around them. Only at a certain height z_* above the canopy, these are totally mixed up by the turbulent air motion. As a consequence, the surface layer is divided into the 'roughness sublayer' that is influenced by single roughness elements and the 'inertial sublayer' where the fluxes are assumed to be horizontally and vertically constant (see Fig. 2.10). The height of the roughness sublayer (z_*) depends strongly on the size, form and distribution of the roughness elements. Rotach (1991) gives an overview over some relationships but mainly for artificial surfaces. For forests, Garratt (1978) found a z_* value of three times the canopy height.

Despite the mentioned problems and limitations, the constant flux layer concept represents the basis for several micrometeorological flux measurement techniques. They all make use of the assumption, that the interesting surface exchange flux is equal to the vertical turbulent flux $F_{c,turb}$ at any height z within the inertial sublayer:

$$F_{c,turb}(z) \approx \text{const.} \approx F_{c,surf} \quad (z_* \leq z \leq 0.1 \cdot h_{PBL}) \quad (2.16)$$

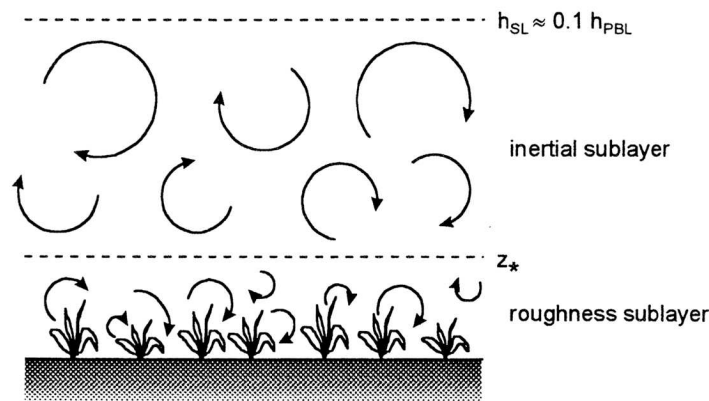


Fig. 2.10: Surface layer (SL) above a homogeneous surface, divided into roughness sublayer (influenced by single roughness elements) and inertial sublayer (vertically and horizontally constant flux).

The turbulent vertical fluxes are measured following two different approaches. The eddy correlation and eddy accumulation techniques (Sections 2.3 and 2.5) try to resolve the instantaneous locally directed upward and downward flux (according to Eq. 2.6) connected with the turbulent eddies. The profile methods (Section 2.4.2), on the other hand, try to determine the turbulent resistance (Eq. 2.5) between different heights (with different trace gas concentrations) within the inertial sublayer. The constant flux

layer methods belong to the most widely used flux measurement techniques, because they allow to measure the trace gas exchange of whole ecosystems under natural environmental conditions. Since the fundamentals of these techniques are quite complex but very important for the objectives of this study, they will be discussed together with the existing application types in full detail in the following sections.

In the following part of the manuscript, all flux quantities (if not indicated otherwise) are meant to be surface exchange fluxes or vertical turbulent fluxes in the inertial sublayer, which are considered to be equal according to the constant flux layer concept (Eq. 2.16).

2.3 Eddy Correlation Method

2.3.1 Ergodicity and Taylor Hypothesis

The most direct physical approach for the measurement of turbulent trace gas fluxes is the application of Equation 2.4 for a horizontal reference plane on a certain height z within the constant flux layer. At each point in space, the instantaneous local vertical flux is equal to the product of the vertical windspeed component w and the trace gas concentration ρ_c . However, the irregular characteristic of turbulent motion implies a strong variation of the instantaneous vertical transport in time as well as in space. Hence certain averaging procedures have to be applied in order to get useful flux estimates. Ideally, an ensemble average should be determined, i.e. an average over many realisations under identical conditions (KF94:255). Thus the surface flux (equal to the vertical turbulent flux at a certain height z) can be written as:

$$F_c = F_{c,\text{turb}}(z) = \left\langle w(z) \cdot \rho_c(z) \right\rangle_{\text{ensemble}} \quad (2.17)$$

For laboratory measurements, this is the most suitable procedure, but it can not be applied in field experiments, because the natural atmospheric conditions are not reproducible. Fortunately it can be assumed, that under stationary conditions, the turbulent motion over a homogeneous surface represents an ergodic system (St88:37), signifying that the ensemble average is about equal to the respective spatial or temporal average (i.e. that the estimates of all three average types converge to the same value):

$$F_c = \left\langle w(z) \cdot \rho_c(z) \right\rangle_{\text{ensemble}} \approx \left\langle w(z) \cdot \rho_c(z) \right\rangle_{\text{area}} \approx \left\langle w(z) \cdot \rho_c(z) \right\rangle_{\text{time}} \quad (2.18)$$

The limitations of this concept are discussed by PD84:99. In micrometeorological flux studies, mainly the time average is applied, since it allows to determine a representative flux with a sensor system fixed at one single point within the inertial sublayer. The trace gas flux is calculated according to Eq. 2.19 as the integral covariance of the time series $w(t)$ and $\rho_c(t)$ over a suitable time interval T_a (see following section). The corresponding flux determination method is commonly called 'eddy correlation' technique, although 'eddy covariance' would be the more appropriate name.

$$F_c = \frac{1}{T_a} \int_{T_i} w(t) \cdot \rho_c(t) dt \quad (2.19)$$

From the time series recorded by a fixed sensor, not only average turbulent properties can be derived. According to 'Taylor's hypothesis' they are also supposed to contain all information about the size distribution of the turbulence elements. Taylor (1938) suggested, that turbulent eddies can be considered to be frozen as they are carried along with the mean wind and pass a fixed point. An eddy of diameter (wavelength) λ_{eddy} , passing the sensor at height z with the mean windspeed $\bar{u}(t)$, will be recorded as a wavelike fluctuation of time period T (or frequency f respectively):

$$T = \frac{1}{f} = \frac{\lambda_{\text{eddy}}}{\bar{u}(z)} \quad (2.20)$$

Taylor's hypothesis has important implications for turbulent flux analysis, since it allows to interpret time series and spectra as representative spatial series and spectra. Thus information about the horizontal as well as vertical structure of the turbulent PBL can be obtained (Rotach, 1991: 27).

2.3.2 Turbulence Spectra

In order to be able to determine turbulent trace gas fluxes according to Equation 2.19, one has to know the distribution of the different eddy sizes (fluctuation periods) and their contribution to the turbulent mixing. On one hand the time average interval T_a has to be long enough to cover the contribution of the largest eddies and on the other hand temporal resolution of the measurements must be high enough to detect the contribution of the smallest eddies as well. The (superposed) wavelike fluctuations produced by the different eddy sizes can be separated and displayed by harmonic spectral analysis (cf. Appendix A). Variance spectra $S_x(f)$ and cospectra $Co_{xy}(f)$ show the contribution of the different frequencies f to the overall variance or covariance of any time series $x(t)$ and $y(t)$. For practical reasons, they are commonly displayed in the form $fS_x(f)$ versus $\log f$. In this representation, the area under the spectral curve is directly proportional to the variance (or covariance) connected to the respective frequency range.

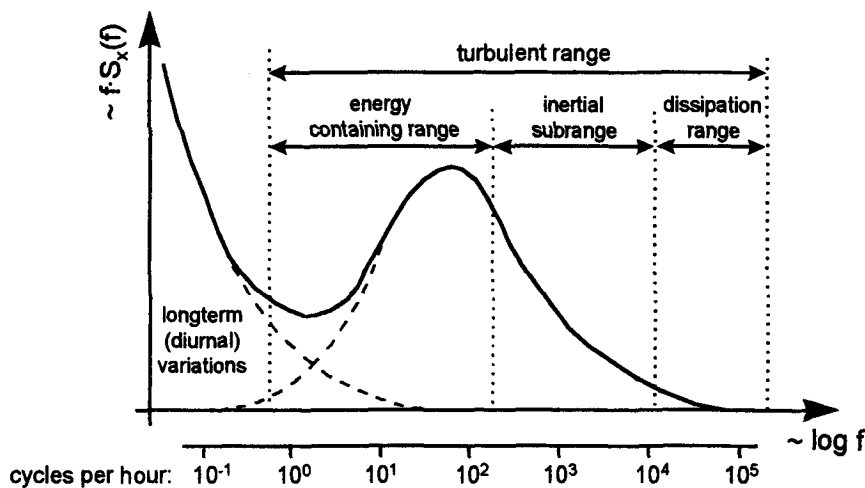


Fig. 2.11: Schematic diagram of spectral distribution of atmospheric fluctuations (e.g. windspeed, temperature, trace gas concentration) near the surface (cf. PD84; Wieringa, 1989).

Figure 2.11 shows a schematic variance spectrum of an air property (e.g. windspeed, temperature, gas concentration) near the surface. The scaling of the horizontal axis is only a rough estimate. The fluctuations due to turbulence are covering a frequency range of several orders of magnitude from about one

cycle per hour to several cycles per second. The width of the distribution and the position of the turbulent peak is dependent on the quantity x as well as on the stability conditions (see Appendix A.6). According to PD84:86, the turbulent variance spectra may partly overlap with longterm variations due to the diurnal cycle and synoptic weather changes. The overlapping is often weak enough to result in a spectral gap (minimum) that separates both ranges (see also Wieringa, 1989). But the gap can also be totally masked due to fast changing weather conditions (moving clouds, thunderstorms, fronts). This causes serious difficulties in the proper detection and separation of turbulent fluctuations. Only the vertical windspeed w is hardly affected by longterm variations and shows an undisturbed turbulence spectrum under ideal surface conditions.

The spectral range of turbulence is usually divided into three parts due to eddy production and destruction considerations (cf. chap. 2.1.2). In the *energy-containing range*, turbulence is produced by buoyancy and shear and thus the largest part of the turbulent kinetic energy is contained there. In the *inertial subrange*, turbulent energy is neither produced nor consumed but transferred to smaller and smaller scales. Finally in the *dissipation range*, turbulent kinetic energy is converted to heat (internal energy). The form of spectra and cospectra can be described mathematically according to Kaimal et al. (1972; 1976). They investigated near surface turbulence spectra in detail and developed semi-empirical models based on similarity considerations (see Section 2.4.1). The resulting functions ('Kaimal-spectra') are described in Appendix A.6; they are the most widely accepted models for turbulence spectra available in literature. Although derived from windspeed and temperature measurements only, they are commonly adopted for other scalar quantities like trace gas concentrations.

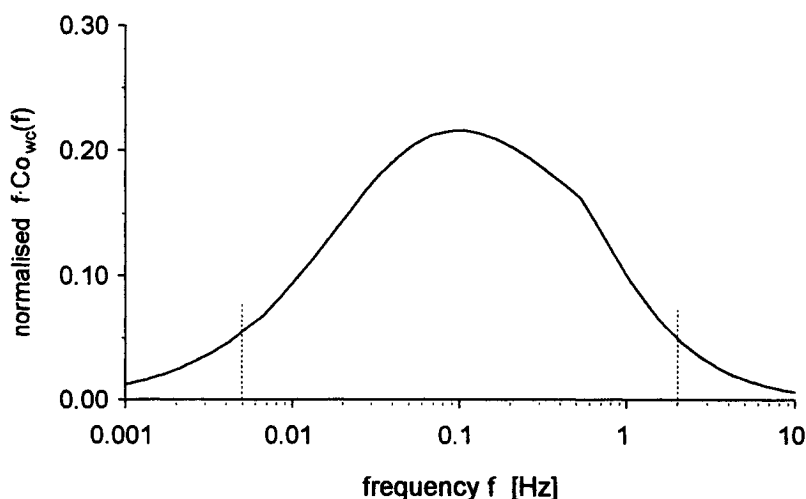


Fig. 2.12: Semi-empirical normalised cospectrum after Kaimal et al. (1972) for a scalar flux under typical daytime (unstable) conditions over low vegetation: measurement height $z = 5$ m, windspeed $u = 5$ m s⁻¹ (after Lenschow, 1995).

The model spectra give important information about the requirements concerning the sensor response and averaging interval for the eddy correlation method. Figure 2.12 shows the Kaimal cospectrum for the turbulent trace gas flux under typical daytime measurements conditions over low vegetation. According to Lenschow (1995), the dashed vertical lines at $f_{\min} = 0.005$ Hz and $f_{\max} = 2$ Hz indicate the frequencies at which the curve falls off to about 20% of its maximum. The area and thus the flux contained within these limits corresponds to about 93% of the total turbulent flux and represents a usually acceptable deviation for micrometeorological measurements. The lower frequency limit f_{\min} corresponds to a time period of 200 s. However, this may not be sufficient as averaging interval T_a , because it allows

the recording of only one cycle (eddy) of the corresponding frequency. For a more representative sampling, an averaging period about one order of magnitude longer is required (Delany, 1993). In most cases, a value for T_a between 10 min and 60 min is applied. On the other end of the spectrum, f_{\max} corresponds to a time period of 0.5 s, which represents an upper limit for the required temporal resolution of the measurements. However, the value estimated from Fig. 2.12 only applies for unstable (daytime) conditions. In stable conditions the covariance spectra are shifted towards higher frequencies (see Appendix A.6) making even faster response times necessary. Usually, a time resolution of ca. 0.1 s (10 Hz) is sufficient for eddy correlation measurements (Monteith and Unsworth, 1990). Thus a total frequency range of about four decades (ca. 0.001...10 Hz) has to be resolved.

2.3.3 Statistical Description of Turbulence

In order to distinguish between turbulent and systematic longterm variations, atmospheric quantities are commonly split into a mean and a fluctuating part:

$$x(t) = \bar{x} + x'(t) . \quad (2.21)$$

This splitting procedure is called 'Reynolds decomposition' after its inventor. The overbar denotes a time average of the variable $x(t)$ over an interval of length T_a , and x' is the instantaneous deviation from it. The averaging time T_a has to be chosen appropriately to cover even the largest eddies (cf. foregoing section). In the most common form, the overbar represents a simple block average over T_a :

$$\bar{x} = \frac{1}{T_a} \int_0^{T_a} x(t) dt . \quad (2.22)$$

However, for a better elimination (filtering) of longterm disturbances in the turbulent range (cf. Fig. 2.11), the overbar may also represent a linear trend function or a running average (see Section 4.1.1). The Reynolds decomposition as described by the Equations 2.21 and 2.22 implies some simple calculation rules:

$$\overline{x'} = 0 \quad (2.23a)$$

$$\overline{x + y} = \bar{x} + \bar{y} \quad (2.23b)$$

$$\overline{\bar{x} \cdot y} = \bar{x} \cdot \bar{y} . \quad (2.23c)$$

Besides the arithmetic mean (Eq. 2.22), also higher statistical moments are represented by a comprehensible short-hand notation:

$$\text{variance: } \text{var}(x) = \overline{x'^2} \quad (2.24a)$$

$$\text{covariance: } \text{cov}(x, y) = \overline{x' y'} . \quad (2.24b)$$

The Reynolds averaging procedure can be applied to all scalar air properties (i.e. gas concentrations, temperature, energy, ...) but also to the wind vector or its directional components respectively. Thus the mean vertical turbulent flux of a trace gas (Eq. 2.19) can be written as

$$F_c = \overline{w \cdot \rho_c} . \quad (2.25)$$

The decomposition of both w and ρ_c then yields

$$F_c = \overline{(\bar{w} + w')(\bar{\rho}_c + \rho_c')} = \overline{\bar{w} \bar{\rho}_c} + \overline{\bar{w} \rho_c'} + \overline{w' \bar{\rho}_c} + \overline{w' \rho_c'} = \overline{\bar{w} \bar{\rho}_c} + \overline{w' \rho_c'} . \quad (2.26)$$

The two middle terms are eliminated according to Equations 2.23a/c. The last term represents the so called eddy covariance between trace gas concentration and vertical windspeed. The first term contains the mean vertical velocity that needs further discussion. The mass conservation over a homogeneous surface prohibits a mean air flow perpendicular to the surface:

$$\overline{\rho_a \cdot w} = 0 . \quad (2.27)$$

ρ_a denotes the density of dry air, since the exchange of water vapour at the surface can affect the mass balance at least in extreme situations. Equation 2.27 is not fully equivalent to a zero vertical windspeed because the surface exchange of sensible heat (warming or cooling of the air) and water vapour induces density variations which are correlated to the vertical motion. Although the corresponding \bar{w} value is only in the order of 10^{-3} to 10^{-4} m s⁻¹ (Chahuneau et al., 1989), it can not be ignored in general. The relative importance for Eq. 2.26 results from the multiplication with $\bar{\rho}_c$, which is often much larger than the turbulent fluctuations ρ_c' . In order to eliminate the average terms, Webb et al. (1980) suggest an alternative representation of the trace gas concentration by the mixing ratio μ_c (in respect to dry air density ρ_a):

$$\mu_c \equiv \rho_c / \rho_a . \quad (2.28)$$

In contrast to the mixing ratio definition used by Webb et al. (1980), μ_c here does not represent a specific (mass) mixing ratio but rather a molecular (or volume) mixing ratio, which is more convenient for trace gas calculations. Thus Equation 2.25 can be rewritten as

$$F_c = \overline{\mu_c \rho_a w} = \overline{\bar{\mu}_c \bar{\rho}_a w} + \overline{\mu_c' (\rho_a w)'} . \quad (2.29)$$

According to Eq. 2.27, the first term equals zero. The second term can be expanded and finally reduced to Eq. 2.30, because some minor terms may be neglected without causing significant error (cf. Webb et al., 1980).

$$F_c = \overline{\bar{\rho}_a w' \mu_c'} \quad (2.30)$$

Relationship 2.30 is assumed to be equivalent to Eq. 2.25 (and 2.26) to a close approximation. The fact, that the eddy flux corresponds to the covariance of w with the mixing ratio μ_c rather than with the absolute trace gas concentration ρ_c can also be explained by an alternative comprehensible consideration. Let us assume a trace gas that is totally passive in the atmosphere and is not exchanged at the surface (i.e. $F_c = 0$). Whereas μ_c is not influenced by physical processes and thus constant in time and space, ρ_c can be altered through changes in temperature (change in total molecular density) or water vapour (dilution effect). Since water vapour and temperature usually show fluctuations correlated to the vertical wind, a covariance of ρ_c with w is induced that does not represent a real flux.

Of special significance for turbulent transport are the fluxes of (horizontal) momentum and sensible heat. They represent the mechanical and thermal turbulence production and are therefore important parameters for the characterisation of the turbulent state of the boundary layer. Moreover, their characteristics are often studied as exemplary for trace gas fluxes, because the momentum (proportional to the horizontal windspeed u) and the sensible heat (proportional to the temperature T) can be determined

faster, cheaper and more accurately than trace gas concentrations. The momentum flux (or shear stress) τ and the sensible heat flux H are written in analogy to Equation 2.30:

$$\tau = -m_a \bar{\rho} \overline{u'w'} \quad (2.31)$$

$$H = c_p m_a \bar{\rho} \overline{w'T'} \quad (2.32)$$

c_p represents the specific heat capacity and m_a the effective molecular mass of the air. The flux of latent heat LE (cf. Section 2.1.4) results from the water vapour gas flux by multiplication with the molar air density, the molecular mass of water m_{H_2O} and the specific heat of vaporisation L_v :

$$LE = L_v m_{H_2O} \bar{\rho} \overline{w'\mu_{H_2O}'} \quad (2.33)$$

For convenience, the turbulent fluxes (2.30...2.33) are often represented in the kinematic form, i.e. divided by the (quasi-) constant factors like air density, heat capacity, etc. Kinematic fluxes consist simply of a covariance term $\overline{w'x'}$, and they are not mass related in contrast to the dynamic forms given by Eqs. 2.30...2.33.

2.3.4 Application of the Eddy Correlation Method

The eddy correlation method needs a generally high temporal resolution in the detection of trace gas concentrations as well as of the vertical windspeed. Additionally the requirements for the precision and synchronicity of the fast measurements are relatively high. The vertical windspeed or even the three-dimensional wind vector can be detected with sufficient precision and temporal resolution by sonic anemometer instruments. For many applications, the performance of propeller anemometers is also sufficient (cf. KF94:215). However, the fast detection of trace gases is a much more difficult task. Only in recent years, appropriate instruments (integration time < 1 s) for some compounds like water vapour, ozone, CO_2 , N_2O , NO_2 or methane have been developed and applied (cf. Baldocchi et al., 1988). They are either based on optical absorption detection (non-dispersive IR, UV, tunable diode laser TDL) or on fast chemoluminescent reactions with photon counting (see e.g. Zeller et al., 1989; Güsten et al., 1992, Wienhold et al., 1994). Such instruments are usually quite expensive and need intensive maintenance. Most of them are therefore not suitable for longterm monitoring purposes.

For the majority of trace gases, no fast sensors appropriate for eddy correlation measurements are available at all up to now. Many compounds have to be scrubbed from the air and accumulated over several minutes in wet denuders, carbon cartridges or cryo-traps before they can be analysed with sophisticated chromatographic and spectrometric methods. Often, the analysis cannot be carried out in the field but has to be done later in the laboratory. A survey of the 'state of the art' of the analytical techniques for most atmospheric trace gases is given in Matson and Harriss (1995).

In the eddy correlation method, data are recorded usually at a fixed rate, i.e. with a constant sampling interval Δt , which is determined by the spectral requirements discussed in Section 2.3.2 and the response characteristics of the sensor. However, a regular continuous recording of w and μ_c is not absolutely necessary for a covariance calculation. A representative number of data points from the time series may be sufficient to get an appropriate covariance estimate. According to KF94:256, 200 data points yield a result with a statistical uncertainty of about 10%. Yet, the response or integration time of the sensor must be still as short as with a continuous measurement. Lenschow et al. (1994) discuss a special implementation of the eddy correlation technique, that takes advantage of the possibility for 'disjunct'

sampling. Air samples are collected quickly within an appropriate time interval Δt into an intermediate storage volume. There they can be analysed with a slower response instrument, until the next sample has to be taken. With the mentioned number of 200 samples for a typical averaging interval of 30 minutes, an analysing time of still less than 10 s would be available. Considering the technical problems, this approach therefore provides only little relaxation compared to the common continuous measurement and does not appear very promising for most applications. Moreover, some common analysing procedures like spectral analysis cannot be performed with intermittent time series.

The eddy correlation theory requires not only fast but also fully synchronous measurements of vertical windspeed and trace gas concentration at the same point. In practice, a certain distance between the two sensors usually has to be kept, so that they do not disturb each other. This sensor separation leads to a loss in covariance, because the contribution of the smallest eddies (smaller than the separation distance) cannot be detected (Businger, 1986; Moore, 1986). A direct in-situ analysis of the ambient air with 'open-path-instruments' could be applied up to now mainly for water vapour and CO₂ (see e.g. Auble and Meyers, 1992). Most eddy correlation systems use 'closed path analysers', i.e. with a sampling tube, the ambient air is directed in a continuous stream from the inlet close to the anemometer (mounted on a mast) to the gas analyser, that is located usually on the ground several meters away from the actual measurement point. In this case, the delay time between both measurements and possible attenuation effects of the tube have to be considered (McMillen, 1988; Leuning and Moncrieff, 1990; Lenschow and Raupach, 1991).

2.4 Semi-empirical Relationships for Turbulent Fluxes

The eddy correlation method for trace gas measurements could be applied in practice only during about the last three decades, and it is up to now only available for a limited number of trace gases. Therefore a need for less direct but more simple methods existed since a long time. As one alternative to the eddy correlation technique, relationships between turbulent fluxes and other statistical properties of the surface layer may be used to determine trace gas exchange. Although the chaotic turbulent motion cannot be described in an exact physical way, the mean state (described through statistical moments like average, variance, etc.) is supposed to be clearly defined under given ideal conditions. According to the Monin-Obukhov-similarity-theory (MOST), originally presented by Monin and Obukhov (1958), the statistics of surface layer turbulence may be described by only few independent governing parameters. Yet, the relationships between the different statistical quantities cannot be derived from first principles. They must be obtained by best fits of arbitrary functions to measured data. The finding of suitable functions is simplified significantly by the application of 'dimensional analysis' (see Section 2.4.1). The different turbulence conditions can be normalised to satisfy one universal relationship and are therefore called 'similar' (see e.g. Arya, 1988: 152). In practice, the turbulent fluxes are related to the corresponding mean profiles or variances in the surface layer (Sections 2.4.2 and 2.4.4) that are generally easier to measure than eddy covariances.

An additional simplification is given by the hypothesis, that the turbulent transfer is fully analogous for all trace gases and also for scalar quantities like temperature or sensible heat (Thom, 1975: 74). This 'scalar analogy hypothesis' has important implications for the determination of the similarity relationships mentioned above, because temperature can be measured much easier and more accurately than trace gas concentrations (the also common term 'scalar similarity' is not used in this context to avoid

interference with similarity theory). But there are legitimate doubts about the general validity of scalar analogy (e.g. Beier and Weber, 1992), because the experimental results available until now show a considerable scatter and are restricted mainly to temperature and humidity measurements. Especially the analogy between temperature and trace gases is questioned, because temperature (sensible heat) is not a purely passively transported quantity but controls the turbulent exchange to a considerable extent especially under extreme stability conditions (cf. Katul and Parlange, 1994). Only a partial analogy is generally found between the fluxes of trace gases and momentum (proportional to horizontal windspeed) which has to be considered always as an active quantity, because it is closely connected to the mechanical turbulence production.

2.4.1 Dimensional Analysis and Similarity-Theory for the Surface Layer

In the atmospheric surface layer (inertial sublayer) under ideal conditions, the description of statistical turbulence characteristics turns out to be relatively simple. The assumption of horizontal homogeneity leads to an essentially one-dimensional problem that can be characterised by the height z and some additional quantities, which are supposed to be constant with height (cf. Section 2.2.3). Table 2.1a shows the set of key variables that has been identified by Monin and Obukhov (1958) to explain all statistical properties of the turbulent motion in the surface layer (see also Holtslag and Nieuwstadt, 1986). By including the surface flux of a particular trace gas as a supplementary variable (Tab. 2.1b), the characteristics of the respective trace gas distribution and transport are also defined.

Tab. 2.1: Key variables for the turbulent transport of a trace gas in the surface layer (constant flux layer): (a) key variables for the turbulent motion according to MOST; (b) additional parameter for the trace gas distribution and transport. All fluxes are given in the kinematic form.

(a) z	height above the surface (limits the size of the eddies and thus the effective mixing length)
g/T	buoyancy parameter (vertical acceleration due to density variations)
$\overline{u'w'}$	vertical surface flux of momentum (related to mechanical turbulence production)
$\overline{w'T'}$	vertical surface flux of sensible heat (related to thermal turbulence production)
(b) $\overline{w'\mu_c'}$	vertical surface flux of the trace gas c

Thus any statistical characteristic q of the turbulent trace gas transport in the surface layer can be described as a unique function of the above set of key variables:

$$q = f(z, g/T, \overline{u'w'}, \overline{w'T'}, \overline{w'\mu_c'}) . \quad (2.34)$$

The appropriate function f must be found empirically (fit to measured data) because of the lack of physical foundation. This is in principle a difficult multidimensional problem, since f is a function of $n = 5$ variables. Dimensional analysis facilitates this task significantly by converting Equation 2.34 into a fully equivalent relationship of *dimensionless* variables:

$$\frac{q}{q_*} = F(\Pi_1, \dots, \Pi_m) . \quad (2.35)$$

The left hand side is made dimensionless by dividing the quantity q of interest by a scaling variable q_* of the same units. On the right hand side, the variables are combined among themselves to dimensionless groups. The new variables Π_i as well as q_* have to be formed by power products of the original set of key variables:

$$q_* = \dots ; \Pi_i = (z)^a \cdot (g/T)^b \cdot (\overline{u'w'})^c \cdot (\overline{w'T'})^d \cdot (\overline{w'\mu_c'})^e . \quad (2.36)$$

According to the Buckingham-Pi-theorem (Arya, 1988: 133; St88:350), exactly $m = n - r$ independent Π -groups can be formed from n variables and r fundamental units involved. In the present example n equals 5 and the fundamental SI-units used are: length (m), time (s), temperature (K), and amount of matter (moles). Therefore only $m = 5 - 4 = 1$ independent Π -group can be formed. Relationship 2.35 thus simplifies to:

$$\frac{q}{q_*} = F(\Pi) . \quad (2.37)$$

For scaling (making dimensionless) any quantity q of interest, so-called 'scaling variables' or 'scales' with simple dimensions like length, concentration, velocity, etc. are formed according to Eq. 2.36. Table 2.2 shows the scaling variables commonly used in surface layer similarity theory. This set of variables is fully equivalent with the one in Table 2.1, since all original key variables were included and may be reproduced by the reversed procedure. The negative signs in Equations 2.39...2.41 and also the constant factor k in Eq. 2.38 are introduced by convention (see later, Eq. 2.44).

Tab 2.2: *Scaling variables for the turbulent transport in the surface layer: (a) scales for the turbulent motion according to MOST; (b) additional scale for the trace gas concentration.*

(a) length scales:	z 'aerodynamic height' (cf. next section)	
	$L \equiv -k^{-1} (-\overline{w'u'})^{3/2} (g/T)^{-1} (\overline{w'T'})^{-1}$	'Obukhov length' (2.38)
velocity scale:	$u_* \equiv (-\overline{w'u'})^{1/2}$	'friction velocity' (2.39)
temperature scale:	$T_* \equiv -\overline{w'T'} \cdot (-\overline{w'u'})^{-1/2} = -\overline{w'T'}/u_*$	(2.40)
(b) trace gas conc. scale:	$\mu_{c*} \equiv -\overline{w'\mu_c'} \cdot (-\overline{w'u'})^{-1/2} = -\overline{w'\mu_c'}/u_*$	(2.41)

Since the variable sets in Tables 2.1 and 2.2 are equivalent, the dimensionless group Π (Eq. 2.37) for the surface layer turbulence can be formed from the scaling variables in Table 2.2. It is evident, that the only possible dimensionless combination is the ratio of the two length scales z and L . Hence, if appropriately scaled, all statistical quantities of the surface layer can be described by a unique similarity function of z/L :

$$\frac{q}{q_*} = F\left(\frac{z}{L}\right) . \quad (2.42a)$$

The empirical similarity function F in Equation 2.42a is much easier to analyse and to fit to measured data than the relationship in Eq. 2.34, because it connects merely two independent variables (q/q_*) and (z/L), and thus it can be displayed in a two-dimensional diagram. The numerical form of the similarity relationship is often determined by first studying the behaviour under special conditions, e.g. neutral or extreme stability conditions (cf. Ga92:50). The surface layer relationships turn out to be particularly simple under neutral conditions, because z/L is zero (due to zero heat flux) and in that case, the scaled quantities q/q_* must be constant:

$$\frac{q}{q_*} = \text{const.} \quad (\text{neutral conditions}) . \quad (2.42b)$$

According to the definitions given in Table 2.2, the vertical kinematic fluxes in the surface layer can be formulated as a product of scaling variables that represent the influence of both quantities of the eddy covariance. The momentum flux is split into two identical factors u_* , the scalar fluxes into a combination of u_* and the respective scalar scaling quantity, i.e. the temperature or a trace gas concentration scale T_* or μ_{c*} :

$$\overline{w'u'} = -u_* \cdot u_* \quad (2.43a)$$

$$\overline{w'T'} = -u_* \cdot T_* \quad (2.43b)$$

$$\overline{w'\mu_c'} = -u_* \cdot \mu_{c*} . \quad (2.43c)$$

It has to be noticed, that u_* is positive by definition; the sign of the other scaling variables is therefore always opposite to the respective flux.

2.4.2 Flux-Profile-Relationships

The similarity theory outlined in the previous section may be used to relate turbulent fluxes to mean quantities (mean profiles and gradients), that can be measured accurately enough with slow response instruments. For convenience, the similarity relationship for the mean vertical concentration gradient $q = \partial\bar{\mu}_c/\partial z$ under neutral conditions is first considered here. According to Equation 2.42b, the quantity of interest has to be made dimensionless by the scaling variables in Tab. 2.2. The resulting 'dimensionless concentration gradient' is then equal to a constant, which is written as $1/k$ by convention:

$$\frac{\partial\bar{\mu}_c}{\partial z} \cdot \frac{z}{\mu_{c*}} = \text{const.} \equiv \frac{1}{k} . \quad (2.44)$$

The 'von-Karman-constant' k which is equal to 0.4 represents the ratio between the effective turbulent mixing length and the distance to the surface (cf. St88:208). It was found to be equal for all air properties. In the general non-neutral case ($z/L \neq 0$), the similarity function according to Eq. 2.42a has to be found. It is commonly written as an extension of the neutral case (Eq. 2.44) with the constant k moved to the left hand side:

$$\frac{\partial \bar{\mu}_c}{\partial z} \cdot \frac{k z}{\mu_{c*}} = \Phi_c(z/L) . \quad (2.45)$$

The Φ -functions were empirically fitted to measured datasets, for convenience separately for the stable and the unstable range. They were found to be generally equal for scalar quantities (trace gases, potential temperature), but not for momentum (or windspeed u) in unstable conditions. Various mathematical forms for the Φ -functions are proposed in the literature but they do not differ very much (cf. Högström, 1988). In this study, the functions originally proposed by Dyer (1974) are used because of their frequent application and their simple numerical form.

$$\Phi_c = \Phi_T = \Phi_u = 1 + 5 \cdot z/L \quad \text{stable conditions } (z/L \geq 0) \quad (2.46)$$

$$\Phi_c = \Phi_T = [1 - 16 \cdot z/L]^{-1/2} \quad (2.47a)$$

$$\Phi_u = [1 - 16 \cdot z/L]^{-1/4} \quad (2.47b)$$

} unstable conditions ($z/L \leq 0$)

In order to get an analytical formula for the profile $\mu_c(z)$, the differential relationship 2.45 has to be integrated over z . It is only meaningful to integrate between two heights z_1 and z_2 within the inertial sublayer and therefore in general only a relationship for a profile difference is obtained. The simple neutral case (Eq. 2.44) leads to the following profile function:

$$\bar{\mu}_c(z_2) - \bar{\mu}_c(z_1) = \int_{z_1}^{z_2} \frac{\partial \bar{\mu}_c}{\partial z} dz = \frac{\mu_{c*}}{k} \int_{z_1}^{z_2} \frac{1}{z} dz = \frac{\mu_{c*}}{k} \ln(z_2/z_1) . \quad (2.48a)$$

This is the famous logarithmic profile form, that can be observed for all air properties in the surface layer under neutral condition. The general (non-neutral) profile function contains additional terms, which represent the deviation from the ideal logarithmic shape:

$$\Delta \bar{\mu}_c = \bar{\mu}_c(z_2) - \bar{\mu}_c(z_1) = \frac{\mu_{c*}}{k} [\ln(z_2/z_1) - \Psi_c(z_2/L) + \Psi_c(z_1/L)] . \quad (2.48b)$$

The Ψ -functions are called 'integrated similarity functions' or 'stability correction functions', because they represent the deviation from the neutral logarithmic profile. Paulson (1970) evaluated the involved integrals analytically from the similarity functions 2.46 and 2.47. The numerical form of the resulting functions are given in Section 4.2. The turbulent trace gas fluxes can be related to a measured profile difference by solving either Eq. 2.45 or 2.48b for the scaling quantity μ_{c*} and inserting it into 2.43c. This results in a differential (2.49) or integral (2.50) flux-profile-relationship:

$$\overline{w' \mu_c'} = - \underbrace{\left(\frac{u_* k z}{\Phi_c(z/L)} \right)}_{=: K_c} \cdot \frac{\partial \bar{\mu}_c}{\partial z} \quad (2.49)$$

$$\overline{w' \mu_c'} = - \underbrace{\left(\frac{u_* k}{\ln(z_2/z_1) - \Psi_c(z_2/L) + \Psi_c(z_1/L)} \right)}_{=: v_{tr}} \cdot \Delta \bar{\mu}_c . \quad (2.50)$$

The trace gas flux is expressed as a product of the mean profile gradient or difference and a factor (K_c or v_{tr}) describing the turbulent state in the respective air layer. In analogy to the similarly looking Fick's

law for molecular diffusion, the term K_c is called 'turbulent diffusion coefficient' or 'eddy diffusivity'. But the analogy has to be regarded rather as formal than physical, because the molecular K-theory predicts fluxes in any concentration field, whereas the above relationships only applies in the special case of the homogeneous stationary constant flux layer. The turbulent exchange is not generally proportional to the local concentration gradient, because the large eddies are able to exchange air masses directly between distant air layers. This fact explains why the extension of the flux-profile-relationships to cases including sources and sinks (e.g. inside a canopy layer or with chemical reactions) generally fails (KF84:89). Some authors like e.g. Oke (1988) propose a direct application of the differential relationship (2.49) by estimating the derivative through a ratio of finite differences, but this simplification is generally not very accurate and unnecessary, because the integral flux-profile-relationship (2.50) can be used without additional approximations.

The factor v_{tr} defined through Eq. 2.50 has units $m\ s^{-1}$ and corresponds to the transfer velocity already introduced in Eq. 2.6. It represents the inverse resistance of the turbulent transport (mixing) between two heights. However, here the relationship is formulated with the mixing ratio μ_c instead of the absolute gas density ρ_c . According to Webb et al. (1980), the use of the mixing ratio profile is more appropriate because it avoids interference due to density effects of temperature and humidity (similar as discussed for the eddy correlation method in Section 2.3.3).

Application of flux-profile-relationships

There exist various application techniques for the measurement of trace gas fluxes according to the flux-profile relationship 2.50. They all require data of the average trace gas mixing ratio at (at least) two different heights z_1 and z_2 within the inertial sublayer. However, they differ in the determination of the transfer velocity v_{tr} :

(a) pure profile method ('aerodynamic method')

v_{tr} is calculated according to Eq. 2.50 as a function of u_* and L . L can be related to u_* and T_* by combining Eqs. 2.38 and 2.43a/b, and these scaling quantities are determined from similarity relationships for wind- and temperature profiles analogously to Eq. 2.48b (cf. Nieuwstadt, 1978; Andersen et al., 1993; Müller et al., 1993):

$$L = - \frac{T \cdot u_*^2}{k \cdot g \cdot T_*} \quad (2.51)$$

$$u_* = \frac{k \cdot \Delta \bar{u}}{\ln(z_2/z_1) - \Psi_u(z_2/L) + \Psi_u(z_1/L)} \quad (2.52)$$

$$T_* = \frac{k \cdot \Delta \bar{\theta}}{\ln(z_2/z_1) - \Psi_T(z_2/L) + \Psi_T(z_1/L)} \quad (2.53)$$

Instead of the normal temperature profile, the difference of the potential temperature $\bar{\theta}$ has to be used for taking into account the adiabatic temperature decrease with height of ca. $0.01\ K\ m^{-1}$ in the neutrally stratified air.

(b) scalar analogy method ('modified Bowen ratio method')

v_{tr} is determined from independent flux and profile measurements of a reference scalar quantity (usually T or H₂O) utilising the scalar analogy hypothesis (cf. Müller et al. 1993; Meyers et al. 1996). The application is problematic, when the reference flux is small.

$$-v_{tr} = \frac{\overline{w'T'}}{\Delta\bar{\theta}} = \frac{\overline{w'\mu_{H_2O}'}}{\Delta\bar{\mu}_{H_2O}} = \dots \quad (2.54)$$

(c) energy balance method ('Bowen ratio method')

This method is based on (b) with the total energy content E (sum of latent and sensible heat) as reference scalar. The total turbulent energy flux is determined from measured non-turbulent energy fluxes R_n and G (cf. Section 2.1.4). The energy profile can be obtained from temperature and humidity profile measurements (cf. Hargreaves et al., 1992; Meixner, 1993). The application is problematic, when the sum of the turbulent energy fluxes (H+LE) is small (Ohmura, 1982).

$$-v_{tr} = \frac{\overline{w'E'}}{\Delta\bar{E}} = \frac{H + LE}{\rho c_p \Delta\bar{\theta} + \rho L_v \Delta\bar{\mu}_{H_2O}} = \frac{R_n - G}{\rho (c_p \Delta\bar{\theta} + L_v \Delta\bar{\mu}_{H_2O})} \quad (2.55)$$

(d) miscellaneous methods

v_{tr} (or u_* and T_* respectively) is determined from momentum and sensible heat flux measurements by other methods, e.g. eddy correlation.

The choice of appropriate measurement heights for the profile techniques is influenced by several aspects. First, the measurement levels should have a large vertical distance in order to get concentration differences large enough that they can be resolved accurately with the available sensors and analytical techniques. According to the near logarithmic profile shapes (Eq. 2.48b) the differences are largest near the surface and decrease quickly with height. Therefore, it would be desirable to set the lower measurement level close to the surface. However, all measurements should be made above the roughness sublayer height z_* (cf. Section 2.2.3), because the similarity relationships are valid only in the inertial sublayer. This is usually a problem over tall vegetation like forests, where often at least the lowest level has to be set within the roughness sublayer due to limitations of tower height and sensor resolution (KF84:73; Schween, 1993).

2.4.3 Displacement Height and Roughness Length

One of the most important parameters in surface layer similarity relationships is the 'height above the surface' z . It is generally not identical with the geometric height above the solid soil but represents an effective distance from the surface as experienced by turbulent eddies. Over vegetated surfaces, it depends on how deep the turbulence can penetrate the canopy layer and is thus determined by the density and the geometry of the roughness elements, i.e. the distribution of plants and leaves (Thom, 1971). For practical purposes, the geometrical height z_g above the ground (soil surface) is measured and the effective aerodynamic height z is described by introducing the so called displacement height d :

$$z = z_g - d \quad (2.56)$$

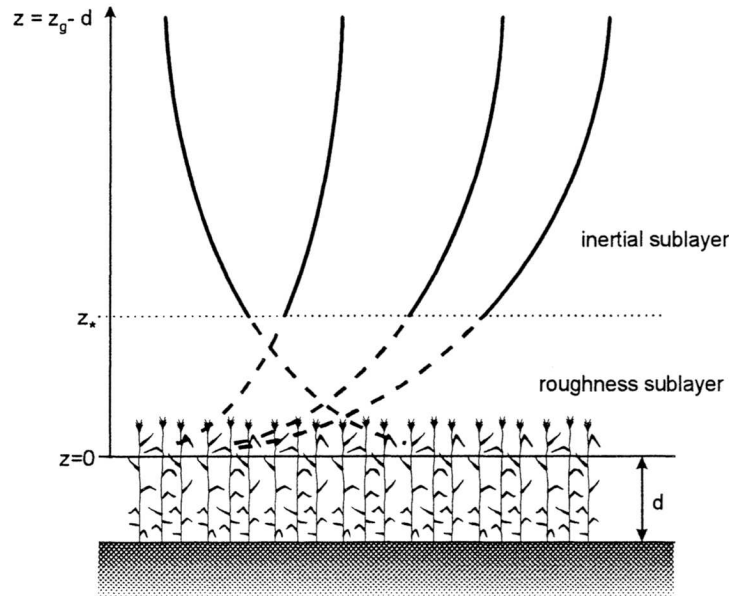


Fig. 2.13: Near-logarithmic profiles of atmospheric quantities (trace gas concentrations, temperature, windspeed; scaled arbitrarily) under varying conditions as observed in the inertial sublayer (solid lines) and extrapolated into the roughness sublayer (dashed lines). All profiles converge at the zero-plane displacement height d above the ground.

The displacement height has a very graphic and comprehensible meaning for the profiles of trace gas concentrations and other quantities in the surface layer. It represents the asymptotic lower limit, where the near-logarithmic profiles of the inertial sublayer converge to, if they are extrapolated downwards into the roughness sublayer or canopy layer (see Fig. 2.13). The real profiles within the roughness sublayer usually deviate from the logarithmic form (see Fig. 2.14). It is commonly assumed, that the displacement height, which is actually a property of the inertial sublayer, is characteristically related to the geometry of the canopy and thus constant for a given (homogeneous) surface and that it is equal for all atmospheric quantities (Rotach, 1991; Ga92:86). However, an experimental verification is very difficult due to the strong sensitivity on measurement errors and non-ideal environmental conditions (e.g. surface inhomogeneity).

For flux calculations with the Bowen ratio or modified Bowen ratio method (Eqs. 2.54 and 2.55), the displacement height is not required. However, in the aerodynamic profile method and variance similarity relationships (see following section), the displacement height may only be neglected if the measurement heights are much larger than the canopy height and thus $z \gg d$ (usual for measurements over bare ground, low or cut grass, harvested agricultural fields). The proper determination of d is most important (and difficult) over tall vegetation like forest. Corresponding experimental methods based on micrometeorological measurements are described by Rotach (1991; 1994), Schween (1993), and Lo (1995). The displacement height may also be estimated from the height of the canopy by the simple empirical relationship 2.57. According to Brutsaert (1982: 116) and Ga92:86, an average value of $\alpha = 2/3$ seems to be fairly representative for many natural vegetated surfaces, in particular for crops and forests. However, some scatter in individual cases has to be expected, mainly due to the different density of the vegetation canopies.

$$d = \alpha \cdot h_{\text{canopy}} \quad (2.57)$$

Another parameter, that was empirically found to be more or less constant for a given surface and thus can serve to simplify the flux-profile-relationships, is the so-called 'roughness length' z_0 . It describes the height above displacement level, where the downward extrapolated windspeed profiles reach zero (see Fig. 2.14), and it can be related to the geometry (height, spacing) of the roughness elements of the surface (Wieringa, 1993). If z_0 is known, it can be used as (theoretical) lower reference level of the wind profile with $u(z_0) = 0$. Thus Equation 2.52 can be reduced and reformulated to give an explicit mathematical function for the wind profile with variable parameters u_* and L :

$$\bar{u}(z) = \frac{u_*}{k} \left[\ln(z/z_0) - \Psi_u(z/L) + \Psi_u(z_0/L) \right] . \quad (2.58)$$

In model calculations, z_0 is often used as (effective) lower limit for turbulent transport and thus for the parameterisation of the turbulent aerodynamic resistance R_a (cf. Hicks et al., 1987).

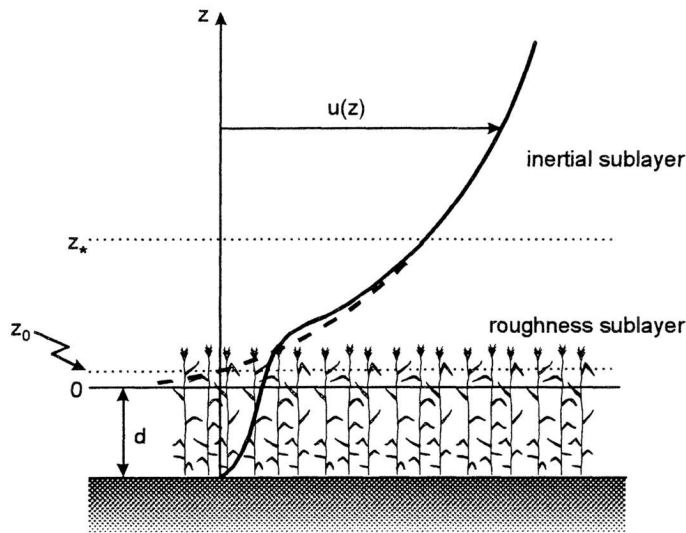


Fig. 2.14: Schematic profile of windspeed $u(z)$ in the inertial and roughness sublayer above and within a crop canopy, with indication of the displacement height d and the roughness length z_0 . Solid line: real profile; dashed line: ideal extrapolated near-logarithmic profile function.

2.4.4 Variance Similarity

In analogy to the profile relationships discussed in Section 2.4.2, similarity theory can be used to relate trace gas fluxes to the corresponding variance of mixing ratio. In practice, the similarity relationships according to Eq. 2.42a are usually written in terms of standard deviation rather than of variance. The standard deviation of a trace gas concentration $\sigma(\mu_c)$ can be made dimensionless simply by scaling with the concentration scale μ_{c*} defined through Eq. 2.41. Since the standard deviation is always positive, it is scaled with the absolute value of μ_{c*} . Thus the similarity relationship takes the form:

$$\frac{\sigma(\mu_c)}{|\mu_{c*}|} = \varphi_c(z/L) . \quad (2.59)$$

Like in the profile methods, the trace gas flux can be determined from this relationship in combination with Eqs. 2.43c and 2.51, if the turbulence parameters u_* and T_* are known. However, whereas the similarity relationships for gradients and profiles are well established and verified in numerous experi-

ments under different conditions (cf. Höglström, 1988), the functions for standard deviations are based on only few experiments and show relatively large scatter (cf. Padro, 1993; Katul et al., 1995). Moreover, the sign of μ_{c*} and thus of the direction of the flux is not defined and has to be obtained by other means, if it is not obvious.

For the flux calculation from standard deviation measurements, there are in principle the same four methods (a)-(d) as described in Section 2.4.2 with the Δ -terms replaced by the corresponding standard deviations. A review over the different techniques is given by Wesely (1988) and Wichura and Foken (1995). The most common technique is the analogue to the modified Bowen ratio method (Eq. 2.54). The assumption, that the similarity function $\varphi_c(z/L)$ is equal for all scalar quantities, leads to the following relationship:

$$\frac{|F_1|}{\sigma_1} = \frac{|F_2|}{\sigma_2} = \frac{|F_3|}{\sigma_3} = \dots \quad (\text{for different scalar quantities } 1, 2, 3, \dots) . \quad (2.60)$$

Wesely (1988) calls this method 'standard deviation ratio', because any trace gas flux can be calculated, if the flux of another scalar and the ratio of both standard deviations are known. It is usually applied using the sensible heat or water vapour flux, because they are easiest to measure with other techniques. The energy balance approach (Eq. 2.55) may also be adopted for standard deviation measurements. Some experimental investigations are reported by Hicks and McMillen (1988). The analogue to the aerodynamic profile method (Eqs. 2.52 and 2.53) is the determination of u_* and T_* by relationships similar to Eq. 2.59:

$$\frac{\sigma(w)}{u_*} = \varphi_w(z/L) \approx \begin{cases} 125(1 - 3z/L)^{1/3} & \text{unstable conditions} \\ 125(1 + 0.2z/L) & \text{stable conditions} \end{cases} \quad (2.61)$$

$$\frac{\sigma(T)}{|T_*|} = \varphi_T(z/L) \approx \begin{cases} 2(1 - 9.5z/L)^{-1/3} & \text{unstable conditions} \\ 2(1 + 0.5z/L)^{-1} & \text{stable conditions} . \end{cases} \quad (2.62)$$

The numerical form of the similarity functions is taken from KF94:16). According to the scalar analogy hypothesis (Section 2.4.1), the form of the φ_T -function (Eq. 2.62) is usually adopted for the variance relationship of trace gas concentrations (Eq. 2.59). The friction velocity u_* may be related in principle to the standard deviations of all three wind components. However, the relationship for $\sigma(u)$ and $\sigma(v)$ seem not to scale uniquely with the surface layer parameter z/L (Ga92:72) and can be used in this context only for neutral conditions. PD84:160 give the following constants as averages of a literature review:

$$\frac{\sigma(u)}{u_*} = 2.4 \quad \frac{\sigma(v)}{u_*} = 1.9 \quad \text{neutral conditions } (z/L = 0) . \quad (2.63a/b)$$

Correlation coefficient

The variances (or standard deviations) of trace gas concentration and vertical windspeed are formally related to the covariance flux through the correlation coefficient r_{wc} , defined as:

$$r_{wc} \equiv \frac{\overline{w'\mu_c'}}{\sqrt{\text{var}(w) \cdot \text{var}(\mu_c)}} = \frac{\overline{w'\mu_c'}}{\sigma(w) \cdot \sigma(\mu_c)} . \quad (2.64)$$

The correlation coefficient is a general measure for the linear dependence of two quantities (time series). The optimal values (no deviations from a linear relationship) are +1 or -1. In contrast, r equals zero, if two quantities have no dependence at all (e.g. white noise). The combination of Equation 2.64 with 2.59, 2.61 and 2.43c yields a relationship for the correlation coefficient r_{wc} only dependent on z/L :

$$|r_{wc}| = [\varphi_w(z/L) \cdot \varphi_c(z/L)]^{-1} . \quad (2.65)$$

Hence, according to similarity theory, the correlation coefficient for turbulent scalar transport is only dependent on the height z and the stability state of the turbulent surface layer. In Fig. 2.15 this relationship is displayed based on the numerical functions given in Eqs. 2.61 and 2.62. The sign of r_{wc} depends on the direction of the flux (emission or deposition). In the stable range, an increase with stability is produced that cannot be found in experimental data. Instead, Businger and Delany (1990) as well as KF94:20 suggest a constant value of about 0.4. The correlation coefficient for the vertical exchange of momentum (vector quantity) is somewhat lower than for the scalar quantities and is always negative due to the surface friction. According to KF94, an overall constant value $r_{uw} \approx -0.35$ represents a good approximation, whereas Hicks (1981) reports a variation of r_{uw} between -0.2 for unstable and -0.4 for stable conditions.

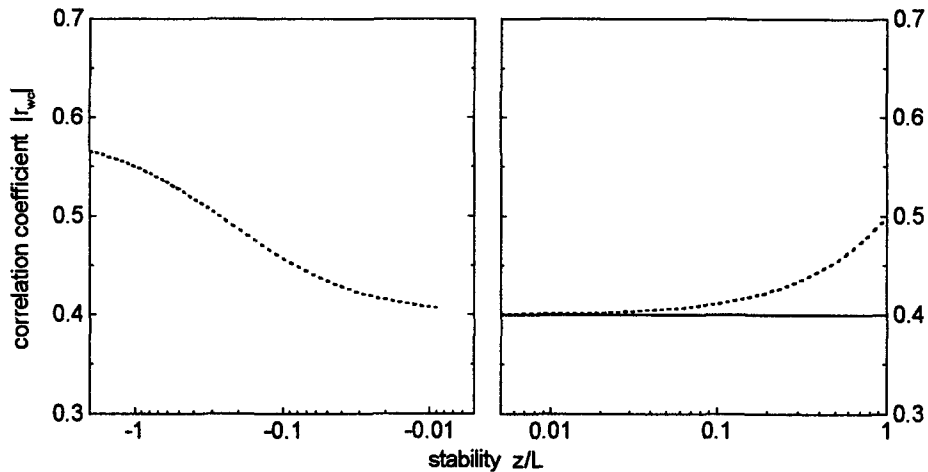


Fig. 2.15: Absolute correlation coefficient $|r_{wc}|$ of a scalar eddy flux as a function of z/L ; dashed line according to Eqs. 2.65, 2.61, and 2.62; solid line according to KF94:20.

With a given (absolute) correlation coefficient according to Fig. 2.15, the magnitude of a trace gas flux can be determined from the corresponding standard deviations as:

$$\overline{w'\mu_c'} = r_{wc} \cdot \sigma(w) \cdot \sigma(\mu_c) . \quad (2.66)$$

Application of Variance Methods

In contrast to the profile methods, the variance similarity methods need fast response trace gas measurements like the eddy correlation technique. However, the requirements for time response and accuracy are somewhat lower. In particular, the levelling and separation of the sensors and the synchronicity of the measurements is less critical than for eddy correlation. The advantages and disadvantages are discussed in detail by Wesely (1988) and Wichura and Foken (1995). To summarise, the most important negative characteristics of the variance methods are:

- use of (semi-) empirical similarity functions, that are not as well defined as the profile functions (larger scatter, fewer experimental results available)
- direction of trace gas fluxes (and stability) can only be determined by additional measurements (e.g. profiles) or has to be known a priori
- uncorrelated noise and trends lead to error in variance but not in covariance measurements

Hence the variance similarity relationships do not show considerable advantages or facilitation compared to eddy correlation method. However, they are often a suitable mean for testing and analysing turbulence measurements (e.g. Rotach, 1991; Eugster, 1994).

2.4.5 Limitations of Monin-Obukhov-similarity

In the previous sections, the relation between fluxes and corresponding profiles or variances was described mainly as a function of the dimensionless group z/L . The ratio between the two length scales z and L (cf. Table 2.2) is the most important scaling parameter for the surface layer (where MOST is valid). The Obukhov-length L itself is defined in Eq. 2.38 as the ratio of a momentum flux and a heat flux term representing the mechanical and thermal turbulence production respectively. Thus L can be used as a measure of dynamic stability like the Richardson number (Eq. 2.2). However, unlike Ri , L is only a function of vertical fluxes and not dependent on height in the surface layer. It therefore represents the general stability state of the whole SL. According to Obukhov (1971), the magnitude of L has a comprehensible meaning as the 'height of the sublayer of dynamic turbulence', i.e. the height of the air layer, where turbulence is dominated by mechanical forces and the influence of buoyancy effects is relatively small. In principle, MOST is restricted to this layer, because it is based on mechanical turbulence production and most scaling variables in Table 2.2 are defined with the help of u_* (cf. Holtslag and Nieuwstadt, 1986). The thermal turbulence effect is described only as a deviation from the neutral case. With the help of this similarity regime consideration, KF94:20 give an alternative definition of the surface layer as the layer where Monin-Obukhov-scaling is valid and thus $h_{SL} = |L|$. Under very stable and low wind conditions, this definition is usually more restrictive than the one given in Section 2.2.3 (10% of PBL height).

Whereas L describes the general stability state of the boundary layer, the ratio z/L is a local stability parameter that is no longer constant but proportional to the height z above the surface. It is closely related to Ri , which is also height dependent. The exact relationship between the two parameters can be derived with the gradient similarity functions for windspeed and temperature (2.46 and 2.47) inserted in Equation 2.2 (cf. Arya, 1988: 163):

$$Ri = z/L \cdot \frac{\Phi_T}{\Phi_u^2} = \begin{cases} z/L & (z/L \leq 0) \\ z/L \cdot [1 + 5 z/L]^{-1} & (z/L \geq 0) \end{cases} \quad (2.67)$$

A graphical representation of this relationship is displayed in Fig.4.24. For unstable conditions, both parameters are equal; in the stable range, z/L tends towards infinity at the critical Richardson number value $Ri_c = 0.2$, implying that the turbulent fluxes vanish.

According to the considerations given above, Monin-Obukhov-similarity is only valid in the stability range $-1 \leq z/L \leq +1$ (Holtslag and Nieuwstadt, 1986). However, observations suggest, that the similarity functions are well applicable for $|z/L| \leq 2$ (Businger et al., 1971; Dyer, 1974), in the unstable range even up to $z/L = -5$ (Ga92:52). This corresponds to an Ri range of $-5 \dots +0.2$ and thus to the forced and

mixed convection domain as displayed in Fig. 2.2. In the intermittent and laminar domains ($Ri \geq 0.2$), no regular turbulent fluxes exist (Kondo et al., 1978) and z/L is not clearly defined. However, several empirical extensions of the profile similarity functions for the intermittent range were proposed mainly for modelling purposes (Louis, 1979; Delage, 1988; Beljaars and Holtslag, 1991, cf. Section 4.2.2). For large negative Ri values (free convection domain), the mechanical shear stress is no longer relevant for turbulence production and therefore u_* must be omitted as a key variable. This results in dimensionless groups totally different from MOST (Arya, 1988: 136). Corresponding similarity relationships are difficult to establish mainly due to experimental problems (Ga92:51). A comprehensive survey of the different scaling domains is given by Holtslag and Nieuwstadt (1986).

2.5 Eddy Accumulation Method

2.5.1 Motivation and Theory

In the last decades, surface exchange of most trace gas species could be investigated only by profile or enclosure methods, since no fast sensors for eddy correlation measurements have been available. However, considering the uncertainties and limitations of this methods (cf. Sections 2.2, 2.4 and 2.6.1) it is generally desirable to have a more direct micrometeorological method like the eddy correlation available for all trace gases. In order to overcome this problem, Desjardins (1972; 1977) proposed a modification of the eddy correlation technique, with the fast response trace gas sensor being replaced by fast response sampling valves combined with slow analysis techniques. The term 'eddy accumulation' (EA), now commonly used for this measurement principle, seems to have been popularised in EPA workshop reports by Hicks and Wesely (1978) and Hicks et al. (1980). The theoretical basis presented by Desjardins (1972) and Hicks and McMillen (1984) is outlined in the following in a slightly modified form (e.g. using discrete sum notation instead of integrals).

The basic idea of the eddy accumulation method is to interpret the vertical turbulent covariance flux (Eq. 2.25) as a weighted mean concentration with the vertical windspeed w as weighting factor.

$$F_c = \overline{w \cdot \rho_c} = \frac{1}{N} \sum_{i=1}^N w_i \cdot \rho_{c,i} =: \frac{1}{N} \sum w \cdot \rho_c \quad (2.68)$$

If so, the weighting and averaging operation can also be done mechanically instead of the usual numerical way. Since the vertical windspeed shows positive *and* negative values, they must be separated in order to get a formulation with only positive weighting factors:

$$F_c = \frac{1}{N} \left(\sum_{w>0} |w| \cdot \rho_c - \sum_{w<0} |w| \cdot \rho_c \right) . \quad (2.69)$$

A fast-response vertical wind sensor drives a conditional sampling system having a similar rapid response characteristic as required for eddy correlation measurements. Air is sampled with a controlled volume flowrate $Q(t) = \xi \cdot |w(t)|$ proportional to the magnitude of the actual vertical windspeed. The proportionality constant ξ takes the units m^2 . The sample air is directed into two different reservoirs, one for upward air motion ($w>0$) and the other for downward motion ($w<0$). After an adequate averaging

time T_a (cf. Section 2.3.2) the accumulated mass of the trace compound in both reservoirs (M_U : upward and M_D : downward) may be determined with slow analytical methods.

$$M_U = \sum_{w>0} Q \cdot \rho_c \cdot \Delta t = \xi \cdot \Delta t \sum_{w>0} |w| \cdot \rho_c \quad (2.70a)$$

$$M_D = \sum_{w<0} Q \cdot \rho_c \cdot \Delta t = \xi \cdot \Delta t \sum_{w<0} |w| \cdot \rho_c \quad (2.70b)$$

$\Delta t = T_a/N$ represents the (constant) measuring and controlling time interval. Hence the trace gas flux can be calculated as:

$$F_c = \frac{1}{N \cdot \Delta t \cdot \xi} (M_U - M_D) = \frac{1}{T_a \cdot \xi} (M_U - M_D) \quad (2.71)$$

The accumulated masses may either be determined through extraction methods or by determination of the sampled air volumes (masses) and the respective mean concentrations. However, the accurate measurement and controlling of air flowrates and sample volumes is a crucial part of the method and can cause considerable errors as pointed out by Hicks and McMillen (1984). A 1% undetected difference between both sampling volumes could for example change the resulting deposition velocity by 1% of σ_w . In many cases this is in the same order of magnitude as the deposition velocity itself! Another problem is the influence of temperature and humidity fluctuations on the absolute trace gas concentration ρ_c as already discussed for the eddy correlation method in Section 2.3.3. Like there, the introduction of the trace gas mixing ratio μ_c (relative to dry air) is very helpful and leads to an alternative more convenient formula for the eddy accumulation flux. Starting with Equation 2.30, one gets:

$$F_c = \bar{\rho}_a \cdot \overline{w' \mu_c} = \bar{\rho}_a \cdot \overline{w' \mu_c} = \bar{\rho}_a \cdot \frac{1}{N} \sum w' \mu_c \quad (2.72)$$

w' represents the instantaneous deviation from the mean vertical windspeed, which may be determined with the help of an online running mean. This formulation is less problematic than Eq. 2.71, because it implies an automatic correction for (at least small) misalignments of the wind sensor. Again the sum is split into updrafts and downdrafts:

$$F_c = \frac{\bar{\rho}_a}{N} \left(\sum_{w>0} |w'| \cdot \mu_c - \sum_{w<0} |w'| \cdot \mu_c \right) \quad (2.73)$$

The partial sums are now related to the average mixing ratios (instead of accumulated masses) in both reservoirs. Regarding the windspeed as weighting factor, the mean mixing ratio is equal to the weighted sum divided by the sum of the weights:

$$\bar{\mu}_{c,U} = \frac{\sum_{w>0} |w'| \cdot \mu_c}{\sum_{w>0} |w'|} \quad ; \quad \bar{\mu}_{c,D} = \frac{\sum_{w<0} |w'| \cdot \mu_c}{\sum_{w<0} |w'|} \quad (2.74a/b)$$

Both denominators must be equal, because the average (and thus the sum) of all w' is zero by definition. They can be written in the shorthand Reynolds notation as follows:

$$\sum_{w>0} |w'| = \sum_{w<0} |w'| = \frac{1}{2} \sum_{i=1}^N |w_i'| = \frac{N}{2} \overline{|w'|} . \quad (2.75)$$

The insertion of (2.74) and (2.75) into (2.73) yields

$$F_c = \frac{\overline{|w'|}}{2} \cdot \bar{\rho}_a (\bar{\mu}_{c,U} - \bar{\mu}_{c,D}) . \quad (2.76)$$

This formula does not include the total sample volumes (or masses). Moreover, the mean mixing ratios do not depend on the proportionality factor between windspeed and flowrate, which may even differ for the upward and downward case. Generally, the trace gas measurement can be decoupled from the total sampled air mass. Only an arbitrary part of the sample air has to be taken for analysis of the mixing ratio, as long as it is representative for the total air mass. Hence the method is relatively robust against uncertainties in the flow control and can be combined easily with a large range of trace gas sampling and analysing systems that might require for example a constant sample flow (see following section). According to Hicks and McMillen (1984), relationship 2.76 is about 40 times less sensitive to an offset error in the vertical windspeed than relationship 2.71.

It has to be noted, that Equation 2.76 is not dependent on assumptions about the probability distribution of the vertical windspeed, which may have a symmetric or asymmetric form. The appearing w -term is called the 'mean absolute deviation' of the vertical windspeed. It is usually closely related to the standard deviation $\sigma(w)$. For the ideal case of a Gaussian distribution, Sachs (1984) gives the following relationship:

$$\frac{\overline{|w'|}}{\sigma_w} = \sqrt{\frac{2}{\pi}} = 0.798 . \quad (2.77)$$

Thus the eddy accumulation flux may be approximated as:

$$F_c \approx 0.40 \cdot \sigma_w \cdot \bar{\rho}_a (\bar{\mu}_{c,U} - \bar{\mu}_{c,D}) . \quad (2.78)$$

2.5.2 Realisation of the Proportional Eddy Accumulation Technique

According to the theoretical concept presented above, the schematic setup of an eddy accumulation system according to Speer et al. (1985) is presented in Fig. 2.16. A sonic or propeller anemometer yields a high resolution vertical wind signal (ca. 10 Hz), that is processed online either with an analog or digital processing unit. The resulting output signals, representing the sign and the magnitude of the vertical wind, are used to control valves that create a proportional sample air flow through the corresponding updraft or downdraft accumulation units. The trace gas of interest may be extracted online from the sample air by means of cryogenic trapping, filter-packs, carbon cartridges, etc.

Alternatively, the updraft and downdraft air samples may be accumulated in bags or canisters, where they can be stored for a later analysis. For this purpose, the setup shown in Fig. 2.16 has to be reversed (accumulation units after pump and control valves). As a third possibility, the sample air can be analysed directly with slow response instruments. It was mentioned in the previous section that not the total sampled air mass has to be scrubbed or analysed. If the air is collected in bags, any sample taken from

the accumulated volume should yield the same average mixing ratio. If an online trapping or analysing system is used, air can be taken continuously from the updraft and downdraft lines.

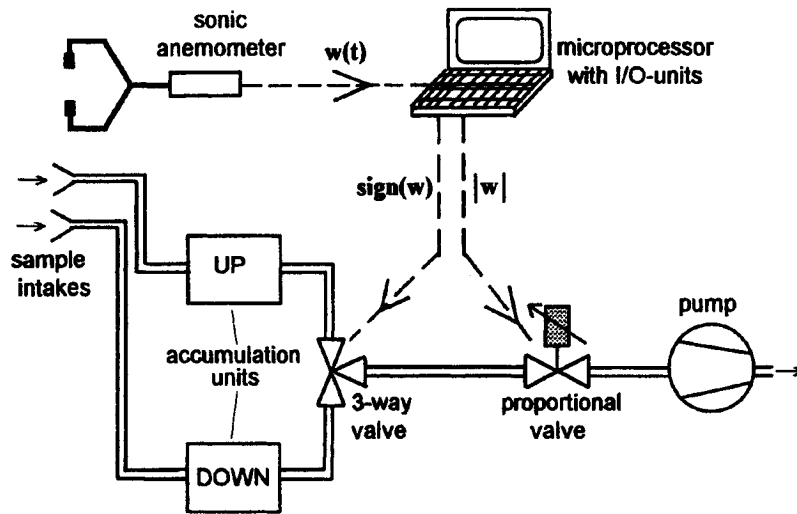


Fig. 2.16: Schematic setup of an eddy accumulation system with proportional sampling flow according to Speer et al. (1985).

The accumulation or averaging time for eddy accumulation systems basically corresponds to the averaging interval of the eddy correlation method (i.e. 10 - 60 min, covering all turbulent time scales). However, with the total mass accumulation technique according to Eq. 2.71, a much longer accumulation time is principally possible. Speer et al. (1985) ran such a system for periods up to 90 hours, however with only little success. The more useful relationships 2.76 or 2.78 only allow averages over the turbulent time scales, since σ_w is not supposed to be constant over longer periods. A method similar to the eddy accumulation concept, especially designed for longterm monitoring of dry deposition processes, was proposed by Hicks et al. (1986). Following Equation 2.7, the ambient air is sampled proportional to the actual deposition velocity, which is estimated online from meteorological measurements. If a trace compound is accumulated from the sample air (e.g. on a filter-pack or in a liquid solution) over a longer period (days, weeks), the resulting mass is proportional to the integrated deposition flux. This method is restricted to absolute deposition measurements and no application results have been reported in literature up to now.

For the technical realisation of an eddy accumulation system, the accurate and fast response control (approximately 10 Hz) of the air sampling - proportional to the actual vertical windspeed - is the most critical part. The most obvious solution seems to be a metering (solenoid) valve, that is controlled by a variable voltage or current. Commercially available solenoid valves usually show a non-linear behaviour as well as a certain hysteresis between opening and closing. Speer et al. (1985) tried to solve this problem by controlling the valve with a combined mass flow meter. However, the successful performance of this system was not proven and seems difficult to achieve, since any flow meter system is either limited by its response time or precision. Reid et al. (1984) built and tested a special diaphragm valve with an electromagnetic actuator that showed a fast response of better than 10 Hz and a satisfying reproducible behaviour. The non-linearity could be compensated by preprocessing of the controlling wind signal (Buckley et al., 1988).

An interesting alternative solution was applied by Neumann et al. (1989). The proportional sample flow was obtained by a system of several parallel two-position-valves of different orifice size. They could be switched in different combinations by a digital processor unit resulting in 256 steps of increasing flowrate. Another approach that uses only two-position-valves was proposed by Beier (1991). Instead of varying the instantaneous flowrate, the air is supposed to be sampled at a constant flowrate but for varying time periods within a fixed control interval. This system was never tested, and it would require valve response times about one order of magnitude faster than the other techniques.

An intrinsic problem of all proposed solutions for a proportional flow control is the limited dynamic range, i.e. the flow resistance and therefore the produced flowrate have a distinct upper and usually also lower limit. Each valve has a maximum orifice and a certain resolution or uncertainty corresponding to an effective threshold near zero, where it begins to react (presumably with a certain starting jump). The resulting dynamic range between these limits has to be used as effectively as possible. Thus the factor between vertical windspeed and flowrate must be chosen in a way, that very high windspeeds (occurring rarely) correspond to flowrates beyond the maximum of the possible range (see Fig. 2.17). For an optimal choice of the dynamic range, the characteristics of the valve as well as the probability distribution of the vertical windspeed have to be taken into account. Perhaps, a dynamic adjustment depending on the actual σ_w would be helpful, but the error introduced by the non-proportionality outside the dynamic range always has to be considered.

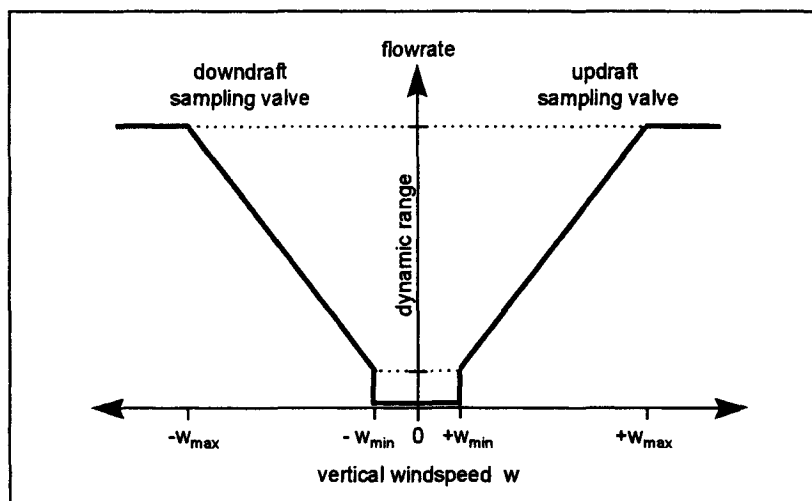


Fig. 2.17: Limited dynamic range for the proportional relationship between vertical windspeed and sampling flowrate of an eddy accumulation system.

This effect and other problems and limitations of proportional eddy accumulation systems can be investigated by mathematical simulations with high resolution time series. Hicks and McMillen (1984) used measured eddy correlation data sets of the wind components u and w as input, whereas O'Brien (1985) created synthetic time series with defined stochastic characteristics. They studied the deviations (errors) introduced by a limited dynamic range, delay times, and offsets in the mean vertical windspeed and found more or less corresponding results. Generally, the relative errors are inversely proportional to the deposition velocity (i.e. the ratio of flux and ambient concentration) and thus strongly depend on the characteristics of the individual trace gas and on the environmental conditions. In order to obtain a deposition velocity with an absolute accuracy of 0.1 cm s^{-1} , a dynamic range of at least two orders of

magnitude is required according to Hicks and McMillen (1984). Additionally, the dead volume has to be smaller than 0.01% of the total sampled air volume and the offset error in the vertical windspeed must be smaller than $0.02 \cdot \sigma_w$. All these requirements are not easy to meet, and they need considerable instrumental efforts.

2.5.3 Relaxed Eddy Accumulation Concept

Considering the complexity of the proportional sampling linked to the magnitude of the w -signal and the poor success of the performed field measurements, Hicks and McMillen (1984) suggested a simplified version of the eddy accumulation method. The average concentrations of updraft and downdraft air is determined without a weighting by the vertical windspeed. Businger and Oncley (1990) formulated and discussed this approach in detail calling it 'conditional sampling', though the alternative and more specific term 'relaxed eddy accumulation' (REA) is generally in use nowadays. Relationship 2.78 was adopted and the effect of the non-proportional sampling was expressed through an empirical factor b :

$$F_c = b \cdot \sigma_w \cdot \bar{\rho}_a (\bar{\mu}_{c,U} - \bar{\mu}_{c,D}) . \quad (2.79)$$

For the purpose of generality, the following considerations are formulated for a kinematic turbulent flux $\overline{w's'}$ of an arbitrary scalar quantity s (with e.g. $s = \mu_c$, $s = T$). Thus a rearrangement of Eq. 2.79 together with Eq. 2.30 gives the following definition for b :

$$b = \frac{\overline{w's'}}{\sigma_w \cdot (\bar{s}_U - \bar{s}_D)} . \quad (2.80)$$

The applicability of the REA approach depends on whether it is possible to understand and describe the quantitative behaviour of the b -factor and hence of the conditional scalar means. They are determined by the overall relationship between w' and s' , that can be described by the bivariate joint frequency distribution (JFD). It represents a two-dimensional histogram showing the frequency of occurrence of pairs of data (w', s') within grid cells of given class intervals (cf. Grossman, 1984). If the JFD is normalised to an integral frequency of 1, it represents a discrete estimation of the theoretical joint probability density function $p(w', s')$. The JFD analysis of turbulence data has been performed not very frequently up to now, in contrast to other evaluation methods like e.g. the common spectral analysis (cf. Appendix A). Originally it was mainly used for the analysis of turbulent shear stress (cf. Raupach, 1981); only in recent years, some investigations on scalar turbulent transfer have been reported (e.g. Maitani and Shaw, 1990; Kroon and Bink, 1996; Katul et al., 1997). Although there is still a considerable lack of theoretical foundation, the JFD analysis may provide additional insight in the mechanisms of atmospheric turbulent transport and is especially suitable to analyse theoretical and practical problems of the REA method.

The basic theoretical model for describing a JFD is a joint Gaussian distribution. It assumes, a linear relationship between both quantities in combination with random noise. The resulting correlation coefficient depends on the relative fraction of the correlated (explained) and the random (unexplained) variances. The Gaussian distribution for a scalar turbulent flux with correlation coefficient r_{ws} and standard deviations σ_w and σ_s is given by Wyngaard and Moeng (1992) as:

$$p_G(w', s') = \frac{1}{2\pi\sigma_w\sigma_s\sqrt{1-r_{ws}^2}} \cdot \exp\left[-\frac{1}{2\cdot(1-r_{ws}^2)}\left(\frac{w'^2}{\sigma_w^2} - 2r_{ws}\frac{w's'}{\sigma_w\sigma_s} + \frac{s'^2}{\sigma_s^2}\right)\right]. \quad (2.81)$$

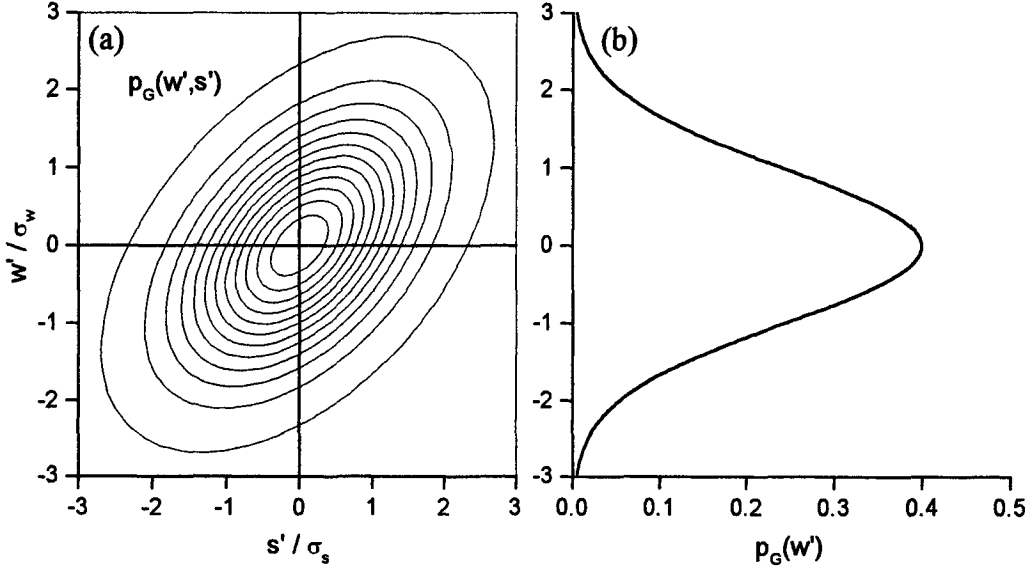


Fig. 2.18: (a) Contour plot of normalised joint Gaussian probability distribution of w' and s' according to Eq. 2.81; (b) corresponding one-dimensional probability distribution of w' .

The corresponding graphic illustration for a typical $r_{ws} = 0.5$ is given in Figure 2.18a as a contour (isoline) plot. For the purpose of general comparability, the w' and s' axes are normalised with the respective standard deviations. Besides the bivariate joint distribution, the respective one-dimensional Gaussian probability distribution of w' is plotted (Fig. 2.18b). It represents the integration of $p_G(w', s')$ over s' . In order to obtain the conditional scalar means for updrafts and downdrafts, the JFD (or joint probability distribution) multiplied with the local scalar value s' has to be integrated over the respective upper and lower half-planes of the bivariate distribution:

$$\bar{s}_U = \frac{1}{0.5} \int_0^{+\infty} \int_{-\infty}^{+\infty} s' \cdot p(w', s') \cdot ds' \cdot dw' \quad ; \quad \bar{s}_D = \frac{1}{0.5} \int_{-\infty}^0 \int_{-\infty}^{+\infty} s' \cdot p(w', s') \cdot ds' \cdot dw' . \quad (2.82)$$

The normalisation factor 0.5 represents the total probability (integral over $p(w', s')$) for each half-plane. For the ideal joint Gaussian distribution (Eq. 2.81), Wyngaard and Moeng (1992) evaluated the integrals analytically and showed that they are proportional to r_{ws} as well as to σ_s :

$$\bar{s}_U = -\bar{s}_D = \frac{2}{\sqrt{2\pi}} r_{ws} \sigma_s . \quad (2.83)$$

If this relationship is inserted in Eq. 2.80, and the covariance flux is replaced according to Eq. 2.66, the b -factor results in:

$$b = \frac{r_{ws} \sigma_w \sigma_s}{\sigma_w \cdot \frac{4}{\sqrt{2\pi}} r_{ws} \sigma_s} = \frac{\sqrt{2\pi}}{4} = 0.627 . \quad (2.84)$$

Thus for an ideal Gaussian distribution, the b -factor is a constant, independent of the correlation coefficient and standard deviations. Under such conditions, the relaxed eddy accumulation represents an independent physical approach and not just an empirical simplification of the proportional eddy accumulation. However, large eddy simulations (Wyngaard and Moeng, 1992) as well as several field experiments yielded b -factors which were on average somewhat lower than the theoretical value in Eq. 2.84 and perhaps not exactly constant. Experimental values for b were mainly derived from high resolution (eddy correlation) datasets of vertical windspeed and temperature, which is easiest to measure of all scalar quantities. Average values for b between 0.54 and 0.60 were found (Businger and Oncley, 1990; Baker et al., 1992; Pattey et al., 1993). However individual 30-min-values sometimes showed a considerable scatter with ranges from 0.2 to 0.9 (e.g. Oncley et al., 1993; Beverland et al., 1996c). From the analogy hypothesis for scalar transport it can be assumed, that the b -factor for trace gases is identical to that for temperature (sensible heat). Only few studies investigated this question up to now (Oncley et al., 1993; Pattey et al., 1993). They found similar values for temperature, H_2O and CO_2 .

It is still uncertain, whether b is absolutely constant or varies systematically in relation to certain turbulence parameters as suggested by similarity theory. Businger and Oncley (1990) proposed b as a general function of stability (z/L). However, only a weak systematic variation was detected, which could not be reproduced by other authors (e.g. Beverland et al., 1996a). Fritsch (1994) investigated the influence of asymmetries in the single w - and s -distributions, but found only little effect as well. Therefore, most investigators either use a constant literature value for b (0.56..0.6) or determine b in-situ from eddy correlation measurements of the sensible heat flux according to Eq. 2.80.

The loss of proportional sampling in the REA technique - compared to the original eddy accumulation concept - results in an increase of the coefficient in Equations 2.78 and 2.79 from 0.4 to about 0.6. Hence the concentration difference that has to be measured is reduced by the factor 1.5. This effect can be partly or fully compensated by the use of a threshold (deadband) around zero vertical windspeed, where neither the updraft nor downdraft sampling is active. However, the exact quantitative effect of a deadband on the b -factor is still a matter of investigations (cf. Businger and Oncley, 1990; Pattey et al., 1993).

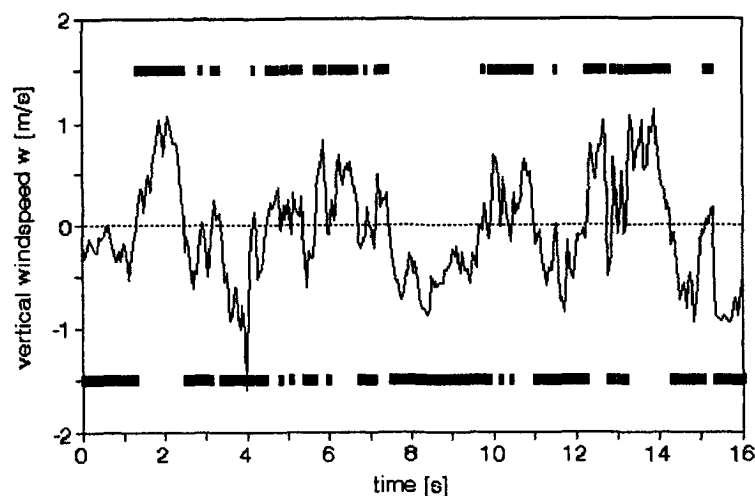


Fig. 2.19: Exemplary high resolution time series of vertical windspeed with indication of updraft and downdraft periods for a moderately unstable situation.

Beside the simplified flow control of the REA technique with only two valve positions (fully open/closed), it has another particular relaxation effect over the normal proportional method. Even if the valve position is controlled at a high frequency of e.g. 20 Hz, the effective switching rate is considerably lower, because the vertical windspeed does not change its sign in every cycle. Fig. 2.19 shows a exemplary high resolution w series with the indication of the updraft and downdraft periods. In this example of a moderately unstable situation, the average time period between consecutive valve switchings is about 0.5 s. Thus for 9 out of 10 controlling cycles (at 20 Hz), the valve is already in the right position from the beginning. This characteristic represents an important relaxation for possible delay effects between the measurement of w and the controlling of the sample flow.

2.5.4 Application of the REA Technique

In contrast to the proportional eddy accumulation method, field experiments with the REA technique provided satisfying results for certain trace compounds: mainly for CO_2 and H_2O (Baker et al., 1992; Oncley et al., 1993; Pattey et al., 1993), but also for methane (Beverland et al., 1996a), isoprene and other hydrocarbons (Valentini et al., 1995; Beverland et al., 1996c; Guenther et al., 1996) and volatilised pesticides (Majewski et al., 1993). However, a verification with reliable independent methods - especially for the latter compounds - was not always possible. Often, the REA systems were operated only under favourable (unstable) daytime conditions with relatively large flux values.

The setup of REA system is at least partly determined by the measured compound and the required accumulation and analysis technique. Some systems may for example require large sampling volumes and flow rates, constant flow rates without interruptions, pre-processing of air (e.g. drying, filtering) or a distinction between gas and aerosols. In the reported field experiments, mainly two setup types were used, which are similar to the proportional EA-systems (see Fig. 2.16) but without the metering valve. The first type (Fig. 2.20a) has only one inlet leading to a pushing pump and a subsequent branching to the conditional sampling (accumulator or sensor) units. Similar setups were used by Oncley et al. (1993) and Pattey et al. (1993) in combination with air sampling bags for subsequent analysis. Majewski et al. (1993) applied a modified system (with sucking pump) using foam plugs as trapping media. During deadband periods (if applied), the air was either exhausted to ambient or it was sampled in a third line/unit as an additional information. The deadvolume (including the pump) before the branching point and the related delay time has to be kept as small as possible or it has to be considered in the controlling of the valves. If this is not done, some air would be directed to the wrong sampling line.

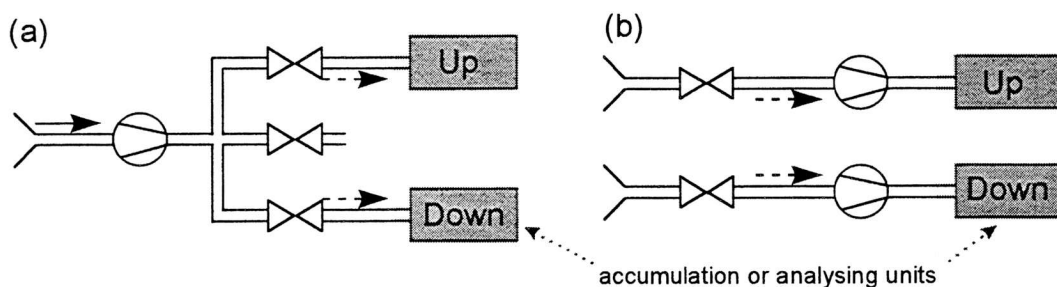


Fig. 2.20: Schematic setup of main REA system types. (a) after Oncley et al. (1993); (b) after Baker et al. (1992).

The second REA setup type (Fig. 2.20b) has two inlets and sampling lines with separate open/close valves and often also two separate (sucking) pumps (Baker et al., 1992; Beverland et al., 1996b; 1997). This solution has hardly any deadvolume problems and is somewhat more flexible concerning the position of the accumulator/sensor units (cf. Section 2.5.2). A range of possible REA setups adapted for various applications and compounds is presented by Delany et al. (1991).

2.6 Spatial Representativeness of Flux Measurements

2.6.1 Source Areas of Micrometeorological Methods

In contrast to enclosure techniques, the surface area representative for micrometeorological flux measurements is not easy to identify. In theory all constant flux layer methods rely on the assumption of an ideal (unlimited) homogeneous surface. In practice however, no vegetated surface is perfectly homogeneous and even an optically uniform canopy often shows spatial variability in the physiological activity and trace gas exchange. These can be caused by variations in the soil characteristics like for example the water and nutrient supply (see e.g. Meixner and Eugster, 1998). Moreover, especially in populated regions, the surface is usually patchy with limited areas of different agricultural and natural vegetation canopies and disturbed by single trees, streets and buildings.

Thus it is of high importance for the micrometeorological methods to have a quantitative information about the surface area, that actually influences the flux measurement at a single point (or several points in a vertical profile). Corresponding models proposed in the literature (cf. Horst and Weil, 1994; Schmid, 1994) are based on turbulent diffusion theory and consider the measured concentration or flux at a certain height z_m as a linear superposition of dispersion plumes of many distributed point sources at the surface. The relative contribution of each elemental surface flux at an upwind distance x and a crosswind distance y to the total measured flux defines its value in the 'source weight function' or 'footprint function' $f(x,y,z_m)$. If a surface with a horizontally homogenous turbulence structure is assumed (i.e. homogeneous roughness and thermal characteristics), the diffusion plumes of all surface point sources have the same shape and differ only for a factor describing their source strength $F_{c,0}(x,y)$. In that case a simple reciprocity consideration (cf. Schmid and Oke, 1990; Schmid, 1994) allows to calculate the source weight function directly from a *single* plume model with the origin at $x = 0$ and $y = 0$.

$$\text{scalar concentration: } f_p(x, y, z_m) \propto \bar{\rho}_{c,\text{plume}}(x, y, z_m) \quad (2.85a)$$

$$\text{scalar flux: } f_F(x, y, z_m) \propto F_{c,\text{plume}}(x, y, z_m) \quad (2.85b)$$

Here the spatial coordinates x and y for the plume are defined in the usual way as positive in the downwind direction and thus opposite to the coordinates in the source weight function f . The concentration and vertical flux distribution in a turbulent dispersion plume may be determined either with a Lagrangian concept using simulations of particle trajectories (Leclerc and Thurtell, 1990; Wienhold et al., 1995) or with an analytical Eulerian approach using surface layer similarity theory (Horst and Weil, 1994; Schmid, 1994). Both concepts were shown to give similar results for f_F under favourable conditions (Horst and Weil, 1992; Finn et al., 1996). The first technique is more general and can be also extended to non-homogeneous conditions but requires considerable computing effort for each individual case. The analytical method in contrast depends on several semi-empirical assumptions based on the

surface homogeneity. However, the source weight function is determined by only few dimensionless characteristics of the surface layer, namely z_m/z_0 , z_m/L and σ_v/u_* . Figure 2.21a shows a contour plot representing the general form of the source weight function. It is small directly in front of the sensor, then rapidly rises to a maximum and falls off more slowly with increasing distance. It also decreases to both sides of the main upwind direction producing an ellipsis-like shape of the isopleths. The distance of the maximum point and the longitudinal extension increases with z_m/L and z_m/z_0 , i.e. with measurement height, stability, and the inverse roughness length. The lateral extension is mainly dependent on the dimensionless crosswind standard deviation σ_v/u_* . For simplification purposes the source weight function is often integrated over the lateral y -dimension (Schuepp et al., 1990). This results, for a given measurement height z_m , in the one-dimensional function $\bar{f}^y(x)$ displayed in Figure 2.21b.

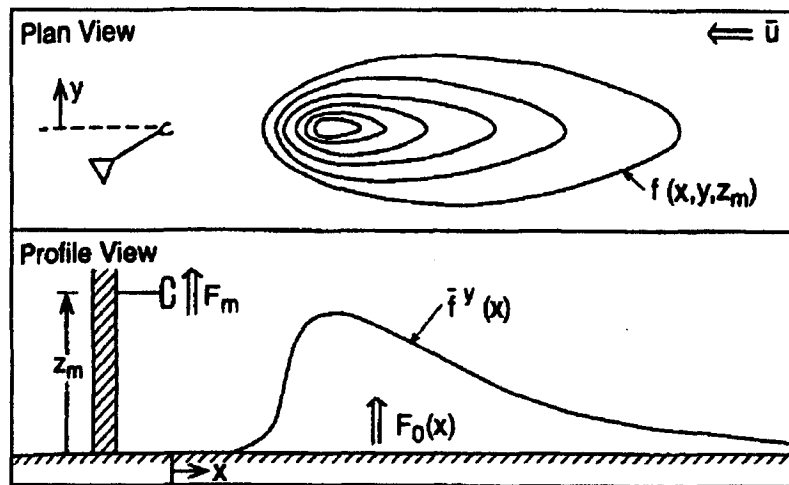


Fig. 2.21: Schematic source area distribution (footprint function) for EC flux measurements (from Horst and Weil, 1994).

Since the source weight function has theoretically an infinite extension, the effective source area influencing a turbulence measurement can only be specified in terms of a given contribution (or accuracy) level P . This might be of interest in practical application for the requirements of surface homogeneity for a given accuracy level. In order to get the limits of a source area $A(P)$, the source weight function has to be integrated over both spatial dimensions:

$$P = \iint_{A=?} f(x, y) \cdot dx dy . \quad (2.86)$$

This can be done in different ways. Horst and Weil (1994) propose an integration of $\bar{f}^y(x)$ from zero up to the 'required fetch-length' $x(P)$. Schmid and Oke (1990) and Schmid (1994) follow an alternative concept, they determine the minimal surface area (in the centre of the source weight function) representing a given integration level P . The limits of this source areas $A_{\min}(P)$ correspond to an isopleth of the source weight function and thus have an ellipsoid form as shown in Fig. 2.21a. The authors give the distance and dimensions of the 50%-areas as a simple parameterisation of the influencing micrometeorological parameters.

It can be stated, that the source areas for eddy correlation flux measurements at a single point (Eq. 2.85b) are generally smaller than for concentration measurements (Eq. 2.85a) under comparable conditions. The main problem for the profile methods is, that each measurement level has its own distinct

source area. As shown in Figure 2.22, it is usually much smaller and closer to the tower for low profile levels than for the higher ones. Thus under inhomogeneous conditions, the profile levels often sense different surface types and no meaningful flux result can be obtained. In contrast, eddy correlation measurements usually yield a more or less average flux of the respective source area. The sensitivity of other methods like the REA or variance similarity technique to non-homogeneous terrain has to be further investigated.

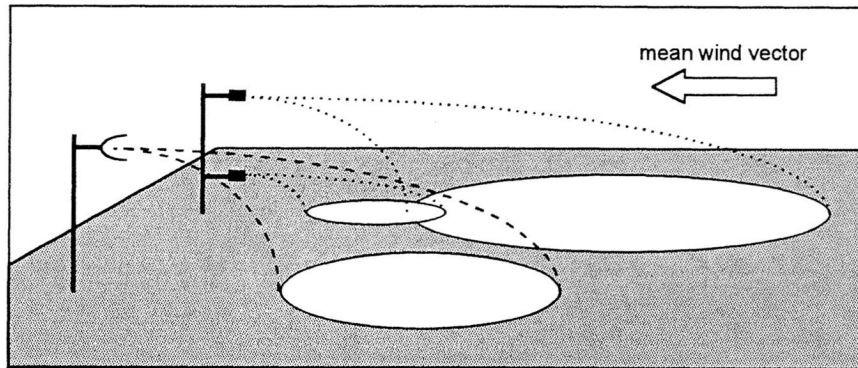


Fig. 2.22: Schematic 50% source areas for an eddy correlation and a profile measurement system.

2.6.2 Comparison and Interpretation of Different Methods

The surface exchange of trace gases and energy at the soil-plant-atmosphere-interface occurs over a wide range of spatial scales from a single leaf or plant up to a canopy, ecosystem or region. Since the interaction between the different scales can be relatively complex and non-linear (Jarvis and McNaughton, 1986), results obtained by different flux techniques operating at different scales cannot be directly compared in general. Micrometeorological methods yield average net fluxes for undisturbed surface (ecosystem) areas with a length scale of about $10^1 \dots 10^3$ m, whereas enclosure measurements cover surface areas or only a plant part of $10^{-2} \dots 10^0$ m and investigate the local exchange under more or less artificial conditions (cf. Section 2.2.2). But also the different micrometeorological methods have not exactly the same source areas as shown in the previous section, depending e.g. on the sensor height and whether eddy covariances or concentration profiles are measured. Figures 2.23 and 2.24 give a survey and a schematic illustration of the different flux scales and methods.

Depending on the required efforts and costs, the application time scale of the flux measurement methods also varies. Small leaf chambers are able to detect variations in the time scale of seconds but their (continuous) application is usually limited to a few days, because they either affect the leaf's metabolism or need intensive attendance (frequent changes of position). Micrometeorological measurements imply always an averaging over a typical interval of about 30 min, but on the other hand, tower-based systems may be operated continuously with little maintenance up to months or even years (e.g. Grace et al., 1996; Goulden et al., 1996; Moncrieff et al., 1996). A novel inverse Lagrangian model approach presented by Raupach et al. (1986) and Raupach (1989) allows to determine the vertical source-sink distribution inside the canopy from measurements of the respective concentration and turbulence intensity profiles. This technique may have the potential to fill the gap between the small scale leaf or soil chamber methods and the integrative micrometeorological methods.

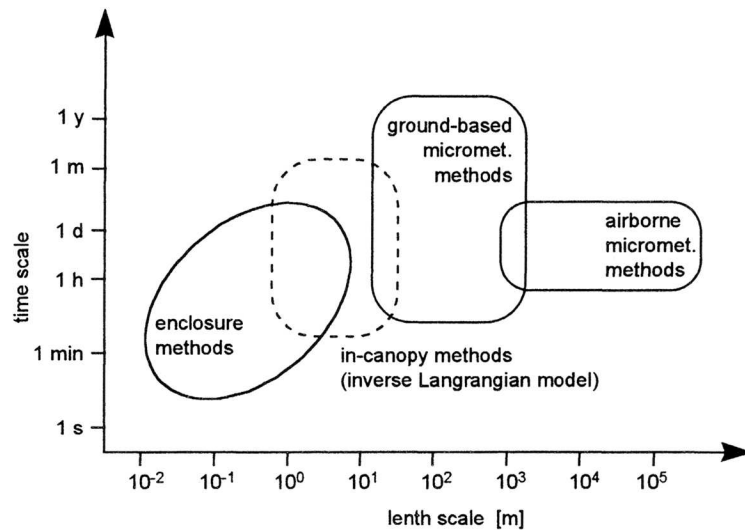


Fig. 2.23: Spatial and time scale addressed by different flux measurements techniques (after Stewart et al., 1989).

Airborne measurements with tethered balloons or airplanes (cf. Desjardins et al., 1989; Desjardins, 1992) are able to integrate over surface areas with length-scales up to 100 km. However, the high costs and the need for infrastructure and manpower limits their application period to a few hours or days.

Besides the methods presented here, there are many other techniques proposed in the literature but they are often limited to special situations or trace gases and not suitable for general application. The internal boundary layer budget method (cf. Wilson and Shum, 1992; Hipps and Zehr, 1995; Denmead, 1995) for example may only be applied for trace gases, that are exceptionally exchanged (emitted) by limited plots.

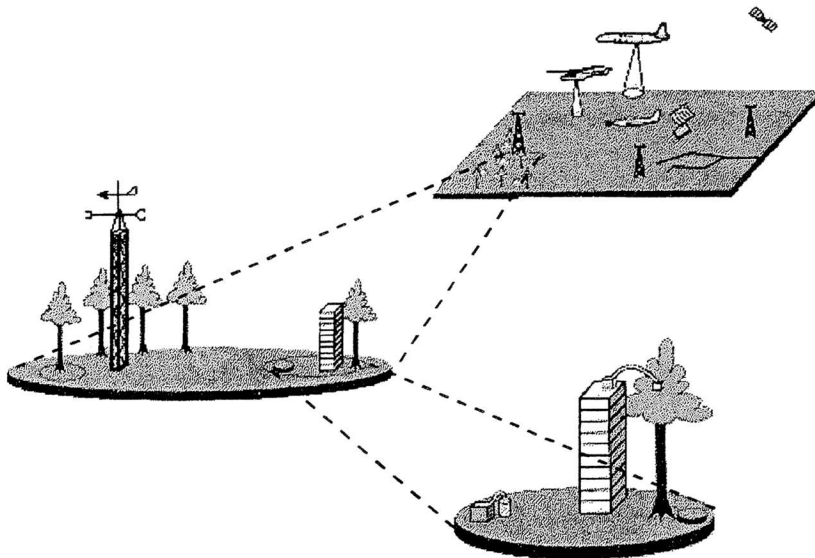


Fig. 2.24: Schematic illustration of the spatial scale addressed by different flux measurement methods (after Nobre et al., 1996).

Historically, the different flux measurement techniques were developed and applied in different science domains (plant physiology, ecology, atmospheric sciences, engineering sciences) and usually addressed different questions and aspects. Only in recent years, increased efforts were made for an integration and

reconciliation of the measurements at different scales (cf. Fig. 2.24). Several combined experiments in different climatic regions were/are carried out or are in preparation: e.g. FIFE (Sellers et al., 1992), HAPEX-Sahel (Goutorbe et al., 1994), BOREAS (Sellers et al., 1991), OASIS (Raupach et al., 1994), CODE (Desjardins et al., 1995), BAT (Rotach, 1997), LBA (Nobre et al., 1996). Beside combined experiments, appropriate models are necessary for the upscaling of small scale measurements to the ecosystem or regional scale (see e.g. Jarvis and McNaughton, 1986). Such models have to consider relatively complex processes like local advection effects at changes between different surface types, the source and sink effects of different plant and soil parts, the turbulent transport and storage within the canopy layer (Grace et al., 1996), as well as possible chemical reactions (e.g. Meixner, 1994).

To summarise, the micrometeorological surface layer methods (EC, REA, profile) cannot address all scales of interest for the study of exchange processes, but they are most appropriate for the intensive as well as longterm investigation of the net exchange of whole ecosystems and hence for nutrient cycle and budget studies. Moreover they represent the lower boundary condition for large scale studies of atmospheric chemistry and transport, and the upper boundary condition for soil and vegetation exchange studies.

3 MEASUREMENTS

3.1 General Description of Field Experiment

3.1.1 Measurement Site and Period

Within the framework of the EU-programme EXAMINE (Exchange of Atmospheric Ammonia with European Ecosystems) an extended field experiment was performed in June and July 1995 (Meixner et al., 1996; Sutton et al., 1996). The field site ($49^{\circ}10' \text{ N}$, $8^{\circ}16' \text{ E}$, 127 m a.s.l.) was located in the Rhine-valley, southern Germany, about 2 km south of the village of Bellheim (Fig. 3.1). The region is a relatively flat (level differences $\leq \pm 2.5 \text{ m}$ within 2 kilometres) and almost forest free agricultural landscape.

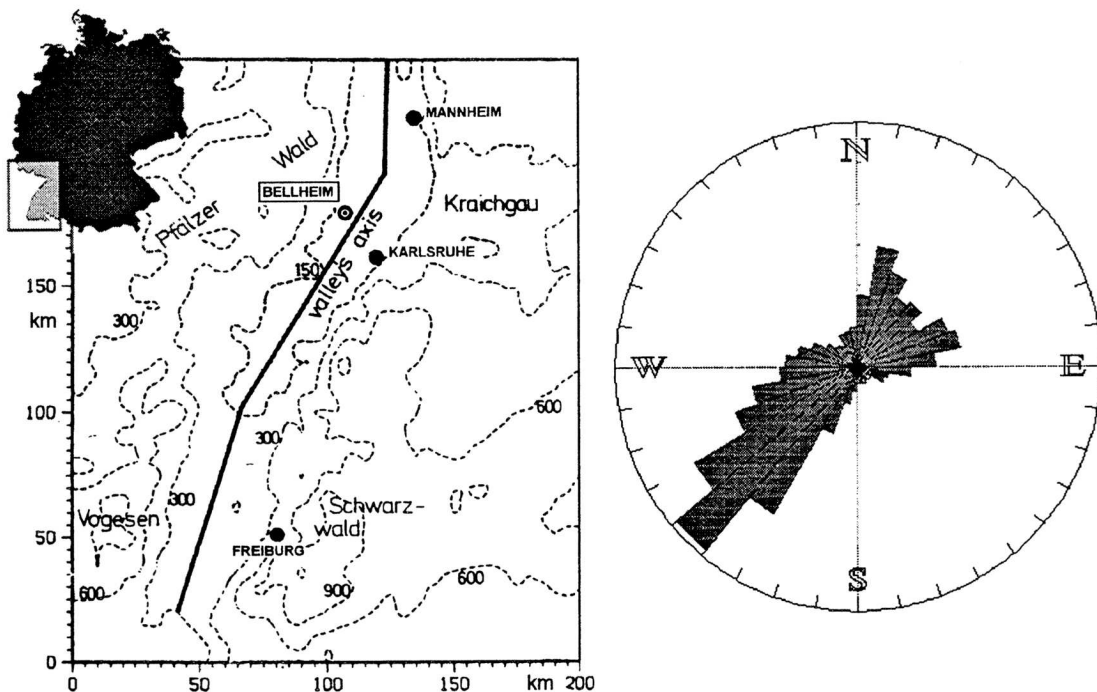


Fig. 3.1: Regional topography around the measurement location near Bellheim, southwestern Germany, with indication of the Rhine valley axis (after Kalthoff and Vogel, 1992); and mean distribution of wind directions near Bellheim for April - Sept 1992 (after Sprung, 1992).

The location was chosen, because it provided a homogeneous cereal crop field with an area of about 7 ha, which is difficult to find in central Europe especially if the vicinity to anthropogenic pollutant sources (e.g. highways) should be avoided. Moreover, micrometeorological data of previous years were available from a nearby tower that had been operated by the 'Institut für Meteorologie und Klimaforschung' (IMK) Karlsruhe for several years (cf. Fiedler, 1992; Sprung, 1993). The data sets showed a pronounced bimodal distribution of the wind direction for the summer months with the main peak from southwest and a secondary maximum from north/northeast. This behaviour can be explained with the topographic conditions of the Rhine-valley (see Fig. 3.1) which has a strong channelling effect (cf. Kalthoff and Vogel, 1992).

A survey of the vegetation around the measurement site during the field campaign is given in Fig 3.2. The field and cultivation pattern is typical for central Europe with many small and few bigger plots and a large variety of crop types. The figure also shows the position of the measurement towers at the northeasterly corner of the main triticale field, that provided a fetch (extension of homogeneous surface) of about 300 metres in the main southwest wind direction. In the east direction the fetch was strongly limited (ca. 100 metres) and from the north, a very strong influence from the adjacent sugar-beet field had to be expected. This situation should allow to study the effect of various source area and fetch conditions on the different flux measurement methods.

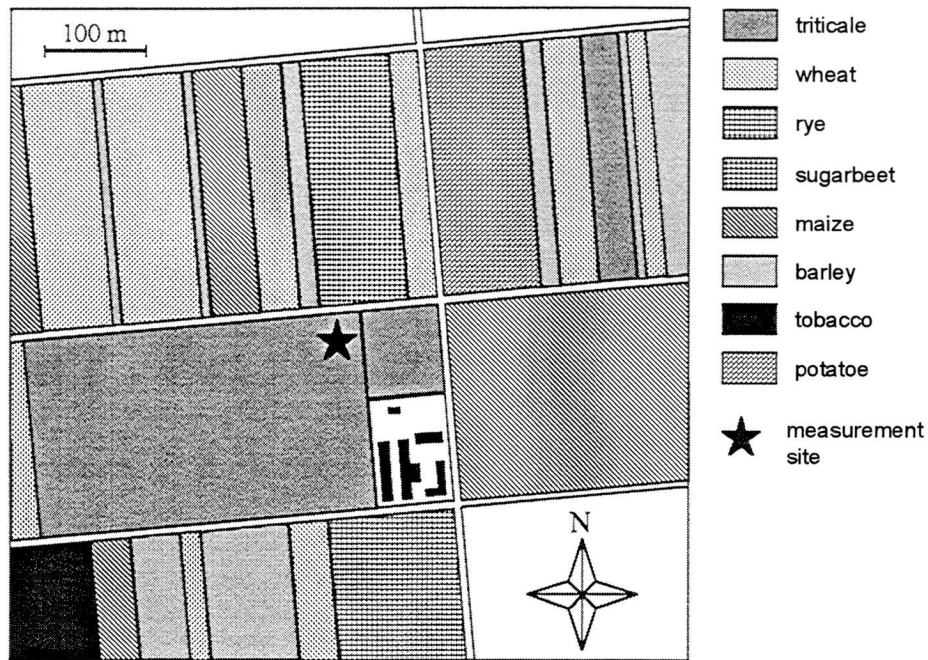


Fig. 3.2: Pattern of agricultural fields around the Bellheim measurement site.

3.1.2 Characterisation of the Triticale Canopy

The triticale field, in which the measurement systems were located, was considered as the main source area for the flux measurements due to the usual distribution of wind directions shown in Figure 3.1. It was therefore investigated intensively. Triticale is an intergeneric hybrid between wheat (*Triticum*) and rye (*Secale*) known since the end of the last century (Stace, 1987). Nowadays triticale becomes more and more important in fodder crop cultivation in Europe (Johnson, 1990).

At the beginning of the measurement campaign, the triticale on the study plot had already reached its maximum height of 1.34 ± 0.08 m. The growing period was terminated and the plants went through their senescence period during the measurement campaign. Some general information and data concerning the triticale field are listed in Table 3.1. The given number of stalks per square metre is not equal to the (seeded) plant density, because each plant usually consists of several stalks (ca. 10). Plant and stalk density were counted on 30 square areas of 0.25 m^2 on 20 June. Leaf insertion heights as well as plant fresh and dry weight (oven dried at $105 \text{ }^\circ\text{C}$ for 24 h) were on 20 June and 4 July.

Tab. 3.1: General information about the triticale field (measurement procedures are explained in the following sections).

field area size		7.54 ha
seeding	25 October 94	triticale 'ALAMO'
fertiliser application	15 March 95	NPK 14:10:20, ca. 1000 kg ha ⁻¹
harvest	21 - 25 July 95	
canopy height	19 / 27 June 95	1.34 ± 0.08 m ²
stalk density	20 June 95	540 ± 220 per m ²
biomass density	20 June 95 4 July 95	fresh: 6.6 kg m ⁻² , dry: 1.6 kg m ⁻² fresh: 6.4 kg m ⁻² , dry: 2.3 kg m ⁻²
total leaf area index LAI	2 July 95	4.9 ± 0.5 m ² m ⁻²

Mainly five different leaf levels could be identified for the triticale crop. Figure 3.3 shows their approximate height distribution. They are numbered beginning at the top flag leaf (L1) down to the bottom (L5). The partial leaf area index (LAI) of the different leaf levels was determined by two different techniques. In the first method, 10 randomly chosen stalks were harvested (19 June) and the area of the leaves was measured in the laboratory with a common computer scanner and an image processing algorithm. The second method was based on a non-destructive optical principle: the LAI-2000 system (LI-COR Inc., Lincoln, Nebraska) utilises a fish-eye lens to measure diffuse light interception by the plant canopy. From readings above the canopy and at different heights within (2 July) the partial LAI of the respective layer could be calculated (see e.g. Gower and Norman, 1991; Welles and Norman, 1991).

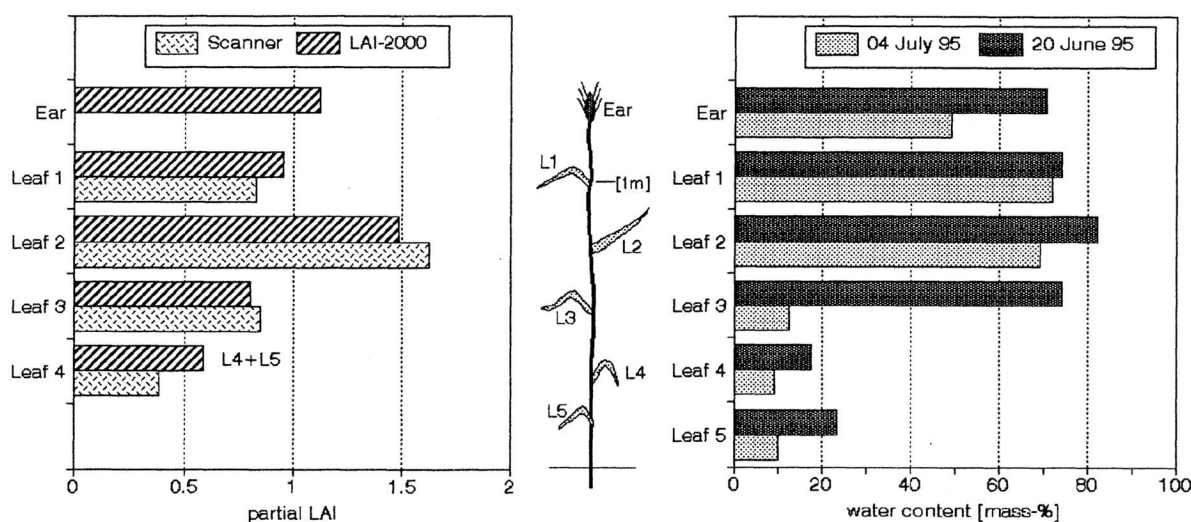


Fig. 3.3: Characteristics of the triticale canopy: (a) leaf area distribution; (b) water content of different leaf levels, determined from the difference between fresh and dry weight.

The results of both techniques are displayed in Figure 3.3a, they agree fairly well. The leaf area of the ear, which also belongs to the photosynthetic active plant parts (cf. Denmead, 1976), could only be estimated by the optical method. The same applies for the lowest leaf (L5) which was already inactive and dried out at the beginning of the campaign. The leaf area of all canopy layers as derived from the optical measurements resulted in a integrated LAI of 4.9 ± 0.5 .

The difference in the biomass measurements given in Table 3.1 are due to the fast senescence development of the triticale during the field campaign. This trend is illustrated by the water content of the individual plant parts shown in Figure 3.3b. The third leaf (L3) experienced a drastic drying out from 70 % to about 10 % water content within only two weeks. Also the 'ear filling' process is indicated by a slight decrease of the ear water content.

3.1.3 Overview of Measured Quantities and Instrumentation

As mentioned in the introduction to Chapter 3, eddy correlation, relaxed eddy accumulation and profile measurements systems were set up and operated simultaneously in the field campaign. An overview of the measured quantities and the corresponding instruments is given in Table 3.2. The detailed setup and components of the individual flux systems are presented and discussed in Sections 3.2 - 3.4. Beside these main flux measurement activities, several additional investigations on trace gas exchange and distribution were performed during the field campaign. They are only partly related to the present study and are therefore not described here in detail. CO₂ and H₂O exchange of single triticale leaves was measured by porometry (Busch et al., 1997). In-canopy profiles of temperature and different trace gases were investigated continuously (Meixner et al., 1996). During twelve nights, profiles of meteorological quantities and trace gas concentrations were measured with a tethered balloon system (Sprung et al., 1996) throughout the nocturnal boundary layer up to heights of 700 m. Some results of these investigations will be used for comparison and interpretation of the micrometeorological flux measurements.

Several supplementary measurements of meteorological and environmental parameters were performed during the field campaign. The additional information was necessary for the control of the flux systems as well as for the evaluation and interpretation of the results. The most important parameters were the wind direction (description of general weather situation, identification of fetch condition), global radiation (characterisation of the photosynthetic activity of the vegetation canopy) as well as relative humidity, surface wetness and rain intensity (identification of problematic environmental conditions for flux measurements).

A compilation of all measured quantities and sensor types is given in Table 3.2. The data of the different instruments were recorded by five independent data loggers (Campbell Scientific, 21X) for the average quantities (10 min means) and a Notebook Computer (Chicony NB5620) for the high resolution eddy correlation time series. The internal clocks of all logging instruments were regularly checked and synchronised.

Tab. 3.2: Survey of all measured quantities in the BELLHEIM'95 campaign relevant for the present study; with information about sensor type, company, calibration and measurement heights.

Measured Quantities for Flux Determination					
<u>Quantity</u>	<u>System</u>	<u>Sensor/Instrument</u>	<u>Company/Type</u>	<u>Calibration</u>	<u>Heights</u>
windspeed	profile EC/REA	3-cup anemometer 3D sonic anemometer	Vector A101M Gill Solent Research	wind channel manufacturer	1.65 / 2.10 / 2.85 / 4.25 m 4.25 m
temperature	profile EC	fine wire thermocouples sonic anemometer	Campbell TCBR-3 Gill Solent Research	- in-situ vs. TC	1.65 / 2.10 / 2.85 / 4.25 m 4.25 m
water vapour	profile EC REA	dew point mirror infra-red gas analyzer infra-red gas analyzer	General Eastern DEW-10 LI-COR LI-6262 LI-COR LI-6262	(abs. meas.) in-situ vs. DEW-10 in-situ vs. DEW-10	1.65 / 4.25 m 4.25 m 4.25 m
carbon dioxide	profile EC REA	infra-red gas analyzer infra-red gas analyzer infra-red gas analyzer	pp-Systems EGM-1 LI-COR LI-6262 LI-COR LI-6262	in-situ vs. LI-COR in-situ vs. cylinder std. in-situ vs. cylinder std.	1.65 / 4.25 m 4.25 m 4.25 m
ozone	profile EC	UV-absorption 253.7nm chemoluminescence	Environment O ₃ 41M IMK Karlsruhe	lab. standard in-situ vs. O ₃ 41M	1.65 / 4.25 m 4.25 m
Additional Micrometeorological Quantities					
wind direction		wind vane	Vector W200P	manufacturer	2.85 m
air pressure		semicond. transducer	Vaissala PTA427	manufacturer	0.8 m
relative air humidity		impedance sensor	Rotronic MP300	lab. vs. dew point gen.	4.25 m
air temperature		Pt100 sensor	Rotronic MP300	manufacturer	4.25 m
rain intensity		tipping rain gauge	Campbell ARG-100	lab.	1.2 m
surface wetness		resistance grid	Campbell 237	-	0.8 / 1.4 m
global Radiation		photocell pyranometer	LI-COR LI200SZ	manufacturer	2.5 m
reflected shortwave radiation		thermal pyranometer	Kipp & Zonen CM5	in-situ vs. LI200SZ	2.5 m
net total radiation		thermal net radiometer	Schulze-Däke	manufacturer	2.5 m
net total radiation		thermal net radiometer	REBS Q*6	in situ vs. Schulze-L.	2.5 m
soil temperature		thermocouples	Omega type J	-	-1 / -2 / -4 / -8 / -16 / -32 cm
soil heat flux		heat flux plates	REBS HFT-1	manufacturer	- 8 cm
soil moisture content		TDR sensors	TRIME-ES P2	manufacturer	- 5 / -10 cm

3.1.4 Tower Setup and Operation Periods

The flux measurement systems and additional instruments were mounted on light mobile tripod towers of ca. 4.5 m height. They had negligible effect on the environmental conditions like radiation, temperature or windfield. Especially the impact on the surrounding triticale canopy was comparatively small, because the towers and sensors could be assembled outside the field and carried afterwards into the right position with minimal destruction of the vegetation cover. This is most important for radiation and low level profile measurements. In order to avoid a mutual interference between the measurement systems, they were distributed on four different masts positioned some 10 m apart (see Fig. 3.4).

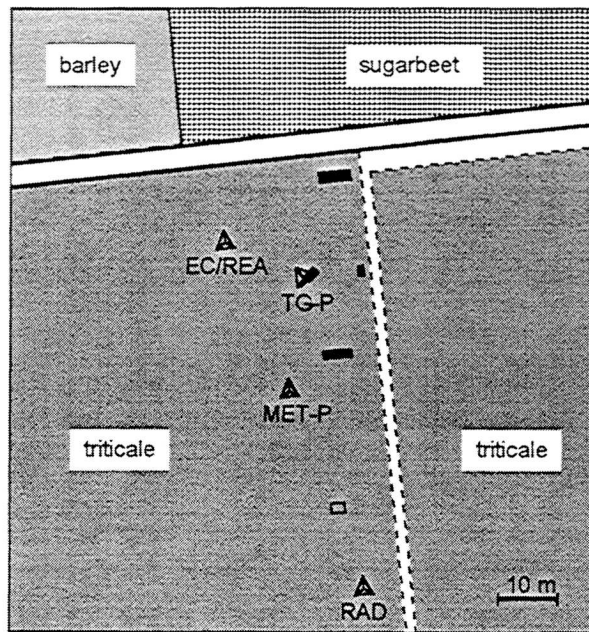


Fig. 3.4: Position of measurement towers in the triticale field; EC/REA: eddy correlation and relaxed eddy accumulation systems; TG-P: trace gas profile system; MET-P: micrometeorological profile systems; RAD: radiation budget system; the additional symbols indicate the position of other measurement facilities not directly related to this study.

One mast (REA/EC) carried the eddy correlation and relaxed eddy accumulation systems and some additional meteorological sensors. The profile systems were installed on two masts, one for the trace gases (TG-P) and one for the meteorological quantities (MET-P). The fourth mast (RAD) with up- and downfacing radiation sensors was more separated from the others towards the south in order to avoid shadowing effects. The masts were located relative to each other approximately on a line northwest-southeast, because these wind directions were supposed to occur most rarely (cf. Fig. 3.1). Thus relatively undisturbed measurements were possible for the main wind directions especially for the southwest sector. In the northeast sector, the road, the footpath between the triticale fields, the lab container and other facilities for the simultaneous ammonia experiment could cause some disturbance mainly in the windfield. Additionally, some small paths (not indicated in Fig. 3.4) through the triticale field were necessary for the installation and maintenance of the measurement systems, but they were kept as narrow as possible.

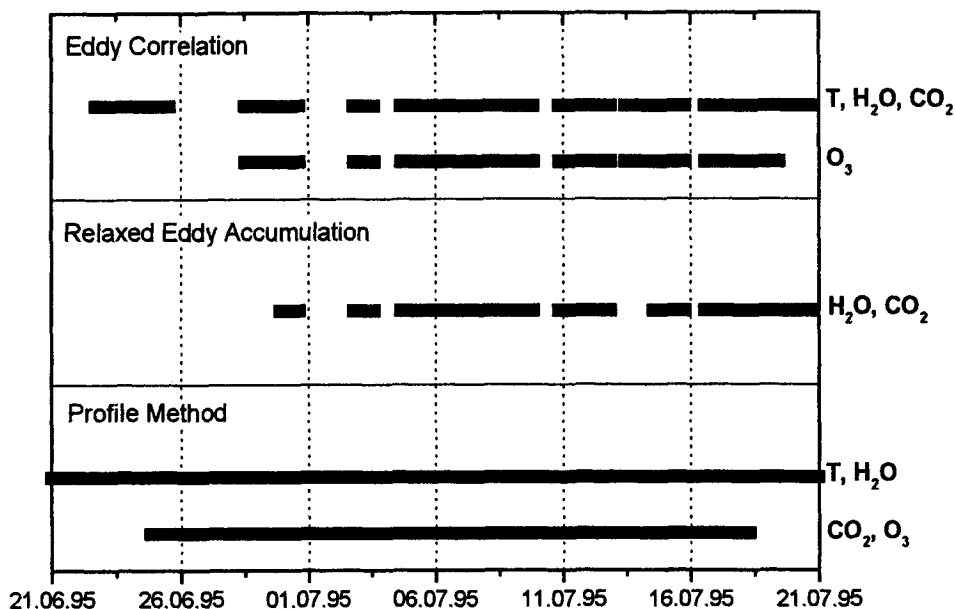


Fig. 3.5: Successful operation periods for different flux measurement systems in Bellheim, June/July 1995; the profile system for temperature and water vapour (part of an energy balance system) was operated from 9 June to 27 July 1995.

The flux measurement activity in the Bellheim'95 campaign was limited mainly to about 30 days from 20 June to 20 July 1995. Only the meteorological profile station (MET-P) was operated somewhat longer from 9 June to 27 July 1995. Eddy correlation measurements for the meteorological quantities (T and H₂O) started on 22 June, whereas the EC system for ozone fluxes and the REA system were available only from 28 June and 29 June on respectively. Fig. 3.5 gives a survey of the different flux systems (methods and quantities) and the effective periods, for which flux measurement data are available. Very short interruptions of one hour or less are not indicated. The interruptions were due to various reasons. Almost all measurement systems were dependent on main power, which broke down a few times during the field campaign. Only the MET-P station could be run practically without interruptions, because it needed only little maintenance and had an independent power supply (car battery and solar panel). The huge amount of eddy correlation data (ca. 50 MB per day) allowed a continuous measurement only for 2 or 3 days. Regularly the full harddisk had to be transferred to a streamer tape, which caused an interruption of several hours. For practical purposes, the flux systems (especially EC and REA) were sometimes turned off intentionally during non-favourable weather conditions (e.g. rain, very low windspeed, etc.) in order to prevent the formation of water in the sampling tubes.

3.2 Profile Systems

3.2.1 Setup and Components

Profile measurements were performed for the trace gases H₂O, CO₂ and O₃. In order to investigate the applicability of the aerodynamic method as well as the closure of the surface energy budget, profiles of windspeed and temperature were also determined. Due to limitations in the available analysing systems (see Section 3.2.3), the trace gases were only measured at two levels. This is usually sufficient for profile methods, although more levels would be desirable. The vertical distance between the two levels

was chosen as large as possible, to obtain possibly large resolvable profile differences. Considering the rule of thumb fetch-to-height-ratio 100:1 (cf. Section 2.6.1), the upper level was set at 4.25 m above ground. This corresponds to an effective aerodynamic height above the displacement level (cf. Section 2.4.3) of about 3.35 m and thus should be sufficient for southwesterly wind directions with fetch length of more than 300 m. The lower level was installed at 1.65 m above ground and thus ca. 30 cm above the maximum height of the cereal plants. In the case of the very dense and uniform triticale canopy with distances of only a few centimetres between individual stalks, this should be sufficient to prevent considerable deviations from the ideal similarity relationships. Although a larger distance from the canopy would have been more appropriate to avoid roughness sublayer effects (cf. Section 2.2.3), a certain compromise has often to be made in order to get resolvable differences especially for CO₂ (KF94:73).

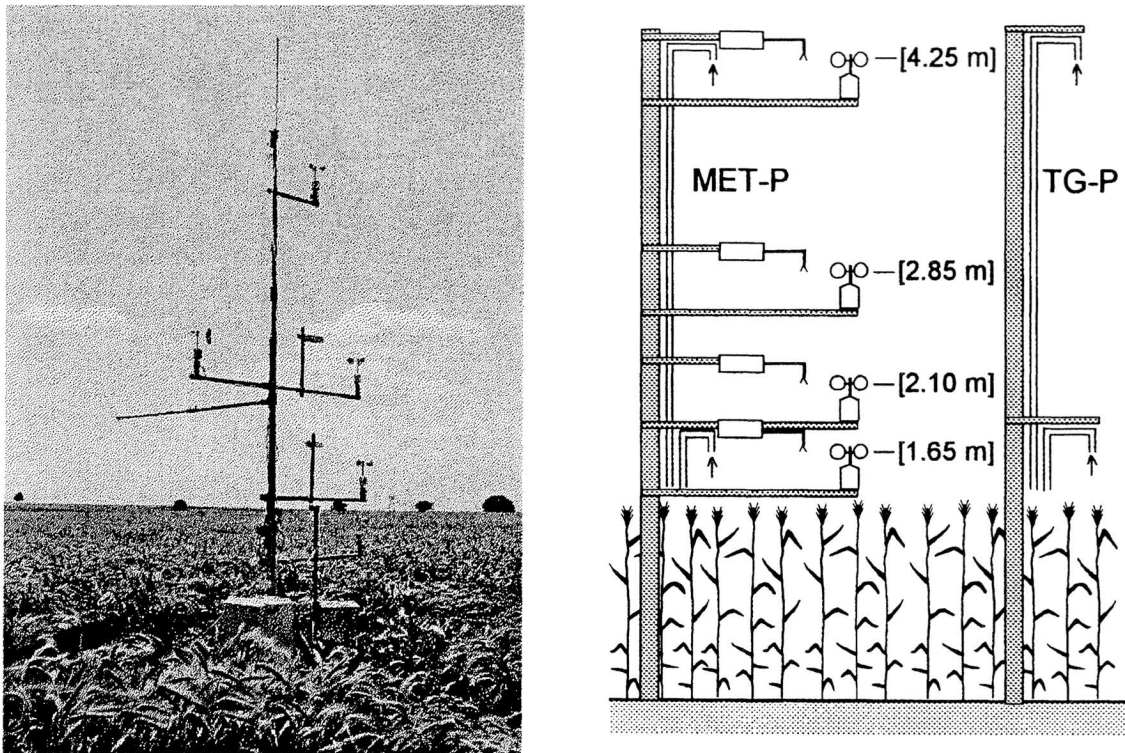


Fig. 3.6: Arrangement of profile measurement levels: (a) picture of the MET-P mast with four levels of wind and temperature measurements; (b) schematic survey of profile measurement levels for different quantities with indication of the canopy height.

For horizontal windspeed and temperature, profile measurements at four different heights were performed. This should allow an independent determination of the displacement height and the roughness length of the triticale canopy. The highest and lowest level corresponded to the sampling points for the trace gas measurements and the remaining ones were placed in between with a logarithmic spacing (Beier and Weber, 1992; Ohmura and Rotach, 1986) at 2.10 m and 2.85 m above ground. This resulted in smaller distances between the lower levels, where the gradients are supposed to be larger. The measurement heights of all profile systems are displayed in Fig. 3.6. Certain profile methods like the (modified) Bowen ratio approach strictly require the different quantities to be measured at exactly the same heights (cf. Section 2.4.2). Although this is not necessary for the aerodynamic profile method, it is often done for practical purposes.

For the application of flux-profile-relationships, the relative precision of the concentration measurements at the different levels (i.e. the precision of the profile difference) is most important, rather than the absolute measurement accuracy. Therefore, the use of independent sensor or sampling units for the different profile levels (like e.g. for windspeed) is usually not the optimal solution for trace gas measurements, because the individual instrumental (squared) errors are added in the calculation of the concentration difference. It is more advisable to use, whenever possible, the same analysing unit for all levels. In this way, the uncertainty in the response curve of the instrument due to calibration errors or variations and drift in sensitivity or offset has only a small (proportional) influence on the measured concentration difference and thus on the resulting flux. This principle was applied in the present campaign for all trace gas profiles (H_2O , CO_2 and O_3). The air from the two profile levels was sampled continuously into Teflon tubes and was directed to the analysing units (see Fig. 3.7). The inlets and analysing system for water vapour was installed at the MET-P mast, whereas the analysers for ozone and CO_2 were situated in the lab container at the edge of the field. Therefore, the air was sampled 16 m away on the TG-P mast and was transported at a high flow speed of about 7 m s^{-2} to the container.

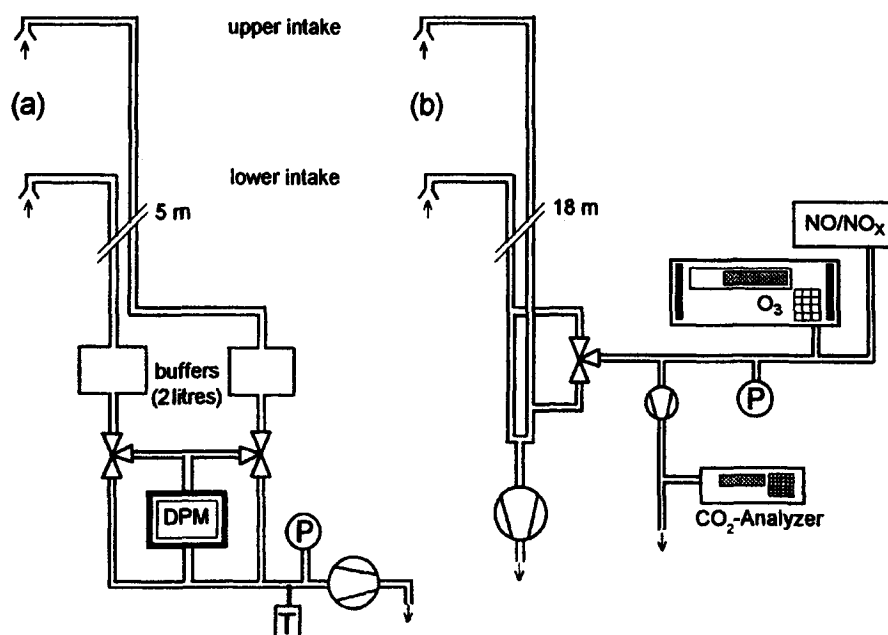


Fig. 3.7: Schematic setup of trace gas analyser systems for the trace gas profiles of (a) water vapour and (b) carbon dioxide and ozone.

Alternating, air from both sampling tubes was directed to the closed path gas analysers. The switching intervals were 3 min for CO_2 and O_3 (2 min for H_2O). During the first minute (40 s for H_2O) of each interval, the system was allowed to adapt to the new concentration, i.e. the measurements were discarded. For the rest of the interval, the signals were logged every second. For each full measurement cycle of 6 minutes (2.5 cycles within 10 min for H_2O), average values and standard deviations for both profile levels were stored. Due to the long sampling lines and the high flow rates, a considerable under-pressure developed in the tubes, that was recorded by a piezoresistive pressure transducer (Data Instruments, Model XT). With the setup illustrated in Fig. 3.6, a possible pressure difference between the two sampling lines was either detected and included in the calculation of the concentration difference, or it was avoided by the use of an additional pump that transferred the air to ambient pressure (CO_2 measurement). Temperature differences were generally compensated through the high heat capacity of the analysers. The different systems are described in detail in the following sections (see also Table 3.2).

3.2.2 Trace Gas Analysers

Water Vapour

The water vapour or humidity profile was measured with a dew point mirror DPM (General Eastern, Dew-10). The DPM is a physically absolute instrument and yields the dew point temperature that is uniquely related to the water vapour partial pressure. As the temperature measurements are very reliable and stable (Pt-100 resistance thermometer), the instrument did not need field calibrations and could be used as standard for the other humidity sensors (impedance sensors, infrared analysers). However, a period of about 20 - 30 s is necessary to stabilise on a certain concentration and to perform an accurate measurement. Therefore, disturbing shorter-time variations were smoothed out by including 2 litre buffer volumes in the sample lines (see Fig. 3.7). In this way, the characteristic time constant was extended to about 4 min (given a flowrate of 0.5 L min^{-1}).

For all closed path sensors, condensation inside the tube is a common problem, that occurs frequently during night under clear sky and low wind conditions (strong radiative cooling). For the present system, condensation events could not be prevented, but they could be detected with the application of additional controlling sensors. Inside the sampling tube near the DPM, the air temperature was measured continuously. With this information, the relative humidity inside the closed path system was determined. If the relative humidity was close to 100% (>98% in the past 20 min) condensation water occurred most likely and the data were rejected. The success of this procedure was checked by comparing the DPM data to the absolute humidity derived from the ventilated open path impedance sensor (Rotronic, MP300), which is less accurate but has (almost) no condensation problems. In the diurnal course, a condensation event appeared fairly clear as a underestimation of the water vapour concentration during night and a big erroneous peak in the morning hours.

Ozone

The ozone concentration profile was analysed with a UV-absorption instrument (Environnement O₃ 41M) provided by the research group of Dr. Güsten of the IMK Karlsruhe. The closed path analyser was equipped with a built-in temperature and pressure correction. Thus the output signal was directly proportional to the trace gas mixing ratio. The sensitivity of the instrument is very stable with a specifically small drift tendency. Therefore, it was calibrated only once before the campaign against a laboratory standard instrument at the IMK. The stability of the calibration was tested by comparing the measurements against another instrument simultaneously operated by the IMK at a distance of about 400 m. The results in Fig. 3.8 show a very good agreement for the whole period despite the different measurement levels.

In order to minimise chemical reactions of the ozone in the sampling tubes (cf. Beier and Schneewind, 1991), they were insulated against solar radiation and a high flowrate of about 6 L min^{-1} led to a very short residence time of < 2.5 s. Additionally, NO and NO_x concentrations in the sample air were monitored in order to identify concentration ratios of the NO-O₃-NO₂ triad that are critical for the flux determination (cf. Vila-Guerau de Arellano and Duynkerke, 1992). The NO/NO_x chemoluminescent instrument (Environnement, AC 31M) was also provided and calibrated by the IMK Karlsruhe.

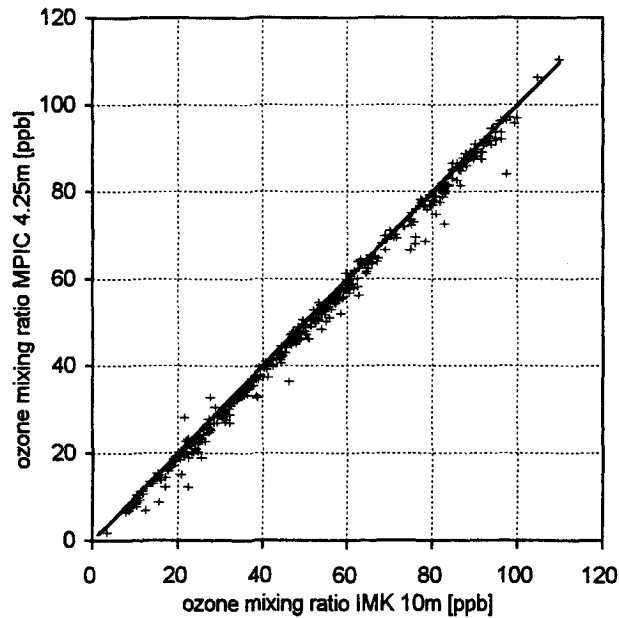


Fig. 3.8: Comparison of ozone mixing ratio between the profile analyser (4.25 m level) and a simultaneously operated instrument of the IMK group (10 m above ground over a maize field) at a distance of about 400 m; well mixed conditions ($u_* > 0.1$) in the period 24 June to 11 July 1995.

Carbon Dioxide

The carbon dioxide profile concentrations were measured by an infra-red gas analyser (pp-Systems, EGM-1). The applicability of this instrument for profile measurements was limited by the digital-to-analog-converter (DAC) output resolution of only 12 bit corresponding to a minimum resolution step of about 1 ppm. However, the problem was relaxed by the averaging over 30 min. Unfortunately, only two high resolution infra-red gas analysers (IRGA) were available for the campaign and they were preferably used for the eddy correlation and accumulation systems (see following sections). The EGM-1 analyser is a single cell instrument with an automated online offset correction. Air is sampled through a CO₂ scrubbing unit (soda lime) once every minute and the resulting offset value is subtracted from the subsequent measurements. The span was determined by calibration against different bottle standards (0, 300, 400 ppm) three times during the field campaign.

3.2.3 Sensors for Meteorological Quantities

The horizontal windspeed profile was measured using 3-cup-anemometers (Vector Instruments, A101M). They are relatively robust but have nevertheless a very low starting and stalling speed between 0.1 and 0.2 m s⁻¹. They were calibrated and cross-checked after the field campaign (29 august 1995) in the wind tunnel of the University of Bonn (Meteorological Institute). All four instruments exhibited a non-linear behaviour, that led to deviations from a simple linear function of more than 5 %. Therefore, the calibration functions were divided into two ranges (with a limit of ca. 3.2 m s⁻¹), for which individual linear relationships were fitted. They showed relative deviations below 2 % (for windspeed > 1 m s⁻¹) and absolute deviations of less than 0.04 m s⁻¹. The wind tunnel calibration resulted in measurement values about 5 - 7 % lower compared to the application of the original manufacturer's calibration. Additionally, differences between individual sensors of up to 2 % were corrected. They would have caused errors in the profile differences (highest minus lowest level) in the order of 10 %. It has to be noticed, that the wind tunnel calibrations provide only corrections of average (non-turbulent) flow

effects. Particular turbulence effects like overspeeding (cf. Busch and Christensen, 1976; Rotach, 1991) could not be investigated with the laminar tunnel flow.

The air temperature profile was measured at four levels with fine gauge thermocouples (Campbell Sci., TCBR-3). The measurement junctions were exposed to the ambient air without radiation shields or artificial ventilation. The very small heat capacity due to wire diameters of only 76 μm together with the natural ventilation (wind) is assumed to prevent significant radiative heating effects (Campbell Scientific, 1991). All four thermocouples were connected to a multiplexer (Campbell Sci., AM25T) inside a heat insulated enclosure. The multiplexer panel represented the common reference junction for all thermocouples; in this way, systematic deviations between the temperature levels were avoided. The reference temperature was measured by an Pt-100 resistance thermometer inside the multiplexer. All temperature signals were sampled at an interval of 1 s, the windspeed signals every 10 s. Averages and standard deviations were calculated online and stored for 10 min intervals.

3.3 Eddy Correlation Systems

3.3.1 Setup and Components

Eddy correlation measurements were performed for the trace gas fluxes of CO_2 , H_2O and O_3 as well as for the fluxes of sensible heat and momentum. The measurement system consisted of a sonic anemometer (Gill Instruments, Solent Research 1012 R2) for the detection of the three-dimensional wind vector and the air temperature, a closed path $\text{CO}_2/\text{H}_2\text{O}$ gas analysers (LI-COR, Li-6262) and a fast response ozone sensor (IMK Karlsruhe, custom-built). They are described in the following sections. The sonic anemometer and the inlets for the trace gas analysers were installed at a height of 4.25 m above ground, equal to the uppermost level of the profile system. This was mainly done for practical reasons, e.g. the possibility for direct crosschecks and calibrations between the systems.

For the (horizontal) arrangement of the eddy correlation sensors and sampling tubes (including the REA inlet system, see later), a compromise had to be made between a minimal mutual disturbance and a minimal separation between the sensors and inlets (cf. Section 4.1). This problem strongly depends on the size and bulkiness of the components and the occurring wind directions. Since measurements with south-westerly winds were assumed to be most important, the sonic anemometer was exposed with a free view in this direction. All other components were installed in the opposite direction to the sonic towards the east. The 1/4" inlet tube for the $\text{CO}_2/\text{H}_2\text{O}$ gas analysers was relatively thin and could be fixed directly to a supporting arm of the sonic (12 cm from the centre) without causing much additional disturbance. The inlet of the ozone analyser was more bulky and was therefore positioned at a larger distance from the sonic head (40 cm). All sampling tube inlets were facing downward and wide enough to avoid sampling of liquid rain or dew water. The whole arrangement is shown in Fig. 3.9.

Data acquisition

The entire high resolution time series of the eddy correlation instruments were recorded and stored in their raw state by an IBM compatible Notebook computer (Chicony NB5620) with an 80386 processor. The analog signals from the trace gas analysers were continuously sampled by the 11 bit analog-to-digital-converter (ADC) of the sonic anemometer for external input.

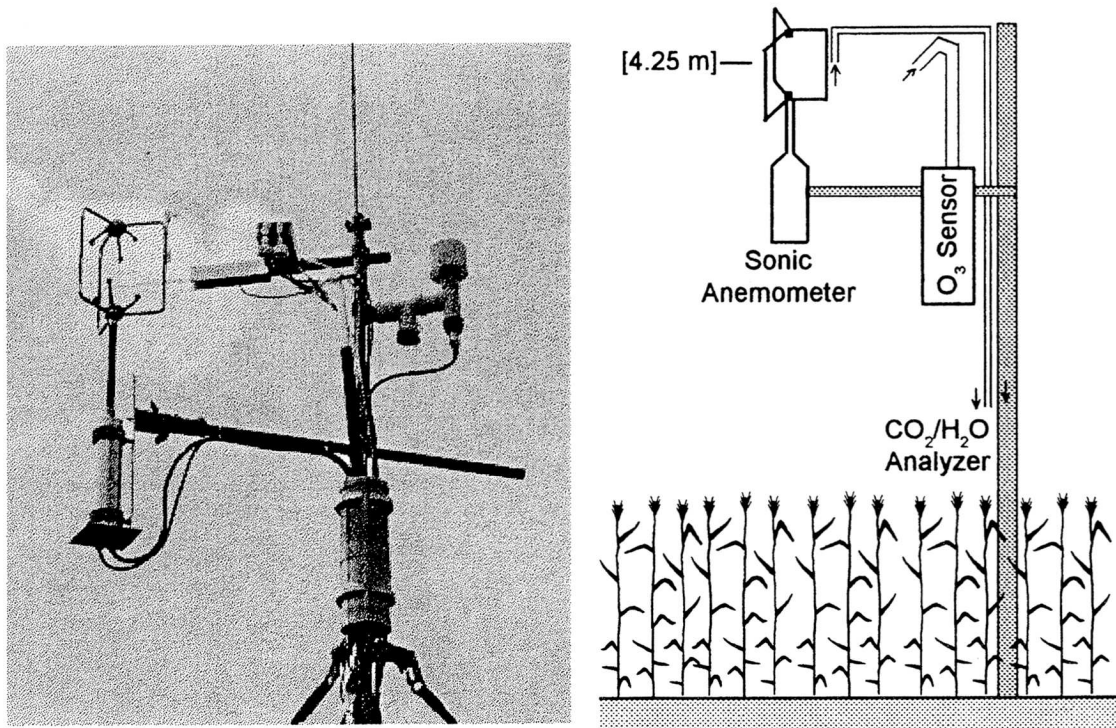


Fig. 3.9: Setup for eddy correlation measurements: (a) sonic anemometer and inlets for trace gas analysers (incl. additional equipment for REA and meteorological sensors); (b) illustration of the entire EC measurement setup.

Together with the digital sonic data, they were then transferred to the computer via an RS232 serial interface. In this way the synchronicity of the different signals was always guaranteed and the entire processing of the wind and temperature signals was done solely in digital form without the influence of electronic noise, which is a problem mentioned by some investigators (e.g. Beier and Weber, 1992). The sonic anemometer recorded and transferred its data at a rate of 20.83 Hz (1250 samples per minute); each sample represented an average of 8 individual sonic measurements. The external analog input channels, however, were converted at a rate of only 10 Hz, and therefore each value occurred about twice in the stored 20.83 Hz data record.

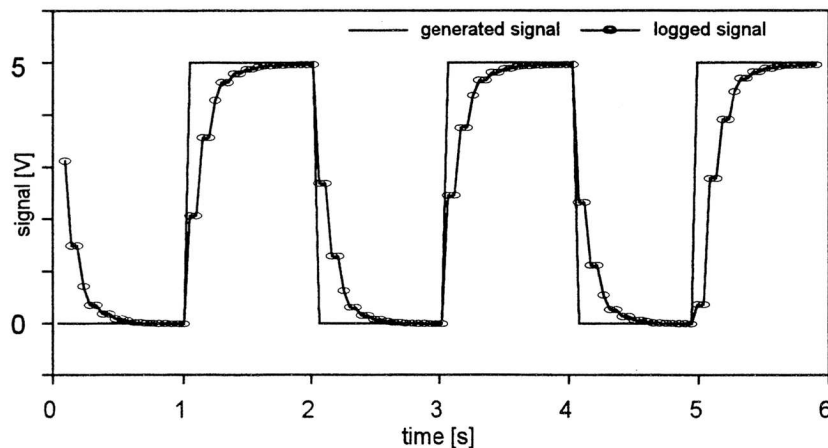


Fig. 3.10: Response of the Gill sonic analog-to-digital-converter (ADC), including the analog RC-prefilter, to a rectangular input signal 0/5V with a switching interval of 1 s.

An additional serious limitation for the data acquisition was created by the analog lowpass prefiltering of the sonic ADC, that is necessary for avoiding aliasing effects (cf. Appendix A.2). Its behaviour was investigated in a laboratory test, where an ideal rectangular signal was generated and sampled via the sonic instrument. The resulting logged signal displayed in Fig. 3.10 exhibits a (relatively slow) exponential response that is typical for analog RC filters, which represent a first order system (cf. Appendix A.7). In order to quantify the attenuation characteristic of the filter, an exponential function (Eq. A.27) was fitted to the step response curves in Fig. 3.10. The fitting parameter τ_R , representing the response time of the ADC prefilter, was determined to about 0.125 s corresponding to a cutoff frequency of 1.3 Hz. Following the recommendations of KF94:262, this filter is clearly too strong; a cutoff frequency of 5 Hz (half the sampling rate) would have been appropriate. According to the manufacturer (Westgarth, 1996, pers. communication) the observed behaviour results from a mistake in the electronics of the sonic instrument. Unfortunately, it was not detected in time and could be corrected only after the measurement campaign.

3.3.2 Sonic Anemometer-Thermometer

Wind Measurements

The principle of sonic anemometry is to determine the windspeed from the flight times of ultrasonic sound pulses travelling across a fixed sound path of length ℓ . A pair of opposite transducers act alternately as transmitters and receivers, sending pulses between themselves. The flight times in each direction t_1 and t_2 are measured; they are related to the speed of sound c and the windspeed v along the sound path:

$$t_1 = \frac{\ell}{c + v} \quad ; \quad t_2 = \frac{\ell}{c - v} \quad . \quad (3.1)$$

Thus the windspeed can be calculated as:

$$v = \frac{\ell}{2} \left(\frac{1}{t_1} - \frac{1}{t_2} \right) \quad . \quad (3.2)$$

The sonic wind measurement is not affected by the speed of sound in the air and thus is independent from atmospheric conditions like pressure, temperature or humidity. By arranging three pairs of transducers in different orientations, the local three-dimensional windvector can be unambiguously derived.

The sonic anemometer instrument used in the present study (Gill Instruments, Solent Research 1012 R2), has three intersecting measurement paths that show a non-orthogonal arrangement with a rotational symmetry (120 deg intervals) around the vertical axis of the instrument (see Fig. 3.9). Each path has an angle of 45 deg with reference to the horizontal. The same symmetric arrangement was chosen for the three thin supporting arms (6.3 mm diam.) making the instrument almost equally suitable for all wind directions. The measured wind components are internally transformed to a cartesian coordinate system with two horizontal and a vertical axis. The built-in microprocessor also provides an online correction of flow distortion effects of the sonic head. The entire probe and its mounting can lead to an attenuation and deflection of the mean wind by a blocking effect, but especially the measured components along each sensor axis are attenuated by formation of a turbulent wake behind the sound transducer. This so-called 'transducer shadowing effect' was investigated and described e.g. by Wyngaard and Zhang (1985), Wyngaard (1988), and Rotach (1991).

The flow distortion behaviour of the used anemometer type, was examined in detail by several authors in wind tunnel experiments. While Mortensen and Hojstrup (1995) found, that the manufacturer's calibration is able to correct and improve the results significantly (although not fully), Grelle and Lindroth (1994) came to the conclusion, that it makes the deviations even worse. Thus it seemed to be necessary to test the performance of our instrument individually. Various experiments were carried out at an open wind tunnel (29 August 1995, University of Bonn) with and without the application of the manufacturer's calibration. Only some important results are presented here. Fig. 3.11 shows the deviation of the absolute windspeed measured by the sonic for different azimuth angles. It turns out, that with the calibration applied, the original underestimation of up to 10% is considerably reduced $\leq 5\%$. Especially the pronounced attenuation effects of the three support arms (at 120, 240 and 0/360 deg) are compensated. This behaviour is in good quantitative agreement with the findings of Mortensen and Hojstrup (1995). The data in Fig. 3.11 are obtained for a pure horizontal airflow (relative to the instrument), but comparable results were found also for sensor tilts of +10 deg and -10 deg (not shown here).

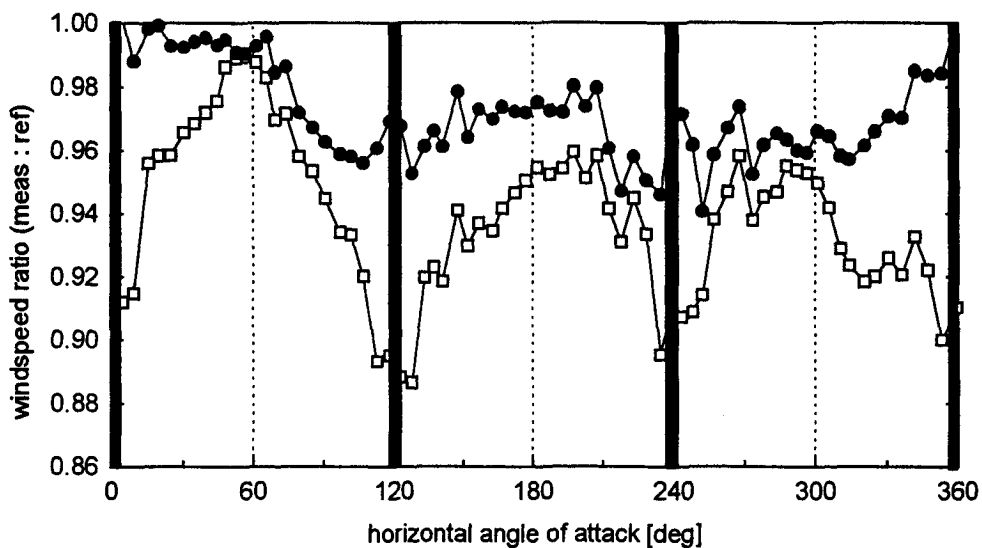


Fig. 3.11: Underestimation of absolute windspeed measured by the Gill sonic anemometer for different wind directions in the wind tunnel experiment: without calibration (open squares) and with the manufacturer supplied calibration (solid circles). The supporting arms (as seen from the centre of the sonic head) are indicated as solid bars.

Flow distortion affects not only the magnitude of the wind vector, but also its angle of attack in the horizontal (apparent wind direction) and in the vertical (apparent pitch or tilt). Tilt errors are particularly important for flux measurements, because they are connected directly to errors in the vertical windspeed (as part of a mainly horizontal windvector). The apparent tilt of the wind vector for horizontal flow in the wind tunnel is displayed in Fig. 3.12a. Beside the three-periodic variations obviously induced by the symmetrically arranged transducers, a one-period modulation over the whole 360 deg range can be identified. This may be assigned (a) to a tilted setup of the turntable, on which the instrument was mounted, (b) to a non-parallel wind tunnel flow, or (c) to a tilted geometry of the sonic transducers compared to the instrument body. Since other authors (Mortensen, 1994; Mortensen and Hojstrup, 1995) found a similar systematic behaviour under different environmental conditions, the effect (c) seems to be most plausible. This explanation implies, that a proper external alignment of the instrument with e.g. a spirit level is difficult. However, this is not very problematic, because an alignment with the

mean flow rather than with the geopotential is usually more suitable in field experiments. It can be achieved by a coordinate transformation relative to the mean wind vector (cf. Section 4.1.3).

In order to study the variations in Fig. 3.12a that are not explicable by a general sensor tilt, this effect was eliminated by fitting and subtracting sine function of period 360 deg from the original data. The resulting deviations are shown in Fig. 3.12b. They are clearly related to the position of the transducer heads indicated in the diagram. However, they are relatively small, hardly exceeding 2 deg.

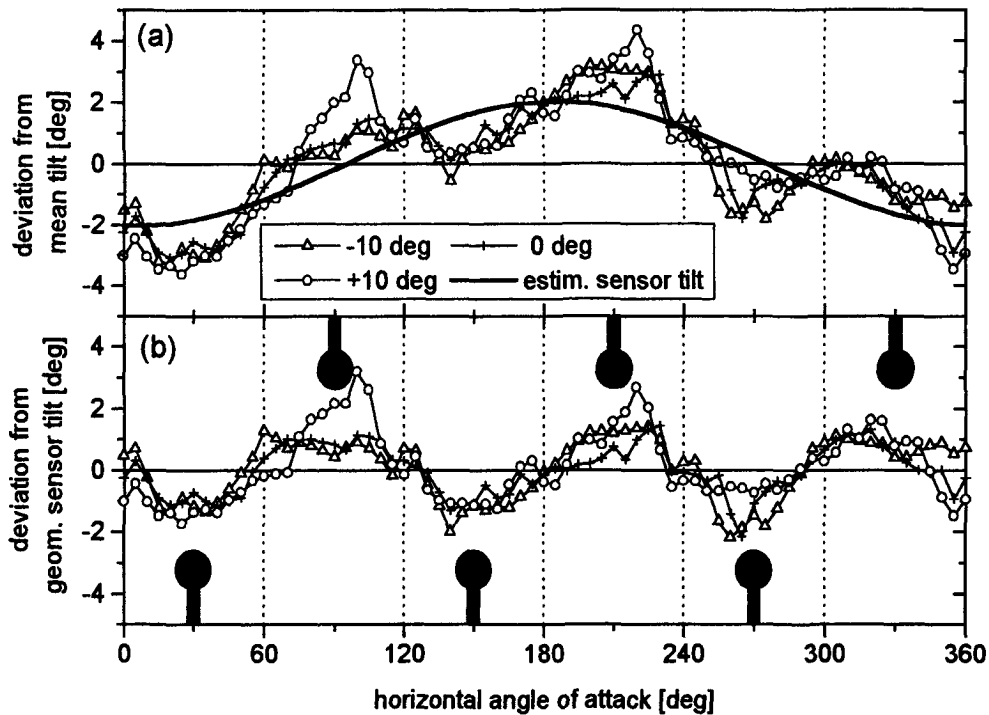


Fig. 3.12: Apparent tilt of the windvector measured by the Gill sonic anemometer for different azimuth angles in a wind tunnel experiment, with application of the manufacturer supplied calibration; (a) deviation from mean tilt (turntable) as given by the legend, the smooth curve represents a fitted one-period sine function; (b) deviation from the sensor tilt (fitted sine function), the position of the upper and lower transducer heads (as seen from the centre of the probe) are indicated schematically.

Due to the positive effect of the manufacturers calibration on the sonic measurements in the wind tunnel and the generally small remaining deviations, no additional corrections for distortion effects were applied to the sonic wind vector output. The mentioned alignment of the coordinate system with the mean flow is a purely mathematical procedure and not only related to the sensor characteristics. It is described in detail in Section 4.1.3.

Temperature Measurements

From the sonic measurements, not only the windspeed but also the air temperature can be derived. Instead of solving the relationships 3.1 for the windspeed v , they can also be solved for the speed of sound:

$$c_{\text{raw}} = \frac{\ell}{2} \left(\frac{1}{t_1} + \frac{1}{t_2} \right). \quad (3.3)$$

However, the resulting value is not exactly equal to the speed of sound c , and therefore it has been specified as c_{raw} . If there is a wind component v_n perpendicular (normal) to the measurement path, the effective travelling distance of the sound pulse is extended, because it deviates from the direct linear way. According to Kaimal and Gaynor (1991) this effect can be expressed in the following form:

$$c_{\text{raw}} = \sqrt{c^2 - v_n^2} . \quad (3.4)$$

For an ideal gas, the speed of sound c is connected to the adiabatic compressibility and thus - via the ideal gas law - to the temperature T (Kneubühl, 1988):

$$c^2 = \left(\frac{dp}{d\rho} \right)_{\text{adiabat.}}^{-1} = \frac{c_p}{c_v} \cdot \frac{p}{\rho} = \frac{c_p}{c_v} \cdot \frac{R}{m} \cdot T \quad (3.5)$$

(p : pressure; ρ : density, c_p, c_v : heat capacity at constant pressure/volume;
 R : general gas constant; m : average molecular mass) .

For measurements in the ambient air, the influence of the variable humidity on the properties m , c_p and c_v has to be considered. According to Iribarne and Godson (1981), they are related to the respective dry air properties (with index d) as follows:

$$\frac{c_p}{c_v} \cdot \frac{1}{m_a} = \frac{c_{pd}(1 + 0.54 \mu_{\text{H}_2\text{O}})}{c_{vd}(1 + 0.60 \mu_{\text{H}_2\text{O}}) \cdot m_{ad}(1 - 0.38 \mu_{\text{H}_2\text{O}})} \approx \frac{c_{pd}}{c_{vd} \cdot m_{ad}} \cdot (1 + 0.32 \mu_{\text{H}_2\text{O}}) . \quad (3.6)$$

The combination of Eqs. 3.4 - 3.6, with the constant properties unified to a single factor, yields the final formula for the calculation of the air temperature from the raw sonic output c_{raw} :

$$T = \frac{c_{\text{raw}}^2 + v_n^2}{403 \cdot (1 + 0.32 \mu_{\text{H}_2\text{O}})} . \quad (3.7)$$

For average temperature calculations, the crosswind v_n can be neglected, because it is additive and several orders of magnitude smaller than the speed of sound. The humidity correction is more important and can amount to about 1 Kelvin. However both effects have to be considered in fluctuation quantities like variances or covariances (cf. Section 4.1.4). The specific advantages and disadvantages of sonic temperature measurements for turbulence studies have been discussed e.g. by Larsen et al. (1993).

For deriving the temperature as well as the windspeed from sonic flight time measurements, the effective pathlength ℓ is necessary. In the investigations of Mortensen and Hojstrup (1995), the individual paths length of the Gill Solent instruments deviated up to 1.3 mm from the nominal length of 149 mm. For the windspeed, such an effect of less than 1% is negligible, yet it is incorporated in the flow distortion correction anyway. However, a 1% error in c corresponds to a 2% error in the absolute sonic temperature resulting in an offset of about 6 K!. Moreover, Mortensen and Hojstrup found a considerable sensitivity of the transducer electronics on the ambient temperature that has a strong influence on the measured flight times (up to 1%). This latter effect is much more problematic than the pathlength, because it shows a strong non-linearity and cannot be described physically. Thus the sonic temperature calculated by Equation 3.7 needs an additional empirical calibration against a reference temperature sensor.

The calibration of the sonic temperature was performed during the field experiment in-situ against the uppermost temperature level (fine-wire thermocouple) of the profile system installed at the same height. For reasons of comparability, only cases with a windspeed of more than 2 m s^{-1} and a relative humidity below 90% were included. Fig. 3.13 shows the deviation of the raw sonic temperature from the reference value. A systematic but non-linear behaviour can be observed. The variation of 3 K is comparable to the 1% deviation in the flight times observed by Mortensen and Hojstrup. It also looks very similar to the results of Laubach and Teichmann (1996). However, they explained the non-linearity with suspected dew and ice formation on the transmitter heads, which can be excluded in the present study.

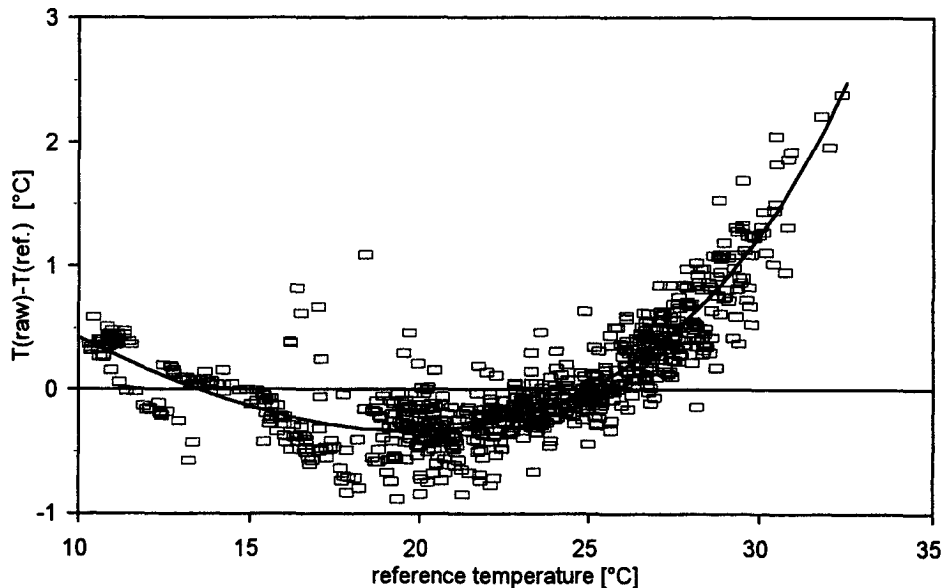


Fig. 3.13: Deviation of sonic derived temperature from reference measurements (thermocouple/Pt-100); square symbols represent selected data with rel. humidity < 90% and windspeed > 2 m s^{-1} ; line curve represents empirically fitted functional relationship (polynomial of 3rd order).

In lack of a satisfying physical explanation of this effect, an empirical correction of the sonic derived temperature values (Eq. 3.7) was performed. A third-order polynomial was fitted to the data displayed in Fig. 3.13 and was applied to all average values. It reduced the deviation from the reference temperature to a mainly statistical scatter typically within $\pm 0.5 \text{ K}$. The discussed effect seems to have no influence on the fluctuating quantities. This was found by a comparison of the temperature variances obtained by the sonic and the profile fine wire thermocouple measurements. They showed a reasonable agreement and no systematic deviations could be observed.

3.3.3 Closed Path Infra-Red-Gas-Analyser

For the fast response detection of water vapour and carbon dioxide concentrations, a closed path infra-red gas analyser (LI-COR, LI-6262) was applied. Air was sampled near the sonic anemometer head (at 4.25 m height) and pulled through a 1/4" teflon tubing of 6 m length down to the analysing unit at the ground (see Fig 3.14). Before it passed the analyser, the air was cleaned by a particle filter with a pore diameter of $2 \mu\text{m}$. The sample airflow was produced by a rotation pump (Brey, G12/07-N) positioned downstream of the IRGA and regulated by the output of a mass flowmeter (MKS, Type 358C) to maintain a constant flowrate of 7.2 sL min^{-1} . The temperature in the analyser chamber was recorded by

the instrument itself; the pressure was measured externally by a piezoresistive transducer (Data Instruments, Model XT) at the analyzer outlet.

The measurement principle of the LI-6262 is based on the absorption difference of infra-red radiation passing alternating through two gas sampling cells (cf. LI-COR, 1992). The reference cell has to contain a gas of known CO₂ and H₂O concentration, while the sample cell is flushed by the gas to be analysed. The absorption of the IR-radiation in both cells is measured by sensors with specific optical bandpass filters (4.26 μm for CO₂ and 2.59 μm for H₂O) that have a negligible overlapping. The sensor signal V_c is a linear function of the difference in absorption between the two cells. In the present study, the reference cell (R) was continuously supplied with zero air (free of CO₂ and H₂O) through a closed circulation loop, which contained a scrubber column with soda lime and the desiccant Mg(ClO₄)₂. In this arrangement, the output signal was only a function of the respective sample air concentration: V_c = f(ρ_c).

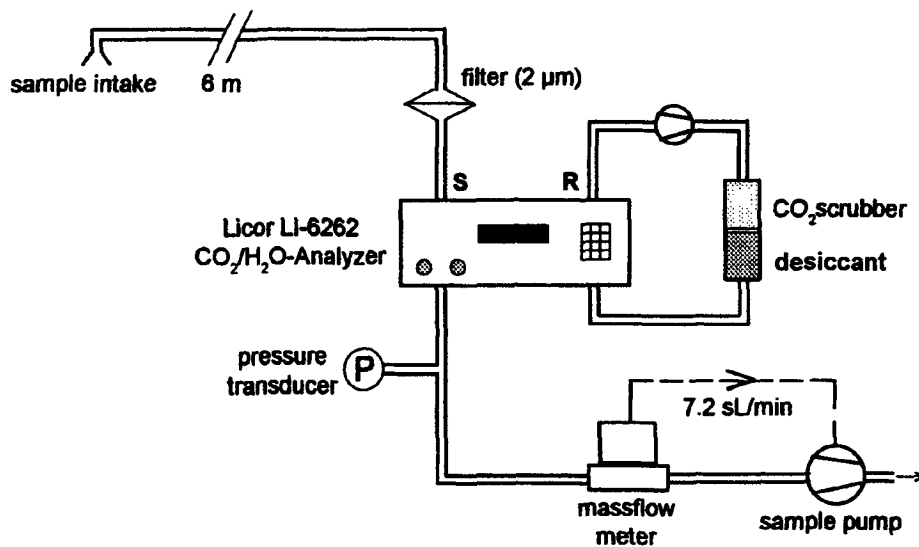


Fig. 3.14: Schematic setup of fast response CO₂ and H₂O measurement system; S: sample cell inlet; R: reference cell inlet.

Yet, according to McDermitt et al. (1993), the trace gas absorption capacity over the short cell length used in the LI-6262 is not constant, because the width of the non-overlapping absorption lines varies with pressure. This effect can be considered in the following way:

$$\frac{V_c}{p} = f\left(\frac{\rho_c}{p}\right) \tag{3.8}$$

Applying the ideal gas law and considering the dilution effect of the air humidity, the relationship for the measured trace gas mixing ratio μ_c (with respect to dry air, cf. Eq. 2.28) takes the form

$$\mu_c = F\left(V_c \frac{p_0}{p}\right) \cdot \frac{T}{T_0} \cdot \frac{1}{1 - \mu_{H_2O}} \tag{3.9}$$

F represents a unique non-linear relationship that is determined empirically by the manufacturer for each instrument at a defined temperature T₀ and pressure p₀. The functions for CO₂ and H₂O are both given as third order polynomials roughly similar in form (but not exactly equivalent) to the logarithmic Lambert-Beer absorption law. Variations and drift in the instrument response (caused by IR-source,

windows and filters, detectors, electronics) are relatively small but necessitate periodic calibration. According to LI-COR (1992), they do not affect the non-linear function 3.9, but can be compensated by a linear adjustment (offset and span) of the raw output signal V_c .

During the field campaign, the CO_2 output of the IRGA instrument was calibrated three times with cylinder standards of 0, 300, and 403 ppm (Deuste-Steininger, accuracy ± 1 ppm) at intervals of two weeks. The resulting variation or drift with time was about 3.5% in the span and 1% (of typical signal values) in the offset. In lack of better information, a linear trend was assigned to both parameters separately. With the same standard gases, also the offset of the water vapour signal could be determined. The span for H_2O had to be calibrated through an online in-situ comparison with the absolute measurements of the dew point mirror (DPM) (see Section 3.2.2). In Fig. 3.15a, the raw LI-6262 output signal is plotted against the reference DPM mixing ratio. Beside the general scatter, the expected non-linear response of the sensor can be observed as well as certain obviously erroneous cases. As mentioned already for the DPM profile system, they can be explained by the formation and residence of condensation water inside the sampling tube. The condensation events to be rejected were detected by comparison with the other humidity instruments (DPM and Rotronic impedance sensor) and by the identification of implausibly low standard deviations of the LI-6262 signal. An influence of condensation water on the CO_2 measurements was not observed. The application of one constant calibration factor for the whole campaign and the subsequent correction of sensor non-linearity as well as temperature and pressure effects according to Eq. 3.9 yielded a satisfying agreement with the reference DPM values (see Fig. 3.15b).

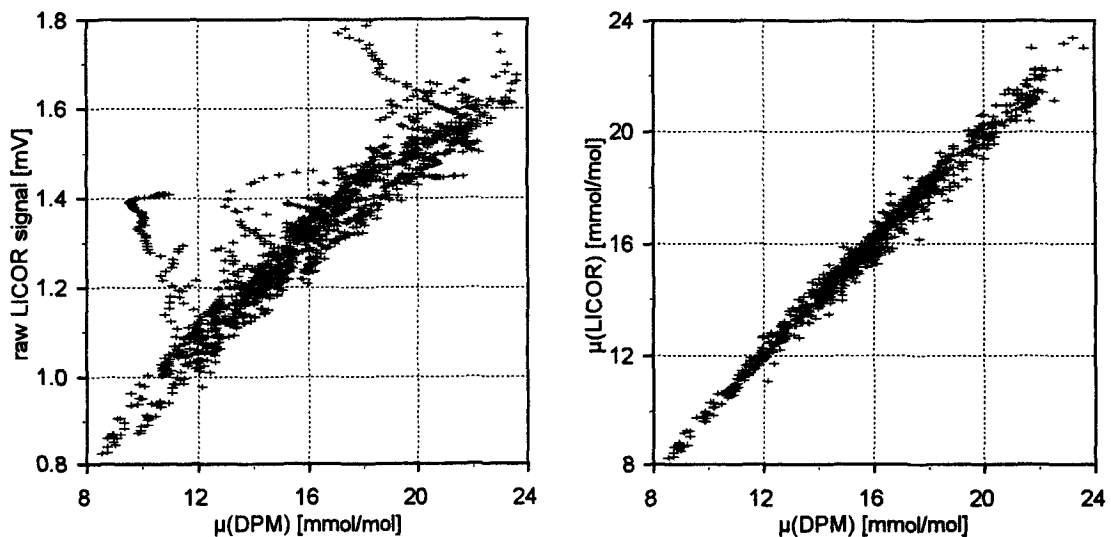


Fig. 3.15: Comparison of LICOR H_2O signal vs. dewpoint-mirror (DPM) measurements of the profile system: (a) raw LICOR voltage signal; (b) calibrated and corrected LICOR mixing ratio.

Time Response Characteristic

The LI-6262 instrument has a nominal response time of about 0.1 s for both CO_2 and H_2O . However, the effective performance depends on the inlet system and on the flow rate through the analyser. Since the sample cell has a volume of 11.9 ml, the chosen flowrate of ca. 7.5 L min^{-1} was high enough to exchange the cell volume 10 times per second. The sampling tube of length $X = 6 \text{ m}$ had an inner diameter $D = 4.35 \text{ mm}$ leading to a minimal average flow velocity $u_t = 8.4 \text{ m s}^{-1}$. According to Equation A.33, the present setup creates a tube-flow with Reynolds numbers higher than 2500 and thus a turbu-

lent flow regime. This has important implications for the damping effect on the trace gas fluctuations discussed in Appendix A.7 and Section 4.1.5. The effective time response characteristic of the entire system was tested in laboratory step response experiments with the same tube length as used in the field experiment (long tube: 6 m) and additionally with a reduced tube length (short tube: 0.5 m). Typical response curves for CO₂ and H₂O with both tube length are displayed in Fig. 3.16. For all cases, the exponential response behaviour is not significantly different from the one in Fig. 3.10 for an ideal step signal and can be entirely assigned to the electronic pre-filtering of the data acquisition system (see Section 3.3.1). This effect is obviously much larger than a possible signal damping caused by the tube flow or by the analyser, which therefore can be neglected.

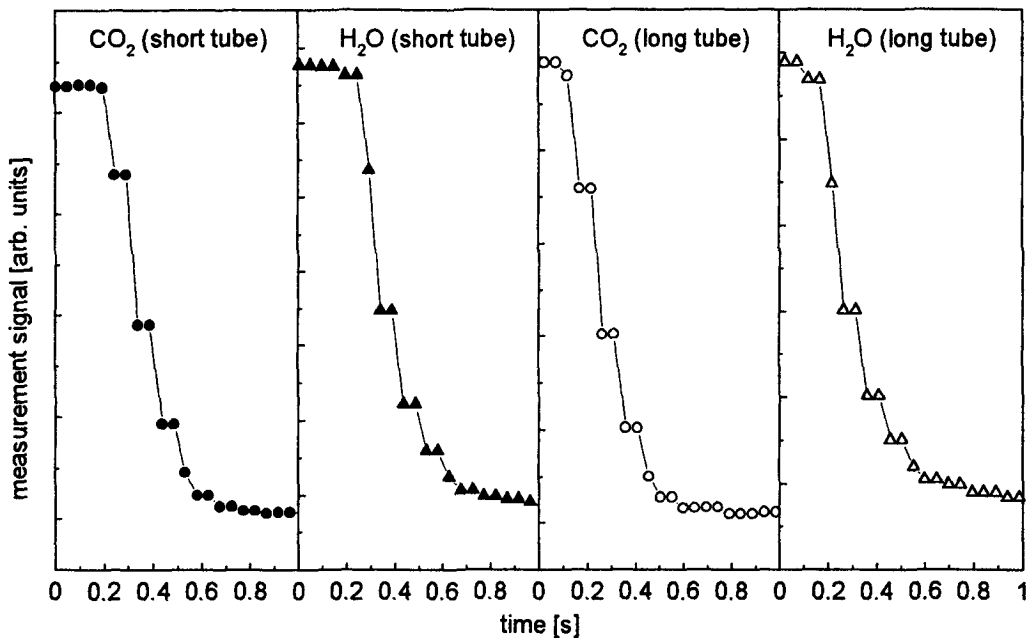


Fig. 3.16: CO₂ and H₂O signal response of the LI-6262 to step changes in concentration (through valve switching between different calibration gases) as recorded by the Gill sonic ADC; two different setups with 0.5 m (short) 6 m (long) sampling tube length were used; tests were performed under comparable conditions to the field measurements (same flowrate, similar temperature and pressure conditions).

The transport of the sample air in the tube from the effective measurement point (inlet) to the analyser (cf. Fig. 3.9 and 3.14) also produced a delay time between the sonic and the trace gas measurements. The time needed for the sample air to pass the tube and reach the sensor can be calculated from the total dead volume and the respective flowrate. For estimating the effective deadvolume, also the tubing inside the instrument and at least half of the sensor cell volume have to be included. With the characteristics given above, a residence time of about 0.8 s (deadvolume: 0.10 litres) for the CO₂/H₂O analysing system is obtained. As explained in Appendix A.7, the response characteristic of the data acquisition system (see above) produces an additional effective delay of $\tau_R = 0.125$ s, resulting in a total value of ca. 0.93 s. This result is only slightly higher than the delay times found in the laboratory step response experiments (not displayed here).

3.3.4 Fast Response Ozone Detector

The fast response ozone detector used for eddy correlation measurements is described extensively by Güsten et al. (1992) and Güsten and Heinrich (1996). The sensor consists of a plate coated with coumarin dye. The coated surface reacts with ozone emitting chemoluminescent light in the range of 400-500 nm, which is detected by a small blue-sensitive photomultiplier. A high performance miniature fan produces a constant air flow rate of about 100 L min^{-1} through the light protected detector chamber. At this flow rate, the sensor shows a response time significantly shorter than 0.1 s (a $1/e$ response time of about 30 ms can be estimated from the reported 90% response time of 60 ms). The air is sampled through a short and wide tube (0.5 m length and 0.02 m inner diameter). The resulting mean flowspeed $u_t = 5.3 \text{ m s}^{-1}$ guarantees a high Reynolds number (Eq. A.33) of about 7000 and thus turbulent flow as well as a short residence time of only ca. 0.1 s. Like for the $\text{CO}_2/\text{H}_2\text{O}$ analyzer, the total delay time of the present setup includes the response effect of the ADC prefilter ($\tau_R = 0.125 \text{ s}$) and therefore can be estimated to about 0.23 s.

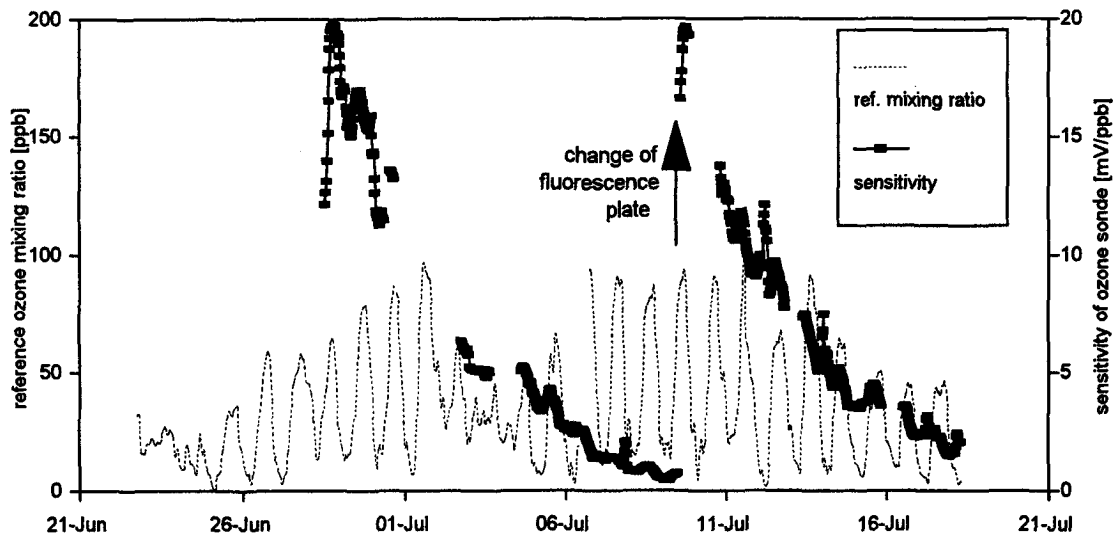


Fig. 3.17: Temporal development of sensor sensitivity of the fast response ozone detector.

The IMK ozone sensor has a fairly linear response characteristic with a detection limit lower than 0.05 ppb, but shows a relatively fast temporal drift in the sensitivity. Therefore, it has always to be accompanied by a parallel operating slow but stable reference O_3 -instrument. In the Bellheim campaign, it was calibrated online against the upper level of the ozone profile measurement (see Section 3.2.2). The observed development of the sensitivity, i.e. the ratio of the sensor signal (with a constant offset of -15 mV subtracted) to the reference ozone concentration, is displayed in Fig. 3.17. The sensitivity is decreasing exponentially with time. Starting with a value of about 20 mV ppb^{-1} on 28 June, it falls below 1 mV ppb^{-1} (5 % of the initial value) within approximately 9 days. For reasons of signal resolution, such low values had to be rejected and the detector plate had to be exchanged (9 July). Hence, two 9-day-periods of useful measurements are available.

3.4 Relaxed Eddy Accumulation System

3.4.1 Setup and Components

Relaxed eddy accumulation (REA) measurements were performed for CO_2 and H_2O surface fluxes. For the planned longterm continuous application, the concept proposed by Baker et al. (1992) seemed to be most appropriate (cf. Section 2.5.4) and was therefore adapted for the present study. A schematic illustration of the whole setup is given in Fig. 3.18. The REA system was coupled to the eddy correlation system described in Section 3.3. The fast response sonic anemometer measurements provided an online signal of the vertical windspeed $w(t)$. According to the direction (sign) of $w(t)$, two solenoid valves were controlled and air was sampled into two separate lines, one for updraft and one for downdraft episodes. Because of the bulkiness of the inlets due to filters and valves, they were positioned about 30 cm away from the sonic head in order to avoid flow distortion effects. The 'dead volume' between the inlets and the valves was about 1 ml. Through 1/4" Teflon tubing of 6 m length, the air was led to the analysing system at the ground. The sample air streams were analysed for CO_2 and water vapour by a differential infra-red absorption instrument. Each line (analyser channel) was flushed by an individual membrane pump (ASF 5010) at a flowrate of about 0.5 L min^{-1} , which was controlled by a manually adjusted rotameter. Buffer volumes of 200 ml were installed in the sampling lines. They were intended to stabilise the underpressure in the tube and to smooth the trace gas concentration signal before reaching the analyser. The analysing unit as well as the conditional sampling valves are described in more detail in the following sections.

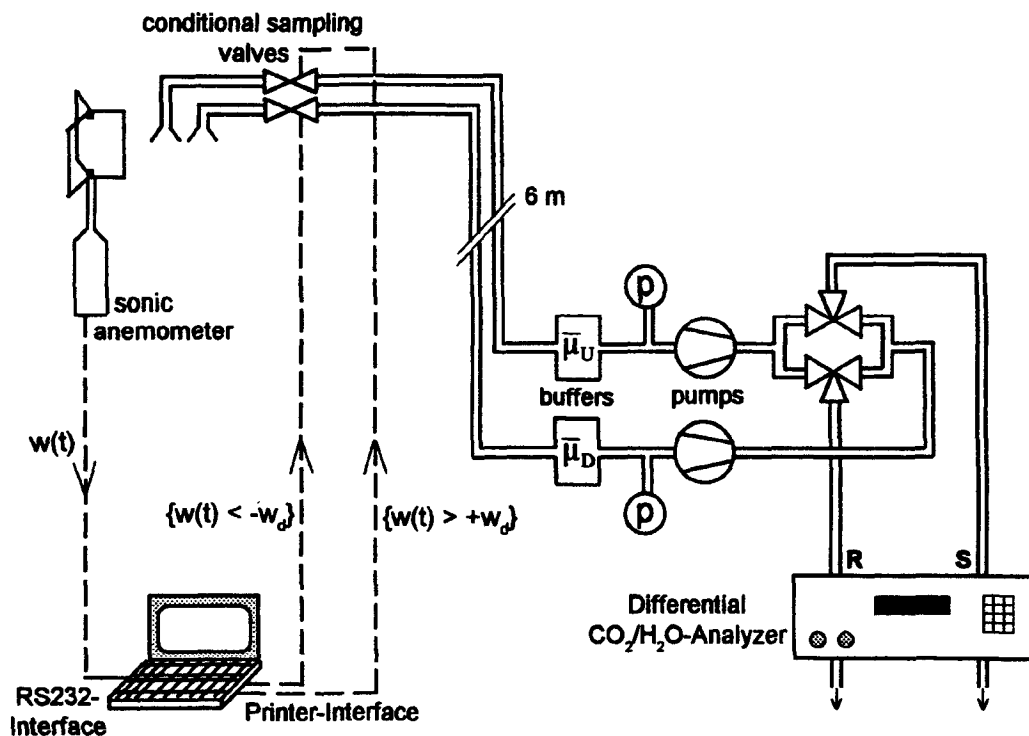


Fig. 3.18: Schematic setup of the applied relaxed eddy accumulation system originally proposed by Baker et al. (1992).

3.4.2 Trace Gas Analysis

The CO₂ and H₂O concentration difference between the updraft and the downdraft line of the REA system was measured with a dual channel infra-red gas analyser (LI-COR, LI-6262). It was the same instrument type as used for the eddy correlation measurements (see Section 3.3.3); but in this case, it was operated in the differential mode, i.e. the two sampling airstreams were directed through the sample and reference channel and the output signal was directly related to the concentration difference. In order to account for offset effects, the sampling lines were switched to the opposite analyser channel through 3-way solenoid valves every 2 minutes. After such a change in ‘polarity’, the analyser signal was ignored for 20 s allowing the system to accustom to the new situation. In the remaining time, the output signal was sampled every second by a data-logger and averaged over a 10 min interval separately for both polarities (‘+’ and ‘-’). Thus two average differences $\Delta^+ \rho_c$ and $\Delta^- \rho_c$ were recorded, which contained an unknown instrumental offset. They are related to the true REA concentration difference (cf. Eq. 2.79) as follows:

$$\Delta^+ \rho_c = (\bar{\rho}_{c,U} - \bar{\rho}_{c,D}) + \text{offset} \quad (3.10a)$$

$$\Delta^- \rho_c = -(\bar{\rho}_{c,U} - \bar{\rho}_{c,D}) + \text{offset} . \quad (3.10b)$$

The unknown offset can be eliminated by subtracting both equations. The subsequent solving for the bracket term yields:

$$(\bar{\rho}_{c,U} - \bar{\rho}_{c,D}) = \frac{\Delta^+ \rho_c - \Delta^- \rho_c}{2} . \quad (3.11)$$

Since both cells of the gas analyser were vented directly to ambient air, the pressure in the measurement cells was assumed to be equal. The same applies for the temperature, because both cells are surrounded by one solid metal frame with a large heat capacity.

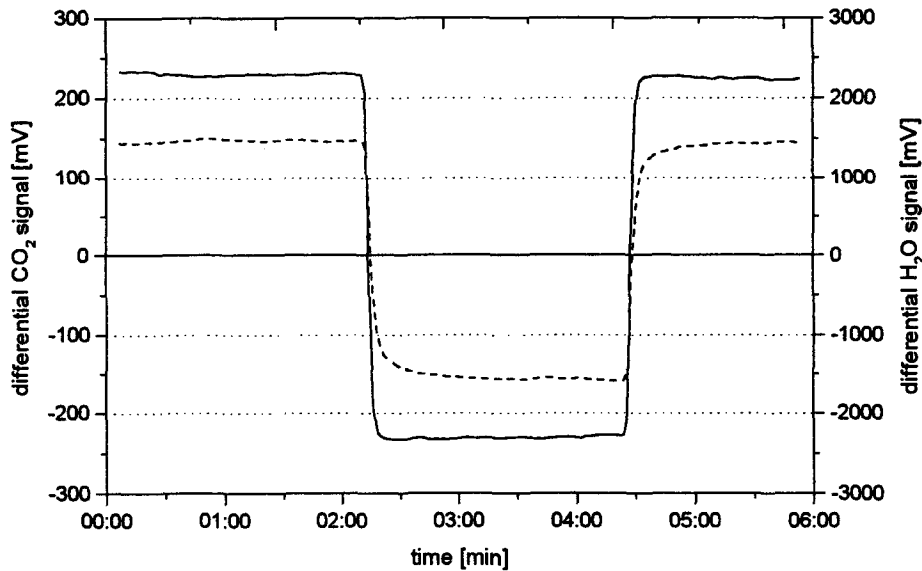


Fig. 3.19: CO₂ signal (solid line) and H₂O signal (dashed line) of the differential REA gas analyser during a calibration with cylinder zero gas (pure N₂) in one sample line and ambient air in the other. The lines were switched (exchanged) two times between the sample and reference channel of the analyser (cf. setup in Fig. 3.18).

In contrast to the alternating measurement systems applied for the concentration profiles (see Section 3.2.2), the differential system applied for REA yielded no absolute concentration values but directly the difference between the 'Up' and 'Down' samples (cf. Eqs. 3.10 and 3.11). Therefore, the analyser could not be calibrated through an online comparison with other instruments. A special procedure using two different calibration gases simultaneously was carried out three times during the field campaign. For the CO₂ calibration, two cylinder standards (300 and 403 ppm CO₂) were applied, whereas the water vapour signal was calibrated with cylinder zero gas (N₂) and ambient air of known humidity. Through the flow routing system displayed in Fig. 3.18, the standard gases were switched several times between the sample and reference channel of the gas analyser. Fig. 3.19 shows an exemplary calibration signal series that illustrate the approximately symmetric behaviour of the differential measurement. The adaptation time after a channel switching is significantly longer for H₂O than for CO₂, which might be caused by sorption processes on the tube wall materials. However, within the provided flushing interval of 20 s (see above), a satisfying response of better than 90% can be observed for both gases.

3.4.3 Conditional Sampling Valves

Valve Characteristics

The sampling valves used for the REA system were directly controlled solenoid valves (Fluid Automation Systems, MINISOL) with a power consumption of about 5 W. Their size, design and construction is illustrated in Fig. 3.20. They have an orifice diameter of 2 mm, and the wetted material (inner surfaces) is stainless steel. The used valve type has a nominal lifespan of 25 million switching cycles. With a typical average REA switching frequency of 1 Hz (cf. Baker et al., 1992), this corresponds to a continuous operation period of several months. In accordance with that nominal value, no wearing effects could be observed during the field operation time of about 20 days in total.

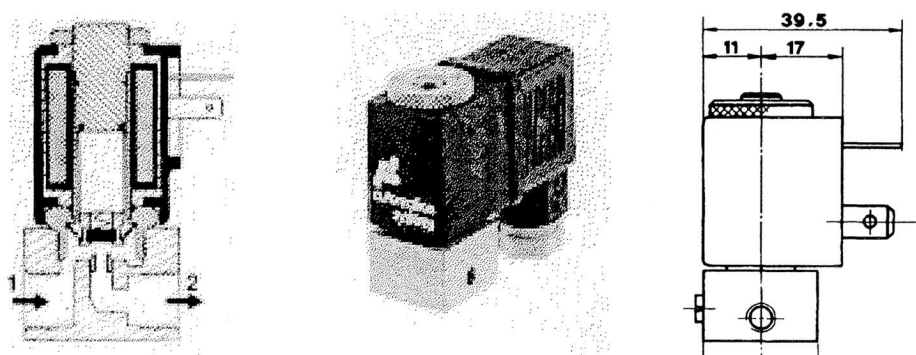


Fig. 3.20: Illustration of design and size (in mm) of the REA sampling valves (Fluid Automation Systems, MINISOL).

In order to test the response time of the solenoid valves, laboratory experiments with artificial rectangular control signals were carried out. A pressure difference was created across the valve by a pulling pump and the flow reaction through the valve was monitored by a fast response pressure sensor (Data Instruments XT). Fig. 3.21 shows the time series of the valve control signal and the dynamic pressure in the tube (proportional to the flow) for different switching rates. For 18 Hz, a regular behaviour with full range amplitudes can be observed in the flow response, similar as for lower switching rates (not shown here). At 36 Hz, however, the amplitudes become smaller and somewhat irregular. At even higher

frequencies, they get totally out of order signifying that the valve is no more able to respond to the control signal. Thus the sonic sampling rate of 20.83 Hz seems to be appropriate for the control of the conditional sampling valves.

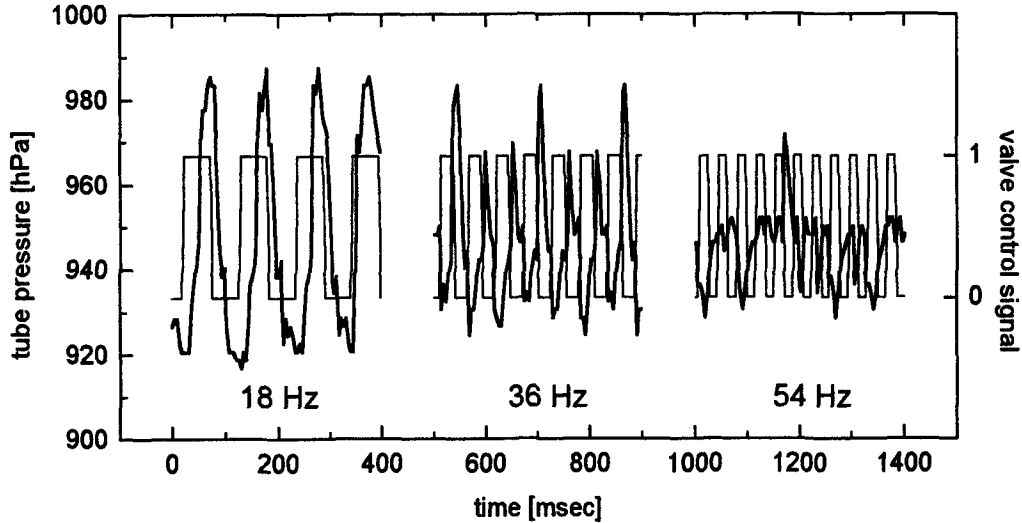


Fig. 3.21: Laboratory test of flow response, recorded as tube pressure (bold line), to an ideal rectangular valve control signal (thin line) of variable frequency.

The time series displayed in Fig. 3.21 also give information about the delay time of the valve response. For all switching rates investigated (4.5 Hz to 54 Hz), the correlation between the rectangular control signal and the flow (pressure) response was calculated. In Fig. 3.22 the correlation coefficient is displayed as a function of the time shift between the two data series. A general delay time in the flow response of about 18 ms can be observed. This value is slightly higher than the 90% response time of 8 - 15 ms given by the manufacturer. The difference may be caused by an additional delay time contribution of the amplifying unit or the response of the pressure sensor.

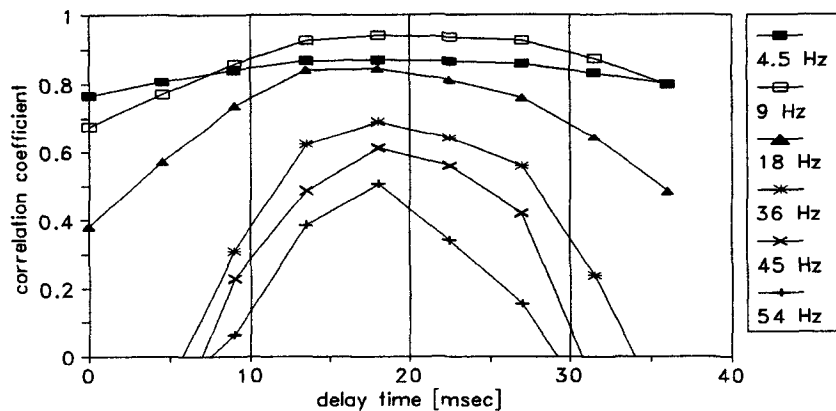


Fig. 3.22: Correlation coefficient vs. delay time of valve control signal and flow response (tube pressure signal) for different switching frequencies.

For an online test of the valve response and pressure conditions of the REA system, the pressure in both sampling lines (at the buffer volume) was recorded during the field experiment. Average, maximum, and minimum values as well as standard deviations were recorded for each 10 min interval. During the last

three days of the campaign, the pressure in the updraft-sampling-line was additionally recorded by the eddy correlation system with a time resolution of 10 Hz.

Valve Control

Since the REA system needed an online signal of the vertical windspeed without delay, the serial communication in the EC system (see Section 3.3.1) between computer and sonic anemometer had to be set to the so-called 'continuous mode'. This mode is not supported by the standard data acquisition software supplied by the manufacturer, and therefore a specific program was developed for the communication as well as for the control of the conditional sampling valves (Fluid Automation Systems, MINISOL). The vertical windspeed signal received at a rate of 20.83 Hz was processed through the following two steps:

1. High-pass filtering: the average value of the past 10 min was subtracted from each new measurement in order to account for offset and drift effects. This filtering procedure produced an estimated effective turbulent fluctuation of the vertical windspeed $w'(t)$.
2. Application of a deadband around zero: the filtered values $w'(t)$ were compared to an absolute threshold (deadband) value $w_d = 0.05 \text{ m s}^{-1}$:
 - $w'(t) > w_d \quad \Rightarrow$ control signal for updraft valve
 - $-w_d < w'(t) < +w_d \quad \Rightarrow$ no control signal
 - $w'(t) < -w_d \quad \Rightarrow$ control signal for downdraft valve

The controlling signals were transmitted via the parallel printer port of the Notebook computer to an amplifier unit, that switched the voltage supply for the normally-closed solenoid valves.

3.5 Determination of Non-turbulent Energy Fluxes

In order to investigate the surface energy budget (Section 2.1.4) and its closure with the turbulent flux measurement methods, the non-turbulent energy exchange i.e. the radiative energy fluxes, the energy storage change in the canopy layer, and the soil heat flux were determined for the triticale field.

3.5.1 Radiation Budget

The total radiative energy exchange of the triticale field was measured with two thermal net radiometers: a Schulze-Lange (SL) and a REBS Q*6 instrument (cf. Tab. 3.2). The SL instrument, which was available only between 26 June and 19 July, is ventilated and therefore considered as more accurate than the non-ventilated Q*6 operated during the whole measurement period (cf. Halldin and Lindroth, 1992). In the period of simultaneous operation, the Q*6 showed two types of deviation from the reference SL instrument. During daytime, it revealed a clear underestimation indicated in Fig. 3.23 by the difference between both sensors. The absolute and relative deviation is strongest at high values. This effect may be explained by a temperature loss (damping) of the up-facing sensor plate due to its relatively high excess temperature compared to the surrounding. The heat can be transferred through thermal radiation, heat conduction along the thermopile and to neighbouring solid parts or convective transport inside the dome volume (Ohmura and Schrott, 1983; Halldin and Lindroth, 1992). Since the sensor temperature of the Q*6 is not known, only an empirical correction is possible. Fig. 3.23 shows a relatively well-defined dependence of the deviation on the (raw) signal itself. A polynomial of second order was fitted to the difference and was used for correct all Q*6 daytime measurements ($R_n > 0$).

During nighttime, the agreement between the two instruments is usually good, but some individual events with a distinct difference (less negative values of the Q*6 instrument) can be identified. This problem was also observed Halldin and Lindroth (1992), and they assigned it to the formation of dew on the upper dome of the non-ventilated Q*6 instrument. This explanation was confirmed for the present case by the limitation of the particular events to high relative humidity (> 85%). Although, the occurrence of this effect can be related to humidity measurements, a direct quantitative description and correction is not possible. Therefore, the SL results were used whenever available. For the remaining periods the corrected Q*6 values were accepted, if the relative humidity was below 85%.

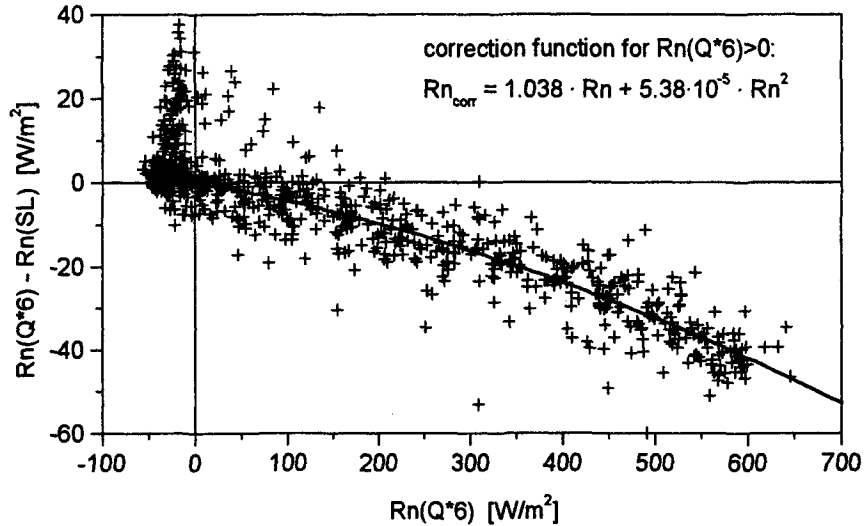


Fig. 3.23: Deviation of the unventilated Q*6 net radiometer measurements from reference values of the ventilated Schulze-Lange (SL) instrument; the line curve represents the polynomial correction function applied for daytime conditions.

3.5.2 Energy Storage in the Canopy

The heat storage change ΔS in the canopy layer consists in principle of two terms: storage change of sensible heat (ΔS_H) and storage change of chemical energy due to assimilation and respiration of CO_2 (ΔS_A). The first term was estimated from triticale biomass density and radiation data in the following way. The Schulze-Lange net radiometer measured the upward and downward radiative fluxes separately. Thus from the difference of the total upward radiation flux and the reflected shortwave flux, which was detected by a down-facing pyranometer, the longwave upward flux $L\uparrow$ could be determined. According to Perrier (1971) it is related to the temperature of the emitting surface by the Stefan-Boltzmann law, corrected for the reflected longwave radiation:

$$L\uparrow = \varepsilon\sigma T_s^4 + (1-\varepsilon)L\downarrow \quad (3.12)$$

The factor ε describes the emissivity of the surface, which was estimated for the triticale crop to 0.96 (Monteith and Unsworth, 1990; Oke, 1987). $\sigma = 5.674 \cdot 10^{-8} \text{ W m}^{-2} \text{ K}^{-4}$ represents the Stefan-Boltzmann constant. Equation 3.12 may be solved for T_s , which represents the temperature of the measured surface. In the present case, it can be interpreted as the average leaf surface or biomass temperature of the triticale canopy. Due to the lack of better information, the heat capacity of the canopy was roughly estimated for the whole period with 'average' values of the fresh and dry weight obtained on 4 July (cf.

Tab. 3.1) and the individual heat capacity of water (cf. Tab. 3.3) and cellulose ($c_{\text{cell}} = 2500 \text{ J kg}^{-1} \text{ K}^{-1}$, cf. Jones, 1992). Thus the canopy heat storage change for a given time interval Δt results in:

$$\Delta S_H = \frac{\Delta T_s}{\Delta t} \cdot [c_{\text{cell}} \cdot 2.3 \text{ kg} + c_w \cdot 4.1 \text{ kg}] = \frac{\Delta T_s}{\Delta t} \cdot 2.3 \cdot 10^4 \text{ J m}^{-2} \text{ K}^{-1} . \quad (3.13)$$

The second storage term ΔS_A can be calculated from the corresponding CO_2 gas flux. According to Thom (1975:98) the biochemical assimilation energy is $1.15 \cdot 10^4 \text{ J}$ per gram CO_2 . This results in an energy assimilation/respiration flux of:

$$\Delta S_A = 0.506 \text{ J } \mu\text{mol}^{-1} \cdot F_{\text{CO}_2} . \quad (3.14)$$

3.5.3 Soil Heat Flux

The heat flux in or out of the soil is equal to the change of heat storage within the soil. It was determined by the so-called combination method (Massman, 1993). The total heat flux $G(0)$ through the soil surface was estimated as sum of the vertical heat flux at a certain depth $G(-z_g)$ within the soil and the heat storage change $\Delta S_G(-z_g \dots 0)$ in the layer above.

$$G(0) = G(-z_g) + \Delta S_G(-z_g \dots 0) \quad (3.15)$$

The vertical heat flux was measured at a depth of 8 cm with three horizontally distributed heat flux plates (REBS, HFT-1). Additionally the temperature course in the layer 0-8 cm was measured with four parallel thermocouple probes at 2 cm and 6 cm depth. For the calculation of the heat storage change in that layer, the volumetric heat capacity C_s of the soil has to be known.

$$\Delta S_G(-z_g \dots 0) = C_s \cdot \int_{-z_g}^0 \frac{\Delta T(z)}{\Delta t} \cdot dz \approx C_s \cdot z_g \cdot \frac{\Delta \bar{T}_{(-z_g \dots 0)}}{\Delta t} \quad (3.16)$$

The effective volumetric heat capacity depends on the bulk density, soil composition and (variable) water content. It can be estimated by fractional addition formula (Hillel, 1980):

$$C_s = \rho_{s,\text{dry}} [(1 - f_{\text{org}}) c_{\text{min}} + f_{\text{org}} c_{\text{org}}] + \rho_w \theta_w c_w . \quad (3.17)$$

The necessary soil characteristics and physical parameters (specific heat capacity c_x of the soil materials) are listed in Table 3.3. The soil characteristics, which can be assumed as constant over the measuring period, were determined in laboratory analysis from soil samples. The density of the dry soil $\rho_{s,\text{dry}}$ was determined by measuring the weight of oven dried (24h at 105°C) soil samples taken with 100 ml cylinders (0-5cm depth). The organic matter content f_{org} (related to the organic carbon content) was determined pyrometrically and the textural fractions with sedimentation cylinders. The volumetric soil water content θ_w is variable and was thus monitored continuously by a 'time domain reflectometry' probe (TRIME-ES P2) horizontally buried at -5 cm .

Tab. 3.3: Soil properties of the triticale field.

textural fractions ⇒ soil type (Hillel, 1988)		18% clay, 62% silt, 20% sand silty loam
organic matter content (dry weight fraction)	f_{org}	2.1%
dry bulk density (0 - 5 cm) ⇒ total pore space	$\rho_{\text{s,dry}}$	1336 50%
volumetric water content (range) ⇒ waterfilled pore space	θ_{w}	9% - 21% 18% - 42%
constant physical properties (Hillel, 1988; Oke, 1987):		
specific heat capacity of mineral matter	c_{min}	800 J kg ⁻¹ K ⁻¹
specific heat capacity of organic matter	c_{org}	ca. 2000 J kg ⁻¹ K ⁻¹
specific heat capacity of water	c_{w}	4200 J kg ⁻¹ K ⁻¹
density of water	ρ_{w}	1000 kg m ⁻³

4 EVALUATION OF COMMON METHODS

The determination of trace gas fluxes is usually not completed with the measurements in the field. A considerable amount of work is necessary for an accurate processing and evaluation of the raw data and for the actual flux calculation. The presentation of the data evaluation and results in the present study is split into two parts. The common measurement methods (eddy correlation and profile) are evaluated and discussed first (in this chapter), based on largely established calculation and correction procedures. The evaluation of the novel REA method follows in Chapter 5; the corresponding procedures are not yet established and thus need additional theoretical development as well as empirical investigations.

The careful evaluation and detailed discussion of the eddy correlation and profile measurements are of high importance in the context of this work due to various reasons: (a) they represent the only available reference for the validation of the REA technique; (b) the high resolution EC datasets are used for the simulative investigation of the REA method and thus have to be of high quality; and (c) the applicability and performance of the profile method is of great interest as a direct alternative to the REA method. In the first two sections of this chapter, the flux calculation and correction are described separately for the EC and profile method. Afterward, the rejection criteria and error estimation are presented jointly for both techniques in Section 4.3. Finally, all results are presented in the context of the environmental and micrometeorological conditions in Section 4.4 (and Appendix B).

4.1 Eddy Correlation Calculations

The high resolution time series measured by the eddy correlation system had been stored entirely in a raw state (cf. Section 3.3.1). Except for the correction of the wind vector for transducer shadowing effects (performed by the sonic instrument), all corrections and flux calculations had to be carried out in post-processing procedures after the field campaign. Unfortunately, no online EC flux calculation software (see e.g. McMillen, 1988; Chahuneau et al., 1989; Gash and Culf, 1996) was available in the present study. However, the following evaluation was intended to contribute to the future development of such a software, and therefore special attention was paid on the applicability of the various procedures in an online calculation algorithm.

Fig. 4.1 gives a survey of the performed processing steps, which will be discussed individually in the following sections. The order of the steps is partly determined by physical considerations. However, some linear operations like windvector coordinate rotation or sensor calibrations are interchangeable with the covariance calculation. Therefore, they were applied to the average covariances and not to the high resolution time series. This procedure minimises the computation time, which is especially important for a (potential) online calculation. Corrections for density fluctuation effects and high frequency attenuation were also performed in an integral way on the covariance values. For interpretation and comparison with other methods, the eddy correlation fluxes calculated for 10 min intervals were finally averaged to 30 min means.

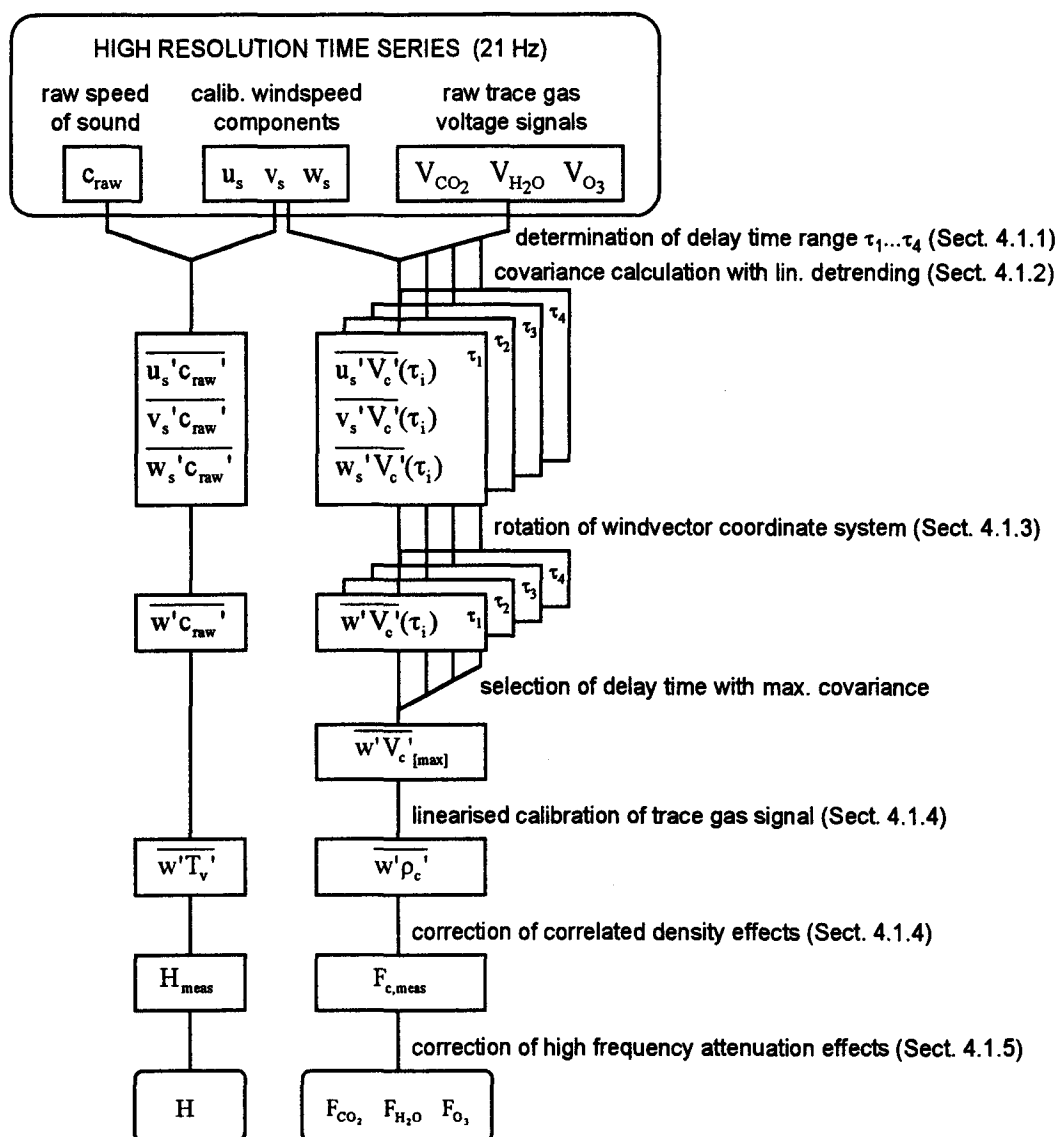


Fig. 4.1: Processing steps for the calculation of scalar eddy correlation fluxes.

Spectral analysis (cf. Section 4.1.6, Appendix A) was performed on selected periods for an exemplary verification of the theoretical assumptions. In these cases, the correction procedures like detrending, vector rotation and calibrations were performed directly on the time series. The variance spectra and cospectra were determined by an FFT algorithm from intervals of 2^{14} data points (ca. 13 min) on which a Hamming window was applied for minimising boundary effects. The spectral estimates were band averaged according to KF94:269.

4.1.1 Delay Time of Trace Gas Measurements

As mentioned in Section 3.3, the recorded trace gas concentrations are delayed compared to the sonic measurements due to the transport of the sample air in the tube and the recursive signal prefiltering of the AD-converter. The total delay time was estimated from physical and geometrical characteristics of the measurement setup to about 0.93 s for the $\text{CO}_2/\text{H}_2\text{O}$ -analyser and 0.23 s for the ozone sensor. However, this values cannot be regarded as generally representative. Since the inlets are horizontally separated from the sonic head, the effective delay time depends also on wind direction and windspeed (cf. Moore, 1986).

For determining the effective delay time of individual trace gas measurements, the cross covariance or correlation function between the vertical windspeed and the scalar time series may be used, as proposed for example by McMillen (1988). It is assumed, that the time lag with the maximal correlation represents the 'true' delay time. Fig. 4.2 shows an exemplary case with the correlation functions for the sonic temperature and the trace gas signals. The correlation was calculated according to Eq. 2.64 with 40 different time shifts τ between -0.5 s and $+1.5$ s. As expected, the correlation of w with T has its maximum at lag zero, since both quantities are derived from synchronous sonic measurements. The maxima (or minima) of the other curves are at lag times 0.35 s for O_3 and about 1.0 s for CO_2 and H_2O . This are slightly higher values than calculated in Section 3.3 (see above). The additional delay may be attributed to the sensor separation (cf. Chahuneau et al., 1989), which had an enlarging effect in the present case, since the wind direction was southwest and the tube inlets were positioned east and hence in the lee of the sonic probe.

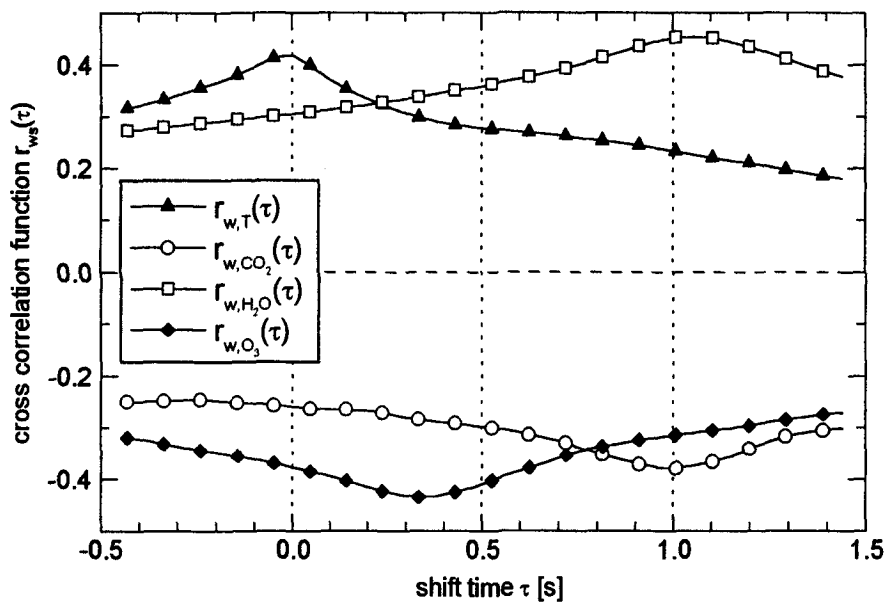


Fig. 4.2: Correlation functions for different (raw) scalar quantities with vertical windspeed w ; 4 July 1995, 17:00 - 17:10; wind direction 220° , windspeed 3.9 m s^{-1} .

In order to get a useful overview of the occurring delay times, cross correlation functions were calculated for the data of four representative days covering the important SW and NE wind directions and various windspeed conditions. For each case and each scalar, the shift time with maximal correlation was identified. The results are combined and plotted as histograms in Fig. 4.3. The average (and most frequent) delay times agree well with the calculated values of 0.93 s and 0.23 s. But all trace gases show a certain scatter in their delay times mainly within a range of about ± 0.2 s around the average, that can be attributed to the influence of the sensor separation under different wind directions. This connection is illustrated in Fig. 4.4 for ozone. The observed variation in the delay times are compared with a theoretical sine function of the wind direction, corresponding to the air travelling time between the sonic sensor and the sample tube inlet 0.4 m apart at a windspeed of 2 m s^{-1} . Sporadic cases in Fig. 4.3 and 4.4 with larger deviations outside the physically plausible range may be due to very low flux values. The corresponding maxima in the correlation functions are easily masked by the effects of non-ideal conditions (non-stationarity, trends, etc.).

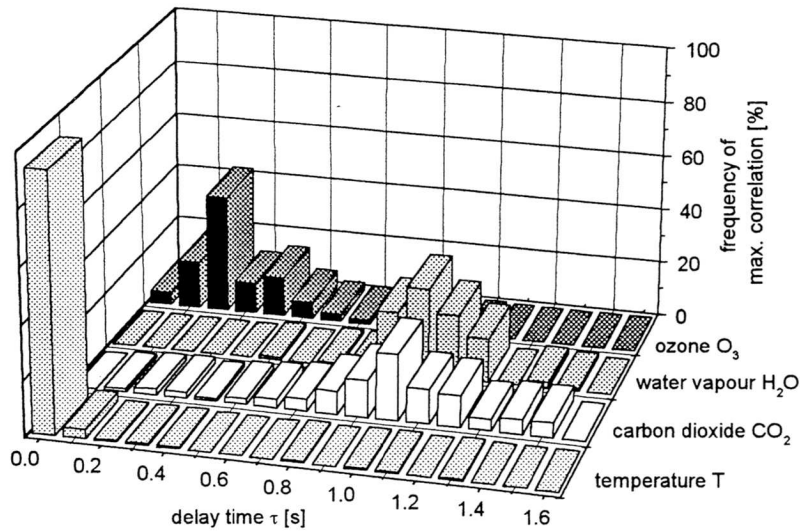


Fig. 4.3: Histograms of shift times with maximal correlation (covariance) between vertical windspeed w and different scalar quantities; eddy correlation datasets (10 min intervals) of 28/29 June and 4/5 July 1995.

For taking into account the observed variation in the delay times, the covariance calculation for the trace gas fluxes was carried out with four different time lags $\tau_1 \dots \tau_4$. The chosen delay times covered the main ranges found above: 0.9 - 1.2 s for CO_2 and H_2O , and 0.1 - 0.4 s for ozone. For limiting the amount of calculations, the delay time was varied only in steps of 0.1 s. As illustrated in Fig. 4.1, the maximum covariance was selected after the coordinate rotation and retained for the final flux determination. This procedure can also be applied in an online computation system.

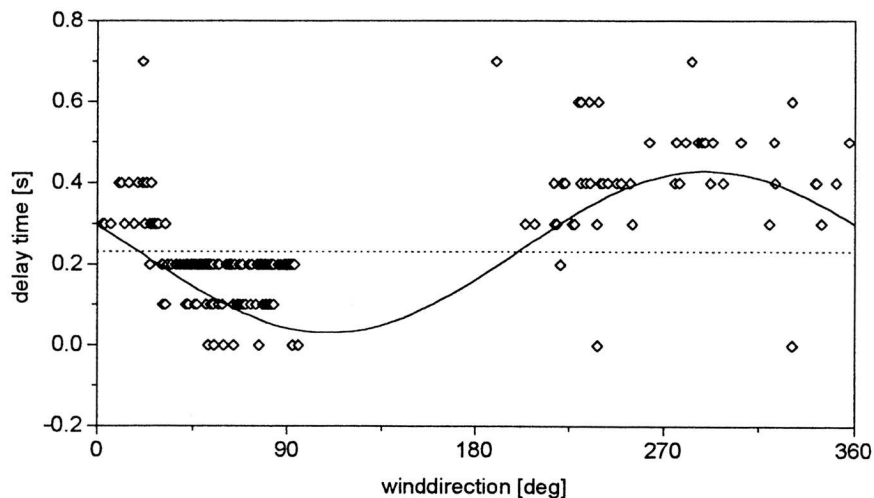


Fig. 4.4: Shift time of maximal correlation between w and ozone concentration plotted against wind direction, determined from eddy correlation datasets (10 min intervals) of 28/29 June and 4/5 July 1995; the horizontal dotted line indicates the average delay time of 0.23 s derived in Section 3.3.4; the sine curve with an amplitude of 0.2 s indicates the theoretical deviation from this average caused by the sensor separation of 0.4 m at a windspeed of 2 m s^{-1} .

Beier and Weber (1992) and Laubach (1996) propose a detailed examination of the delay time effects in the frequency domain. One method is the analysis of the (smoothed) quadrature spectrum, which represents the out-of-phase-covariance. Another method is the study of the cumulative cospectrum (ogive). It

is a very sensitive indicator of possible delay times, which always cause one or more changes of sign along the cospectrum (see Appendix A). However, this spectral analysis methods are not yet well established. Moreover, they need much computational effort, which is not necessary in usual cases.

4.1.2 Detrending and Covariance Calculation

The recorded eddy correlation datasets represent discrete synchronous and equally spaced time series. Given two series x_i and y_i ($i = 1 \dots N$), the covariance can be computed as:

$$\overline{x'y'} = \frac{1}{N} \sum_{i=1}^N (x_i - \bar{x})(y_i - \bar{y}) . \quad (4.1)$$

The mean values in the formula do not necessarily represent arithmetic averages but rather a 'mean course' of the quantities with the turbulent fluctuations removed. Non-turbulent variations or trends in the atmospheric quantities may be caused by diurnal changes or mesoscale effects (caused by topography, fronts, etc.). However as indicated in Fig. 2.11, they are often difficult to be distinguished clearly from turbulent fluctuations. Therefore, no general rule can be given for an appropriate detrending or filtering of turbulent time series. Fig. 4.5 shows an illustrative example of the most commonly applied techniques. Beside the simple constant arithmetic average, a running mean can be calculated and subtracted from the original dataset. This corresponds to a high-pass filter with a characteristic cutoff-frequency that depends on the width and the form of the convolution window (see e.g. Mazzoni, 1996).

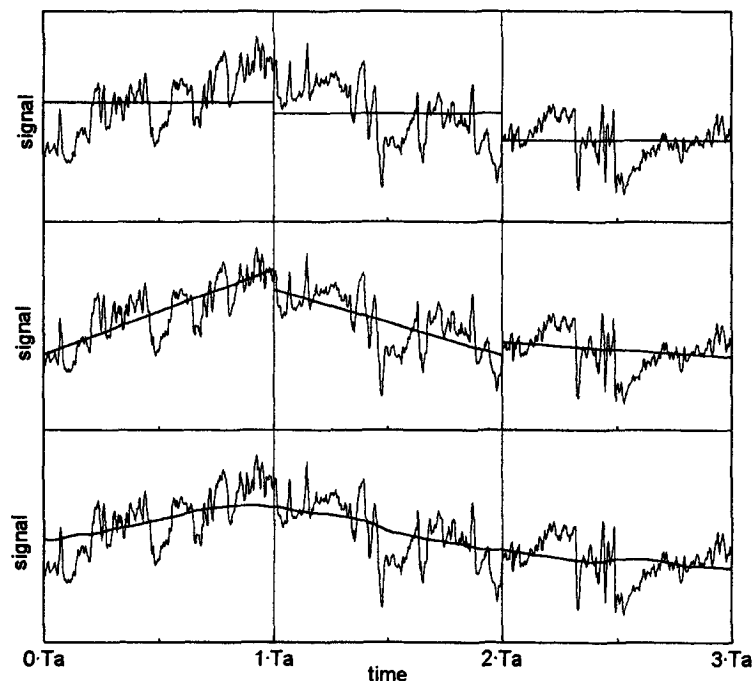


Fig. 4.5: Decomposition of a high resolution time series into mean and turbulent part: (a) with block average over the interval T_a , (b) with a linear trend function, (c) with running mean (low pass filter) of width T_a .

The appropriate choice of the cutoff-frequency is problematic. If it is too high, the filter may damp also turbulent fluctuations and thus lead to an underestimation in the eddy correlation flux. The alternative method is the subtraction of a linear trend determined by means of least squares regression. A linear

trend corresponds to a variation with infinitely long period and therefore does not interfere with turbulent fluctuations. On the other hand, linear detrending may not be able to remove relatively fast non-linear changes. A detailed discussion of trend removal is given e.g. by KF94. For the present study, a linear detrending was chosen, because it is more conservative and easier to apply than a running mean. Additionally it can be performed as well in online calculation algorithms. The mean quantities (\bar{x}, \bar{y}) in Equation 4.1 are known in principle only at the end of each averaging interval. However, the terms can be expanded and rearranged so that the covariance calculation may be carried out online in a single pass. In the case of a constant arithmetic average (no detrending), the rearrangement leads to the following relationship (with the indices i omitted):

$$\overline{x'y'} = \frac{1}{N} \sum xy - \frac{1}{N^2} \sum x \cdot \sum y \quad (4.2)$$

All three sum terms can be accumulated in a single pass through the time series and the covariance is obtained by a few final operations. The incorporation of an online linear detrending requires a more complex proceeding. Assuming two linear trends in x and y , (4.1) takes the form:

$$\overline{x'y'} = \frac{1}{N} \sum (x - [A + B \cdot i])(y - [C + D \cdot i]) \quad (4.3)$$

Gash and Culf (1996) show, that this sum formula can be reformulated to result in the following expression:

$$\overline{x'y'} = \frac{\sum xy}{N} - \frac{2(2N+1)\sum x\sum y}{N^2(N-1)} + \frac{3\sum x\sum iy}{N^2(N-1)} + \frac{3\sum ix\sum y}{N^2(N-1)} - \frac{6\sum ix\sum iy}{N^2(N-1)(N+1)} \quad (4.4)$$

In this form, the coefficients A , B , C and D of the linear regression functions are replaced by sum terms including products of x and y with the time index i . As in the case of (4.2), all occurring sums can be calculated on a single pass through the time series. Equation (4.4) was generally used for all eddy covariance calculations in the present study. The covariances of the raw scalar quantities (c_{raw} , V_{CO_2} , V_{H_2O} , V_{O_3}) with all wind components (u_s , v_s , w_s) were determined at four different time lags (cf. Fig. 4.2).

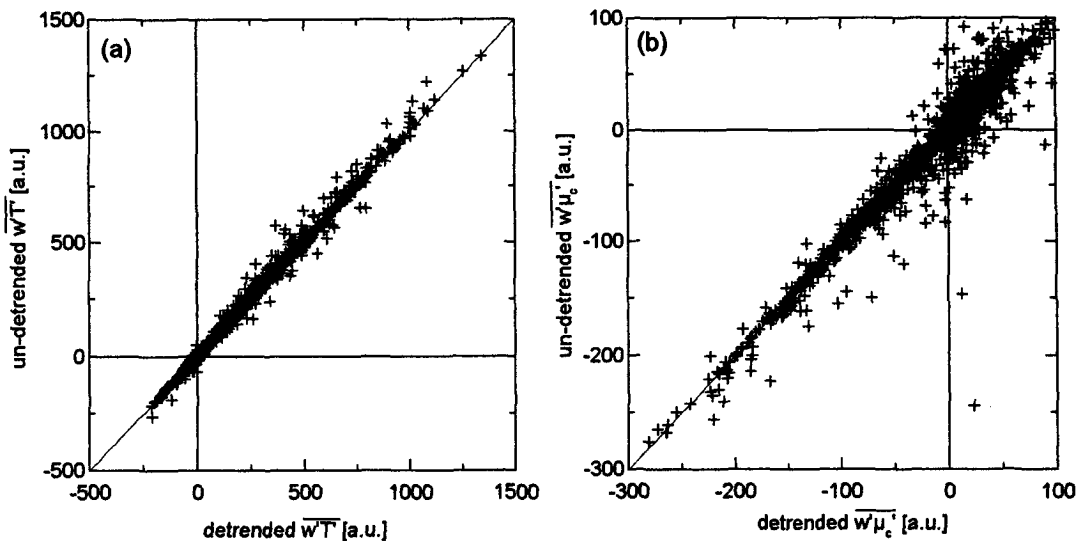


Fig. 4.6: Effect of linear detrending on scalar fluxes: (a) sensible heat flux; (b) CO_2 flux; displayed in arbitrary units.

Trends affect the covariance calculation only if they occur simultaneously in both time series. The effect of unremoved trends can be estimated as the covariance of the pure trend functions. Given two linear trends with total changes Δx and Δy over the whole averaging interval T_a , the covariance results in:

$$\overline{x'y'}_{[\text{trend}]} = \frac{1}{T_a} \int_0^{T_a} \left(-\frac{\Delta x}{2} + \frac{t}{T_a} \Delta x \right) \cdot \left(-\frac{\Delta y}{2} + \frac{t}{T_a} \Delta y \right) \cdot dt = \frac{\Delta x \cdot \Delta y}{12} \quad (4.5)$$

For turbulent fluxes, the decisive factor in this trend induced covariance is the vertical windspeed w , since its mean value is usually not supposed to show distinct diurnal or synoptic variations like the other atmospheric quantities. For the temperature and trace gas concentrations, higher trend effects have to be expected, especially in the morning and evening hours when daytime induced changes are maximal and during the night, when turbulence is relatively weak. The importance of trend effects for the flux measurement depends on the relative magnitude of the linear trends (Δw , $\Delta \mu_c$) compared to the respective turbulent fluctuations ($\sigma(w)$, $\sigma(\mu_c)$). Fig. 4.6 shows a comparison of raw (with trend) and detrended fluxes of CO_2 and sensible heat (temperature). The trend effect is larger for the CO_2 flux signifying that the corresponding concentration change is relatively large compared to the turbulence induced fluctuations. The deviations are largest for small and positive CO_2 fluxes, which occur mainly in the morning and in the evening as well as during the night.

4.1.3 Coordinate Rotation of the Wind Vector

The sonic anemometer yields the wind vector components u_s , v_s , w_s relative to an orthogonal coordinate system aligned with the instrument (Gill Instruments, 1992). But for the determination of the turbulent surface fluxes, the wind components u , v , w related to the micrometeorological coordinate system as introduced in Fig. 2.8 are required (McMillen, 1988). The micrometeorological system is aligned with the mean air flow which deviates from the fixed instrument system not only in the horizontal due to varying wind directions, but also in the vertical. This latter difference has to be attributed to a deviation from the geopotential plane either of the anemometer (instrument tilt) or of the mean airstream (caused by topography or inhomogeneous surface). The transformation from the instrument to the micrometeorological system can be achieved by a rotation of the coordinate system by two angles (cf. Chahuneau et al., 1989; Lohse et al., 1990):

$$\alpha = \arctan\left(\frac{\overline{v}_s}{\overline{u}_s}\right) \quad ; \quad \beta = \arctan\left(\frac{\overline{w}_s}{\sqrt{\overline{u}_s^2 + \overline{v}_s^2}}\right) \quad (4.6)$$

α describes the horizontal (azimutal) and β the vertical rotation of the sonic coordinate system into the mean wind flow. α represents simply the wind direction; for the present field measurements, it is well comparable with the wind direction measured by the windvane sensor. The vertical rotation angle β can be interpreted as apparent tilt of the sensor: negative β values indicate an inclination of the sonic head against the windvector, positive values an inclination with the windvector. The observed β values of the entire field campaign are plotted in Fig. 4.7a against the wind direction. They show a systematic dependence of a roughly sinusoidal form, which may be attributed to a westward tilt in the sensor geometry or setup (cf. windtunnel experiments, Fig. 3.12). However, the tilt is relative to the air streamlines and not to the geopotential or ground plane. Hence, it may also result from the inhomogeneous surface around the eddy correlation tower with canopies of different height. Disturbances like the nearby road or the lab container may also influence the mean airflow and cause a local deviation from the horizontal.

For obtaining the vertical eddy flux, the wind measurements have to be rotated with the given angles. Thereby the average values, but not the instantaneous fluctuations, of the vertical and lateral wind components w and v are forced to zero. With the matrix calculus notation, the corresponding transformation of the wind components may be written as:

$$\begin{bmatrix} u \\ v \\ w \end{bmatrix} = \underbrace{\begin{bmatrix} \cos\beta \cos\alpha & \cos\beta \sin\alpha & \sin\beta \\ -\sin\alpha & \cos\alpha & 0 \\ -\sin\beta \cos\alpha & -\sin\beta \sin\alpha & \cos\beta \end{bmatrix}}_{[R_{\alpha\beta}]} \times \begin{bmatrix} u_s \\ v_s \\ w_s \end{bmatrix}. \quad (4.7)$$

Due to the linear characteristic of this transformation, it may as well be performed on the average covariances instead of the time series. The covariances of the three sonic wind components with any scalar quantity x are rotated in exactly the same way as the wind components themselves. Hence for the vertical flux, the following expression results from Eq. 4.7 (cf. Chahuneau et al., 1989):

$$\overline{w'x'} = -\sin\beta \cos\alpha \cdot \overline{u_s'x'} - \sin\beta \sin\alpha \cdot \overline{v_s'x'} + \cos\beta \cdot \overline{w_s'x'}. \quad (4.8)$$

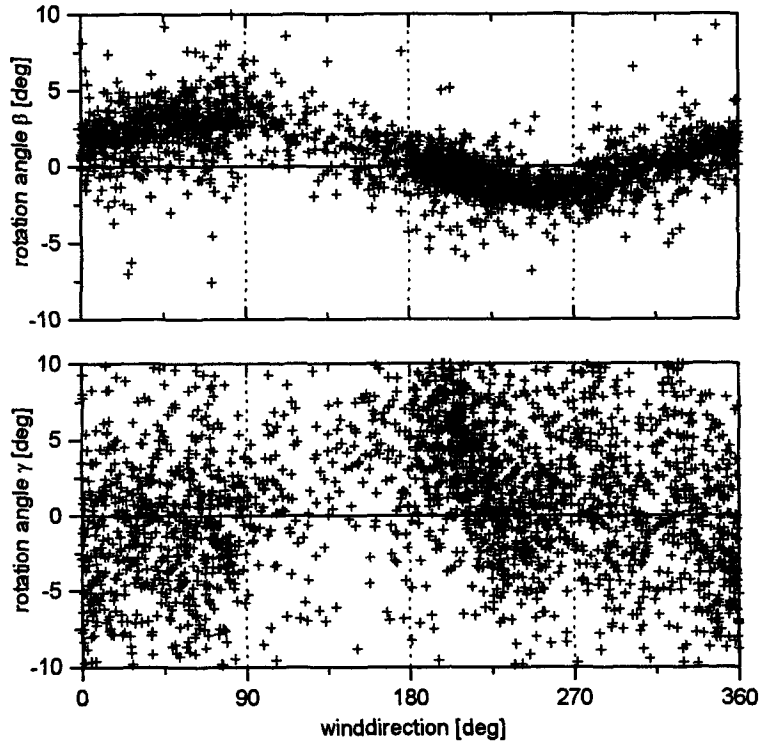


Fig. 4.7: Estimated sonic windvector rotation angles dependent on wind direction: (a) 2nd (vertical) rotation angle β ; (b) potential 3rd rotation angle γ (around u-axis).

The effect and success of the rotation procedure can be evaluated best by examining the momentum flux (Eq. 2.31), because it is most sensitive to misalignment of the coordinate system. Small deviations can even change its sign as reported by McMillen (1988) and Wienhold et al. (1994). The coordinate transformation of the momentum flux is more complicated since both components (horizontal and vertical wind component) have to be rotated simultaneously. In this case, the whole Reynolds stress tensor $[T]$ (cf. St88:66) containing the variances and covariances of all wind components has to be transformed.

$$[\mathbf{T}] = \begin{bmatrix} \overline{u'u'} & \overline{u'v'} & \overline{u'w'} \\ \overline{u'v'} & \overline{v'v'} & \overline{v'w'} \\ \overline{u'w'} & \overline{v'w'} & \overline{w'w'} \end{bmatrix} \quad (4.9)$$

The rotation of a symmetric tensor in an orthogonal system can be calculated with the help of the transposed rotation matrix (Lohse et al., 1990; Wienhold et al., 1994):

$$[\mathbf{T}] = [\mathbf{R}_{\alpha\beta}] [\mathbf{T}_s] [\mathbf{R}_{\alpha\beta}]^T. \quad (4.10)$$

Through the two described rotations, only the u axis is definitely fixed (aligned with the mean wind vector), the v and w axes have still a degree of freedom to rotate about u , corresponding to a lateral sensor tilt. McMillen (1988) states, that the alignment within the v - w -plane is not clearly defined and that several procedures are possible: (a) an alignment of the w axis with the geopotential vertical, (b) an alignment of the w axis perpendicular to the surface, and (c) an alignment, that forces the covariance of v and w to zero. For the situation in Bellheim, the first requirement is more or less fulfilled through the adjustment of the sonic sensor with a spirit level. The second requirement is difficult to achieve, since the "surface" plane is not always well defined, especially in inhomogeneous terrain. At the Bellheim site, at least the ground was fairly flat and aligned with the geopotential. McMillen himself used the third solution, i.e. an additional rotation around the u axis by an angle γ , that is defined by the requirement $\overline{v'w'}_{\text{rot}} = 0$. With some mathematical transformations, an explicit formula for γ can be derived:

$$\gamma = \frac{1}{2} \arctan \left(\frac{2 \overline{v'w'}}{\overline{v'v'} - \overline{w'w'}} \right). \quad (4.11)$$

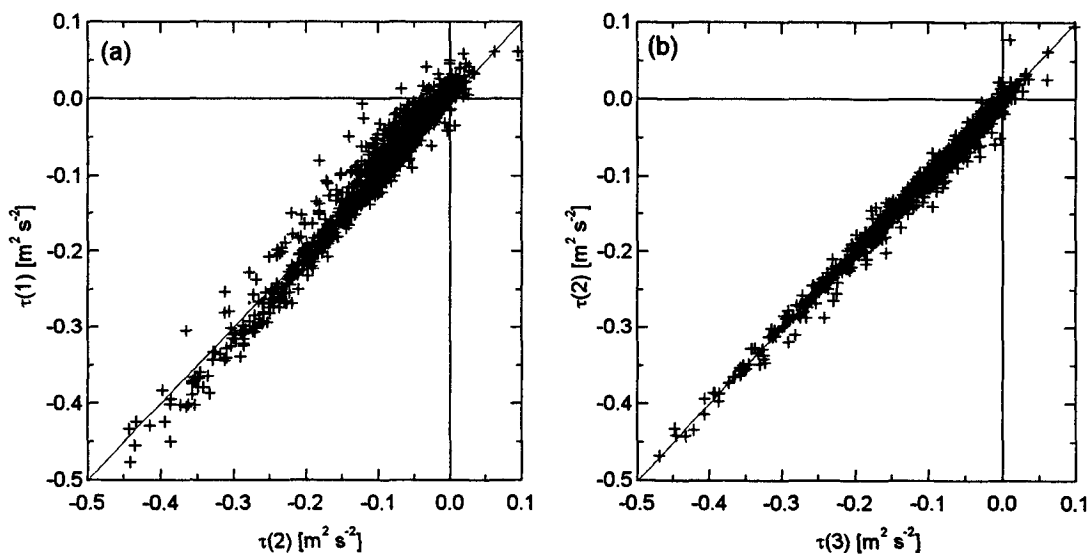


Fig. 4.8: Comparison of momentum flux τ (a) after 1st and 2nd rotation with angle β ; (b) after 2nd and 3rd rotation with angle γ (only cases with windspeed $> 1.5 \text{ m s}^{-1}$ included).

Although this third rotation is applied by several authors (e.g. McMillen, 1988; Wienhold et al., 1994; Eugster, 1994), it remains questionable, especially in non-ideal terrain. Under ideal conditions with a constant wind direction in the surface layer, $\overline{v'w'}$ is supposed to vanish (Busch, 1973: 9). But field measurements may be affected by many non-ideal influences like inhomogeneities in the source area or

the distortion of the measured turbulent flow by the sonic head, leading to effective non-zero values of $\overline{v'w'}$. A correction of such an interference by the proposed rotation is generally not possible (see also Chahuneau et al., 1989) and may lead to physically meaningless results. In order to check the effect of a potential third rotation for the case of the present study, the angle γ was calculated by Equation 4.11. The resulting values are significantly larger than those for β (see Fig. 4.7), and no systematic dependence of γ on the wind direction could be found. Moreover, the comparison in Figure 4.8 shows that the third rotation has a much smaller effect on the momentum flux than the second rotation, despite the generally larger angle. Chahuneau et al. (1989) also observed only a negligibly small effect of the third rotation on scalar fluxes. Since no satisfying physical interpretation nor an empirical necessity for the third wind vector rotation could be found, it was generally not applied to the field measurements. This seemed to be a more consequent solution than the one reported by McMillen (1988), who omitted the third rotation, if the angle γ got larger than the somewhat arbitrary limit of 10 deg. However, more specific investigations are necessary to find an optimal solution for this problem.

For illustrating the effect of the performed vertical rotation on the field data, the relative change of the momentum flux is plotted in Fig. 4.9a against the angle β . In order to reduce the scatter produced by low wind and extreme stability conditions, only cases with an absolute windspeed higher than 1.5 m s^{-1} are included. The results show an almost linear dependence on β with a proportionality of about 7% per degree. This behaviour agrees with the theoretical studies of Rayment and Readings (1971), who found a fairly linear dependence within ± 15 deg with a 100% change for about 12 deg. They also show with spectral analysis, that this sensitivity can be attributed mainly to an interference in the low frequency range. In certain cases, the momentum flux remains positive even after the rotation procedure. This makes no physical sense and indicates a general failure of the eddy correlation technique.

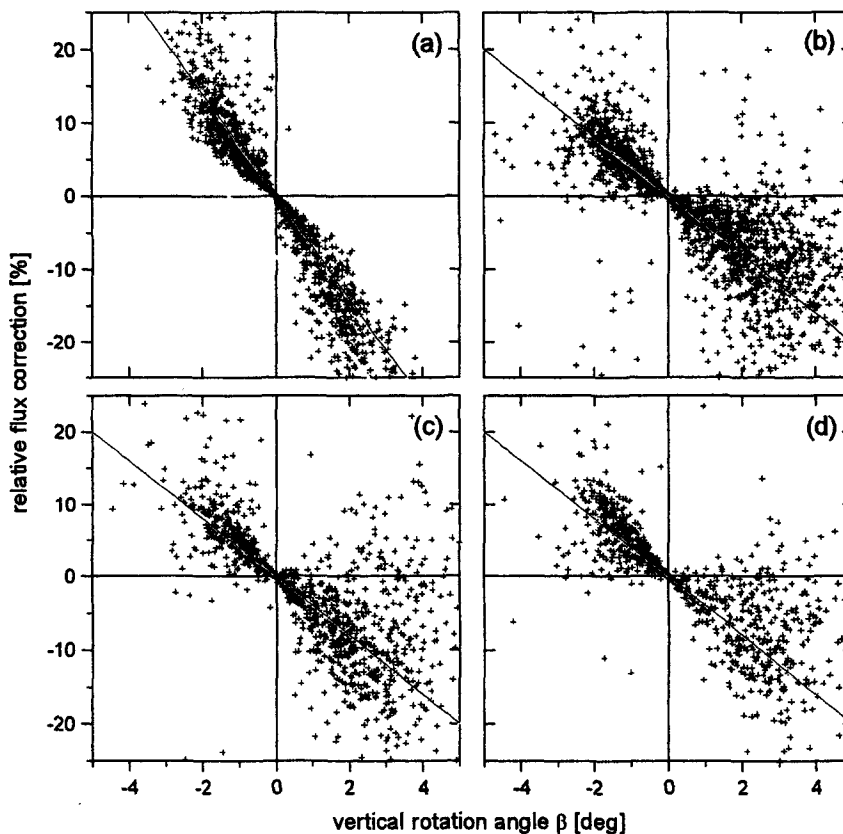


Fig. 4.9: Effect of vertical wind vector rotation (angle β) on different fluxes: (a) momentum flux; (b) sensible heat flux; (c) CO_2 flux; (d) ozone flux (only cases with windspeed $> 1.5 \text{ m s}^{-1}$ included).

The rotation effect on the scalar fluxes, displayed in Fig. 4.9b-d, is somewhat smaller than for the momentum flux. The linear curves drawn by eye indicate average relative flux corrections of 4 - 5 %. This finding is in good agreement with literature values reviewed by Brutsaert (1982: 192). The systematic dependence on the rotation angle can be explained by the influence of the covariance between the horizontal windspeed u and the concentration μ_c on the unrotated flux. The term $u'\mu_c'$ is supposed to be larger than the vertical turbulent flux, because $\sigma(u)$ is generally larger than $\sigma(w)$ (see Section 2.4.4) whereas the correlation coefficients are of similar magnitude (cf. KF94:20). The stronger rotation effect in the momentum flux results from the influence of the maximally correlated terms $\overline{u'u'}$ and $\overline{w'w'}$ in the misaligned covariance (cf. Eq. 4.9 and 4.10).

4.1.4 Calibration and Correction for Correlated Density Effects

The preceding calculations yielded the covariances of the vertical windspeed with the raw signals for the scalar quantities (trace gases and sonic temperature). In principle, the sensor calibrations can easily be applied to variances and covariances, since the characteristic of most instruments is linear or can be linearised in the observed range. However, attention has to be paid, which quantity is actually measured by the sensor. The trace gas analysers used here, like most others, are sensitive to the absolute trace gas density ρ_c , although they often display their measurements as mixing ratios. Since ρ_c is a unique function of the raw voltage signal V_c , the covariance could be calibrated in the following way:

$$\overline{w'\rho_c'} = \left(\frac{d\rho_c(V_c)}{dV_c} \right) \cdot \overline{w'V_c'} \quad (4.12)$$

In the case of a linear calibration (ozone, cf. Section 3.3.4), the derivative just equals the line slope. For the non-linear characteristics of the CO₂/H₂O-analyser (see Section 3.3.3), the calibration factor corresponds to the local gradient of the functions. The resulting covariance in Eq. 4.12 is not generally equal to the final turbulent flux. According to the theoretical consideration in Section 2.3.3, the covariance with the mixing ratio μ_c (Eq. 2.30) is required instead. Since the absolute gas density is additionally influenced by temperature, pressure and humidity conditions in the measured volume, the relation between μ_c and ρ_c becomes:

$$\mu_c \equiv \frac{\rho_c}{\rho_a} = \frac{\rho_c}{\rho_0} \cdot \left(\frac{T}{T_0} \right) \left(\frac{p_0}{p} \right) (1 + \mu_{H_2O}) \quad (4.13)$$

$\rho_0 = 44.60 \text{ mol m}^{-3}$ describes the gas density at standard conditions $T_0 = 273.15 \text{ K}$ and $p_0 = 1013 \text{ hPa}$. According to Webb et al. (1980), the insertion of Equation 4.13 into the eddy covariance formula 2.30 leads to the following expression, which is often termed 'Webb-correction':

$$F_c = \overline{w'\rho_c'} + \overline{\mu_c} \left(\overline{w'\rho_{H_2O}'} + \frac{\overline{\rho}}{\overline{T}} \overline{w'T'} \right) \quad (4.14)$$

The influence of the different air properties appears as an additive correction term including the covariances of the corresponding quantities with w . The effect of correlated pressure variations is neglected, since they are comparatively small (cf. St88:162). It has to be noted, that relationship 4.14 is valid for open-path measurements as well as within a closed-path system. However, all covariance terms have to be determined for the same point (i.e. within the measurement cell for a closed-path instrument). Con-

sidering the two relationships 2.30 and 4.14, there are mainly three ways to determine the trace gas flux F_c in practice:

- 1) The covariances of temperature and humidity with the vertical windspeed are measured and used to correct the covariance of ρ_c with w according to Eq. 4.14 (e.g. Suyker and Verma, 1993; Güsten et al., 1996)
- 2) The correlated air density effects are avoided through a suitable measurement setup: the sample air is brought to common temperature and humidity conditions before detection. This can be achieved by conducting the sample air through a closed-path system. Temperature fluctuations are damped in a very effective way through contact with the tube walls (cf. Eq. 4.15), and humidity fluctuations can be removed by pre-drying the sample air (e.g. Wienhold et al., 1994). In this case, the correction term in Eq. 4.14 can be set to zero.
- 3) The fluctuations of temperature and humidity in the measurement volume are determined by fast response sensors and used for the calculation of $\mu_c(t)$. Thus Equation 2.30 can be evaluated directly (e.g. Laubach and Teichmann, 1996).

Solution (3) may be problematic, if not all properties are measured at the same point and with the same time resolution. For the present field measurements, solutions (1) and (2) were used for correcting the covariances resulting from Eq. 4.12. Since no drying of the sample air was performed, the humidity correction in Eq. 4.14 had to be applied to the full extent. Flow induced damping of the humidity fluctuations in the sampling tube is assumed to be generally small (see following section). The damping of the temperature fluctuations, however, was much more effective, because it is determined mainly by the heat exchange with the tube walls. According to Wienhold et al. (1994) and Leuning and Judd (1996), the corresponding attenuation factor η_T , which acts uniformly on all frequencies, can be estimated by

$$\eta_T(\text{tube}) = \exp\left(-0.088 \text{Pr}^{-0.5} \text{Re}^{-0.2} \frac{X}{D}\right). \quad (4.15)$$

Pr is the Prantl number, which equals about 0.72 for air (Hicks et al., 1987). X and D designate the length and the inner diameter of the tube respectively. With the X, D and Re values given in Section 3.3, the attenuation factor (4.15) results in 10^{-17} for the CO₂/H₂O-system and 0.64 for the O₃-sensor. The extreme difference in the values is completely caused by the different X/D ratios of the systems; the Reynolds number has almost no influence due to the small exponent. Consequently, the temperature correction in Eq. 4.14 could be omitted for the CO₂ and H₂O fluxes. For the ozone instrument, which almost behaved like an open-path system, the temperature correction term had to be multiplied by the attenuation factor $\eta_T = 0.64$.

The quantitative effect of the described correction (Eq. 4.14) on a particular trace gas flux depends on the eddy covariances of temperature and water vapour. They correspond to the energy fluxes of sensible heat H (2.32) and latent heat LE (2.33). Considering the tube attenuation effect discussed above and assuming typical environmental conditions $T = 15^\circ\text{C}$ and $\rho = 42.24 \text{ mol m}^{-3}$, Equation 4.14 can be rewritten as:

$$F_c \approx \overline{w'\rho_c'} + \bar{\mu}_c \cdot (0.23 \text{ LE} + \eta_T 1.17 \text{ H}) \cdot 10^{-4} \text{ mol J}^{-1}. \quad (4.16)$$

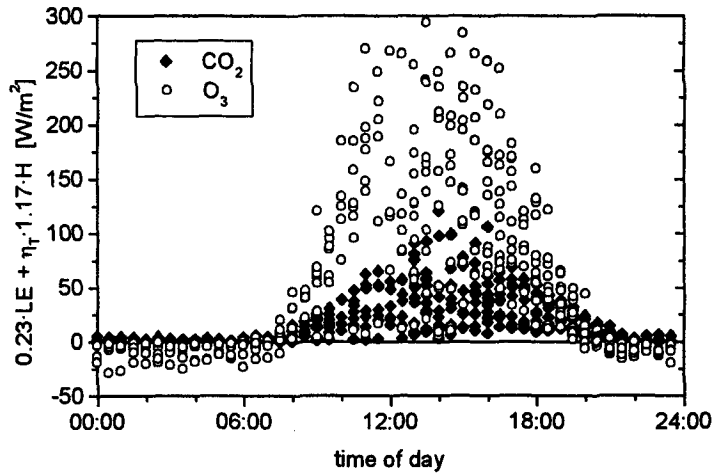


Fig. 4.10: Correction term for measured CO_2 and O_3 fluxes due to correlated air density fluctuations according to Equation 4.16.

When expressed as heat fluxes (Eq. 4.16), the correction effects of temperature and humidity fluctuations can be directly compared. The effect of the sensible heat flux is basically five times larger than the effect of the latent heat flux. However, the damping effect of the sampling tube especially on the temperature fluctuation have to be considered. In Figure 4.10 the daily course of the bracket term, i.e. the relative contributions of H and LE to the Webb-correction is plotted for the different trace gas fluxes. The magnitude of the correction is determined by the daily cycles of the energy fluxes. The correction is mostly positive or near zero, because negative latent heat fluxes are very rare and negative sensible heat fluxes during nighttime are generally small. Since temperature fluctuations are entirely smoothed out in the sample flow reaching the CO_2 -analyser, the corresponding absolute correction is significantly smaller than for ozone. However the relative importance of the 'Webb-correction' for the different trace gases depends strongly on the average ambient mixing ratio $\bar{\mu}_c$, which is multiplied with the bracket term in Eq. 4.16. Since the ambient CO_2 concentration is generally large compared to the turbulent fluctuations (and thus to the eddy flux), the relative correction is often above 20% (see Fig. 4.11). In contrast, the ambient concentration of ozone is comparatively low and the correction is mostly below 20%. In particular, the ozone deposition is always related to the ambient concentration and therefore it is not possible that high ambient concentrations occur simultaneously to very low fluxes.

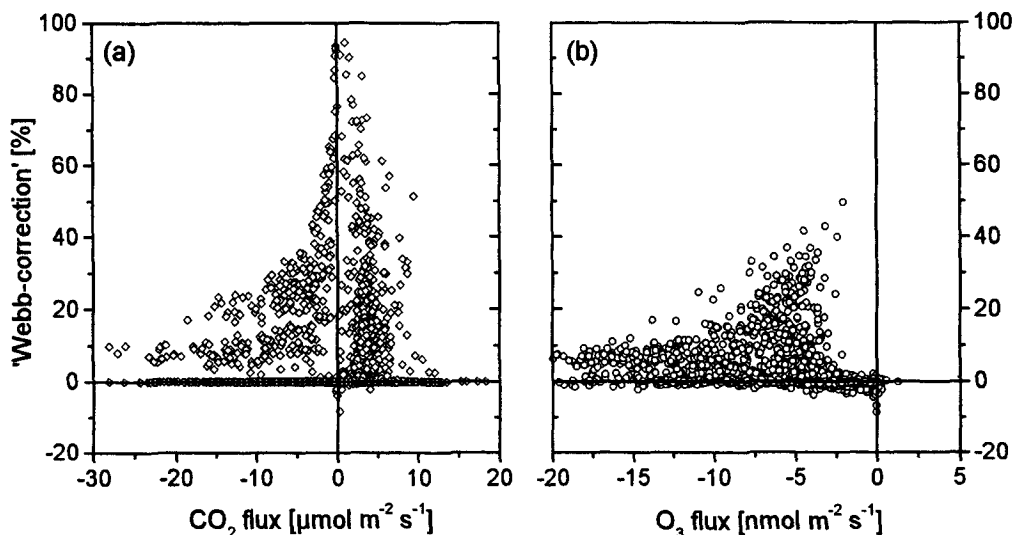


Fig. 4.11: Relative 'Webb correction' vs. trace gas flux for CO_2 and O_3 .

Another effect of correlated density fluctuations has to be considered for the temperature covariance derived from sonic measurements. According to Eq. 3.7, the air temperature is not a totally unique function of the speed of sound c_{raw} measured by the sonic instrument, but depends also on the air humidity $\mu_{\text{H}_2\text{O}}$ and the windspeed normal to the sonic path v_n . This parameters vary usually in correlation to w and therefore affect the eddy covariance calculation. For the kinematic heat flux, obtained by a simple calibration from the raw speed of sound, Schotanus et al. (1983) derived the following additive correction:

$$\overline{w'T'} = \left(\frac{dT(\bar{c}_{\text{raw}})}{dc_{\text{raw}}} \right) \cdot \overline{w'c_{\text{raw}}'} - 0.32 \bar{T} \overline{w'\mu_{\text{H}_2\text{O}}'} + 0.005 \bar{v}_n \overline{w'v_n'} \quad (4.17)$$

Due to the 45 degree inclination of the sonic path, the crosswind fluctuation v_n' is composed of contributions of u' as well as w' depending on the wind direction. Therefore the crosswind correction term is *more difficult to determine than for other instruments with orthogonal sonic paths*. However it is of similar magnitude as the vertical momentum flux (see also Lohse et al., 1990). Figure 4.12 shows the cumulative distribution of the estimated crosswind correction (using $\overline{u'w'}$) in comparison to the water vapour correction. For a quantitative interpretation, both terms are given in units W m^{-2} . The estimated crosswind correction is significantly smaller than the water vapour correction and mostly below 5 W m^{-2} . Therefore, it was generally neglected.

Because of the condensation events in the closed-path H_2O -analyser, the water vapour covariance used in Eq. 4.17 is not always available. However, this is no major problem, since the temperature covariance flux is used in the present study mainly in two ways:

- 1) Test of the energy budget closure of the eddy correlation system (Section 6.1.2): this test is only possible, if the water vapour flux is also available; thus the sensible heat flux can be determined according to Equation 4.17
- 2) Determination of the stability parameter z/L according to Eq. 2.38: for this purpose, the uncorrected covariance is used, since it is close to the covariance of the virtual temperature (see Kaimal and Gaynor, 1991) which is the appropriate quantity for stability characterisation.

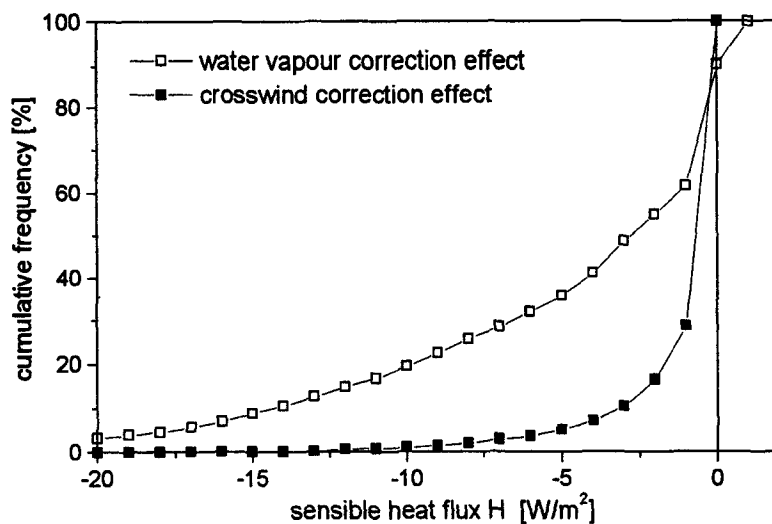


Fig. 4.12: Cumulative frequency distribution (ogive) of the water vapour and crosswind correction term for the sensible heat flux; the crosswind term was estimated from the vertical momentum flux and the horizontal windspeed u .

4.1.5 Correction for High Frequency Attenuation

In Sections 2.3.2 and 2.3.4, the requirements for the temporal resolution of eddy correlation measurements were discussed, taking into account the spectral distribution of the eddy covariance. In practice, the resolution of most measurement systems is limited by various factors including the physical response characteristics of the sensor itself as well as the system setup and the data acquisition. They cause an attenuation of the measured high frequency fluctuations leading to an underestimation of the variances and covariances. Most of the important effects are discussed by Moore (1986) and Zeller et al. (1989). A survey of their results, applied to the present eddy correlation system, is given in Appendix A.7 and A.8. The attenuation effects, which have to be considered for the instrumental setup used, are:

- electronic prefiltering of the AD-converter (Appendix A.7.1)
- sonic path averaging (Appendix A.7.2)
- tube sampling (Appendix A.7.3)
- sensor separation (Appendix A.8.2)

The individual damping effects are quantitatively described by spectral transfer functions, which represent the attenuation factor for the spectrum or cospectrum as a function of the frequency (see Eqs. A.20; A.33). They were combined in order to obtain the total effective transfer function $T_{wc}(f)$ for the eddy covariance (cf. Eqs. A.46; A.46):

$$Co_{wc}(f)_{meas.} = T_{wc}(f) \cdot Co_{wc}(f)_{true} \quad (4.18)$$

The effect of the high frequency attenuation on measured cospectra is illustrated in Figure 4.13. The total damping effect (integrated over the cospectrum) depends strongly on the form and peak position of the cospectrum, which is mainly a function of stability (cf. Fig. A.3). Stable cospectra have generally a larger contributions in the high frequency range above 1 Hz, where the damping effect is strongest. The validity of the estimated transfer functions is tested in the following Section by comparing damped model cospectra with measured cospectra.

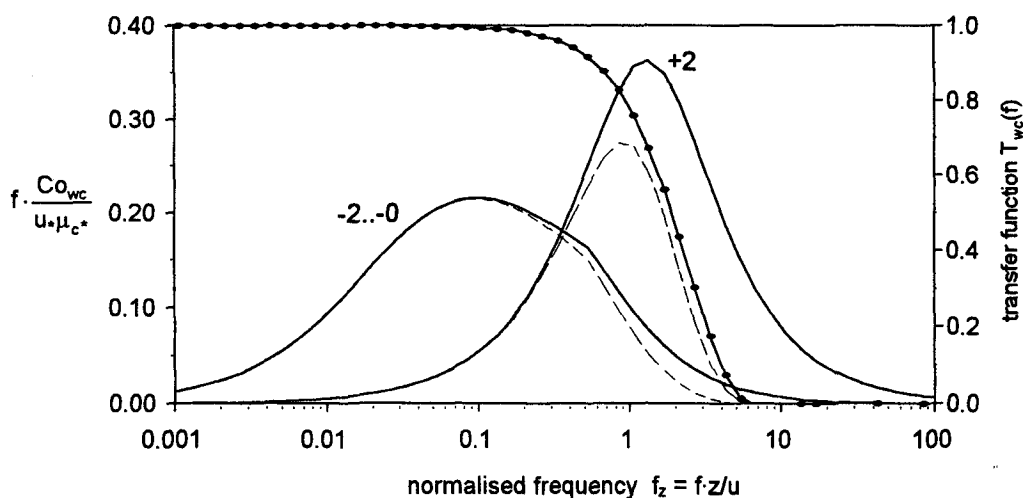


Fig. 4.13: Normalised ideal cospectra (solid lines, after Kaimal) and damped cospectra (dashed lines) for scalar fluxes under different stability conditions (indicated as z/L). The total transfer function (circles) for the high frequency damping effect was determined according to Eq. A.46 for a windspeed $u = 2 \text{ m s}^{-1}$ and lateral sensor separation $s_{lat} = 0.2 \text{ m}$.

If the spectral transfer characteristic of an eddy correlation system is known, the integral attenuation effects for the measured flux can be corrected or compensated in the following ways:

- 1) direct individual correction: multiplication of the measured cospectrum with the inverse of the transfer function (according to Eq. 4.18) and integration of the corrected cospectrum (cf. Laubach and Teichmann, 1996)
- 2) individual cospectral similarity: application of the transfer function to measured cospectra of another scalar quantity, which is not (or only little) affected by attenuation problems (e.g. sonic temperature), and determination of the integral damping factor (Horst, 1997)
- 3) general cospectral similarity: like 2) but with a theoretical cospectral model (Moore, 1986; Moncrieff et al., 1997)

The first two solutions require the calculation of individual cospectra for each measurement interval and therefore need intensive calculation and analysis. This is not appropriate for longterm (operational) measurements. Moreover, the first approach fails for frequencies which damped too much, and the second approach does not work if the reference flux is near zero. For the present flux evaluation, the third approach was chosen. It represents a fast and simple method, which is very robust and can therefore be applied in automated algorithms. The accuracy may be lower than for the other more direct methods, but it should be still sufficient for a flux estimation better than $\pm 10\%$. The net effect for the underestimation of the measured covariance is determined by integrating the unaffected and the damped cospectrum over the whole frequency range and by calculating the ratio of both:

$$\eta_{wc} \equiv \frac{\overline{w' \mu_c'}_{(meas.)}}{\overline{w' \mu_c'}_{(true)}} = \frac{\int_0^{\infty} T_{wc}(f) \cdot Co_{wc}(f) \cdot df}{\int_0^{\infty} Co_{wc}(f) \cdot df} \quad (4.19)$$

This relationship was evaluated with the general model-cospectra of Kaimal (Eq. A.23) and the transfer function A.46 for different conditions. Since the cospectra and the transfer function depends on the windspeed u , the stability z/L , and the lateral sensor separation s_{lat} , the integral flux recovery factor η_{wc} was calculated for various meaningful combinations of the three parameters:

- windspeed: $0.5 \text{ m s}^{-1} \leq u \leq 8 \text{ m s}^{-1}$
- stability: $-2 \leq z/L \leq 2$
- sensor separation: $0 \leq s_{lat} \leq 0.4 \text{ m}$

Following the suggestion of Moore (1986), an empirical function of the parameters was fitted to the simulated η_{wc} values by a multiple nonlinear regression procedure (least squares method). The following functional form was found to be appropriate:

$$\eta_{wc} = A(u, s_{lat}) + B(u, s_{lat}) \frac{1}{1 + 0.5 \cdot z/L} \quad (4.20)$$

$$A(u, s_{lat}) = 0.896 - 1.840 s_{lat} - 0.203 u + 0.304 u \cdot s_{lat}$$

$$B(u, s_{lat}) = 0.113 + 1.572 s_{lat} + 0.181 u - 0.281 u \cdot s_{lat}$$

The maximal deviation of this function from the individual data points was only 1.5%. The general form of Equation 4.20 with two parameters A and B and the presented dependence on stability was adopted

from the relation for the peak frequency of the cospectrum (cf. Horst, 1997). The additional influences were implemented by making A and B a function of windspeed and sensor separation. The relation to both individual parameters is linear (see Fig. 4.14), but since both effects are not independent of each other, an additional nonlinear term ($u \cdot s_{\text{lat}}$) had to be included. As shown in Section A.8.3, the sensor separation effect is dominant for high windspeeds, whereas it is covered by the analog filter effect for low windspeeds.

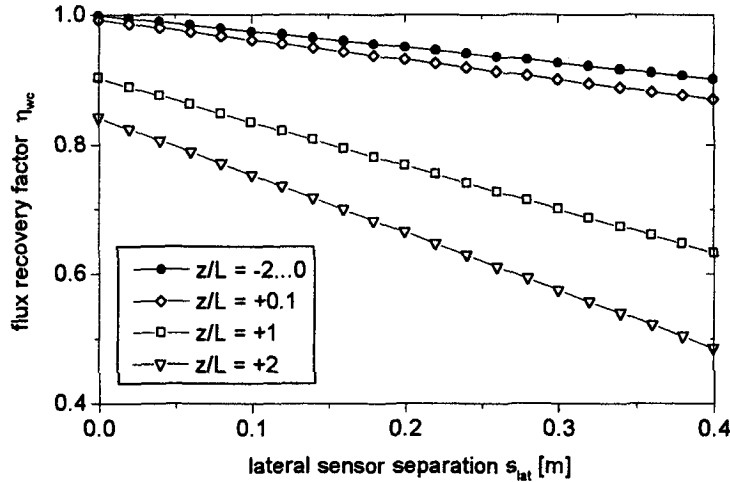


Fig. 4.14 Flux recovery factor due to high frequency attenuation of trace gas fluxes as a function of lateral sensor separation for $u = 1 \text{ m s}^{-1}$ and four different stability conditions.

In Figure 4.15, the bivariate dependence of the recovery factor η_{wc} on stability and windspeed is displayed. The recovery of the measured flux decreases (due to increased attenuation) with both factors, but especially the influence of stability is strongly non-linear. It has to be considered, that windspeed and stability are not independent quantities in the surface layer. Therefore, not all combinations can occur under natural conditions, which is illustrated by the distribution of the field observations in Fig. 4.15. In unstable and near-neutral conditions the recovery factor varies only little; it is mostly above 0.9 except for very high windspeeds. Stable conditions with $z/L > 0.1$ are always connected to very low windspeeds. With increasing stability, the damping effect also increases quickly up to the minimum of $\eta_{\text{wc}} \approx 0.65$ (for a lateral sensor separation of 0.2 m).

Analogous to Eqs. 4.19 and 4.20, the spectral attenuation effect on the temperature covariance (sensible heat flux) was parameterised using the transfer function A.47. In this case, the empirical function for the integral flux recovery factor η_{wT} could be simplified significantly, since there is no sensor separation effect and the windspeed influence is already included in the normalised frequency f_z . Thus η_{wT} only depends on stability and never falls below about 0.97. The following regression function had a maximal deviation of only 0.5% from individual calculated data points:

$$\eta_{\text{wT}} = 0.847 + 0.140 \cdot \frac{1}{1 + 0.5 \cdot z/L} \quad (4.21)$$

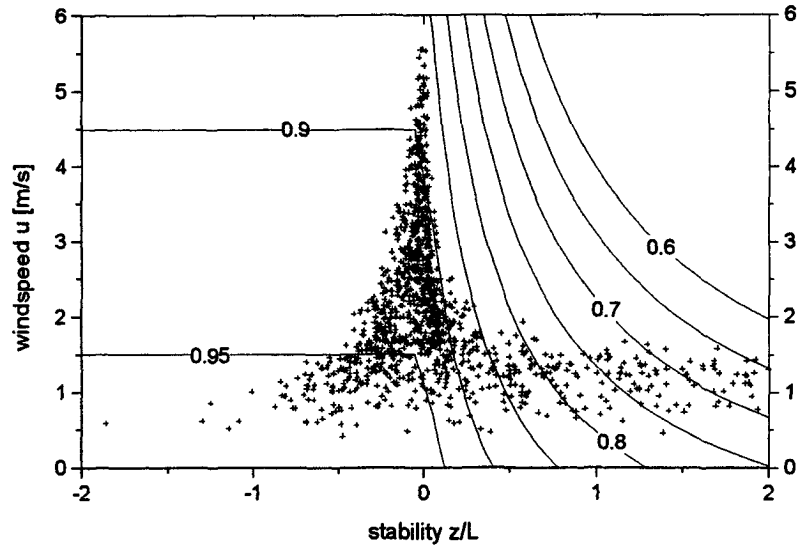


Fig. 4.15: Damping factor due to high frequency attenuation of trace gas fluxes as a function of stability (z/L) and windspeed (u) for a sensor separation of 0.2 m. The combinations of z/L and u observed in the field campaign are indicated by crosses.

4.1.6 Spectral and Integral Similarity Relationships

The high resolution eddy correlation datasets contain in principle all information about the turbulence structure and transport in the surface layer. Thus not only the average covariance flux but many other turbulence characteristics can be determined and analysed. Statistical properties, which are scaled according to the surface layer similarity theory (cf. Section 2.4.1), may be compared directly to common similarity relationships derived from other field measurements. In this way, the consistency of the eddy correlation measurements can be tested and potential deviations from the assumed ideal turbulence structure (due to wind field distortion, advection effects, etc.) may be identified. Idealised assumptions concerning the analogy of scalar transport (Section 2.4), the form of turbulence spectra (Section 4.1.5), or the quantitative relationship between different statistical quantities are used in various contexts in the present study and need to be tested to a reasonable extent.

Integral similarity relationships

First, the integral similarity relationships for correlation coefficients (and standard deviations) are investigated. They are important to estimate the quantitative relationship between trace gas fluxes and the corresponding scalar standard deviations for the application in simulations studies (Section 6.3), error estimations (Section 4.3), and flux measurements (variance method, cf. Section 2.4.4). The correlation coefficients r_{wc} of the vertical turbulent transport were determined according to Equation 2.64. For that purpose, the calculation procedure for the eddy covariance as presented in the previous sections was slightly modified. All corrections which are assumed to act equally on the covariance and the standard deviations (i.e. the Webb-correction and some specific high frequency damping effects) were not applied, because they are eliminated in Eq. 2.64.

Since a meaningful and accurate correlation coefficient can only be determined with a turbulent flux which is significantly different from zero, values below a certain threshold flux (specified in Table 5.1) were not used. The resulting experimental correlation coefficients for all scalar fluxes are plotted in Figure 4.16 against the stability parameter z/L . For comparison, the corresponding similarity function given by Eq. 2.65 and Fig. 2.15 is also displayed.

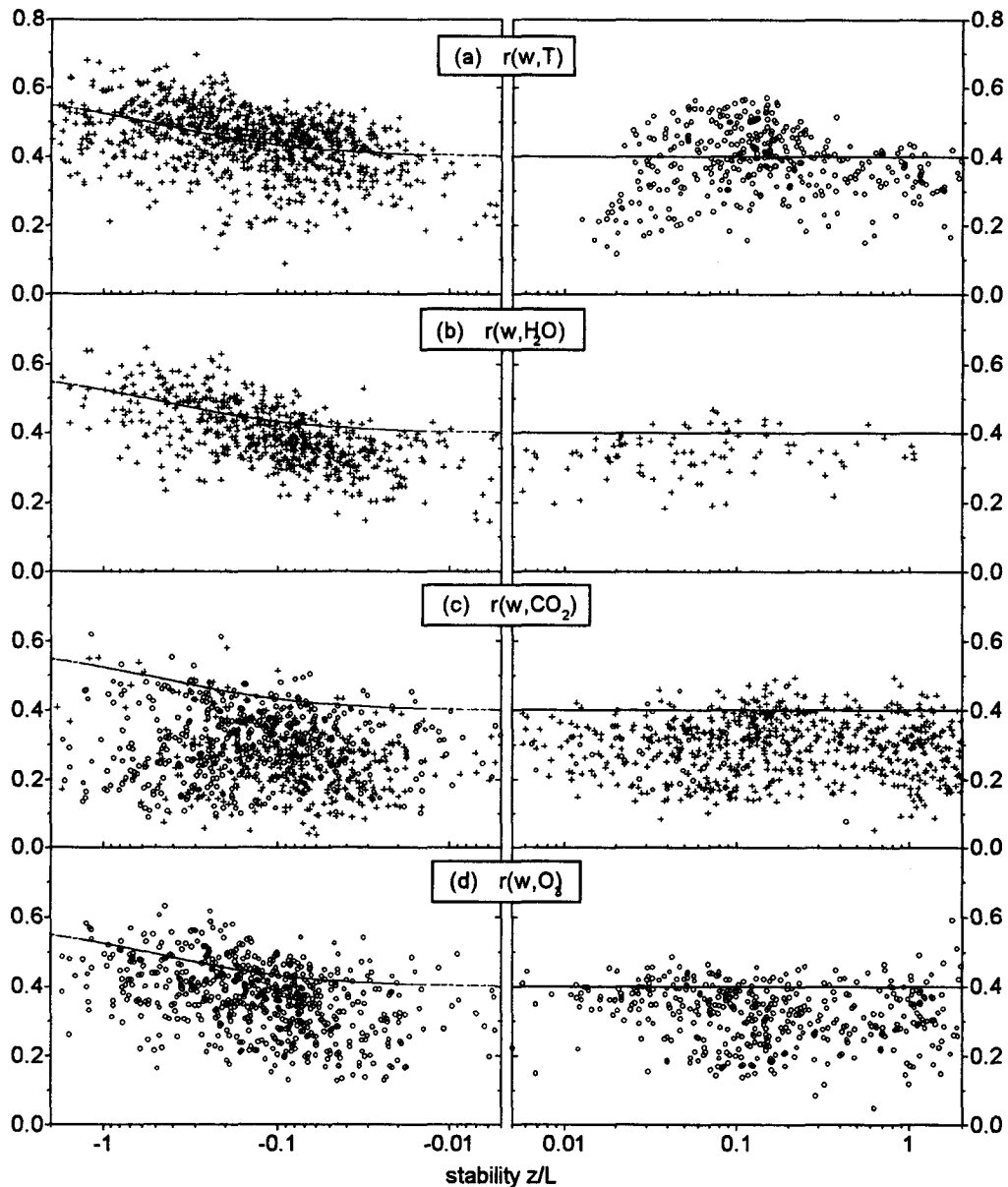


Fig. 4.16: Absolute correlation coefficients of different scalar fluxes as a function of stability z/L : (a) temperature; (b) H_2O ; (c) CO_2 ; (d) O_3 ; cross symbols indicate positive correlation, open circles indicate negative correlation; the solid lines represent the similarity relationship according to Fig. 2.15 and Eq. 2.65.

For the temperature, the measured data agree fairly well with the similarity function. Although the data show a considerable scatter, no clear systematic deviation from the theoretical model can be observed. The tendency for lower values in near neutral cases might be due to a too small rejection threshold. The correlation coefficients of the trace gas fluxes, in contrast, show a predominant underestimation yet of different magnitudes. For the water vapour, the results differ mainly for moderately unstable conditions, whereas the strongly unstable cases agree well with the similarity function. In the stable range only few results, hardly representative, are available due to the almost vanishing H_2O flux during night. The deviations for CO_2 and ozone are generally larger and occur for all stability conditions. In the stable region, the underestimation is fairly uniform leading to relatively constant values over the whole range, as predicted by the similarity relationship by KF94. This behaviour supports the validity of the high frequency correction model, which corrected damping effects of up to 50% for strongly stable conditions.

For a quantitative overview of the correlation coefficient results, the average values and the spread of $r(w,s)$ for the different scalars are compiled in Table 4.1. The data were classified according to their sign (i.e. the direction of the flux) and the stability conditions. The stability classes were chosen with respect to the observed systematic variation with z/L .

Tab. 4.1: Arithmetic averages and standard deviations of correlation coefficients for the vertical turbulent transport of scalar quantities; data are classified with respect to the sign and the stability conditions.

stability range	$r(w,T)$	$r(w,H_2O)$	$r(w,CO_2)$	$r(w,O_3)$
strongly unstable $-2 \leq z/L \leq -0.1$	0.47 ± 0.09	0.44 ± 0.08	0.29 ± 0.11 -0.30 ± 0.11	-0.40 ± 0.09
moderat. unstable $-0.1 \leq z/L \leq 0$	0.41 ± 0.08	0.34 ± 0.07	0.24 ± 0.08 -0.31 ± 0.08	-0.33 ± 0.09
stable $0 \leq z/L \leq +2$	-0.38 ± 0.09	0.34 ± 0.06	0.30 ± 0.08 -0.29 ± 0.08	-0.32 ± 0.08

Beside the generally low values for the trace gases already mentioned, it is noticeable that the correlation coefficients for water vapour and ozone are very similar, whereas the carbon dioxide shows significantly smaller results. This findings could indicate, that the turbulent scalar transport is not analogous for all scalars as usually assumed (cf. Section 2.4). However, the difference in the correlation coefficients might also be caused by instrumental shortcomings. In contrast to the covariance, the standard deviations are strongly influenced by instrumental (uncorrelated) noise, which adds to the natural turbulent variance and thus lowers the correlation coefficient calculated according to Eq. 2.64.

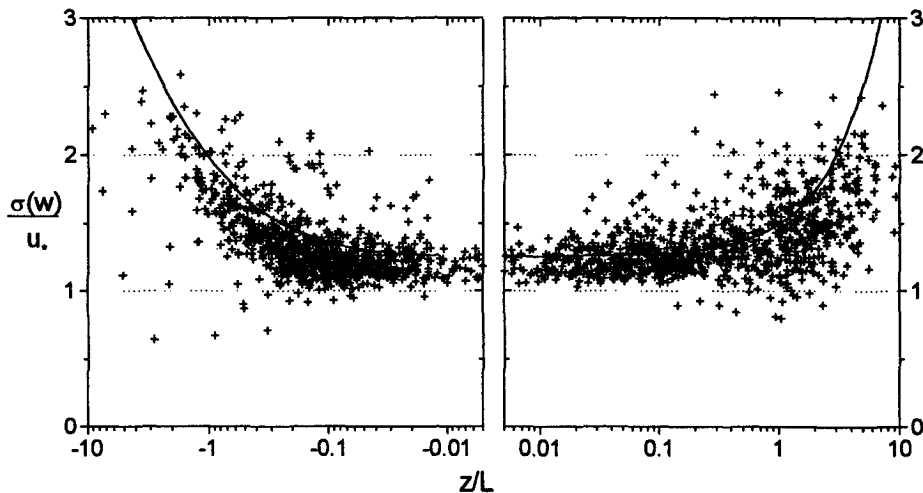


Fig. 4.17: Standard deviation of vertical windspeed normalised with the friction velocity as a function of stability z/L . The solid line represents the MO-similarity relationship according to Eq. 2.61.

The magnitude of the instrumental noise is difficult to estimate, because it may be composed of several individual effects (physical sensor noise, electronic signal processing, digitalisation, etc.). A negative influence of the w -measurement on the correlation coefficients can generally be excluded as shown in

Figure 4.17. The normalised standard deviation of the vertical windspeed is compared to the corresponding similarity function (Eq. 2.61). A generally fair agreement can be observed with some slightly lower values in the unstable and very stable range. They would lead to an overestimation rather than an underestimation of the correlation coefficient. An instrumental noise effect of the trace gas analysers seems to be more likely, because the observed underestimation in Fig. 4.16 corresponds to the expected signal to noise ratios. They are assumed to be most unfavourable for trace gases like CO_2 with small relative fluctuation signals (cf. Section 4.4.3) and also for moderately unstable conditions with most effective vertical mixing (high σ_w) and thus relatively low trace gas fluctuations (low σ_c). More detailed information about the noise effect of the trace gas measurements is provided by the analysis of the variance spectra presented in the following paragraph.

Spectral Similarity Relationships

A detailed spectral analysis of the high resolution eddy correlation time series is beyond the scope of the present study. However, exemplary checks of the spectral forms is a very useful tool for testing the proper performance of the eddy correlation method and measurement systems. When individual spectra are plotted, a relatively large (random) scatter has to be expected, depending on the bandwidth used for frequency averaging (cf. Appendix A.5). Figure 4.18a shows an exemplary cospectra for the ozone flux of an individual 30 min interval under unstable midday conditions. The averaging bandwidth was chosen to yield equidistant points on the logarithmic frequency scale (cf. KF94:269). Thus the scatter is larger in the low frequency range, where the density of harmonic frequencies is small. As a reference, the corresponding model spectra proposed by Kaimal et al. (1972) is also displayed (cf. Appendix A.6). Like all similarity relationships, they represent an average form, which was obtained by the combination of many individual spectra under comparable homogeneous conditions (composite spectra). An alternative graphical representation is the cumulative cospectrum formed by integration over the frequency axis. The resulting ogive (cf. Appendix A.5) is displayed in Figure 4.18b again with the corresponding Kaimal-function.

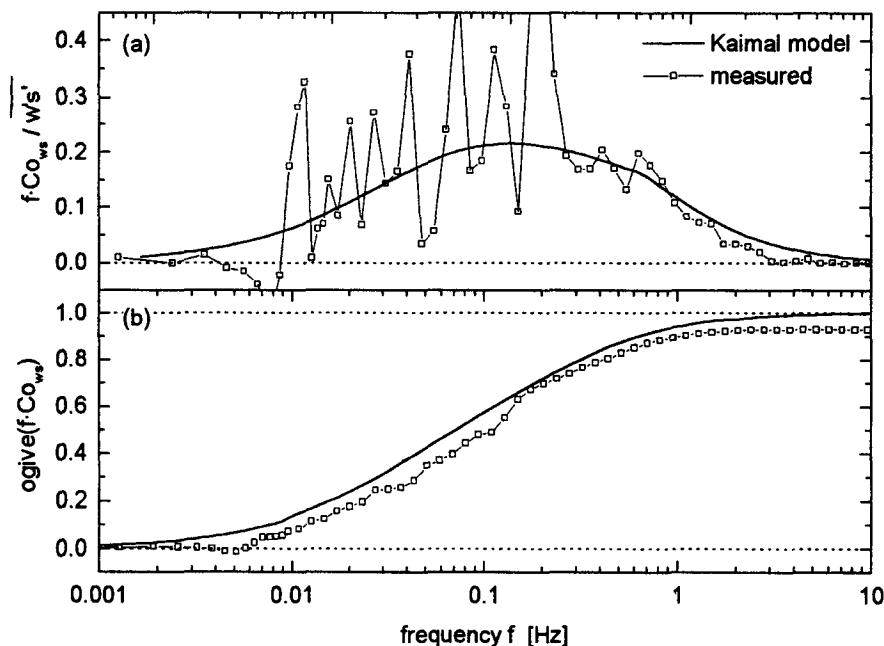


Fig. 4.18: (a) individual normalised cospectrum and (b) ogive of the ozone flux for a 30 min interval under unstable daytime conditions in comparison to the corresponding Kaimal model (4 July, 15:00 - 15:30; SW wind direction, $z/L = -0.2$, $u = 2.5 \text{ m s}^{-1}$).

In the ogive representation, the strong variations between neighbouring frequencies are totally smoothed out and a good agreement with the spectral model can be noticed. The generally lower values of the measured ogive are induced by a small negative contribution at the low frequency end which might be caused by a slight non-stationarity or inhomogeneity effect (cf. Laubach, 1996). On the other hand, the integration of the measured spectrum does not yield the full (corrected) flux value, due to the high frequency damping discussed in Section 4.1.5.

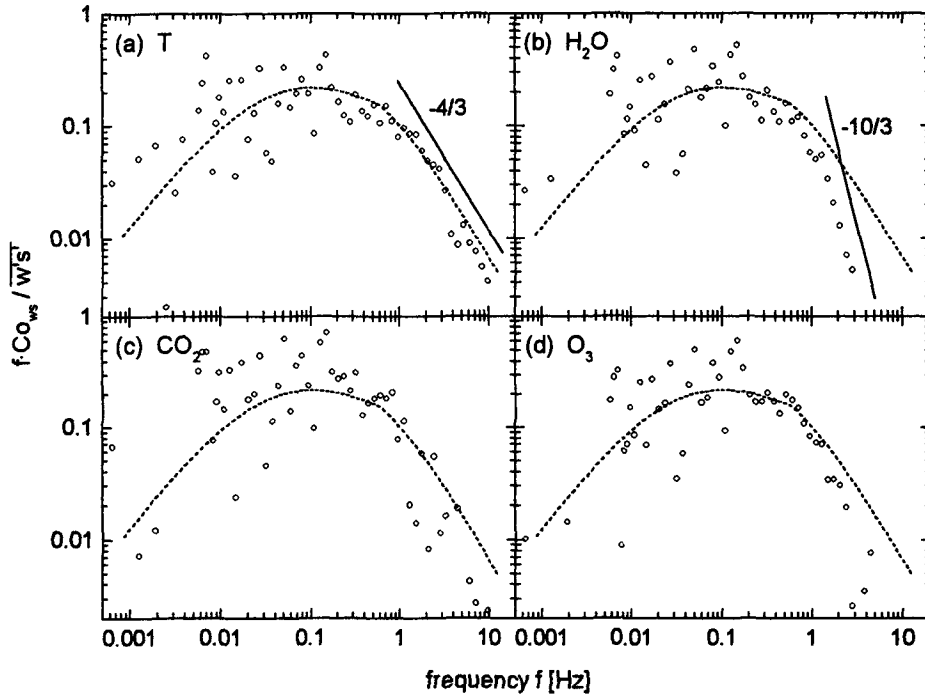


Fig. 4.19: Double-logarithmic plot of cospectra for different scalar fluxes of an individual 30 min run (same as in Fig. 4.18) compared to the corresponding Kaimal model; straight lines indicate power laws for the undisturbed and damped inertial subrange.

Another qualitative verification concerns the characteristic decrease of the cospectra in the inertial subrange following a power law. In a double logarithmic plot as presented in Fig. 4.19, it corresponds to a linear slope of $-4/3$ (cf. Fig. A.4). This behaviour is generally found for the sensible heat flux between about 1 Hz and 10 Hz. For the trace gases, the respective range is strongly affected by the high frequency attenuation of the analysing systems, which produce a steeper decrease. As shown by Eugster (1994), a first order damping filter follows a power law with exponent -2 and thus changes the slope to $-10/3$. This effect can be observed most clearly for H_2O , whereas the cospectra for O_3 and CO_2 show a considerable scatter at high frequencies.

Figure 4.20 shows a second example of the high frequency part of the cospectra for sensible and latent heat in a more detailed picture. For comparison it includes the cospectral similarity function not only in the ideal form but also subjected to the high frequency damping model (for H_2O) as described in Section 4.1.5. The ideal curve agrees well with the observed temperature cospectrum, for which the damping is assumed to be very small. The damped similarity function deviates from the ideal form in the same way as the measured H_2O cospectrum. This exemplary cases illustrate, that the spectral model used for the correction of the high frequency attenuation worked reasonable well.

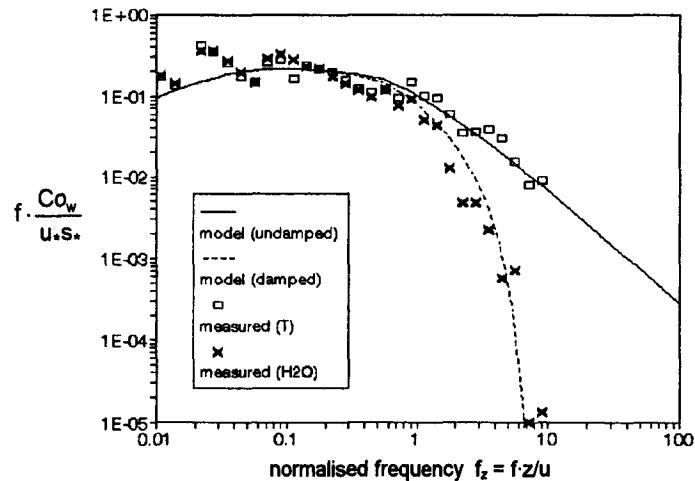


Fig. 4.20: Comparison of ideal and corrected cospectral model with measured cospectra of temperature and water vapour flux under unstable conditions (4 July 1995, 17:00-17:30, $u = 3.2 \text{ m s}^{-1}$).

The turbulent power (variance) spectra of atmospheric quantities can be described by similarity relationships as well. They follow a power law with exponent $-2/3$ in the inertial subrange (cf. Appendix A.6). Figure 4.21 displays the high frequency range of an individual power spectrum in a double logarithmic plot. The temperature again follows best the ideal linear slope over almost two frequency decades. The H_2O spectrum is damped for frequencies above 1 Hz, like the corresponding cospectrum, but with a slope of $-8/3$ (Eugster, 1994). At very high frequencies, the influence of the digitalisation noise leads to a slight increase, which is however negligible for the total variance. For CO_2 and O_3 the same behaviour should be observed because the respective signals were subjected to the same high frequency attenuation effects. However, the ozone spectrum follows more or less the ideal undisturbed slope and the CO_2 spectrum shows an even slower fall-off. This discrepancy indicates a considerably high noise level for O_3 and especially for CO_2 which was only partly removed by the electronic filter. Considering the results of the spectral analysis, it can be stated that the correlation coefficients presented above (Tab. 4.1) are affected by instrumental noise to a varying extent. The results are consistent by the fact that the correlation coefficients for H_2O (with very small noise effects) agree best with the common similarity function, whereas the results for CO_2 (with largest noise effects) show the largest deviation. An appropriate removal of the noise effects is generally difficult and beyond the scope of this study.

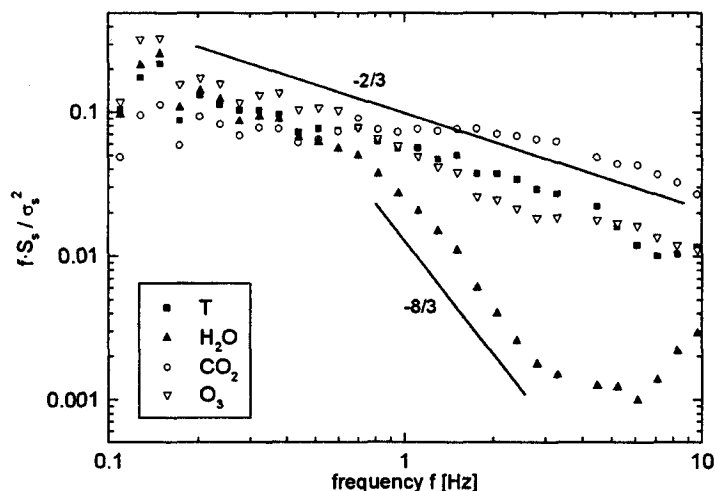


Fig. 4.21: Double-logarithmic plot of power spectra for different scalar quantities (same run as in Fig. 4.18); straight lines indicate power laws for the ideal ($-2/3$) and damped ($-8/3$) inertial subrange.

4.2 Aerodynamic Flux-Profile Calculations

Among the profile techniques presented in Section 2.4.2, the aerodynamic method represents the only 'pure' profile method. It allows to determine trace gas fluxes solely from average profile data of wind-speed, temperature and trace gas concentration and is therefore most suitable to analyse the specific problems and limitation of profile methods. The basic formula for flux evaluation is given by Equation 2.50: the turbulent trace gas flux is described as product of a concentration difference $\Delta\bar{\mu}_c$ between two heights and the corresponding transfer velocity v_w , which is a function of the turbulence parameters u_* and L . In the aerodynamic profile method, u_* and L are calculated from profile measurements of wind-speed and temperature according to Equations 2.51 - 2.53. They represent an implicit nonlinear equation system for three unknowns (u_* , T_* , L), that cannot be solved analytically. The relationships also contain the effective aerodynamic heights z_i of the measurement levels, that depend on the (a priori) unknown displacement height d (Eq. 2.56). Hence there are actually four unknown parameters: u_* , T_* , L , and d . The available number of equations for the determination of these parameters depends on the number of measurement points, since Equations 2.52 and 2.53 can be formulated for each (independent) pair of profile levels. Three or more windspeed and temperature measurements are usually necessary in order to obtain a defined (or over-defined) equation system, which has to be solved by suitable numerical algorithms as described by Nieuwstadt (1978), Kramm (1989) or Schween (1993).

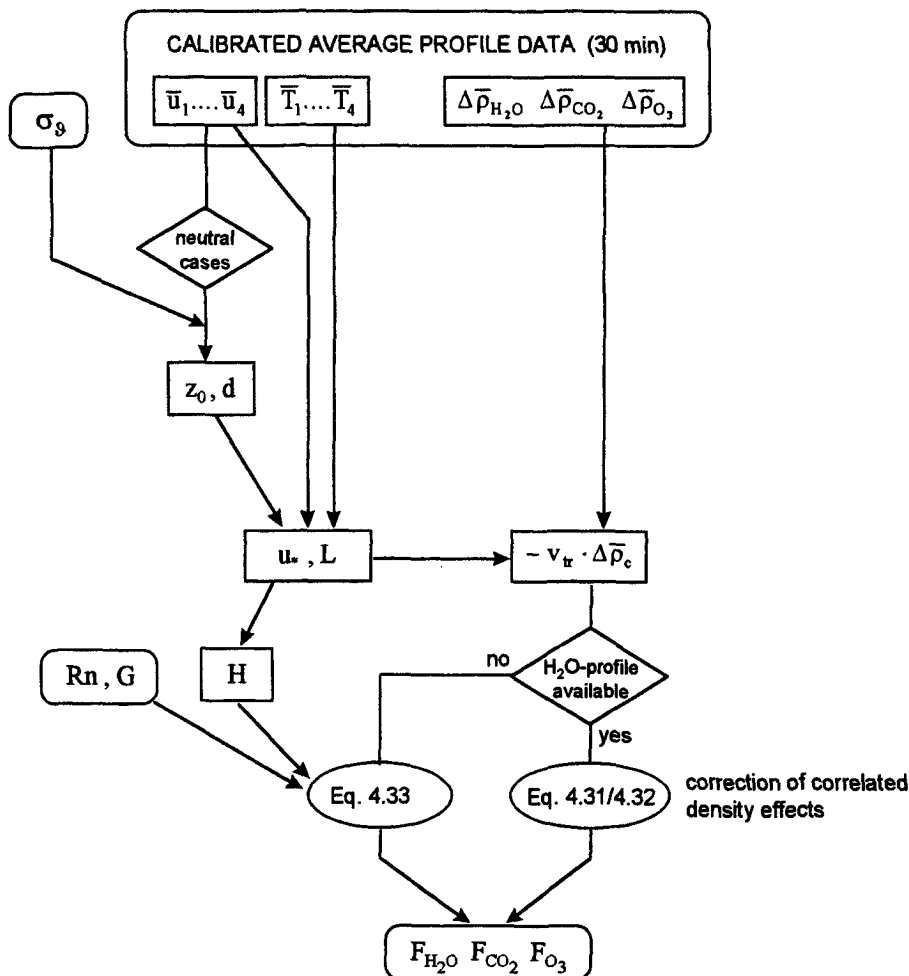


Fig. 4.22: Processing steps for the calculation of scalar fluxes by the aerodynamic profile method.

It was also found by the same authors, that a simultaneous determination (fit) of all four parameters for each time interval (i.e. 30 min) can lead to considerable stochastic as well as systematic errors in the results. They may be caused by even small deformations of the measured profiles and produce a large scatter of the individual values for the displacement height, which is supposed to be a constant characteristic of the vegetated surface (cf. Section 2.4.3). Often even physically meaningless values ($d < 0$ or $d > h_{\text{canopy}}$) are obtained. The results can be improved, if prescribed constant values for d and also for the aerodynamic roughness length z_0 are introduced in the flux-profile calculation (cf. Nieuwstadt, 1978, Berkowicz and Prahm, 1982; Ammann, 1992). z_0 is used as the lower boundary condition for the windspeed profile, which is most important for the determination of the transfer velocity. Especially the parameter d is not only important for the profile method, but it is of general interest in micrometeorological studies over vegetated surfaces. As part of the aerodynamic height z (Eq. 2.56), it occurs in many quantities and relationship based on Monin-Obukhov-similarity-theory (e.g. stability, spectral forms, etc.).

The general approach for the aerodynamic flux evaluation as applied in the present study is illustrated in Fig. 4.22. First the quasi-constant parameters z_0 and d were determined for the triticale field (cf. Section 4.2.1). With their help, the transfer velocity was calculated from the windspeed and temperature profiles (Section 4.2.2). Finally, the flux was calculated as the product of the transfer velocity and the trace gas concentration difference, which was corrected for water vapour dilution effects (Section 4.2.3).

4.2.1 Determination of z_0 and d

Under the assumption, that the parameters z_0 and d are constant for a given surface area, the determination can be restricted to special favourable situations (cf. Wieringa, 1993). They have to be chosen in order to minimise the deformation effects on the profiles and to reduce the number of unknowns, which have to be fitted simultaneously. This was obtained by the following restrictions, which were met in 370 of totally 1440 cases (30 min intervals):

- good fetch conditions: $180^\circ < \text{wdir} < 260^\circ$ (cf. Fig. 3.2)
- high windspeed: $u > 3 \text{ m s}^{-1}$ at 4.25 m above ground
- near neutral conditions: $-0.02 < \text{Ri} < 0.02$ (cf. Erisman, 1990)

With the last limitation, T_* and z/L could be set to zero and the equation system reduced to the logarithmic wind profile relationship (following from Eq. 2.52):

$$u(z_g) = \frac{u_*}{k} \ln \left(\frac{z_g - d}{z_0} \right). \quad (4.22)$$

With the four measured windspeed levels, a non-linear least square regression was performed for the three unknowns d , z_0 and u_* (one degree of freedom). The results were abandoned, if the sum of squared errors was larger than $0.01 \text{ m}^2 \text{ s}^{-2}$, corresponding to an error in the windspeed measurement of 0.1 m s^{-1} . In this way, cases without convergence of the iteration routine or without satisfying fit were sorted out. The individual values for z_0 are plotted in Fig. 4.23 against the wind direction. They vary roughly within one order of magnitude (ca. 0.04 - 0.4 m) but do not show a significant dependence on the wind direction. The average results are given in Table 4.2. Whereas the d values were averaged on the normal linear scale, the z_0 values were averaged in the logarithmic scale, because of their large relative scatter.

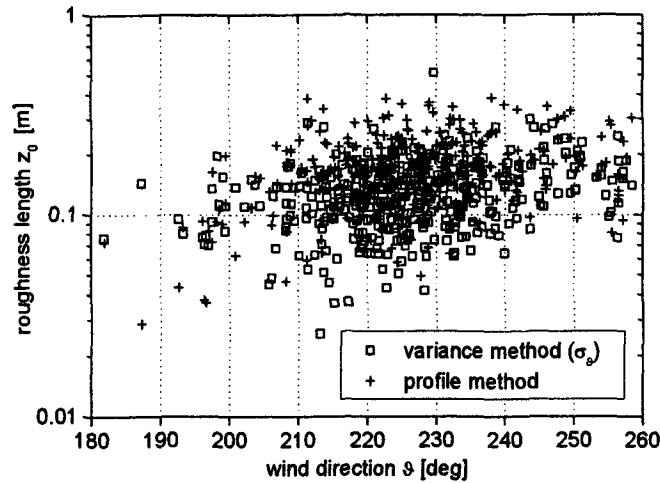


Fig. 4.23: Dependence of calculated roughness length z_0 on wind direction.

If only the average estimates of z_0 and d should be determined, a time saving simple alternative to the procedure above can be performed. All wind profiles can be averaged and a single regression fit is necessary for the calculation of effective average values for the surface parameters. The respective results are also given in Table 4.2; they are almost identical to the average values derived from the individual wind profiles.

Tab. 4.2: Averages estimates (and standard deviations) of the displacement height d and the aerodynamic roughness length z_0 for the triticale field derived by different methods. The variance similarity and eddy correlation method do not allow an independent determination of d and z_0 ; yet they provide an independent u_* value that was combined with the profile data.

method	roughness length z_0	displacement height d
individual profile fit (4 levels)	0.16 ± 0.07 m (n = 370)	0.77 ± 0.18 m (n = 370)
averaged profile fit (4 levels)	0.16 m	0.79 m
variance similarity (with σ_s)	0.12 ± 0.05 m (n = 370)	0.91 m
eddy correlation	0.09 ± 0.04 m (n = 151)	1.02 m
surface geometry (Eq. 2.56)		0.90 m

Despite the restriction to favourable conditions, the determination of d and z_0 from profiles alone may still be problematic due to an inherent coupling of both parameters in the profile relationship 4.22 (cf. Wieringa, 1993). They are inversely correlated and therefore even a small error in a wind measurement may lead to large deviation in the 'partitioning' of both quantities. For a quality check and a further improvement of the results, an external independent estimation of either z_0 or d (or both) have to be used. They may be obtained (a) from literature values and general parameterisations related to the geometric structure of the surface (cf. Rotach, 1991; Wieringa, 1993; Schween, 1993) or (b) from other flux measurement methods like eddy correlation (Nieuwstadt, 1978; Ammann, 1992) or variance measurements (Erisman and Duyzer, 1990; Beljaars and Holtslag, 1991). The last method is particularly

interesting, since z_0 can be estimated simply from the standard deviation of the wind direction ϑ measured by a windvane. Such instruments are relatively simple and cheap but nevertheless accurate. They are usually part of automated weather stations and profile systems. Since it is assumed that the wind direction ϑ is stationary over a typical micrometeorological averaging period with only small variations ϑ' (and thus $\sin(\vartheta') \approx \vartheta'$), the standard deviation of the lateral windspeed v can be estimated from the standard deviation of the wind direction ϑ :

$$\sigma_v = \bar{u} \cdot \sigma_\vartheta . \quad (4.23)$$

A combination of Equations 4.22, 4.23 and 2.63b under neutral conditions leads to the following relationship for z_0 :

$$z_0 = (z_g - d) \cdot \exp\left(\frac{1.9 k}{\sigma_\vartheta}\right) . \quad (4.24)$$

In this expression, the coupling between the unknowns z_0 and d (i.e. $\partial z_0 / \partial d$) is much smaller than in Eq. 4.22 for typical profile levels. Therefore, even a rough estimate for the displacement height (e.g. according to Eq. 2.57) yields a satisfying result for z_0 . Relationship 4.24 was evaluated using the σ_ϑ measurements of the windvane instrument, which was installed on the third profile level ($z_g = 2.85$ m) of the MET-P tower. The results obtained for southwesterly wind directions (triticale field) are plotted in Figure 4.23 and the average value is presented in Table 4.2. It is lower than the results of the profile evaluation and is closer to the value derived from eddy correlation measurements. The corresponding displacement height (determined with the help of the average wind profile) is higher than derived from the profile measurements alone and agrees much better with the geometrical relationships (fraction of the canopy height) given in the literature.

The average values of z_0 and d in Table 4.2 determined by the variance method were generally used for the evaluation of all profile measurements. Although they are representative in a strict sense only for source areas within the triticale field, they were also used for other wind directions with limited fetch, because a better or physically more meaningful estimate could not be found.

4.2.2 Numerical Calculation of Turbulence Parameters

As mentioned at the beginning of Section 4.2, the transfer velocity has to be determined from the turbulence parameters u_* , T_* , and L , which are coupled among themselves and with the wind and temperature profiles by the equations 2.51 - 2.53. With prescribed values for z_0 and d (see previous section) and four profile levels, totally eight independent equations are available (2.51, 4×2.52, 3×2.53). They represent an over-defined nonlinear equation system for the three unknowns with 5 degrees of freedom. Nieuwstadt (1978) proposed an overall (multivariate) least square regression for solving such a system. However, this procedure combines the fitting of the wind and temperature profiles and needs a relative weighting of the errors of both quantities. This is difficult to estimate, because the deviations of the measured profiles are more likely due to non-ideal conditions than due to stochastic measurement errors. Under extreme conditions, the resulting stability could even have a different sign than expected from the temperature profile alone, which is physically not meaningful.

A separated fitting of the temperature and windspeed profile therefore seems to be more robust, although it may look mathematically less elegant. The friction velocity u_* (Eq. 2.52) was estimated as a

weighted mean from the differences of the profile levels with z_0 . The weighting factors g_i take into account the different relative accuracy of the windspeed measurements.

$$u_* = \frac{1}{\sum g_i} \sum_{i=1}^4 g_i \cdot \frac{k \cdot \bar{u}(z_i)}{\ln(z_i/z_0) - \Psi_u(z_i/L)} \quad (4.25)$$

For the scaling temperature T_* the averaging procedure is somewhat more complicated, since no absolute lower limit (like z_0) is available. In order to treat all measurement levels equally, the weighted average of all possible profile differences was calculated. Again the weighting factor represents the different relative accuracy of the measured temperature differences. It grows with increasing distance of the profile levels.

$$T_* = \frac{1}{\sum g_{ij}} \sum_{i < j} g_{ij} \cdot \frac{k \cdot ([T(z_j) - T(z_i)] + 0.01[z_j - z_i])}{\ln(z_j/z_i) - \Psi_T(z_j/L) + \Psi_T(z_i/L)} \quad (4.26)$$

T_* and u_* are given as a function of the unknown stability parameter L . All three quantities are connected by the following relationship (rewritten from Eq. 2.51):

$$L = -\frac{T \cdot u_*^2}{k \cdot g \cdot T_*} \quad (4.27)$$

The three equations 4.25 - 4.27 form together a coupled non-linear system of equations for the three unknowns u_* , T_* and L . It could be solved by a simple iteration procedure in the order given above beginning with a near-neutral value for L . Usually, a satisfying result (change in $L < 1\%$) was obtained in this way after only few iteration steps (< 10). The stability correction functions Ψ_x used in Eqs. 4.25 and 4.26 were taken from Beljaars and Holtslag (1991). They are based on the well known integrated similarity functions given by Paulson (1970) and Dyer (1974):

$$\Psi_c = \Psi_T = 2 \cdot \ln\left[\frac{1+x^2}{2}\right] \quad (4.28a)$$

$$\Psi_u = 2 \cdot \ln\left[\frac{1+x}{2}\right] + \ln\left[\frac{1+x^2}{2}\right] - 2 \tan^{-1}(x) + \pi/2 \quad (4.28b)$$

$$\Psi_c = \Psi_T = \Psi_u = -5 z/L \quad (z/L \geq 0). \quad (4.29)$$

The integration variable $x = \Phi_u^{-1}$ is given by Equation 2.47b. In the stable range, Beljaars and Holtslag proposed an empirical extension of the stability function (Eq. 4.29) beyond the critical Richardson number, which takes into account that turbulent exchange also occurs in the intermittent regime (cf. Kondo et al., 1978). Their functions are applicable up to $Ri \approx 1$ corresponding to a z/L value of about 5 (see Fig. 4.24):

$$\Psi_c = \Psi_T = 1 - \left(1 + \frac{2}{3} \cdot \frac{z}{L}\right)^{3/2} - \beta \left(\frac{z}{L} - \frac{\gamma}{\delta}\right) \cdot \exp\left(-\delta \frac{z}{L}\right) - \frac{\beta\gamma}{\delta} \quad (z/L \geq 0) \quad (4.30a)$$

$$\Psi_u = -\frac{z}{L} - \beta \left(\frac{z}{L} - \frac{\gamma}{\delta}\right) \cdot \exp\left(-\delta \frac{z}{L}\right) - \frac{\beta\gamma}{\delta} \quad (z/L \geq 0). \quad (4.30b)$$

The empirical parameters are given as $\beta = 0.667$, $\gamma = 5$ and $\delta = 0.35$. For small z/L , the functions 4.30 and 4.29 are more or less identical. But approaching the critical Richardson number, 4.29 tends towards

infinity leading to zero fluxes (and an infinitely large z/L), whereas 4.30a/b yield small but finite fluxes over the intermittent range. Naturally, the relative uncertainty in this range is very large due to the small fluxes and the specific adjustment of the empirical functions derived from data of the Cabauw tower (The Netherlands, cf. Beljaars and Holtslag, 1991). Yet, the parameterisation is more realistic and robust for a broader stability range than the classical relationship 4.29 and was therefore preferred for the present evaluation.

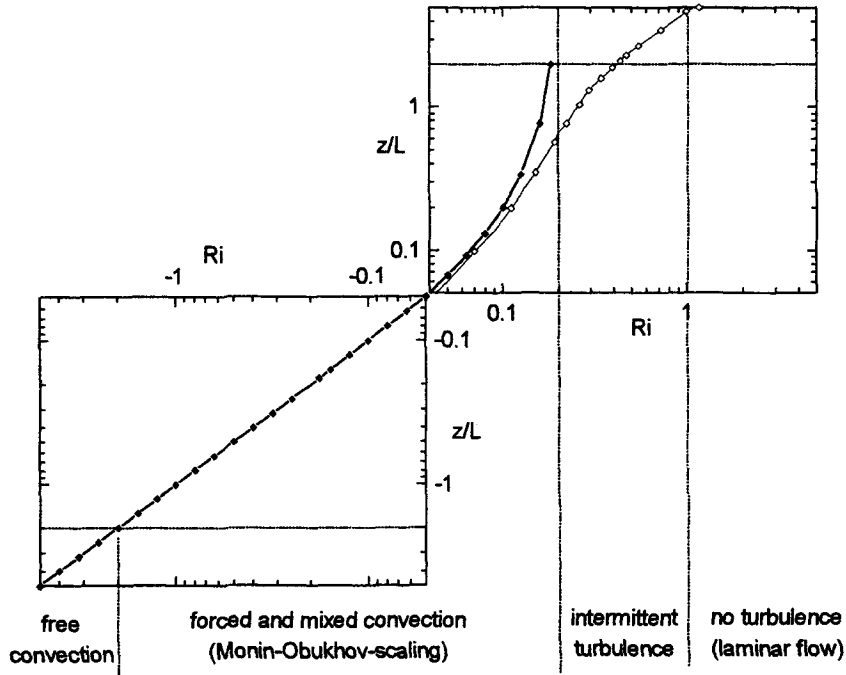


Fig. 4.24: Relationship between z/L and Ri resulting from Eqs. 4.29 (Dyer, 1974; solid symbols) and 4.30 (Beljaars and Holtslag, 1991; open symbols) respectively.

4.2.3 Flux Calculation and Correction

As already discussed in Section 4.1.4, the trace gas analysers are generally measuring the absolute gas density rather than the mixing ratio, which is required for the flux calculation according to Equation 2.50. The mixing ratio is defined by Equation 4.13 depending on pressure, temperature and humidity. Since the sample air of the different profile levels was brought to common temperature and pressure before analysing (see Section 3.2.2), the profile difference is particularly influenced by the humidity profile (cf. Webb et al., 1980):

$$\Delta\bar{\mu}_c \approx \frac{1}{\langle\bar{\rho}_a\rangle} \left[\Delta\bar{\rho}_c + \langle\bar{\rho}_c\rangle \Delta\bar{\mu}_{\text{H}_2\text{O}} \right]. \quad (4.31)$$

The triangular brackets signify a vertical average over the investigated air layer in addition to the time average. Assuming equal turbulent diffusivity (transfer velocity) for all scalar quantities, this leads to:

$$F_c = \langle\bar{\rho}_a\rangle v_{\text{tr}} \Delta\bar{\mu}_c = v_{\text{tr}} \left[\Delta\bar{\rho}_c + \langle\bar{\rho}_c\rangle \Delta\bar{\mu}_{\text{H}_2\text{O}} \right]. \quad (4.32)$$

The last term can be easily identified as the vertical gas concentration difference introduced by the variable dilution effect of water vapour. Relationship 4.32 is equivalent to the 'Webb-correction' for

eddy correlation fluxes (4.14 or 4.16 without a temperature correction). Thus, in analogy to Equation 4.16 one can write:

$$F_c \approx v_{tr} \Delta \bar{\rho}_c + \bar{\mu}_c \cdot 0.23 \text{ LE} \cdot 10^{-4} \text{ mol J}^{-1} . \quad (4.33)$$

In Equation 4.32, the water vapour difference for exactly the same profile levels as for the trace gas is required. However, in Equation 4.33, the water vapour flux may be determined from any profile measurements or even by different methods. If H₂O profile measurements were available, the trace gas fluxes were calculated according to 4.32. However in cases of condensation water in the H₂O system, fluxes were evaluated using Eq. 4.33 and the latent heat flux was determined by closing the energy budget of the surface (cf. Eq. 2.9):

$$\text{LE} \approx \text{Rn} - \text{G} - \text{H}_{\text{aerod}} . \quad (4.34)$$

4.3 Data Rejection and Error Estimation

Flux measurement systems are difficult to run on a completely operational basis. Beside intentional or unintentional interruptions (cf. Section 3.1.4), the measurements may be disturbed in many ways. Often the measurements are spoiled to a degree that makes a rejection of the data necessary. The criteria applied in the present case and the corresponding rejection statistics are given in Section 4.3.1.

An appropriate presentation of measurement results also includes the specification of error ranges or confidence intervals. They are usually derived either from known instrumental characteristics like noise level, linearity, cross sensitivity and instantaneous or longterm reproducibility given by the manufacturer or determined individually under controlled laboratory conditions. If the resulting quantity needs intermediate calculation steps, the error propagation rules of independent Gaussian statistics are generally applied. However, the situation is much more complex for micrometeorological flux measurements. Their validity and quality does not simply depend on the proper calibration and operation of the sensors like for example the accuracy of a concentration measurement. Fluxes have to be calculated as a combination of various concentrations (difference or time series) and air properties (air velocity, flow rate, pressure, temperature, etc.). Moreover they are crucially influenced by the local environmental conditions in the field, the setup of the instruments, and the data processing applied. Each of the influencing quantities may contribute in various ways to the error of the flux results (cf. Businger, 1986). Only few of these error sources have an ideal random (i.e. independent Gaussian) characteristic, most of them cause a systematic deviation from the ideal behaviour. Some effects, which can be predicted from turbulence theory and instrumental characteristics, are described in Sections 4.3.2 to 4.3.4.

4.3.1 Rejection Criteria and Final Datasets

The instrumental problems leading to failures of the flux measurement system were already discussed in Chapter 3. The main source of sensor misbehaviour was the occurrence of condensation water in the sampling tubes of the closed-path water vapour systems (cf. Section 3.2.2 and 3.3.3). It occurred regularly during clear sky and weak wind conditions (see also following sections). Condensation events usually started around midnight and lasted into the morning hours, in extreme cases until midday.

Additionally, some eddy correlation measurements had to be rejected due to logging failures (short data gaps) and too low sensitivity of the fast drifting ozone sensor. Table 4.3 gives an overview of the various effects and corresponding rejection criteria applied to the field data.

Tab. 4.3: Overview of rejection criteria for (a) eddy correlation and (b) profile flux measurements. The individual rejection effects are quantified separately (independent from the application of other criteria); the combined effect for the various fluxes is shown at the end.

(a) EDDY CORRELATION		quantity	rej. percentage
instrumental problems:	- logging failure (data gaps > 5 %)	all	4.4 %
	- condensation in tube ($\sigma_{\text{signal}} < 2.5$ mV)	H ₂ O	43.2 %
	- low sensor sensitivity (< 5 % of max.)	O ₃	11.8 %
methodological problems:	- extreme stability ($ z/L > 2$)	all	13.3 %
	- low wind eddy corr. ($r_{\text{uw}} > -0.1$)	all	19.5 %
total combined rejection:		H ₂ O	55.4 %
		CO ₂	24.6 %
		O ₃	35.4 %
(b) AERODYNAMIC PROFILE METHOD			
instrumental problem:	- condensation in tube (hum. > 98%)	H ₂ O	34.7 %
methodological problem:	- extreme stability ($z/L > 10$)	all	< 0.5 %

Beside the instrumental problems, there are also methodological limitations for the flux determination, which were discussed in Chapter 2 and in Sections 4.1 and 4.2. The most important one is the requirement for fully developed turbulence and the applicability of the surface layer similarity. The determining parameter is the atmospheric stability z/L (or Ri alternatively). Figure 4.25 shows the frequency distribution of z/L as determined by the aerodynamic profile method. The limitation in the unstable range was not important in the present case, because no extremely unstable conditions occurred. On the other side, the distribution is extremely 'long-tailed' in the stable domain. The application of the eddy correlation method was limited to $z/L < 2$ leading to a considerable rejection percentage of 13.3 %. With the extended similarity functions presented in Section 4.2, the profile method experienced almost no rejection.

An additional indicator for the existence of fully developed undistorted turbulence is the correlation coefficient between the horizontal and the vertical windspeed component r_{uw} . KF94:20 give an average value of -0.35 ; data were rejected if $r_{\text{uw}} > -0.1$. Positive or near-zero values may be caused by flow distortion (sensor head, tower assembly or nearby obstacles) or non-stationarity effects. They mainly become important under low wind conditions as illustrated in Figure 4.26. Beside the main influence of the windspeed, a secondary dependence on the wind direction (east-north-east: mast and container) but no significant effect of stability could be observed.

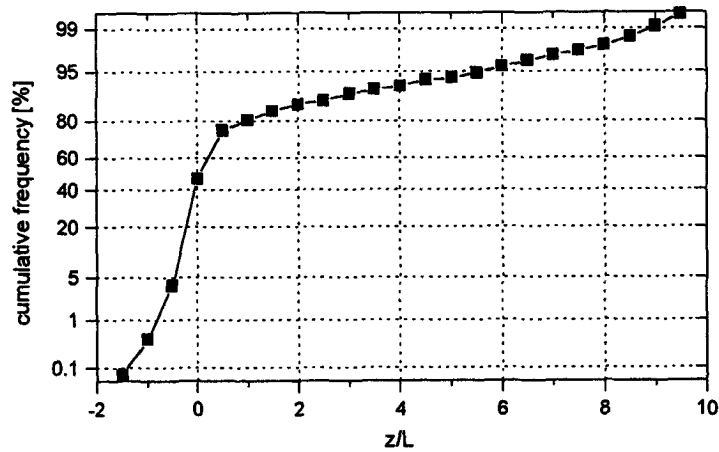


Fig. 4.25: Cumulative frequency distribution (ogive) of the stability parameter z/L determined by the aerodynamic profile method for the whole field campaign.

The fetch condition (depending on wind direction), which is especially important for the applicability of the profile method (cf. Section 2.6.1) is not used here as a rejection criterion, because there exists no generally accepted detailed rejection model and thus the effect of inhomogeneous source areas on the different trace gas fluxes will be analysed in the following. The final flux datasets with all rejection criteria applied are plotted as time series in Appendix B together with some important micrometeorological parameters. The flux results of the REA method, which are also displayed there, will be discussed in Chapter 5.

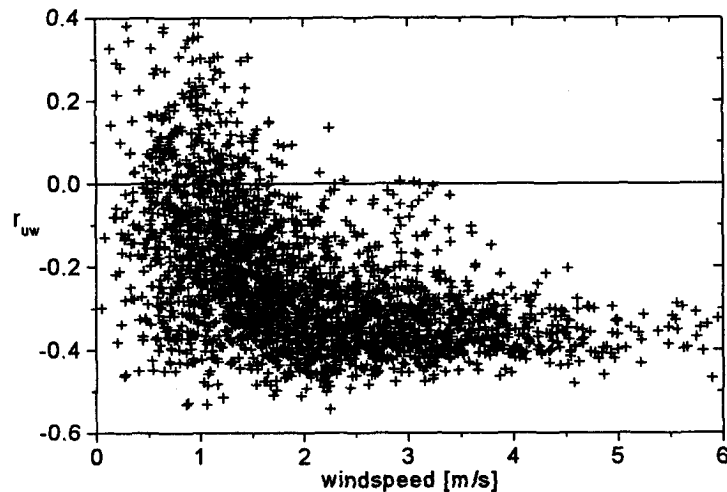


Fig. 4.26: Dependence of correlation coefficient r_{uw} (measured by sonic anemometer) on windspeed.

4.3.2 Theoretical Uncertainty of Finite Turbulence Measurements

Measured eddy correlation fluxes represent an average covariance over a time interval T_a . This implies a statistical uncertainty of the estimate due to finite sampling. The uncertainty is also influenced by the assumption of ergodicity and the Taylor hypothesis (see Section 2.3.1), because a temporal average at a fixed point instead of an ideal ensemble average is performed. Due to the autocorrelation of the turbulence time series, the individual fast response measurements are not independent of each other, and thus the number of degrees of freedom is effectively lower than the actual number of samples. This effect is described by the integral time scale τ_x (for a given atmospheric quantity x), which is determined by the

corresponding turbulence spectrum. It can be directly related to the peak frequency or peak wavelength of the spectrum (KF94:44/63):

$$\tau_x \approx \frac{1}{6.3 \cdot (f_{\max})_x} = \frac{(\lambda_{\max})_x}{6.3 \cdot \bar{u}} \quad (4.35)$$

The peak wavelength for the vertical windspeed $(\lambda_{\max})_w$, scaled with the height z , is determined by a similarity function of z/L (cf. Kaimal et al., 1972). With the resulting time scale τ_w , the relative error of a scalar eddy correlation flux F_c due to limited sampling can be estimated according to Lenschow et al. (1994) as:

$$\frac{\sigma(F_c)}{|F_c|} \leq \frac{2}{|r_{wc}|} \sqrt{\frac{\tau_w}{T_a}} \quad (4.36)$$

The value of the time scale is most unfavourable under unstable conditions with low windspeed, when the peak frequency is lowest. Extreme conditions observed in the Bellheim experiment (see Fig. 4.27) were $z/L = -0.8$ and $\bar{u} = 1 \text{ m s}^{-1}$ corresponding to $\tau_w \approx 3 \text{ s}$. With $T_a = 1800 \text{ s}$ and $r_{wc} \approx 0.4$, this results in an maximum relative error of about 20%. For neutral and positive stability or higher windspeed, the error becomes smaller but is always over 5%. Since the described effect basically represents the spatial and temporal variation of the turbulent flux, it presumably applies in a similar way for the profile technique and other surface layer methods. However, it is not clear, whether the effect is quantitatively the same for simultaneous measurements at the same location.

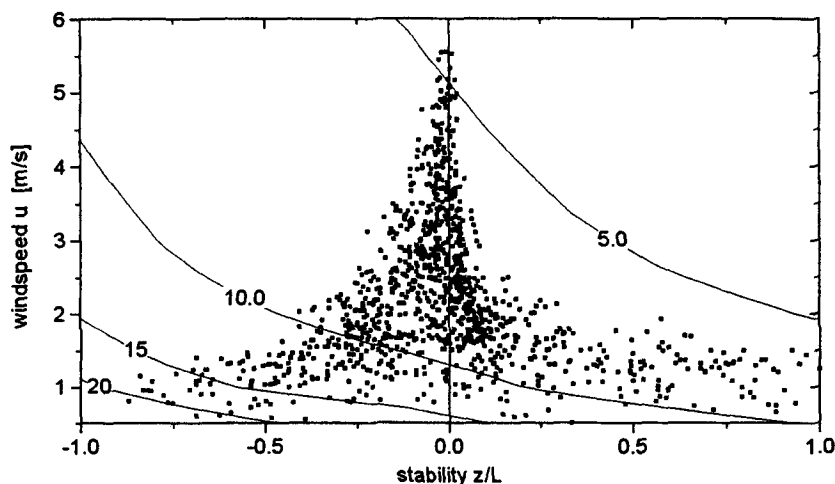


Fig. 4.27: Isolines of random error (%) of flux measurements due to finite temporal sampling, dependent on windspeed u and stability z/L . The scattered points indicate the connection between windspeed and stability (for $z = 3.35 \text{ m}$) as observed in the Bellheim experiment.

The described effect represents a general source of uncertainty for turbulent flux measurements, that can not be avoided or substantially reduced, unless very long averaging times are applied. However, averaging times much longer than about 30 min would lead to a considerable loss of information (considering the usually pronounce diurnal flux variations) and are therefore hardly useful for most studies. All other error sources discussed in the following paragraphs are therefore only relevant, if they are comparable or larger in magnitude relative to this general uncertainty.

4.3.3 Instrumental Noise and Measurement Resolution

Every sensor is affected by a certain level of instrumental noise, which is represented by the fluctuation of the output signal for a totally constant input. The variations can often be considered as uncorrelated (ideal 'white' noise), i.e. each individual value is totally independent from the neighbouring ones. Hence, the error effect on the trace gas flux can be estimated based on simple error propagation laws. In all micrometeorological techniques, the noise effect of the wind sensors is usually negligible compared to the trace gas detection noise.

Eddy Correlation Method

For the eddy correlation method, Lenschow and Kristensen (1985) give the following expression for the effect of an analyser noise level $\sigma(\mu_c)_{\text{noise}}$ on the measured flux:

$$\sigma(F_c) \approx \sigma(w) \cdot \sigma(\mu_c)_{\text{noise}} \sqrt{\frac{\Delta t}{T_a}} \quad (4.37)$$

This error has an absolute rather than a relative characteristic (in contrast to Eq. 4.36) representing an effective detection limit for the flux measurement. The factor $\sigma(w)$ mainly depends on the atmospheric stability with largest values in the unstable range. In the Bellheim experiment, typical $\sigma(w)$ values for unstable and neutral conditions were about 0.4 m s^{-1} ; for stable situations they were generally smaller. The noise level $\sigma(\mu_c)_{\text{noise}}$ of the trace gas sensor depends on the sampling interval Δt . For the CO_2 measurements, it was determined (by test measurements with a constant concentration) to about 0.4 ppm with $\Delta t = 0.1 \text{ s}$. Thus for an averaging time $T_a = 30 \text{ min}$, Equation 4.37 yields a flux error (1σ -detection limit) of about $0.05 \mu\text{mol m}^{-2} \text{ s}^{-1}$. This is very small compared to the observed flux range of $-20 \dots +10 \mu\text{mol m}^{-2} \text{ s}^{-1}$ (see Appendix B). For H_2O and ozone, the relative effect is similar or even smaller and thus may be neglected in practice. Of course a certain number of flux values, especially during nighttime, may be close to zero resulting in an relative error of 100% or more. However, for these cases the relative error is hardly relevant, but the flux results are significant as absolute values, i.e. compared to other values in the diurnal cycle and concerning the contribution to daily or longterm totals.

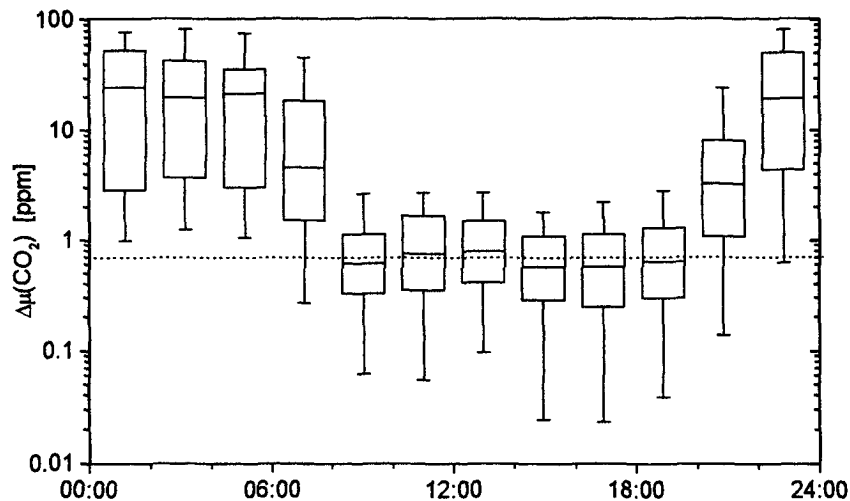


Fig. 4.28: Distribution of absolute profile difference of the CO_2 concentration dependent on the time of day for the whole measurement campaign, displayed as boxplots (for explanation see Appendix C). The dotted line represents the maximum error limit due to digitalisation.

Profile Method

For the profile measurements of H₂O and O₃, the random noise is smoothed out by averaging over 30 min to a similar degree like for the eddy correlation method. It thus can be generally neglected compared to the finite sampling error described in Section 4.3.2. Though, for the CO₂ measurements it was already mentioned that the digitalisation had a very low resolution of only about 1.4 ppm. According to Lenschow and Kristensen (1985), digitalisation noise has a similar effect as ideal white noise, if the quantisation step is small compared to the natural variations. But in the present case, the observed CO₂ profile differences are often well below 1 ppm especially during daytime (see Fig. 4.28). In the extreme case, only one discrete value is produced for the whole averaging interval resulting in a mean absolute error of 0.7 ppm (half of the digitalisation step). This maximum error level is also indicated in Figure 4.28 by the dotted line. Under daytime conditions, about half of the measured differences are below this limit resulting in an average random flux errors of 100% or more!

4.3.4 Systematic Error Sources

A systematic error effect, which is relatively easy to quantify, is the calibration uncertainty of the trace gas analysers. Errors in sensitivity (span) and linearity propagate proportionally to the flux results for both eddy correlation and profile methods. Errors in the offset have only an indirect influence as far as they affect the span. For the EC-LICOR as well as for the profile analysers, the effect of (local) non-linearity is negligible and the variation (drift) of the span was generally below 5%. For the fast response ozone sensor, the situation is somewhat worse. The fast drift in sensitivity (see Fig. 3.17) did not allow a very accurate estimation of the offset (uncertainty ca. ± 5 mV). The induced relative error of the sensitivity depends on the ozone concentration and on the sensitivity itself. For the worst case of the minimal accepted sensitivity of 1 ppb mV⁻¹, the relative error reaches 100% at an ambient concentration of 5 ppb, which was rarely observed even during nighttime (cf. Appendix B). For daytime concentrations of 20 - 100 ppb, the maximal resulting error is 5 - 25 %.

Beside the calibration error, there are a variety of other systematic error sources for the flux results. Some of them were already described and corrected in the course of the flux calculations. However, the correction procedures are based on idealised assumptions and may not always be fully appropriate:

- Trends (EC) in the time series have an absolute error characteristic not proportional to the turbulent flux. They were corrected by linear detrending (for 10 min intervals). The remaining error due to non-linear trends ('red noise') may be of the same order of magnitude like the correction effect described in Section 4.1.2.
- Correlated density variations (EC and profile) have also an absolute error characteristic and were accounted for by integral correction of the covariance (Webb-correction). The remaining error is assumed to be significantly smaller than the correction effect described in Section 4.1.4.
- High frequency damping (EC) has a relative error characteristic (proportional to turbulent flux) and was corrected by a spectral model. The remaining error is assumed to be significantly smaller than the correction effect described in Section 4.1.5. In the accepted range of stability, the relative correction was always below 50%.

Other uncorrected systematic effects can only be treated by more or less coarse checks and rejection criteria:

- Errors due to chemical reactions with NO_x affect the ozone profile measurements (Lenschow and Delany, 1987; Vila-Guerau de Arellano and Duykerke, 1992). However, for non-urban environments, the effect on the flux is usually less than 10% (Güsten and Heinrich, 1996).
- Extreme cases of EC sonic flow distortion were identified and rejected by correlation coefficient $r_{uw} > -0.1$ (see Section 4.3.1)

The profile technique is generally most sensitive to systematic deviations of the different profile levels. In the present case, systematic effects for the trace gas profiles were mostly avoided by the special setup of the analysing systems (see Sections 3.2.1 and 3.2.2). However very small differences in pressure or temperature are sometimes difficult to identify but may still have a significant effect on the flux results.

4.4 Environmental Conditions and Flux Results

The field measurements described in Chapter 3 and the calculation procedures described in the preceding sections, yielded a considerable flux dataset, which is entirely displayed in Appendix B. In the following, the results are summarised and illustrated with exemplary case studies. For an appropriate interpretation and verification of the flux results, detailed information about the environmental conditions are necessary. Therefore, the behaviour and influence of general weather conditions (i.e. radiation, wind direction) as well as the local stability and ambient trace gas concentrations are presented and analysed in connection to the flux results.

4.4.1 General Weather Conditions

The synoptic or mesoscale weather conditions during the field campaign are characterised in Figure 4.29 by the daily means of global radiation, rainfall, wind direction and barometric pressure. Two typical weather situations can be identified: (a) south-westerly wind periods (SW) connected with the passage of a low pressure system, with reduced global radiation due to cloud cover and significant rain events; (b) north-easterly (NE) wind periods connected to high pressure systems and usually clear sky conditions with high irradiation.

The values plotted in Fig. 4.29 are daily averages (or totals) and therefore yield only limited information about the behaviour of the respective parameters. Many meteorological quantities show characteristic diurnal variations driven by radiation effects. Figure 4.30 displays the diurnal variations of a typical SW and NE day respectively. The incoming solar radiation in the SW case is very non-stationary indicating a fractional (and probably moving) cumulus type cloud cover. The windspeed is comparatively high ($2 - 4 \text{ m s}^{-1}$), but also shows considerable fluctuations. However, the wind direction is fairly stable during the whole day. The NE case exhibits an almost contrary behaviour. The radiation curve is smooth and undisturbed indicating a perfect sunny day. The windspeed is low but rather stationary; it reveals a clear diurnal variation which is less significant in the SW case. The wind direction in Fig. 4.30b goes through a specific diurnal cycle, changing between almost opposite directions. The resulting daily average displayed in Fig. 4.29 shows a north-easterly value, because it was calculated as a vector average of the horizontal windspeed and thus predominantly represents the wind direction during day-time when the windspeed was usually higher than during night.

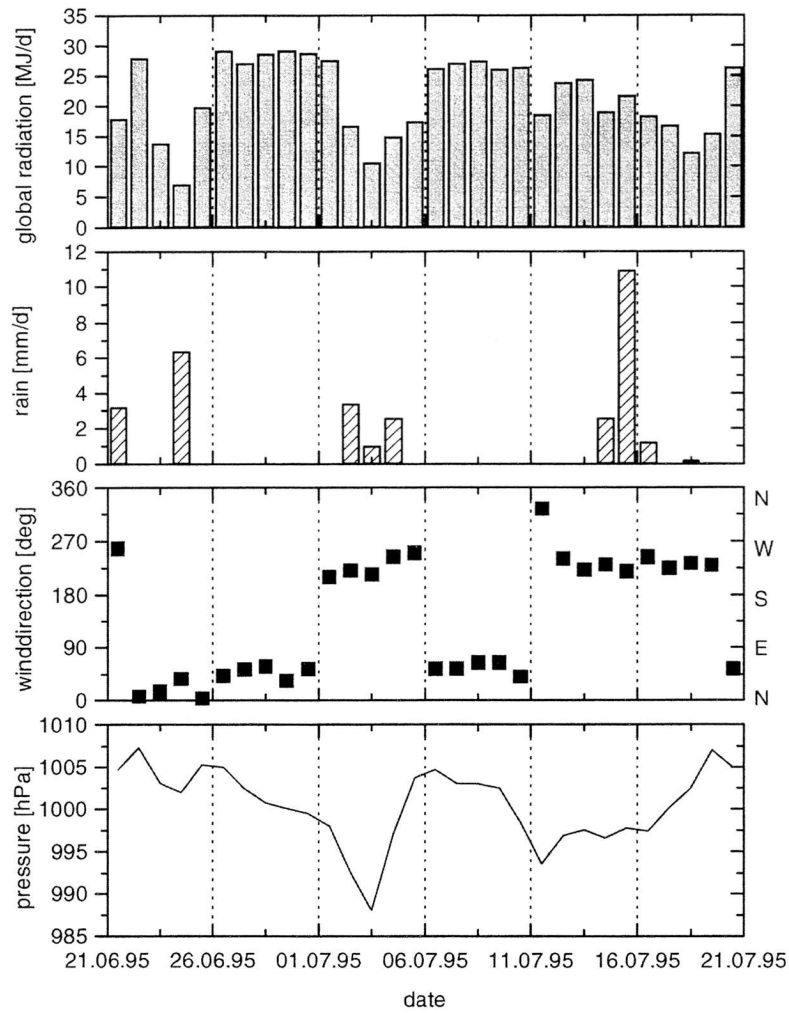


Fig. 4.29: Daily means or totals of (a) global radiation, (b) rainfall, (c) wind direction and (d) barometric pressure during the Bellheim '95 campaign.

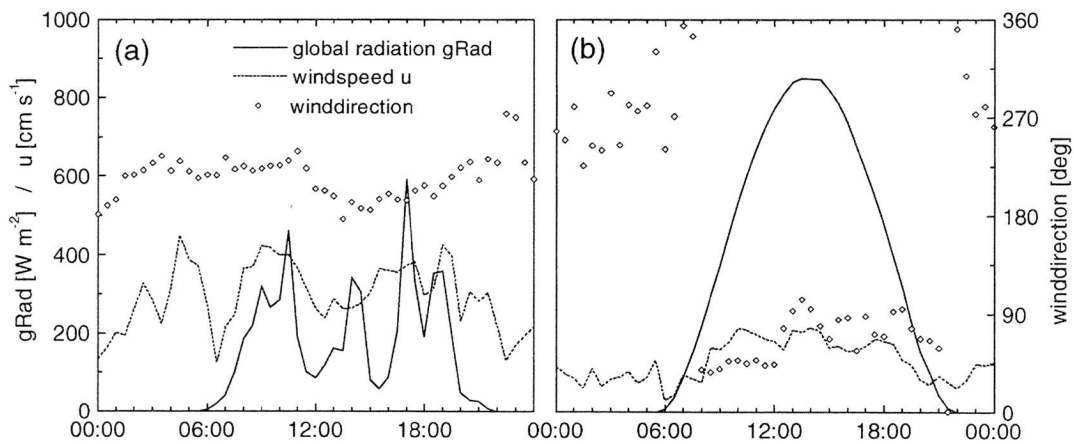


Fig. 4.30: Diurnal variation of global radiation, windspeed and wind direction on two exemplary days: (a) 3 July 95, SW situation; (b) 7 July 95, NE situation.

The marked diurnal cycle of the wind direction is characteristic for all NE (high pressure) cases and can be interpreted with the help of tethered balloon soundings (Sprung et al., 1996). In Figure 4.31 the wind direction at the surface and at 300 m above ground are plotted for a 6-days period from 4 July to 10

July 1995. The soundings are only available for nighttime, but they represent more or less the geostrophic mesoscale flow. During SW wind conditions (4/5 July), the wind direction near the ground does not show a significant deviation from the mesoscale wind direction. In NE mesoscale flow, however, the wind direction near the ground turned to north or often even to south-west and thus created a local counter-current flow. This happened mainly during nights when the windspeed was very low leading to an extremely stable stratification and a very shallow (or even non-existent) nocturnal boundary layer. Accordingly, the turning of the wind direction (counter flow) was usually limited to less than about 50 m above ground.

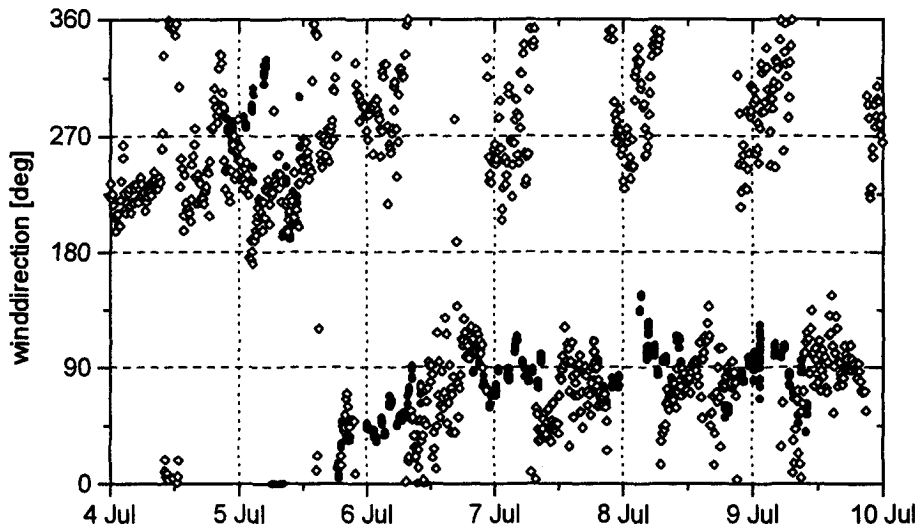


Fig. 4.31: Comparison of wind direction near the surface (open diamonds) and at 300 m above ground (solid circles) determined by tethered balloon soundings.

The counter-current flow may be explained by topography induced airflow (e.g. drainage flow) within the Rhine valley, which shows up only if the near surface layer is decoupled from the higher layers and thus from the geostrophic flow. A similar behaviour of nighttime counter-current flows in the Rhine valley is reported by Kalthoff and Vogel (1992) for the Karlsruhe region. However they observed a turn of wind direction from south-east (geostrophic) to north (surface). They explained their observations with the friction-caused 90° -turn of the geostrophic wind direction in the NBL and the strong channeling effect of the local topography.

4.4.2 Source Area and Fetch Conditions

Due to the varying wind direction during the field experiment, the trace gas exchange of different surface areas and vegetation types was measured by the flux systems. Beside the direction of the observed source areas, also their distance and size is important for the interpretation of the flux results and the comparability of different methods. The source area position and dimensions may be quantified in terms of probability by an integration of the corresponding flux or scalar source weight function (or 'footprint', cf. Section 2.6.1). In the following, the 50 % source area concept as defined by Schmid (1994) is used to interpret the flux results. For profile methods, no direct source area for the determined flux is defined; each level of the scalar profile has its own footprint. Figure 4.32 shows exemplary cases of 50% source areas of the EC and upper profile measurements for the most frequent south-westerly wind direction. The size and distance from the sensor depends strongly on the stability. EC flux source areas lie within

the triticale field for unstable neutral and moderately stable conditions. Source areas for scalar quantities (i.e. concentration profile measurements) are significantly larger for the same measurement height and may exceed the triticale field even under neutral conditions. The source areas for the lower profile levels (not displayed in Fig. 4.32) are considerably smaller.

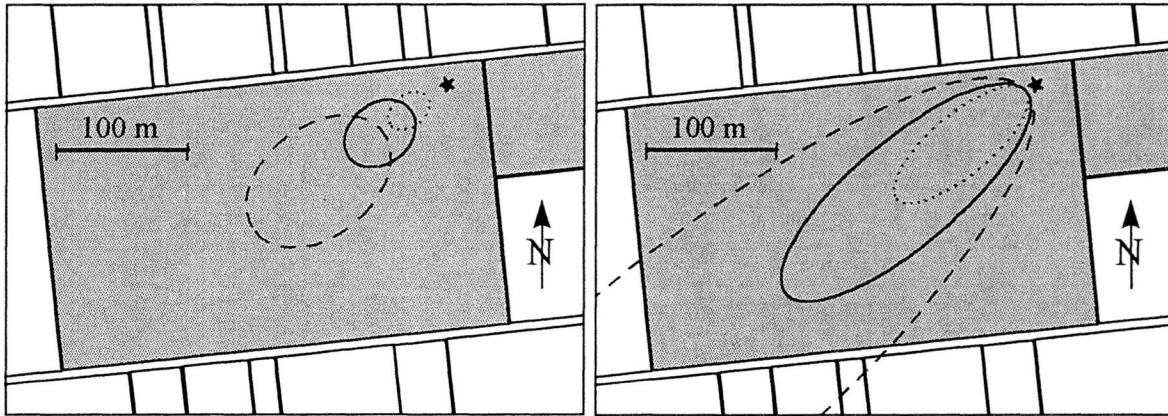


Fig. 4.32: 50% source areas for SW wind direction (triticale field) for (a) eddy correlation measurements and (b) highest profile measurement; moderately unstable ($z/L = -0.2$), — neutral ($z/L = 0$), - - - moderately stable ($z/L = +0.2$).

A general overview over the dimensions of the source areas for the relevant sensors and their dependence on stability is given in Figure 4.33. The EC flux source area is only given up to $z/L = +0.1$ due to numerical problems (cf. Schmid, 1994). It is generally smaller by a factor of about 2 - 3 in comparison to the corresponding scalar source areas (upper profile level). The far end distance of the lower profile level is about 6 times smaller compared to the upper level. While the 50%-source-area for the scalar profiles starts always very close to the measurement tower (< 10 m, not indicated in Fig. 4.33), the near end of the flux source area increases also considerably with stability (see also Fig. 4.32).

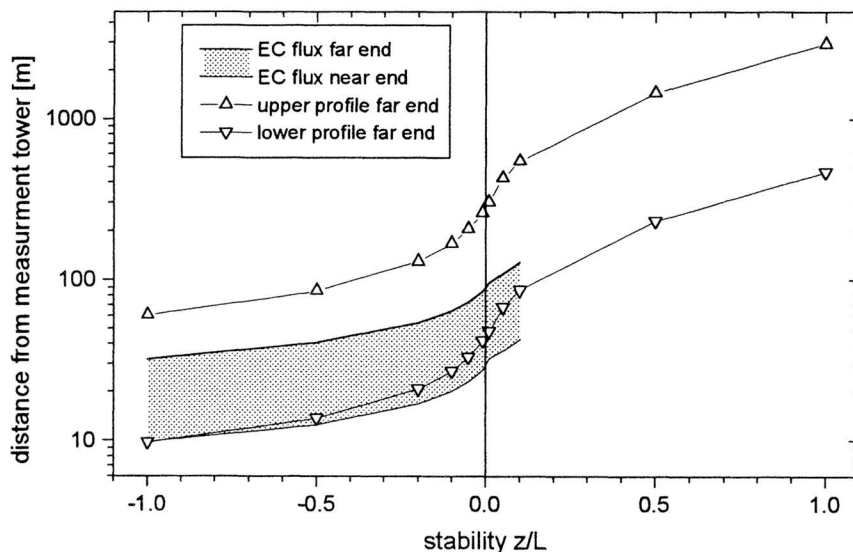


Fig. 4.33: Far (and near) distance of the 50% source area for eddy correlation flux measurements (at 4.25 m) and for the highest (4.25 m) and lowest (1.65 m) scalar profile as a function of stability (after Schmid, 1994).

For a quantitative comparison of the source area dimensions, with the given vegetation pattern at the Bellheim site, the fetch length of the triticale field is plotted in Figure 4.34b against the wind direction. For convenience, the x-Axis starts with 90 deg (easterly wind). In the south-westerly sector, the fetch length of the triticale field is highest: between 180 and 350 m. This is mostly sufficient for the EC fluxes and also for the profile method under unstable conditions. For other wind directions, there is a considerable influence of the surrounding agricultural plots that were mainly in the growing state in contrast to the senescent triticale field. Between 80 and 170 deg, the fetch is generally larger than 100 m. This might be still sufficient for EC but not for profile measurements except for extremely unstable situations. For wind directions around north (360 deg), the triticale fetch is very small: only about 15 m for the EC/REA tower including the road (see also Fig. 3.4). Since the EC source area starts at a distance of 10 m or more from the tower, the triticale has almost no influence on the EC flux measurements in this sector and the fluxes are predominantly representative for the growing sugarbeet or the neighbouring fields. For the profile method, limited fetch conditions are always problematic, because the source areas always start very close to the measurement tower, and the influence on the lower and upper profile level are generally different.

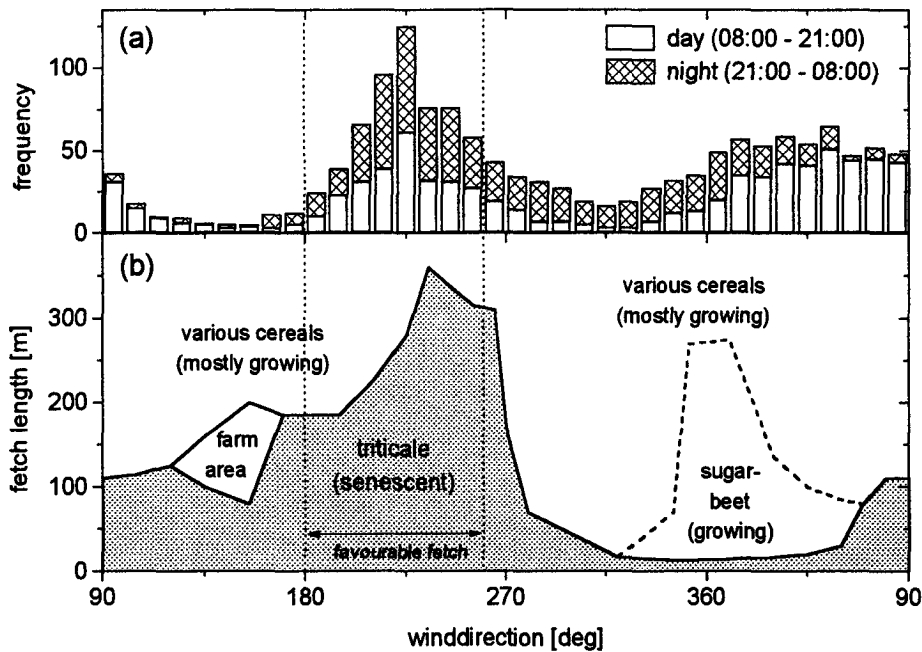


Fig. 4.34: (a) histogram of wind direction; (b) fetch distances vs. wind direction.

Considering the entire fetch situation at the Bellheim site, the wind direction range between 180 and 260 deg is declared as 'favourable fetch condition' (cf. Fig. 4.34). This sector will be used in the following for various comparisons and verification procedures. It contains the peak frequency of wind directions, which occur about half and half during daytime and nighttime. The measured trace gas fluxes in this sector are meant to be representative for the triticale field. According to the boxplots displayed in Figure 4.35, they are significantly different from the fluxes of other wind directions and thus of the surrounding plots. The largest difference is observed for the CO_2 exchange. It is bidirectional for the triticale with emphasis on the positive side (respiration), but predominantly negative (assimilation) for the other crops, which were mainly in the growing state. The difference for the water vapour and ozone fluxes is less significant. However they tend to be smallest for the triticale field. The gaps in Figure 4.35 are due to very few cases (<10) in the respective sectors, that did not allow to draw a representative value range.

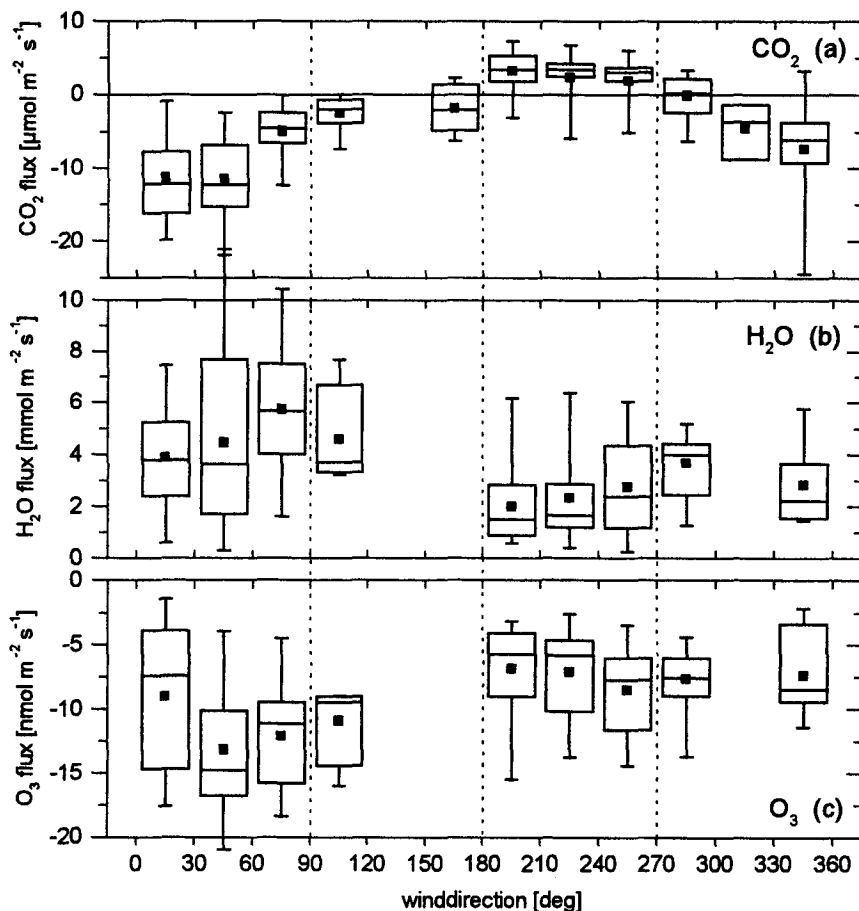


Fig. 4.35: Overview over trace gas flux results for (a) CO_2 , (b) H_2O , and (c) O_3 dependent on wind direction; the distribution of values within each class is indicated by a boxplot (description see Appendix C).

4.4.3 Senescence Development of the Triticale Field

The flux exchange characteristic of the triticale field was not only different from the surrounding area (Fig. 4.35), it also changed considerably during the measurement campaign. This development is illustrated in Figure 4.36 by the flux measurements on two days with SW wind conditions, the first in the middle and the second at the end of the measurement campaign. The two chosen days have comparable radiation conditions, both strongly affected by fractional cloud covers. In the first case, the main part of the energy gain at the surface (net radiation) is converted into latent heat by transpiration of the triticale plants. This leads to a very low or even negative Bowen ratio with values between -0.4 and $+0.7$. In the second case, the water vapour (latent heat) loss is comparatively small. The net radiation is predominantly converted into sensible heat, which is illustrated by high Bowen ratio values of 1 - 4.

An even more drastic change is observed for the CO_2 flux. For the daytime period, it reverses the direction from negative (net assimilation) to positive (net respiration). In the second case (17 July) the CO_2 emission is almost constant during the whole day, meaning that the assimilation activity had totally ceased. The ozone fluxes show general deposition for both days, but also with a significant decrease in magnitude. The behaviour is very similar (with opposite sign) to the water vapour flux.

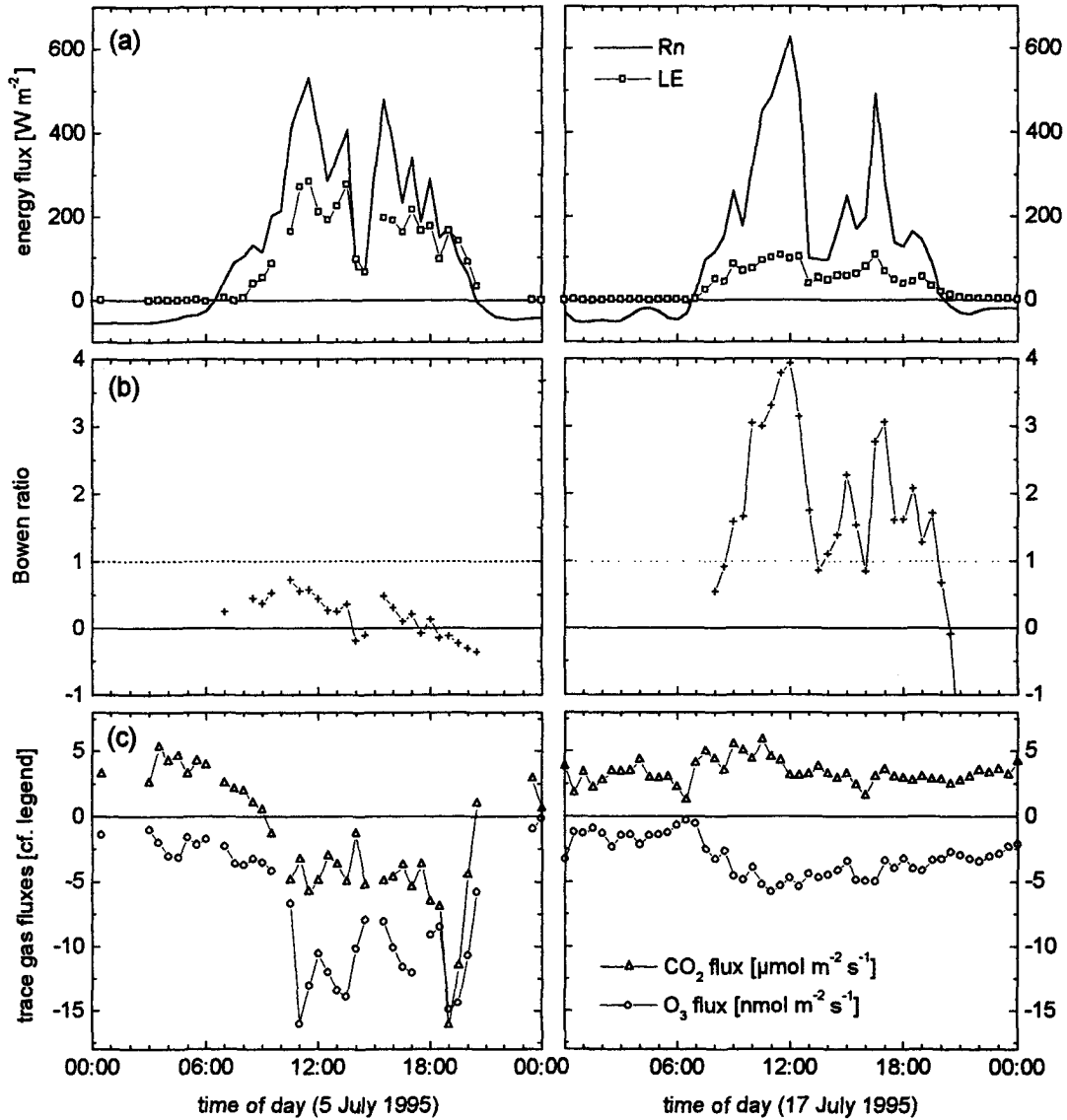


Fig. 4.36: Comparison of eddy correlation fluxes and microclimatological conditions of the triticale field between early (5 July 95) and late senescence (17 July 95): (a) net radiation flux R_n and latent heat flux LE ; (b) Bowen ratio $\beta = H/LE$; (c) trace gas fluxes of CO_2 and O_3 .

The development of the net ecosystem exchange measured by the micrometeorological methods can be interpreted considering the leaf scale exchange. The metabolic activity of the leaves was checked by porometry (leaf chamber measurements, cf. Busch et al., 1997) and by measurements of the plant water content (Fig. 3.3b). Figure 4.37 gives a survey over the periods for which transpiration activity was observed at the different leaf levels. While the flag leaf (L1) remained alive and active nearly until harvest, the lower leaves turned from green to yellow and dried out one after the other during the measurement campaign. Due to gaps in the porometric measurements, the end of activity could not always be dated very accurately. Especially the contribution of the ear causes some uncertainties. According to Denmead (1976) and Bort et al. (1994), the ears of cereals (as long as physiologically active) should be considered as active plant parts. However, for the present case, no direct exchange measurements of the ear were made and the end of the activity could be estimated only very roughly. According to Fig. 4.37, the two uppermost leaves were definitely active on 5 July, whereas on 17 July only the flag leaf possibly remained active. The strong decrease of transpiration (by a factor of about 3) at comparable radiation conditions can be explained by the much larger leaf area of the second leaf level (cf. Fig. 3.3a). The

decrease of the active leaf area may also explain the observed reduction of ozone deposition in Fig. 4.36, because it is mainly attributed to stomatal uptake (see e.g. Leuning et al., 1979).

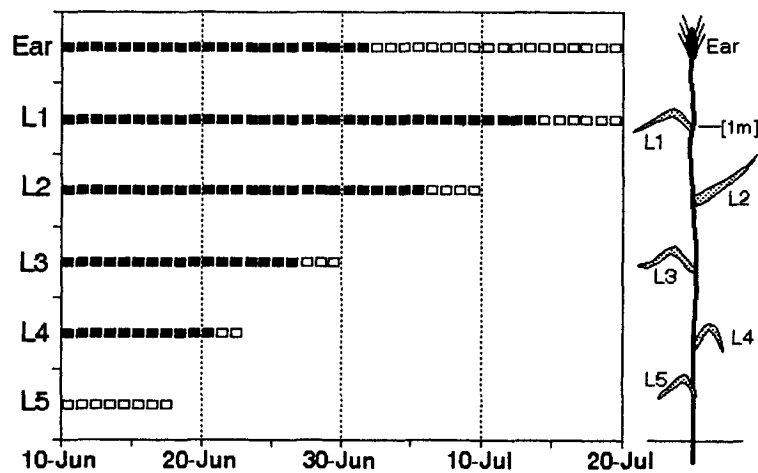


Fig. 4.37: Periods of metabolic activity (transpiration) at the different leaf levels of the triticale canopy (cf. Busch et al., 1997); solid squares signify full activity, empty squares signify partial or uncertain activity (lack of information).

The decrease of evaporation and the consequent increase of the Bowen ratio is represented also in the temperature excess of the canopy relative to the ambient air temperature. Figure 4.38 shows the development of the temperature difference for maximum solar radiation during the measurement campaign. The canopy temperature was calculated from the longwave upward radiation flux as described in Section 3.5.1. In the first part, the strong transpiration was able to cool down the leaves below ambient temperature. However, with progressing senescence the leaf area available for transpiration decreased and the radiative energy input could no longer be carried off as latent heat. Consequently the leaf temperature and the sensible heat loss to the ambient air increased. This development is important not only in relation to plant physiology, but it also has an influence on the atmospheric stability and thus on the turbulence structure over the triticale field.

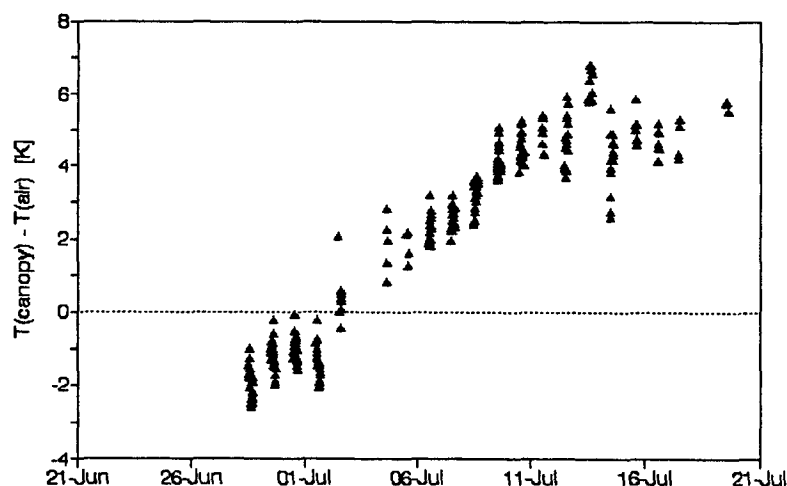


Fig. 4.38: Temperature excess of the triticale canopy (derived from thermal radiation) compared to ambient air temperature under high light conditions (global radiation above 750 W m^{-2}).

The transpiration activity of the triticale leaves displayed in Fig. 4.37 should not be considered as representative for the assimilation activity as well. The CO_2 exchange depends much more on the light conditions and also on the chlorophyll content of the leaves, which underwent a fast degradation (yellowing) during the senescence. Figure 4.39a shows, that already at the beginning of the field experiment, only the first two leaf levels were assimilating, whereas the lower ones were almost inactive or respiring during daytime. The assimilation rate of the flag leaf decreased relatively fast with developing senescence (Fig. 4.39b), much faster than the respective transpiration activity. Thus at the end of the campaign (see e.g. 17 July in Fig. 4.36), the net CO_2 exchange represented mainly the respiration of the soil, which was fairly constant during the whole day.

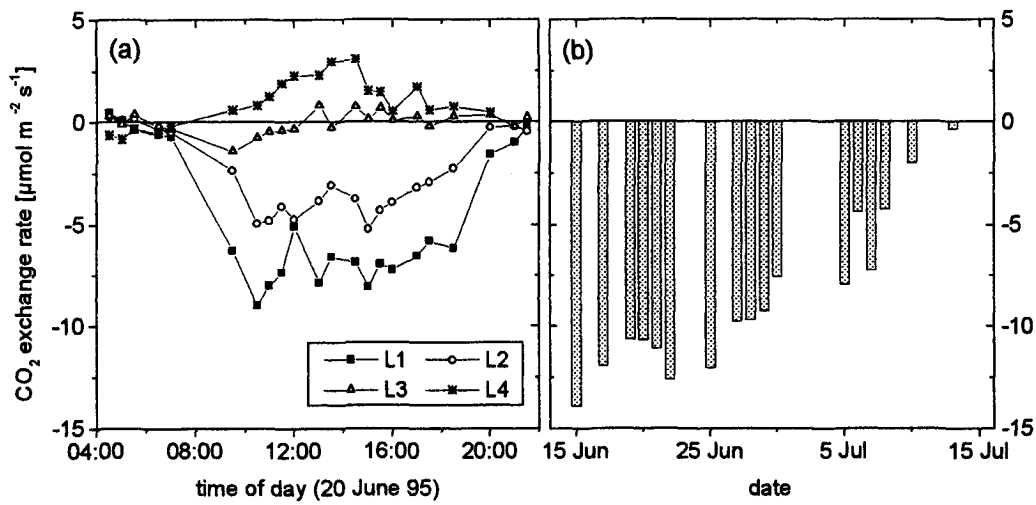


Fig. 4.39: Leaf level CO_2 exchange rates of the triticale canopy: (a) different leaf levels of one stalk on 20 June; (b) daily maximum assimilation of several flag leaves during the entire observation period (after Busch et al., 1997).

4.4.4 Diurnal Variation of Fluxes and Concentrations

In the preceding sections, the strong influence of the type and state (growing, senescent) of the source area vegetation on the trace gas exchange was demonstrated. It was also shown that the trace gas exchange of the investigated agricultural fields usually shows a distinct diurnal variation. The emission and uptake characteristics of the vegetation are strongly connected to the metabolic activity, which is controlled by environmental parameters (light, temperature, humidity). However, beside this biological mechanism, the atmospheric conditions also have a direct (physical) effect on the trace gas exchange. The turbulence structure and intensity regulates the vertical transport (supply, dispersion) inside and above the vegetation, and the ambient concentration determines the diffusion potential for the respective trace compound.

For trace gases like ozone, which show an absolute deposition, the various influences on the flux can be quantitatively described by the simple resistance model presented in Section 2.1.3. It implies a negative proportional dependence on the ambient concentration (Eq. 2.7), which defines the deposition velocity v_d . Figure 4.40 shows the diurnal variation of the ozone flux together with the ambient concentration and calculated deposition velocity during the whole measurement campaign. Both parameters $\mu(\text{O}_3)$ and v_d vary by about one order of magnitude in the diurnal course and therefore contribute to the observed flux variation to a similar degree. Yet the concentration cycle shows a slight positive and the deposition velocity a negative phase shift compared to the deposition flux.

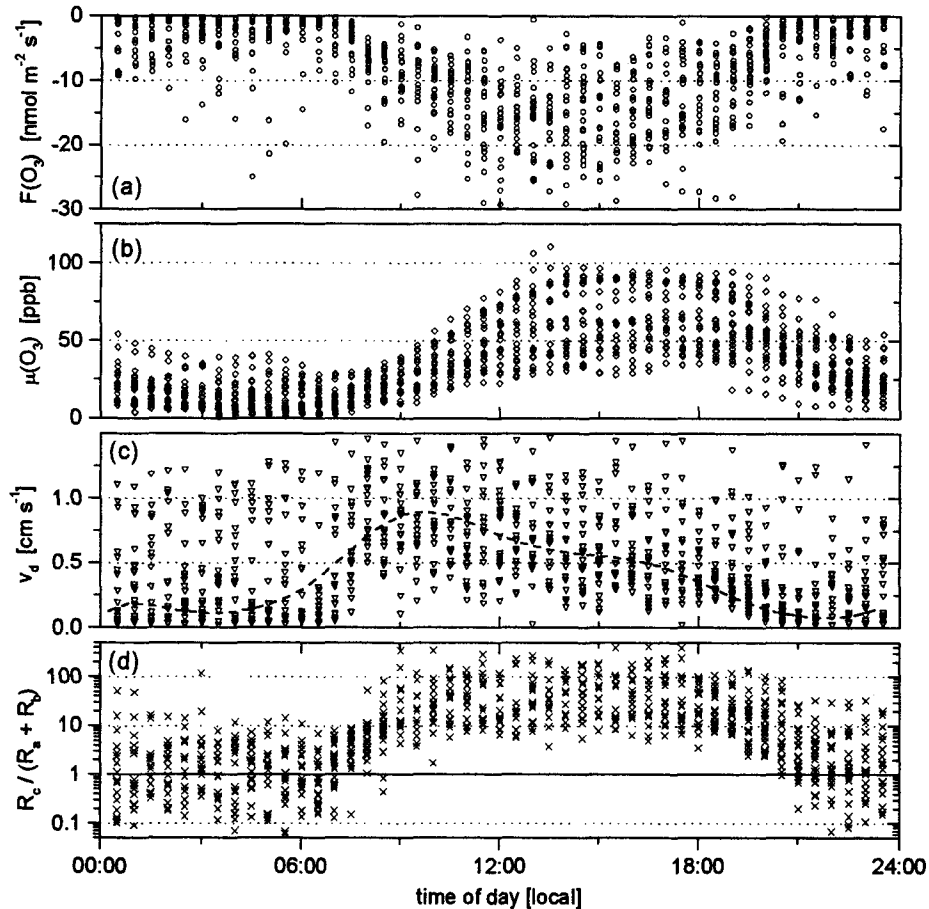


Fig. 4.40: Diurnal variation of ozone flux, ambient concentration, deposition velocity and relative contribution of aerodynamic resistance; all quantities are related to an upper level $z = 4.25$ m; the smoothed lines are polynomial regressions of 9th degree based on a logarithmic y-scale.

The magnitude of the deposition velocity depends on the transfer resistance of turbulent mixing, molecular diffusion, and surface uptake (metabolic or physico-chemical) as described by Eq. 2.7. The turbulent and quasi-laminar boundary layer resistances R_a and R_b are mainly a function of windspeed and stability and can be quantified independently based on surface layer properties (cf. Hicks et al., 1987). The surface resistance R_c is then determined as the residual term in Eq. 2.7. The relative importance of the resistances is illustrated in Fig. 4.40d. It shows that the effect of R_c is dominant during daytime, when R_a and R_b are small due to high turbulence intensity (high windspeed and unstable conditions). Consequently, the deposition is mainly limited by surface characteristics like the stomatal aperture. At night, the influence of R_a and R_b becomes much more significant because of the usually low windspeed and the stable thermal stratification. Turbulent mixing in the nocturnal boundary layer is considerably reduced and thus the ozone deposition is generally small.

Whereas the ozone flux is at least partly determined by the ambient concentration, a different behaviour is observed for H_2O and CO_2 . The water vapour mixing ratio plotted in Figure 4.41 shows only weak diurnal variations not clearly related to the course of the evapotranspiration flux (cf. Appendix B). The CO_2 concentration on the other hand follows a distinct diurnal cycle with relatively constant low values during the day and higher values with a large scatter at night. In contrast to ozone, the ambient concentration is positively correlated to the respective flux variations. This indicates, that the surface flux has an influence on the ambient concentration rather than vice versa, which can be explained by the diurnal variation of the atmospheric boundary layer (cf. Section 2.1.2). Especially during nighttime, the exchange of trace gases with higher air layers is often restricted by the limited height of the NBL.

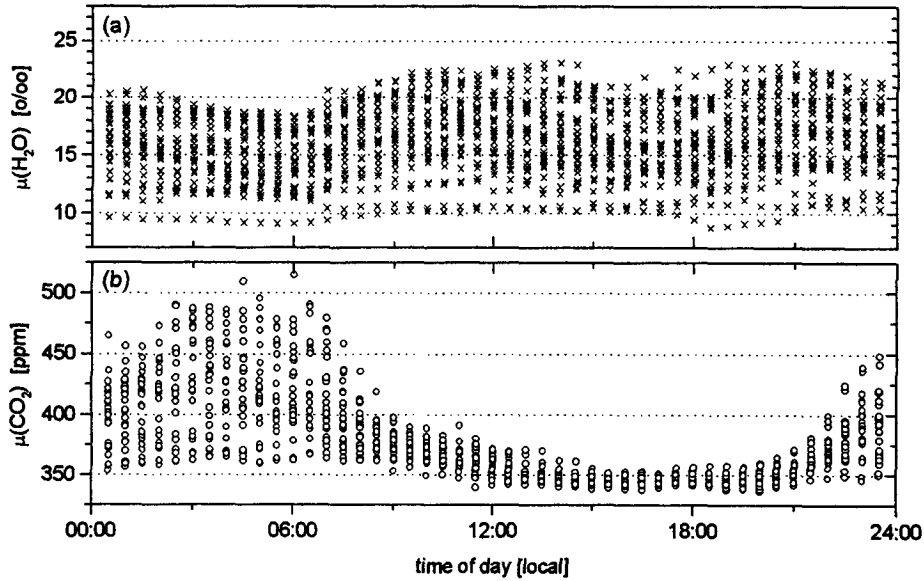


Fig. 4.41: Ambient mixing ratios (at $z = 4.25$ m) of H_2O , and CO_2 dependent on time of day for the whole measurement campaign.

Due to the generally weak turbulence and the correspondingly large concentration gradients in the NBL, a considerable part of the vertical exchange may be connected to occasional gusty turnovers (see e.g. Nappo, 1991), which are not covered appropriately by the micrometeorological flux methods. The large variation in the ambient concentration leads to non-stationary conditions as well as to a violation of the constant flux concept. For depositing species like ozone, the effect is not very problematic, because the fluxes concerned are small anyway. But for compounds like CO_2 , which are emitted by metabolic activity insensitive to the ambient concentration, the nocturnal exchange may represent a substantial part of the total surface exchange. Thus the large absolute measurement errors during nighttime can lead to considerable uncertainties in the diurnal and longterm budget of the respective compound (cf. Grace et al., 1996; Moncrieff et al., 1996; Yang et al., 1997).

5 EVALUATION OF REA METHOD

For a comprehensive investigation and validation of the relaxed eddy accumulation method, the general theoretical concept as well as practical application problems have to be studied in detail. For this purpose, several simulation studies were performed using the eddy correlation time series measured in the Bellheim field experiment. Numerical simulations based on measured high resolution time series represent a very useful way to investigate the applicability of the REA technique under various conditions and to analyse the quantitative effect of various disturbing factors. In a first step (Section 5.1) the theoretical applicability is tested by simulating an 'ideal' REA system without any technical restrictions. Yet, a real REA system applied in the field may suffer from various non-ideal effects and error sources due to instrumental limitations and environmental conditions. Their influence is investigated in a second step (Section 5.2). Based on the findings of the simulation studies, the measurements with the REA test system operated in the field are evaluated (Section 5.3).

5.1 Simulation of Ideal REA System

5.1.1 Simulation Procedure and Conditioning of Time Series

The relaxed eddy accumulation concept described in Section 2.5.3 relates the trace gas flux to the standard deviation of the vertical windspeed and the difference of the conditional mean updraft and downdraft concentrations (cf. Eq. 2.79). The theoretical applicability of this approach depends on the general behaviour of the coefficient b , which is assumed to be either constant or varying systematically in a well defined way with common turbulence parameters like z/L . In order to investigate the behaviour of the REA b -factor, it was simulated numerically using the eddy correlation time series as input. The b -factor for the various scalar fluxes was determined according to Eq. 2.80 (repeated here for convenience):

$$b_s = \frac{\overline{w's'}}{\sigma_w \cdot (\bar{s}_U - \bar{s}_D)} \quad (5.1)$$

The b -factors were simulated first for an 'ideal' REA system, i.e. a perfect conditional sampling system, that is not affected by technical problems like a finite response time, sensor tilt or a non-constant sampling flow. In order to minimise possible non-ideal effects in the eddy correlation measurements, a careful pre-conditioning of the datasets was performed. In principle, it corresponds to the correction procedures for the eddy correlation method (Section 4.1). Yet those corrections were applied mainly to the integral covariances, whereas in the present case, the entire high resolution time series had to be corrected. A survey of the conditioning and calculation steps is given in Figure 5.1. Corrections for correlated density effects (cf. Section 4.1.4) and high frequency attenuation (cf. Section 4.1.5) were not applied to the time series. This is not problematic in the first case ('Webb-correction'), because it affects the conditional mean difference $(\bar{s}_U - \bar{s}_D)$ in the same way as the eddy covariance flux (cf. Pattey et al., 1992). Thus the ratio of both quantities in Eq. 5.1 is not influenced. The effects of high frequency damping and instrumental noise (limited precision) are also assumed to be small. Yet they are more complex and will be analysed in detail in Section 5.2.

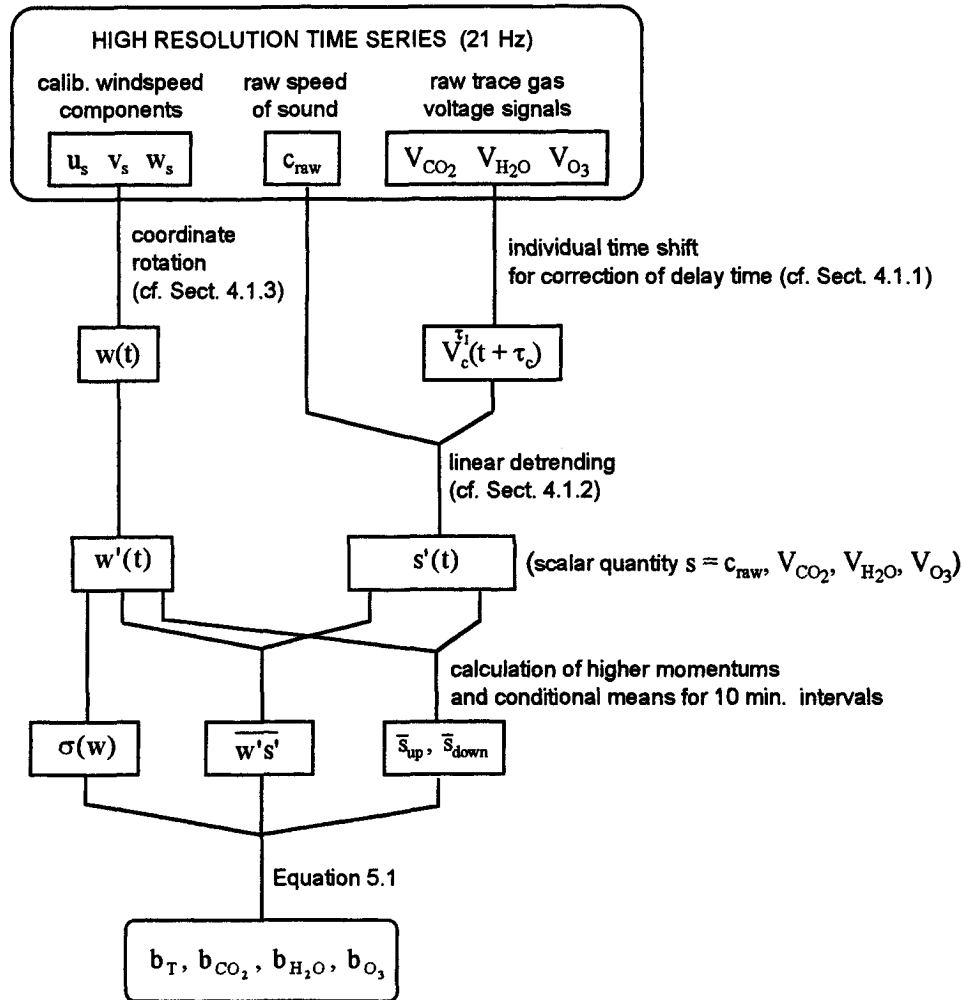


Fig. 5.1: Processing steps for the calculation of ('ideal') REA b-factors.

The procedure described in Figure 5.1 yielded b-values for the various measured scalar quantities, i.e. for temperature as well as for the concentrations of CO₂, H₂O and O₃. In order to avoid unfavourable environmental conditions, the same rejection criteria as reported for the eddy correlation method (cf. Tab. 4.3) were also applied to the REA simulations. An additional threshold rejecting small fluxes was supposed to prevent large relative uncertainties in the b-values. The threshold limits for the different scalar fluxes are listed in Table 5.1. They were chosen as about 5 % of the full range of observations.

Tab. 5.1: Rejection threshold of small absolute flux values for simulation of REA b-factors (and for the determination of correlation coefficients in Section 4.1.6).

scalar flux	range of observations	rejection threshold
$\overline{w'T}$	$-0.05\dots+0.4 \text{ K m s}^{-1}$	$\pm 0.01 \text{ K m s}^{-1}$
$F(\text{CO}_2)$	$-20\dots+10 \text{ } \mu\text{mol m}^{-2} \text{ s}^{-1}$	$\pm 2 \text{ } \mu\text{mol m}^{-2} \text{ s}^{-1}$
$F(\text{H}_2\text{O})$	$0\dots12 \text{ mmol m}^{-2} \text{ s}^{-1}$	$\pm 0.05 \text{ mmol m}^{-2} \text{ s}^{-1}$
$F(\text{O}_3)$	$-30\dots0 \text{ nmol m}^{-2} \text{ s}^{-1}$	$\pm 1 \text{ nmol m}^{-2} \text{ s}^{-1}$

5.1.2 b-Factors for Different Scalar Quantities

According to the Monin-Obukhov-similarity-theory, dimensionless turbulence characteristics like the b-factor should either be constant or depend only on the dimensionless parameter z/L within the surface layer. Thus for an overview of the b-factors calculated for the four different scalar quantities, the results are plotted in Figure 5.2 against the stability parameter z/L . The b-values for the different scalar quantities (temperature and trace gas concentrations) are all of similar magnitude roughly around 0.6. Yet, there is a considerable scatter of the individual values especially for the trace gases. In the unstable range, the average value of the b-factors is slightly below 0.6 and no systematic dependency on the stability can be observed. In contrast, in the stable range the b-values seem to increase towards higher stabilities where they take values mostly above 0.6.

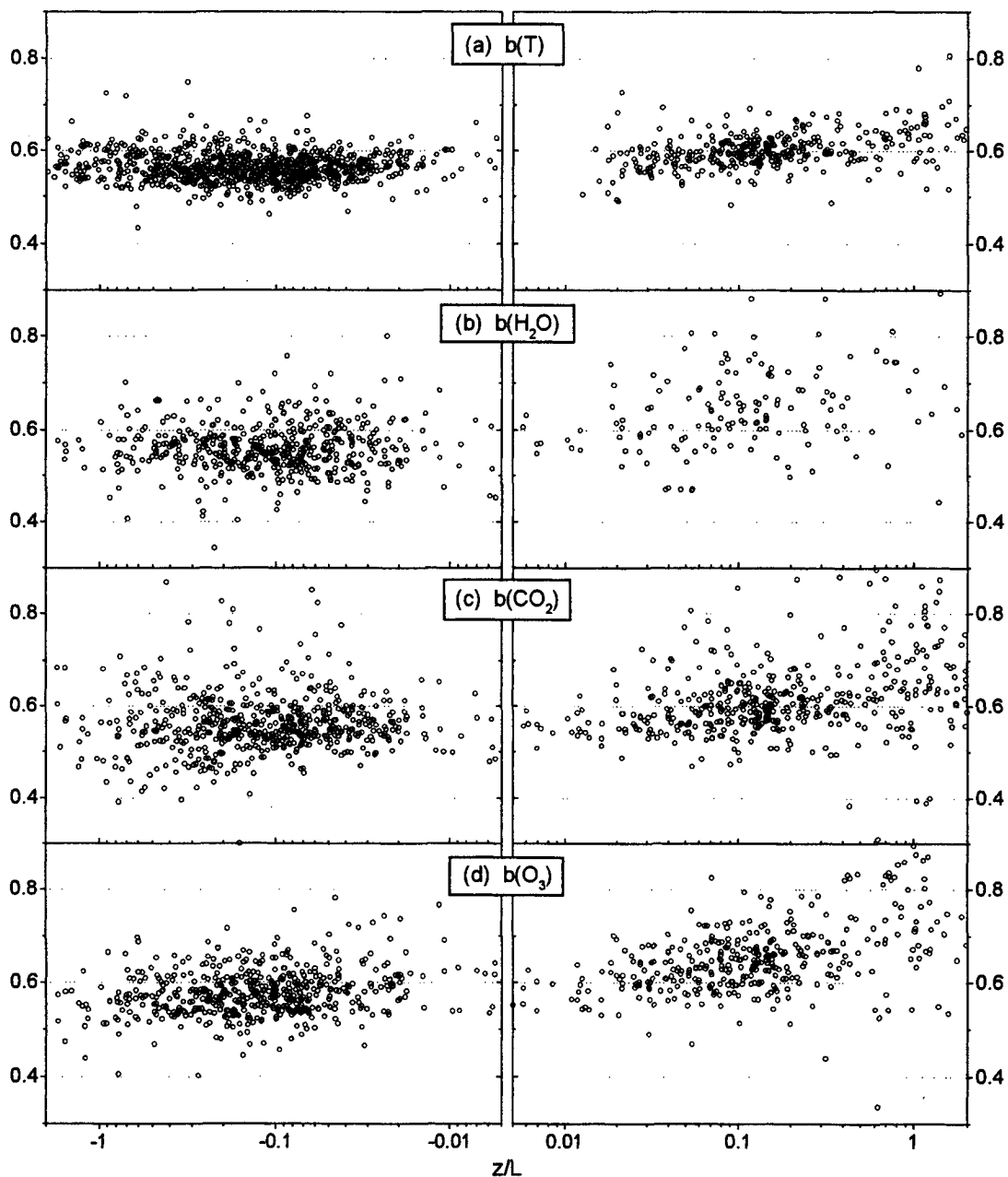


Fig. 5.2: *b*-factors derived from measured EC time series plotted against the stability parameter z/L for various scalar quantities: (a) temperature: $n = 1421$; (b) H_2O : $n = 1067$; (c) CO_2 : $n = 662$; (d) O_3 : $n = 944$; (n = no. of 10 min samples).

For a more quantitative overview, statistical parameters of the sample distributions are compiled in Table 5.2. In order to minimise the effect of extreme values (outliers), the median and inter-quartile range instead of the arithmetic mean and standard deviation is given. According to the observed systematic variations, the stability range was divided into 5 classes: one class for the unstable conditions and four classes for stable conditions. For the water vapour, only few values in the stable range are available. They were therefore pooled into a single class.

Tab. 5.2: Median and inter-quartile range of b-factors for various scalar quantities; data were classified to the five indicated stability (z/L) classes; each class contains between 50 and 1000 individual samples.

stability range	b(T)	b(H ₂ O)	b(CO ₂)	b(O ₃)
-2 ... 0	0.563 (0.545 - 0.585)	0.557 (0.529 - 0.588)	0.556 (0.528 - 0.592)	0.574 (0.543 - 0.628)
0 ... 0.06	0.581 (0.559 - 0.598)	0.644 (0.591 - 0.719)	0.566 (0.547 - 0.611)	0.606 (0.583 - 0.641)
0.06 ... 0.2	0.596 (0.582 - 0.614)		0.595 (0.567 - 0.629)	0.648 (0.607 - 0.675)
0.2 ... 0.6	0.609 (0.593 - 0.632)		0.613 (0.584 - 0.650)	0.670 (0.638 - 0.716)
0.6 ... 2	0.636 (0.603 - 0.660)		0.668 (0.614 - 0.776)	0.763 (0.673 - 0.877)

In the unstable range, the median b-values show no significant differences among the investigated scalar quantities. The mean deviations from the median indicated by the inter-quartile range are relatively small, their relative magnitude is typically between 5 % and 10 %. Under stable conditions, the values show a moderate but systematic increase with stability up to 0.63 or higher. In order to describe the behaviour of the b-factor under stable conditions analytically, a regression function has to be fitted to the measured data. However, if the scatter of the data points is large, it is very difficult to choose an appropriate functional form. Moreover, the common least squares regression algorithm is particularly sensitive to non-Gaussian characteristics of the sample points, i.e. to outliers and asymmetric distributions. This problems seem to be least pronounced for the b-factor of temperature (cf. Fig. 5.2a). In this case, a simple linear regression was applied, which resulted in the following numerical relationship:

$$b(T) = 0.627 + 0.030 \cdot \log_{10}(z/L) \quad + 0.01 < z/L < +2 \quad . \quad (5.2)$$

The suitability of this function can be tested by analysing the distribution of the measurement points (residuals) around the fitted curve. In Figure 5.3a the regression line is plotted together with the box-plots for the different stability ranges as defined in Tab. 5.2. Over the whole stable range, the data are distributed in a fairly symmetric and homogeneous way around the regression line. The applicability of the least squares method is also demonstrated by the good agreement of the arithmetic averages and the median values in the individual classes. For the trace gases, such favourable conditions could not be observed. As shown in Figure 5.3b for CO₂, there is a considerable difference between arithmetic averages and medians in stable conditions. An asymmetric distribution with large deviations on the upward side leads to arithmetic means that are generally higher than the more representative medians. In that

case, least squares methods fail to give a useful functional estimate for the relationship of b and z/L . However, the linear function 5.2 derived for $b(T)$ also seems to fit the median values of $b(\text{CO}_2)$ fairly well. Only in the most stable class, a deviation of the median - but also a significantly larger scatter - is observed. The results for O_3 and H_2O in Table 5.2 show less agreement with Eq. 5.2, they are generally higher. Yet the fluxes of these trace gases were usually very low during the night (cf. Appendix B and Fig. 4.40) and thus strongly affected by measurement errors (cf. Section 4.3). The nocturnal CO_2 exchange, in contrast, was of the same magnitude like the corresponding daytime values, because it was not limited by low turbulence intensities or extreme ambient concentrations.

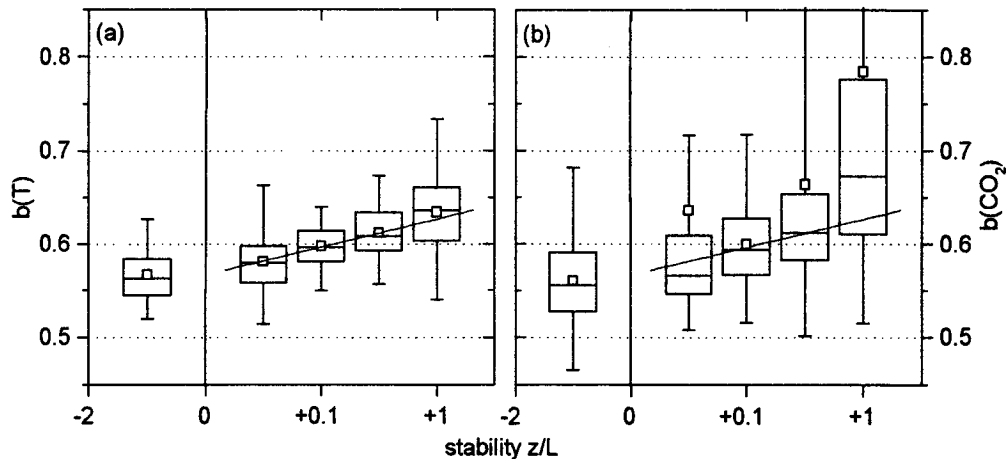


Fig. 5.3: Box-plots of b -factors for different stability classes as defined in Table 5.2 for (a) temperature and (b) CO_2 . Square symbols indicate the arithmetic mean and the straight line in the stable range represents the linear regression line function given by Eq. 5.2.

As mentioned at the beginning of this section, z/L is the most obvious influencing parameter for the b -factor according to similarity theory. The identification of other potential controlling variables is generally problematic, because most of them are somehow correlated to the stability through characteristic variations in the diurnal cycle. It is thus difficult to decide, whether an observed correlation is due to a direct physical influence or due to indirect dependency of both quantities on z/L . This problem can be avoided, if only unstable cases are considered, where no relation between b and z/L was found. In Figure 5.4, $b(T)$ values for unstable conditions are plotted against the wind direction corresponding to different fetch length (cf. Fig. 4.34).

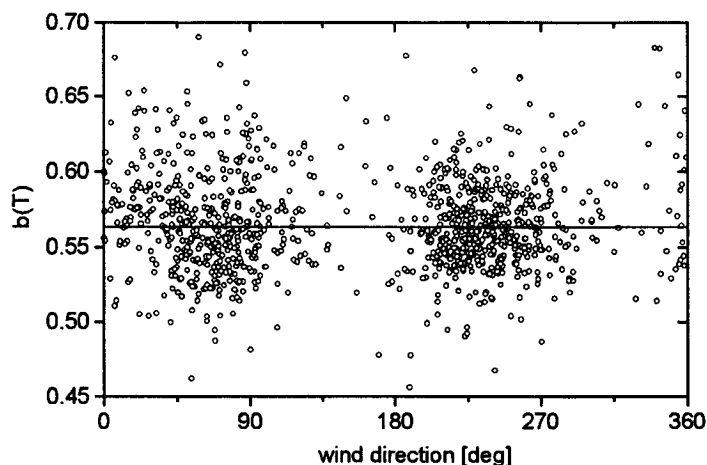


Fig. 5.4: REA b -factor for temperature plotted vs. wind direction for unstable conditions.

The data points crowd within the SW wind sector representing generally large fetch and in the NW sector representing small fetch lengths. However, no significant dependence of the b-values can be observed. The same is true for many other parameters investigated. Even if simultaneous b-factors for different scalars are compared (Figure 5.5), the correlation coefficient is very small and hardly significant. Thus z/L seems to be the only influencing parameter for the b-factors and the residual variability has a the characteristic of a random-noise.

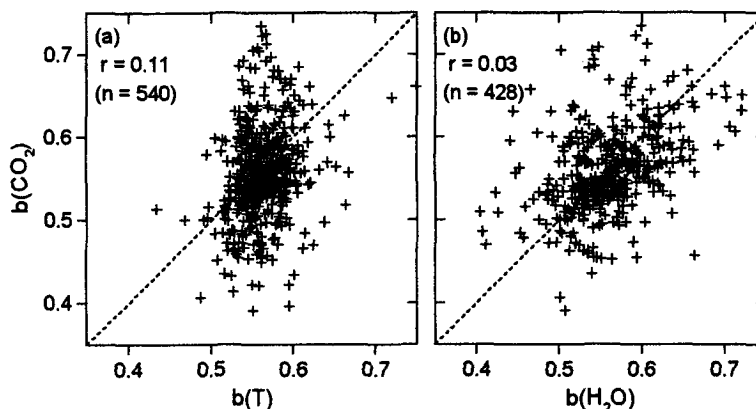


Fig. 5.5: Comparison of individual b-factors for different scalar quantities under unstable conditions: (a) $b(\text{CO}_2)$ vs. $b(T)$; (b) $b(\text{CO}_2)$ vs. $b(\text{H}_2\text{O})$.

Measurement errors of fast response eddy correlation systems may also have an influence on the experimental b-values. As far as the random scatter is concerned, the observed variability for unstable conditions are more or less in agreement (or even smaller) with the general uncertainty of finite time turbulence measurements discussed in Section 4.3.2. For stable conditions, the scatter especially for the trace gases is larger than expected, probably due to small fluxes, non-stationarity effects, or instrumental errors. However, no evidence could be found for an influence of instrumental errors and limitations on the *systematic* variation of the (average) b-values.

5.1.3 Relation between b-Factor and Bivariate Distribution

It was shown in Section 2.5.3, that the REA b-factor for a scalar flux $\overline{w's'}$ is generally determined by the bivariate joint frequency distribution (JFD) of the vertical windspeed w and the scalar quantity s (Eqs. 2.80 and 2.82). Moreover, it was deduced, that an ideal joint Gaussian distribution always yields the same constant b-factor of 0.627 (Eq. 2.84). Consequently, the observed systematic deviation of the b-factor - especially in unstable conditions - from the ideal Gaussian value has to be connected to departure of the JFD from the Gaussian form.

For the description of the tow-dimensional JFD, the quadrant analysis concept is often applied. However, there is no consistent terminology for the quadrants in literature, since individual terms were originally used for the study of momentum (Raupach, 1981) and sensible heat flux (Wilczak and Businger, 1983). The naming chosen here is illustrated in Figure 5.6; it is mainly based on Wilczak and Businger but with a differentiation for the direction of the flux (emission or deposition). It describes the type of instantaneous vertical transport in relation to the mean flux. Quadrant flux contribution with the same direction (sign) as the mean flux are termed 'direct' the others (with opposite direction) 'indirect'. The direct upward and downward flux events are also called 'ejections' and 'sweeps' respectively (cf. Katul et al., 1997a).

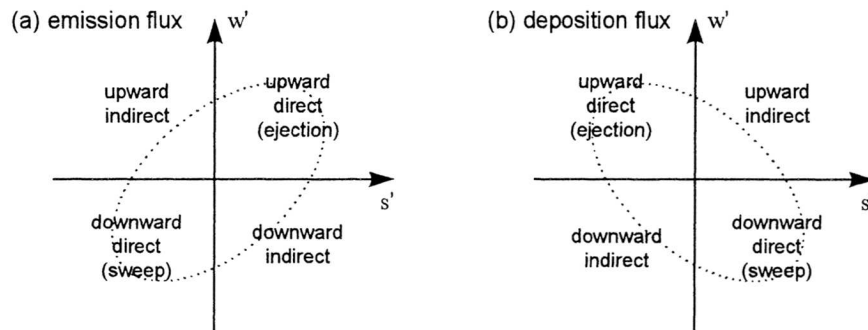


Fig. 5.6: Illustration of quadrant terminology describing the type of instantaneous vertical transport for (a) mean emission and (b) mean deposition fluxes.

Figure 5.7 shows the JFD of some individual measurements as contour plots. Two typical examples for an unstable (daytime) and a stable (nighttime) case were chosen. The displayed distributions can be regarded as representative for all scalar quantities investigated, since no significant differences were found among them. However, some cases (small CO_2 or ozone fluxes) suffered from the fact that no smooth contour plot of the JFD could be produced due to the limited digitalisation resolution. Also the direction of the flux seems to have no significant influence on the JFD apart from the general orientation.

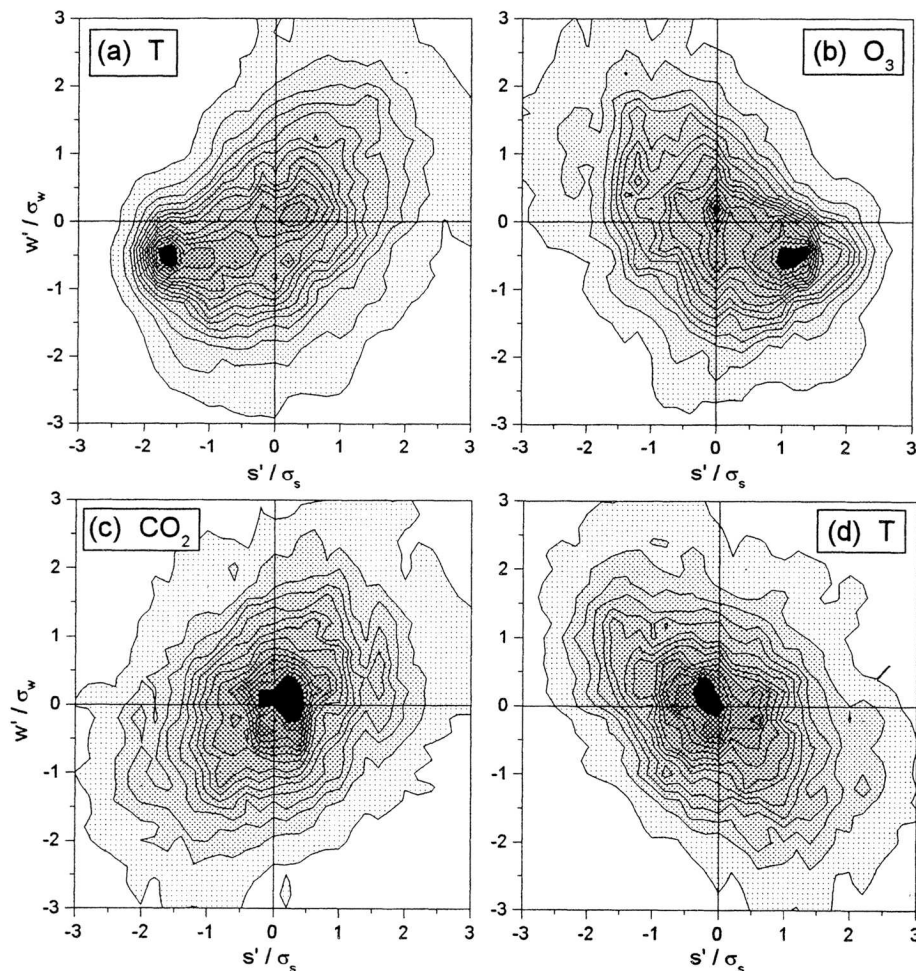


Fig. 5.7: Normalised measured JFD of vertical windspeed w and different scalar quantities s displayed as contour plots (isoline interval: 0.015; black represents >0.2): (a)&(b) temperature and ozone on 4 July 1995, 16:50 - 17:00, unstable conditions with $z/L \approx -0.2$; (c)&(d) CO_2 and temperature on 15 July 1995, 00:10 - 00:20, stable conditions with $z/L \approx +0.1$.

A distinct difference can be observed between the unstable (a,b) and the stable (c,d) cases. The latter follow the ideal joint Gaussian distribution (Fig. 2.18) reasonably well; both the direct and indirect flux quadrants are fairly symmetric and the highest frequency is near the centre of the coordinate system. In contrast, the unstable cases are highly skewed with a peak frequency in the sweep quadrant. This peak can be assumed to represent the almost constant scalar profile of the convective boundary layer and is an absolute limit for the scalar values. The scalar deviations in the opposite direction (ejection quadrant) are obviously larger than in the sweep quadrant but occur less frequent. They are connected to upward motion and thus represent near surface conditions. The shape of the JFD in the ejection quadrant does not show particular differences among the stable and unstable cases in Fig. 5.7.

The analysis of the entire JFD as displayed in Fig. 5.7 requires time-consuming data manipulation and gives mainly qualitative information, i.e. the quantitative comparison to the ideal Gaussian is difficult. Therefore the evaluation is simplified by using conditional means (integrals) either of the half-planes (especially upward and downward motion) or of the four quadrants. Taking into account the very similar behaviour of all scalar quantities, the following analysis mainly concentrates on the JFD of vertical windspeed and temperature, which is assumed to be measured with lowest relative noise level of all scalars. Common integral quadrant characteristics are the total sweep and ejection frequencies (time fractions) and the ratio of the two (cf. Wilczak and Businger, 1983; Katul et al., 1997). The sweep-ejection-ratio for the w-T-distribution determined for all cases is displayed in Fig. 5.8 as a function of stability. It gives a quantitative description of the different skewness observed in the exemplary cases in Fig. 5.7. In the stable range, the values scatter around unity indicating a general symmetric JFD. In the unstable range, they show a systematic variation with z/L . The asymmetry is largest for extremely unstable conditions and decreases towards the ideal symmetric value for near neutral conditions.

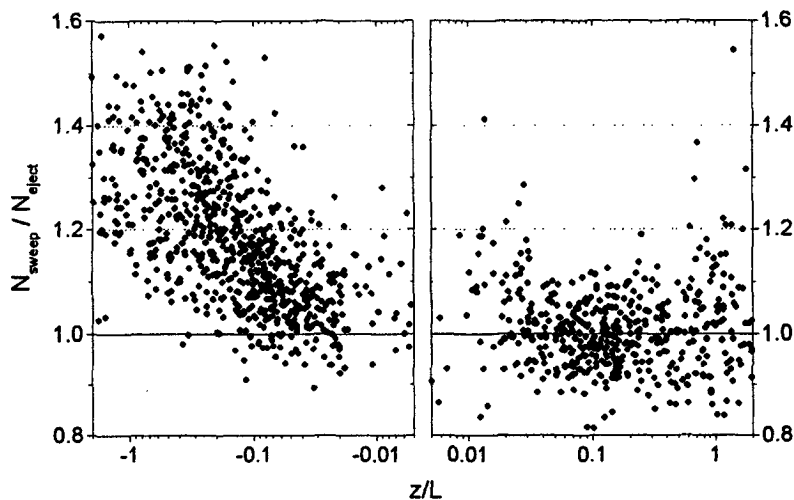


Fig. 5.8: Ratio of time fractions (normalised integral frequency) spent in the sweep and ejection quadrant for the temperature (sensible heat) flux as a function of stability.

The ideal joint Gaussian JFD as described by Eq. 2.81 implies two principle characteristics: (a) a Gaussian form of the one-dimensional distributions of w' and s' , and (b) a linear relationship between the two quantities. The second requirement signifies, that the data points are homogeneously distributed around a linear regression line $s' = \alpha + \beta \cdot w'$. The offset α equals zero due to the use of the prime quantities and the slope β is defined as (Sachs, 1984):

$$\beta \equiv \frac{\overline{w' s'}}{\sigma_w^2} = r_{ws} \frac{\sigma_s}{\sigma_w} \tag{5.3a}$$

According to Sachs (1984) and Baker et al. (1992), the linear relationship between two quantities implies, that if the dataset is divided into sub-groups (here updrafts with $w > 0$ and downdrafts with $w < 0$), the means in each group ($\overline{w}_U, \overline{s}_U$) and ($\overline{w}_D, \overline{s}_D$) fall on the regression line. Consequently, the slope β can be estimated from the averages of the sub-groups in the following way:

$$\beta_{est} = \frac{\overline{s}_U - \overline{s}_D}{\overline{w}_U - \overline{w}_D} \tag{5.3b}$$

If the assumption of linearity is valid, the combination of Eqs. 5.3a and 5.3b with Eq. 5.1 yields the following simple expression for the REA b-factor depending solely on the w-distribution:

$$b = \frac{\sigma_w}{\overline{w}_U - \overline{w}_D} \tag{5.4}$$

As pointed out by Katul et al. (1996), this expression is directly related to the flatness or kurtosis (tendency for long tails) of the w-distribution. For an ideal Gaussian distribution, Eq. 5.4 equals the ideal value 0.627 (cf. Eq. 2.84), whereas longer tails lead to higher values, because they have a stronger influence on σ_w than on the conditional averages. The corresponding experimental results are displayed in Figure 5.9. They indicate a generally positive deviation of the flatness in comparison to the Gaussian model. In the unstable range, the deviation is uniform and amounts to about 2%. This is also valid for moderately stable conditions; but with increasing positive stability, the kurtosis grows considerably. It can be concluded, that the assumption of linearity is violated in the present data, because it would lead to b-factors that are generally higher than the ideal value of 0.627 (as displayed in Fig. 5.9). In contrast, the experimental results presented in the previous section are predominantly lower than 0.627!

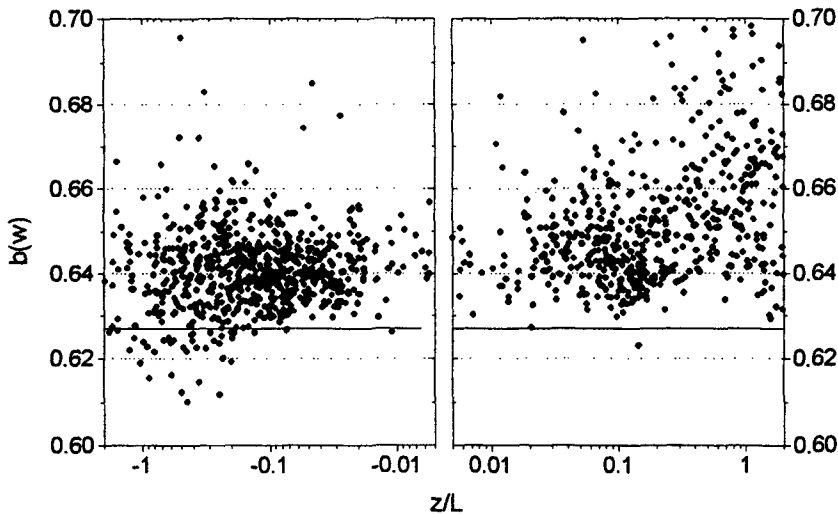


Fig. 5.9: Experimental REA b-values derived from the one-dimensional w-distribution alone according to Eq. 5.4, dependent on stability; the horizontal line indicates the ideal Gaussian value 0.627.

The deviation of the observed JFD's from the ideal linear model may be quantified by the ratio of the estimated (Eq. 5.3b) and the true regression line slope (Eq. 5.3a). The reference value for the ideal case is $\beta_{est}/\beta = 1$. The corresponding results are plotted in Fig. 5.10 against stability. They show relatively

constant large values in the unstable range and decrease towards unity in the stable range. This systematic dependence is more or less inverse to the behaviour of the simulated b-factors in Section 5.1.2. Hence a generally strong relationship between the b-factor and the non-linearity of the joint frequency distribution can be stated.

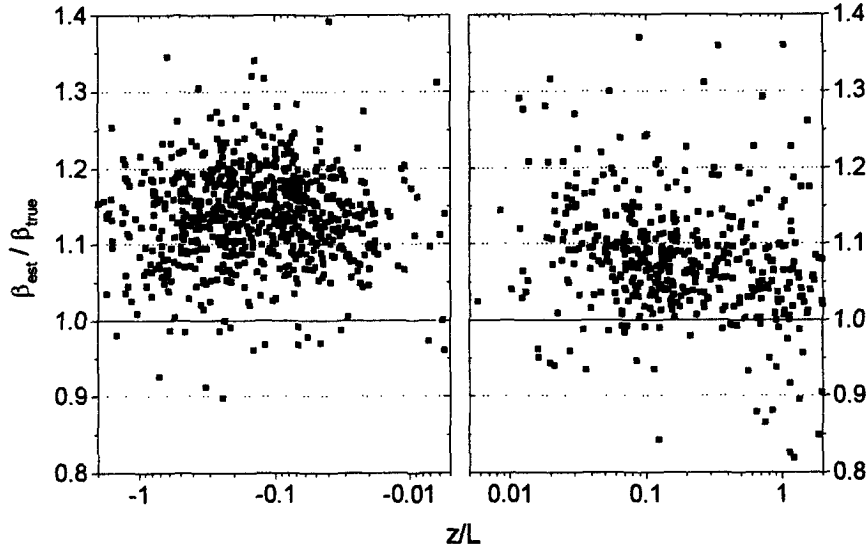


Fig. 5.10: Deviation from linearity of the w - T -distribution determined as the ratio of the estimated (Eq. 5.3b) and the true slope (Eq. 5.3a) of the linear regression line.

5.1.4 Effect of a Deadband

It was discussed in Section 2.5.3 that the relaxation of the eddy accumulation method - ignoring the magnitude of the vertical windspeed for the conditional sampling - leads to a smaller scalar difference $\Delta s = (\bar{s}_U - \bar{s}_D)$, which is less favourable for practical measurements. The application of a deadband in the REA method (cf. Sections 2.5.3 and 3.4.3) represents a relatively simple modification of the pure sign-dependent conditional sampling. The conditional scalar means for updrafts and downdrafts are determined only outside a certain w -threshold $\pm w_d$ as illustrated in Figure 5.11:

$$\bar{s}_U = \frac{\int_{w_d}^{\infty} \int_{-\infty}^{\infty} s \cdot p(w, s) \, ds \, dw}{\int_{w_d}^{\infty} \int_{-\infty}^{\infty} p(w, s) \, ds \, dw} \quad ; \quad \bar{s}_D = \frac{\int_{-\infty}^{-w_d} \int_{-\infty}^{\infty} s \cdot p(w, s) \, ds \, dw}{\int_{-\infty}^{-w_d} \int_{-\infty}^{\infty} p(w, s) \, ds \, dw} \quad (5.5)$$

The use of a deadband corresponds to a simple binary weighing of the air sampling with the vertical windspeed. It leads to generally larger conditional mean differences, as illustrated in Figure 5.11, and therefore to lower b-values depending on the deadband width. For the ideal joint Gaussian distribution, the deadband effect on b had to be determined by a numerical evaluation of the integrals in Eq. 5.5, and therefore an exact functional relationship is not available. For an adequate analytical description, the following relationship was fitted to the data in the range $0 \leq w_d/\sigma_w \leq 2$ by least squares regression:

$$b(w_d) = b_{\infty} + (b_0 - b_{\infty}) \cdot \exp\left(-a \cdot \frac{w_d}{\sigma_w}\right) \quad (5.6)$$

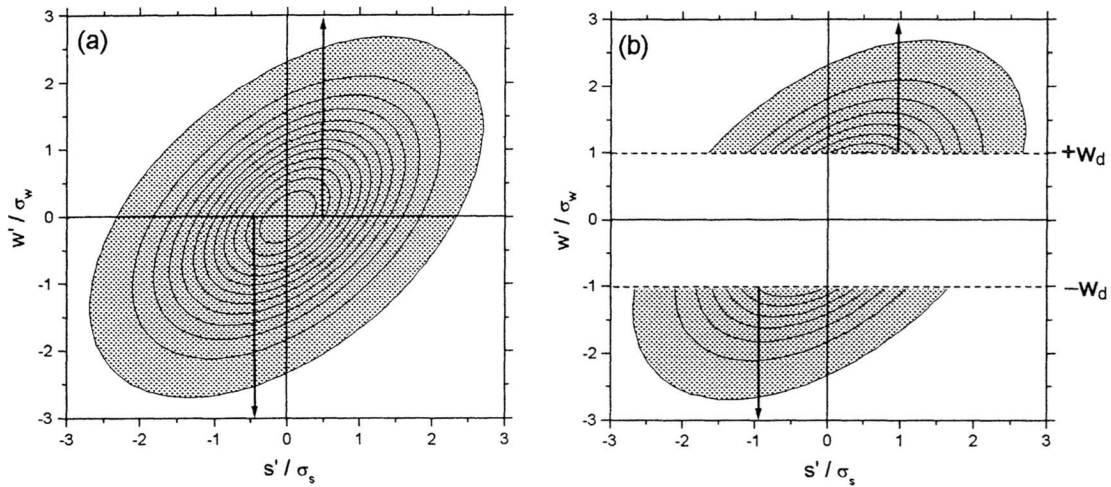


Fig. 5.11: Illustration of the deadband application on the conditional scalar means (indicated as arrows): (a) conditional mean difference without deadband; (b) increased conditional mean difference with a deadband.

For the purpose of general applicability, the deadband half-width w_d was normalised with the standard deviation of the vertical windspeed. Eq. 5.6 describes an exponential decay with an initial zero-deadband value $b_0 = 0.627$ (cf. Eq. 2.84) and an asymptotic baseline value b_∞ for an infinite deadband width. The numerical results for the fitting parameters (b_∞ and a) are given in Table 5.3. In order to test the validity of this relationship for real environmental conditions, simulation studies with variable deadbands were performed on the experimental eddy correlation data sets. Figure 5.12 shows the simulated b -values for temperature as a function of the normalised deadband. Stable and unstable cases are separated in two individual plots. Taking into account the variations of the b -factors reported in Section 5.1.2, the stable cases were further divided for the fitting of the deadband function (Eq. 5.6). The resulting regression curves are also plotted in Fig. 5.12; the corresponding numerical parameters are listed in Table 5.3. The b_0 values were not fitted but prescribed as given in Table 5.2.

Tab. 5.3: Numerical parameters of the fitting function in Eq. 5.6 describing the deadband effect of the ideal Gaussian JFD and of experimental data under various stability conditions.

	b_0 (fixed)	b_∞	a
ideal joint Gaussian distribution	0.627	0.144	1.04
experimental EC data: $z/L = -2...0$	0.563	0.282	1.71
$z/L = 0...+0.06$	0.581	0.210	1.21
$z/L = +0.2...+0.6$	0.627	0.183	1.27

The difference between moderate and extremely stable conditions is largest for zero deadband and reverses its sign at about $w_d/\sigma_w = 0.6$. The scatter for even large deadband widths is surprisingly low. In unstable conditions, the variability is generally larger but no systematic dependence of the deadband function on z/L could be found. The large random-like variability may be explained by the effect of limited sampling time (cf. Section 4.3.2) which is problematic especially for unstable conditions with significant contribution of large eddies.

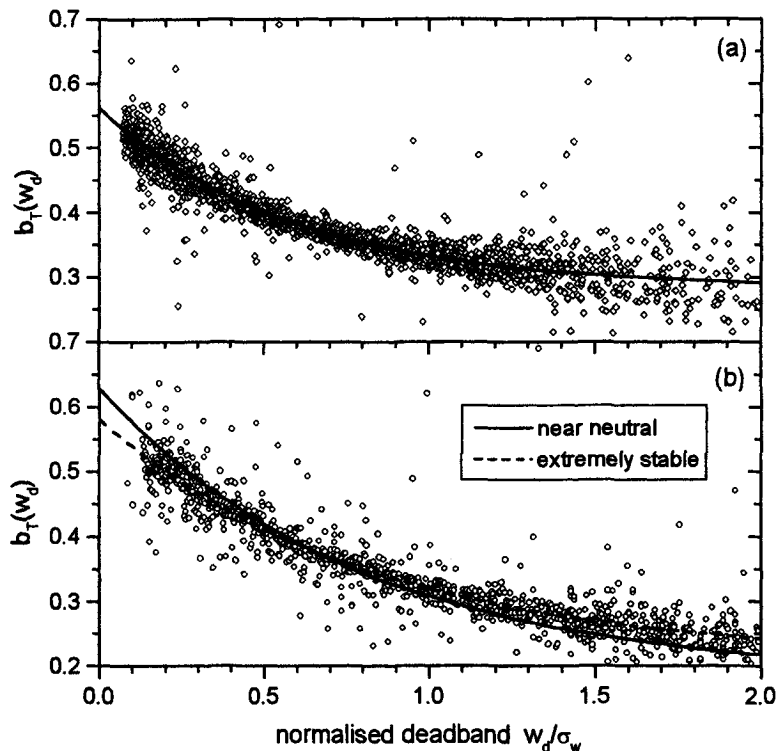


Fig. 5.12: b -factors derived from EC time series of temperature with variable deadband width: (a) unstable conditions; (b) stable conditions; the indicated lines represent fitting curves according to Eq. 5.6, the corresponding numerical parameters are listed in Tab. 5.3.

5.2 Simulation of Non-Ideal REA Systems

A real REA system operated in the field may suffer from various non-ideal effects not considered in the previous section. They may be caused by instrumental limitations as well as unfavourable environmental conditions. In this chapter the different error effects are studied individually by simulation with the eddy correlation data or with the ideal joint Gaussian distribution. The latter represents an ideal reference model which might be suitable for some purposes, since the deviation of the measured JFD's (cf. Section 5.1.3) were often not very large. The analysis of experimental data is mainly performed with the sonic temperature measurements because of their low noise level. The individual error sources are studied first in a general way, before they are quantified for the specific REA setup used in the field experiment. The resulting effects are generally analysed in terms of flux recovery rates, that are to be described by suitable parameterisation schemes.

The results of the simulation studies will be summarised in Section 5.3 with respect to the present REA field measurements. The findings are necessary for the choice of an appropriate evaluation strategy as well as for the error estimation and the interpretation of the resulting REA fluxes.

5.2.1 Measurement Errors in the Vertical Windspeed

Because the vertical windspeed is used in the REA method for the instantaneous valve control, an appropriate correction for measurement errors (as described for the EC method in Section 4.1) is not always possible. The main error source is a misalignment between the wind field and the sensor, which may be caused by non-homogenous terrain, a tilted sensor setup or wind distortion around the sensor

head. Possible consequences are a systematic offset in w and an interference by the horizontal wind-speed component. In the eddy correlation method, offset effects do not have to be considered, because they are always eliminated in the covariance calculation.

Online Detrending

Constant offsets in the w -signal can be removed by online high-pass filtering. However, the mentioned error effects are usually not constant but show longterm trends due to variations in wind speed and direction. Since online filter functions are always asymmetric, they can not perform an accurate detrending but always show a certain lag behind the true signal change. It has to be distinguished between recursive and non-recursive filters (McMillen 1988; Dillmann, 1991). The first type requires only few calculations and shows a good cutoff characteristic. However, the disadvantage of recursive filters is their relatively complex spectral behaviour with a non-constant time shift, i.e. low frequencies are delayed stronger than high frequencies. For convenience and simplicity, a very simple non-recursive filter was applied in the present case for the online detrending of the vertical windspeed (cf. Section 3.4.3): a block average over the last 10 min. This may not be the optimal solution but its effect is easy to quantify. Such a filter produces a running mean which is shifted to an ideal central average by 5 min. The effect of this lag leads to a systematic error in the estimated \bar{w} whenever there is a trend in the respective time series. As before in Section 4.1.2, the trend effects are analysed assuming ideal linear behaviour with a change Δw within a 10 min interval. Thus the deviation (bias) of the estimated to the true \bar{w} due to the 5 min lag can be estimated as:

$$w_{\text{bias}} \equiv \bar{w}_{\text{est}} - \bar{w}_{\text{tru}} \approx \frac{1}{2} \Delta w . \quad (5.7)$$

The influence of the bias in the average vertical windspeed depends on its relative magnitude compared to the turbulent fluctuations (described by σ_w). Thus the normalised bias w_{bias}/σ_w was determined from the eddy correlation dataset according to Eq. 5.7 and the corresponding frequency distribution is displayed in Figure 5.13. It is representative for stable as well as unstable conditions. For more than 90% of the cases the relative bias lies within the range $-0.3\dots+0.3$.

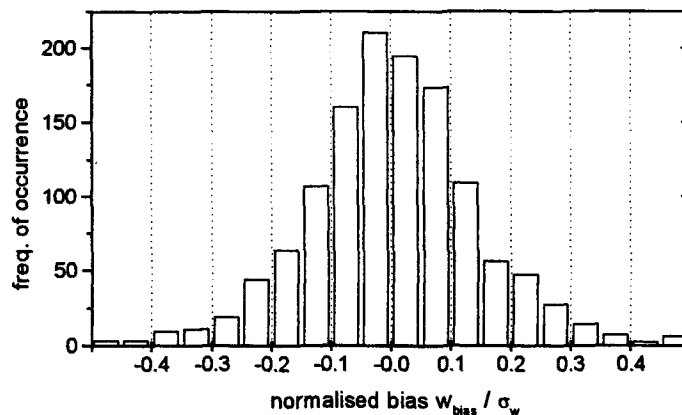


Fig. 5.13: Histogram of normalised bias in the vertical windspeed due to trends according to Eq. 5.7.

Effect of Biased Conditional Sampling

The effect of the w -offset on REA measurement is firstly investigated by simulation with the ideal Gaussian JFD. The integration limit between updraft and downdraft events is set to varying values of $w_{\text{bias}} \neq 0$. The obtained results for the conditional scalar means are displayed in Figure 5.14. For a

positive bias, the updraft conditional mean increases with w_{bias} almost linearly. For small bias values, this effect is nearly compensated by the simultaneous decrease in the (absolute) biased downdraft mean. However, for larger values, the downdraft mean approaches the total mean and thus converges towards zero. As a result, the conditional mean difference grows with the bias in a nonlinear way. The relative flux recovery could be approximated by a quadratic function of the normalised bias. Due to the symmetric form of the Gaussian JFD, the effect is symmetric for positive and negative w_{bias} values.

$$\frac{F_{\text{bias}}}{F_{\text{ideal}}} = \frac{\Delta \bar{s}_{\text{bias}}}{\Delta \bar{s}_{\text{ideal}}} = 1 + 0.137 \cdot (w_{\text{bias}} / \sigma_w)^2 \quad (5.8)$$

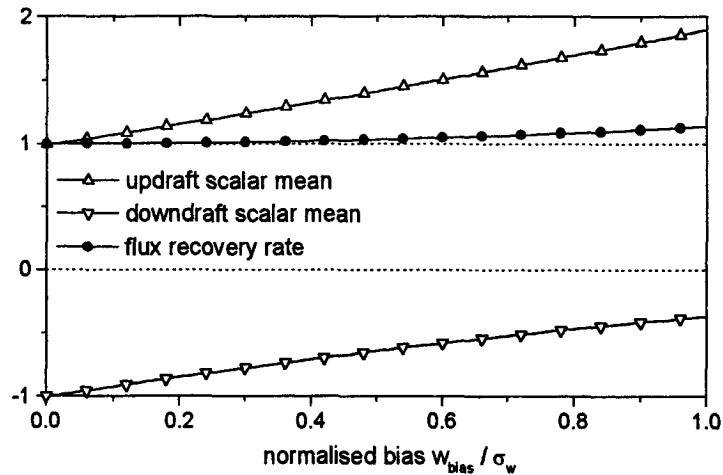


Fig. 5.14: Conditional means for updrafts and downdrafts and resulting flux recovery determined from the ideal joint Gaussian distribution as a function of the normalised w -offset.

In a second step, the bias effect was tested with the experimental EC dataset of w and T . In order to obtain results for a big range of normalised bias values, the numerical simulation was carried out with six fixed values: ± 3 , ± 10 and $\pm 30 \text{ cm s}^{-1}$. The results are shown in Figure 5.15 separated for stable and unstable conditions.

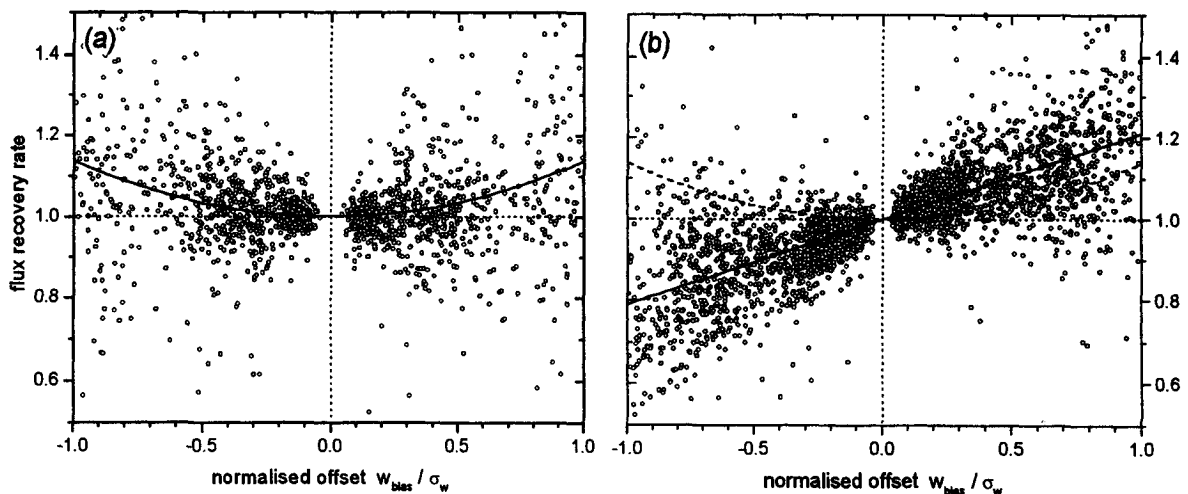


Fig. 5.15: Flux recovery rate determined from the EC measurements of w and T as a function of the normalised w -offset: (a) stable conditions, with indication of Eq. 5.8 (solid line); (b) unstable conditions, with indication of Eq. 5.8 (dashed line) and Eq. 5.9 (solid line).

In the stable case, a large scatter is observed, and it is difficult to decide, whether the theoretical function given by Eq. 5.8 is a better average estimate than unity. For small relative offsets (< 0.3), the variations stay mainly within about $\pm 10\%$. For unstable conditions, the displayed variations are much more systematic. In contrast to the behaviour of the Gaussian JFD (dashed line), the deviations are not generally positive, but depend on the sign of the offset. The overall relationship in Fig. 5.15b can be approximated by the following linear relationship (indicated as solid line), which was determined by least squares regression:

$$\frac{F_{\text{bias}}}{F_{\text{ideal}}} = \frac{\Delta \bar{s}_{\text{bias}}}{\Delta \bar{s}_{\text{ideal}}} = 1 + 0.21 \cdot (w_{\text{bias}} / \sigma_w) . \quad (5.9)$$

Tilt Effect without Bias

Beside the bias effect, the misalignment of the wind measurement causes a disturbance of the vertical windspeed fluctuations by the horizontal wind component, which have a higher correlation with the transported scalars than w . In the eddy correlation method, this effect was accounted for by a coordinate rotation of the scalar flux vector (Section 4.1.3). The correction effect showed a systematic dependence on the vertical tilt angle similar for all scalar quantities (cf. Fig. 4.9). This relationship has also been tested for the REA method. In Figure 5.16 the relative error of the temperature flux determined with the unrotated w time series is plotted against the vertical tilt angle. The points show a relatively large scatter but nevertheless a systematic dependence can be observed. It may be approximated by the dashed line which represents a flux error of -4% per degree of vertical tilt. Thus the rotation effect on the REA flux is well comparable to the respective findings for the eddy correlation method in Section 4.1.3.

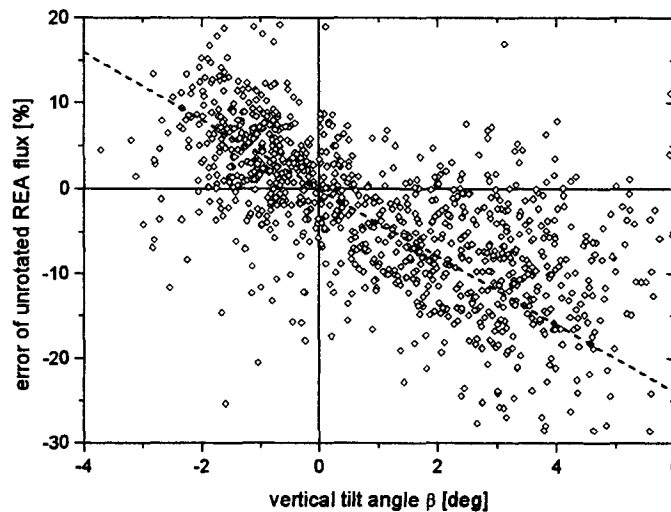


Fig. 5.16: Effect of vertical tilt angle of the wind measurements on the REA temperature flux; the dashed line indicates a proportional relationship of -4% per degree.

5.2.2 Delay Time of Conditional Sampling

An inherent problem of the REA technique is the delay between the windspeed measurement and corresponding conditional sampling. Unlike in the eddy correlation method, it can not be corrected by an adjustment of the time series (cf. Section 4.1.1). The total delay time in REA measurements is caused by various factors:

- Discretisation of the w-measurement and the valve controlling cycle:

It depends on the measurement interval Δt as well as on effective integration time. Baker et al. (1992) assume an instantaneous w-measurement (at the end of each interval) and derive a statistically average delay time of $0.5 \cdot \Delta t$. The sonic anemometer used in the present experiment was operated with a measurement interval of 48 ms. Within each interval, it performs eight full measurements and yields the average at the end. This corresponds to an integration over Δt and thus the average delay time also equals Δt .

- Execution time for the online data processing and controlling:

It is usually much smaller than the other contribution and thus can be ignored.

- Limited response of the sampling valves:

It depends on the technical characteristics of the valves. The effective response time of the valves used in the present study was determined in Section 3.4.3 to about 18 ms.

- Longitudinal sensor separation:

The separation s_{long} between the anemometer and the sampling inlets along the wind direction can be interpreted as a virtual delay time between the vertical windspeed and the scalar quantity: $t = s_{\text{long}}/u$ (u = mean horizontal windspeed). In the present setup, the sensor separation was 30 cm. Thus the maximal time shift for a typical windspeed range of 1 - 6 m s^{-1} is about ± 0.3 s. If the inlets are on the windward side of the wind sensor, the time lag is negative, otherwise positive.

Combining all this effects, the total average delay time can be estimated as:

$$\bar{t}_{\text{del}} = \Delta t + t_{\text{valve}} + \frac{s_{\text{long}}}{u} \quad (5.10)$$

For the present setup, delay time values between -0.25 s and $+0.35$ s can be expected. Since the effect on the covariance is assumed to be symmetric (for positive and negative delays), the following analysis is restricted to positive delay times.

Eddy reversal frequency

The delay time affects the REA measurement whenever the sampling valves change their state. Thus the effect of the delay time depends on the switching frequency, or alternatively on the average time for which the valve remains in a certain switching state. For a quantitative description of this characteristic, Baker et al. (1992) propose the following definition of the 'eddy reversal frequency' (erf):

$$\text{erf} \equiv \frac{2}{\bar{t}_{\text{U}} + \bar{t}_{\text{D}}} \quad (5.11)$$

It represents the average frequency (in Hz) of the valve switching and equals the inverse average duration of the updraft and downdraft events. It seems obvious, that the eddy reversal frequency in the surface layer - like e.g. the turbulence spectra - is determined by the respective micrometeorological condition. Therefore it was tried to parameterise the erf similar to the spectral similarity functions presented in Appendix A.6. The erf was determined from the EC time series of the vertical windspeed according to Eq. 5.11 and was normalised with the measurement height z and the mean windspeed u (cf. Eq. A.19):

$$\text{erf}_z = \text{erf} \cdot \frac{z}{u} \quad (5.12)$$

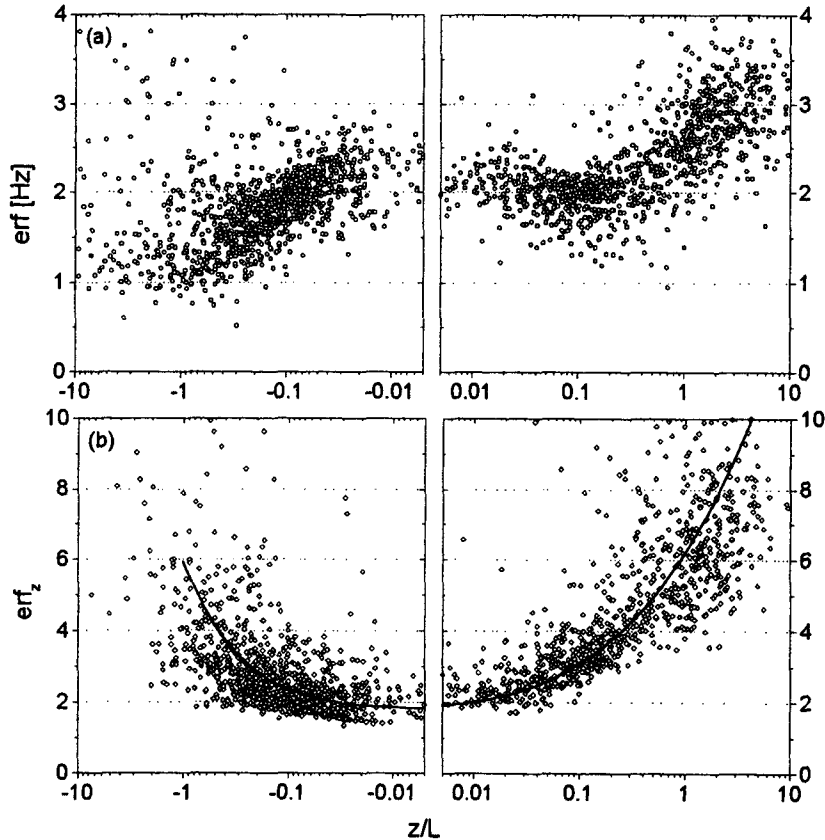


Fig. 5.17: (a) Raw and (b) normalised eddy reversal frequency plotted against stability; with indication of fitted similarity function (solid line) corresponding to Eq. 5.13.

Following surface layer similarity theory, the resulting dimensionless values are only a function of the stability parameter z/L . This relationship is examined graphically in Figure 5.17. For comparison, the original erf is also plotted. It indicates, that the normalisation produces a more concise dependency on z/L with the lowest value of about 1.8 at neutral condition and an increase with positive and negative stabilities similar to e.g. Fig. 4.17. The displayed similarity relationship was approximated by the following functions:

$$\text{erf}_z(z/L) \approx \begin{cases} 1.8(1 - 5z/L)^{2/3} & -1 \leq z/L \leq 0 \\ 1.8(1 + 40z/L)^{1/3} & z/L > 0. \end{cases} \quad (5.13)$$

It can be observed in Fig. 5.17b, that the relationship is relatively well defined in the stable range, whereas for strong instability, the number of data is limited and the scatter is large. Although an increase of erf_z with $-z/L$ can be clearly noticed, the course of the similarity relationship for large negative stability has to be regarded as only a rough estimate. Beyond $z/L = -1$, too few measurements are available for a representative fit.

Flux attenuation due to delay time

With the relationships in Eqs. 5.12 and 5.13, the eddy reversal frequency can be estimated from micrometeorological quantities and can serve as a fundamental parameter for the quantification of the delay time effect. Baker et al. (1992) propose a theoretical model based on the simple assumption, that the probability distribution for the transported scalar quantity is uniform during all updraft and down-draft events (i.e. independent on whether the sign has just changed or not). For this case, the following linear function for the flux recovery rate can be derived:

$$\frac{F_{\text{del}}}{F_{\text{ideal}}} = \frac{\Delta \bar{s}_{\text{del}}}{\Delta \bar{s}_{\text{ideal}}} = 1 - 2 \cdot \bar{t}_{\text{del}} \cdot \text{erf} \quad (5.14)$$

In order to test this model or, if necessary, to find a more appropriate relationship, simulations with the EC time series of w and T were performed for various delay times between 0 and 0.5 s. The experimental flux recovery rates for the delay time of 0.1 s are plotted in Figure 5.18. Unlike predicted by Eq. 5.14, the recovery rates show a clear non-linear dependence on erf, although there is a considerable scatter in the data points. The average course may be approximated by a polynomial relationship of second order. It is also found, that the delay time has a nearly linear effect on the flux loss. Thus the flux recovery rate can be estimated generally by the following function of the delay time and the eddy reversal frequency:

$$\frac{F_{\text{del}}}{F_{\text{ideal}}} = 1 - \bar{t}_{\text{del}} \left[0.017 \cdot \text{erf} + 0.22 \cdot \text{erf}^2 \right] \quad (5.15)$$

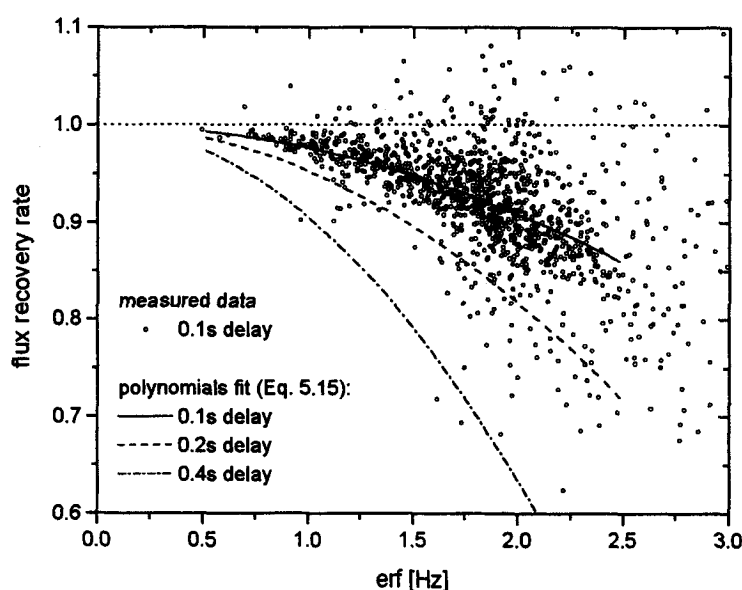


Fig. 5.18: Flux recovery rate of the sensible heat flux calculated by the REA method from the EC time series with a delay time of 0.1 s. The lines indicate the polynomial fit function Eq. 5.15 for various delay times.

Other High Frequency Attenuation Effects

The time delay between the vertical windspeed measurement and the trace gas sampling can be regarded as a high frequency attenuation effect. Such effects were quantified and corrected in the EC method by spectral transfer functions (cf. Sections 4.1.5 and A.8) e.g. for sensor separation and sonic path averaging. These corrections can not be applied to the REA method a priori. The effect of a limited resolution of the wind sensor was investigated in an exemplary way by a simulation analysis with damped w and T signals. The time series were subjected to a symmetric low-pass filter with a rectangular window of 1 s width before the determination of the conditional means and the covariance flux. The results are displayed in Figure 5.19. Whereas the covariance fluxes are reduced by the high frequency damping by about 20 %, the conditional means are not significantly affected. This indicates, that the temporal resolution of the wind measurement is not critical for the REA method and that high frequency attenuation effects which act on w alone (and not on the correlation between w and the scalar) can be neglected.

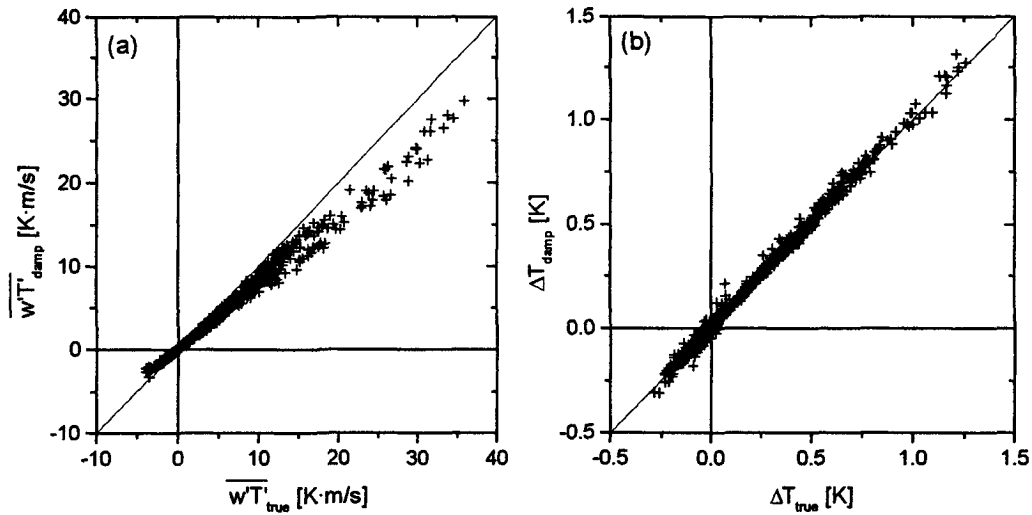


Fig. 5.19: Effect of individual high frequency damping of w and T on (a) the eddy covariance flux; (b) the conditional sampling difference.

5.2.3 Non-Constant Conditional Sampling Flow

Beside the fast response of the sampling valves, also a constant sampling flow during the open state is required by the REA concept. In practice, a fully constant flow switched on and off instantaneously is difficult to obtain and may require a complex and very fast flow controlling system. The experimental setup used in the present study (cf. Section 3.4) represents a relatively simple system which may experience considerable pressure and flow variations. It is therefore essential to know the effect of non-constant sampling flows on the resulting concentration difference. Under the ideal assumption of Baker et al. (1992) that the probability distribution of the sampled scalar quantity is uniform during the updraft and downdraft events (see previous section), the effect would be negligible. However this assumption is questionable.

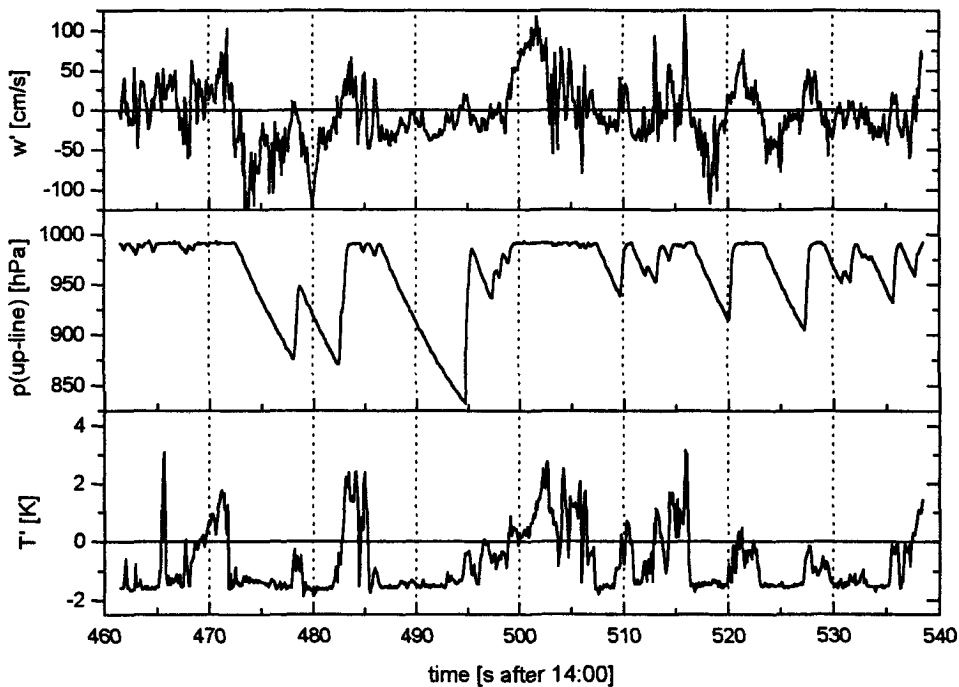


Fig. 5.20: Typical time series of vertical windspeed, updraft sampling line pressure and temperature fluctuations in unstable daytime conditions (20 July 1995, 14:00).

An experimental control or test of the conditional sampling flow is not possible with common mass flow meters or controllers, because they have typical response times in the order of one second. As mentioned in Section 3.4.4, pressure measurements are fast enough for the examination of fast fluctuating flows. In order to monitor the pressure fluctuations in the intake line of the REA test system, the pressure in the updraft line was recorded with high temporal resolution (20 Hz) by the EC data acquisition unit during two days at the end of the field campaign. An extract from the time series of tube pressure together with the controlling vertical windspeed and the sonic temperature is given in Figure 5.20. It can be observed, that during the closed state of the valve, the continuously operating pump depletes the air within the sample line (including the buffer volume, cf. Fig. 3.18) leading to an almost linear pressure drop. When the valve opens, the underpressure (depleted air) is compensated (replaced) almost immediately.

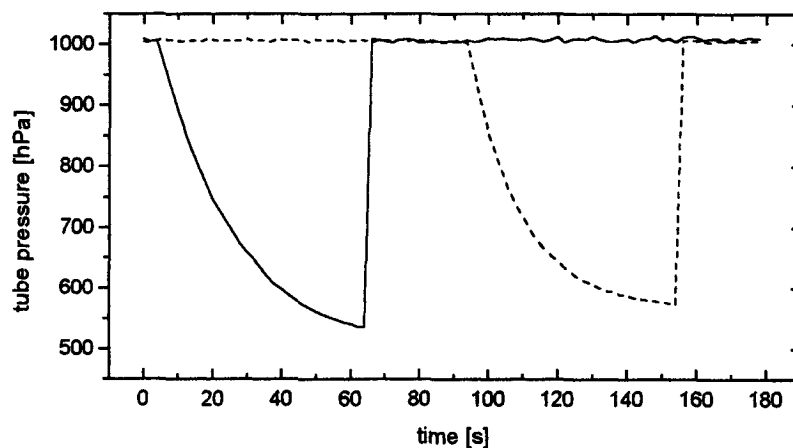


Fig. 5.21: Pressure response within the intake lines of the REA system to a closing and opening of the intake valves; solid curve: updraft sampling line, dashed curve: downdraft sampling line.

The same behaviour was observed in a laboratory test of the sampling system, where the pressure response to a longer closed interval in both intake lines was monitored. Figure 5.21 shows, that the pressure in both lines (controlled by two different pumps) drops in the same way: almost linearly at the beginning and tending towards the maximum pressure difference of the membrane pumps of about 500 hPa. Under natural atmospheric conditions with eddy reversal frequencies between 0.5 and 3 Hz (cf. previous section) the pressure response is always in the linear range. The observed pressure effect produces a non-constant conditional sampling flow of the REA system. The flow is much larger at the beginning of each sampling interval just after the opening of the valve. This leads to a strong overweighing of the air concentration sampled just after each change of the sign of w (eddy reversal). The overweighing effect depends on the underpressure built-up within the line and thus on the time for which the valve was in the closed state before. The influence of this behaviour was investigated by the following simulation with the EC datasets. For the calculation of the conditional means, the first value after each eddy reversal was weighted with the time, for which the vertical wind was in the opposite state before, whereas all other values were equally weighted with their sampling interval $\Delta t = 48$ ms.

The simulation results are displayed in Figure 5.22. It shows the flux recovery rates obtained with the weighted conditional means. The recovery rates lie mainly between 0.2 and 0.6 (damping factor 2-5) and thus demonstrate that the REA method is very sensitive to the non-constant sampling flow resulting from the applied setup proposed by Baker et al. (1992). The results shows a slight dependence on the eddy reversal frequency with better recoveries for higher frequencies. This behaviour may be explained by the fact, that the underpressure effect becomes less important for shorter switching intervals. The

results for temperature and CO₂ reveal random as well as systematic differences. For CO₂ the scatter is somewhat larger and the values are about 25% lower on average. For the other trace gases, similar results were obtained.

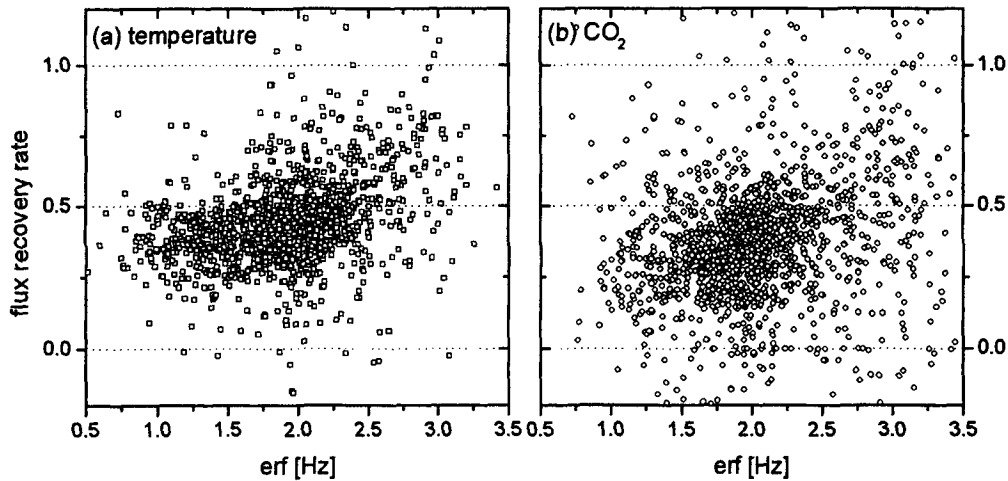


Fig. 5.22: REA flux recovery rate for (a) temperature and (b) CO₂ obtained by simulation with the EC time series assuming a non-constant sampling flow.

These results indicate a particular non-ideal characteristic of the used REA setup that leads to a general damping of the measured conditional mean difference. A survey and quantitative comparison of all systematic error effects studied so far will be presented in the following section with respect to the evaluation of the REA field measurements.

5.3 Evaluation of Measured REA Fluxes

Based on the findings of the simulation studies in the foregoing sections, the REA field measurements during the Bellheim campaign are evaluated in the following. Especially the non-ideal characteristics of the used REA setup have to be considered. They need to be compensated as far as possible in the flux calculation (Section 5.3.1), but they also influence the data rejection criteria (Section 5.3.2) as well as the error estimation of the flux results (Section 5.1.3).

5.3.1 Calculations and Corrections

The calculation of the REA fluxes is basically described by the relationship in Eq. 2.79. It relies on a known b-factor which was shown to be well defined for an ideal system as a function of stability and deadband width (cf. Section 5.1). However, the findings of the simulation studies in Section 5.2 indicate, that the REA system used in the present study suffered from several systematic error effects. They are compiled in Table 5.4 with their quantitative effect on the flux results (given as error ranges which comprise about 95% of the cases). Among the listed effects, the non-constant sampling flow analysed in Section 5.2.3 is by far the most important problem. It causes a reduction of the measured flux (i.e. of the concentration difference) by a factor of 2 to 5. The other effects are significantly smaller and of similar magnitude like the errors of the common micrometeorological methods discussed in Section 4.3.

Tab. 5.4: Systematic error effects of the REA test system applied in the Bellheim field experiment.

effect	relative flux error (including ca. 95% of cases)
w-measurement: - offset	-10% ... +10%
- vertical tilt of wind vector (without offset)	-20% ... +10%
delay time: - valve control response (66 ms)	0% ... -10%
- total, including sensor separation	0% ... -25%
non-constant sampling flow	-40% ... -80%

There are basically two ways, in which the described error effects can be accounted for. The first way is to correct the measured concentration difference $\Delta\bar{\mu}_c = (\bar{\mu}_{c,U} - \bar{\mu}_{c,D})$ for each individual effect as parameterised in Section 5.2. With the corrected difference, the flux could then be determined according to Eq. 2.79 using the 'ideal' b-factor. However, this procedure has the disadvantage, that the variability in the non-constant flow effect (Fig. 5.22) is too large for an appropriate parameterisation and that the mutual interference between the various effects is not considered. Therefore it was decided to use the second alternative way: the overall combined error effect is included in the so-called 'effective' b-factor. It is estimated for each individual case by simulation with the corresponding EC *temperature* measurements including all known systematic error sources of the REA system. In addition to the effects listed in Table 5.4, also the applied deadband with a constant absolute width of 5 cm s^{-1} (cf. Section 3.4.3) can be directly incorporated in the simulation. The resulting effective b-factor b_{eff} can be inserted in Eq. 2.79 together with the error-affected measured concentration difference to yield a corrected trace gas flux. A schematic overview of the entire REA flux evaluation is given in Fig. 5.24.

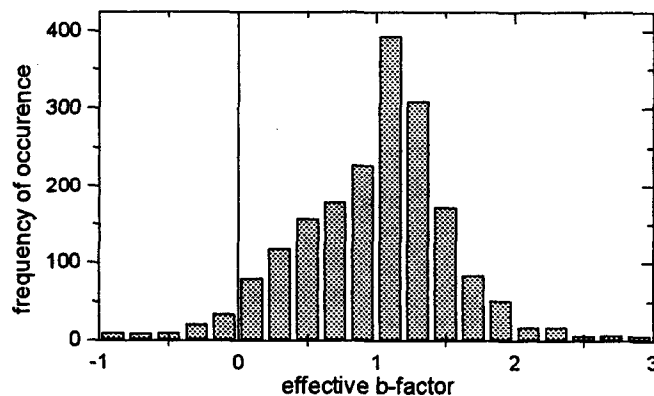


Fig. 5.23: Histogram of effective b-values simulated with EC temperature time series for the correction of the non-ideal characteristics of the REA field measurements.

The described evaluation procedure was performed for each 10 min interval. The combined effect of all non-ideal characteristics led to a general decrease in the simulated conditional mean difference and thus to an increase in the effective b-factors. The histogram in Figure 5.23 shows, that they are on average about two times higher than the ideal values in Tab. 5.2. However there is a large scatter including even some negative values (i.e. concentration difference and flux have opposite signs).

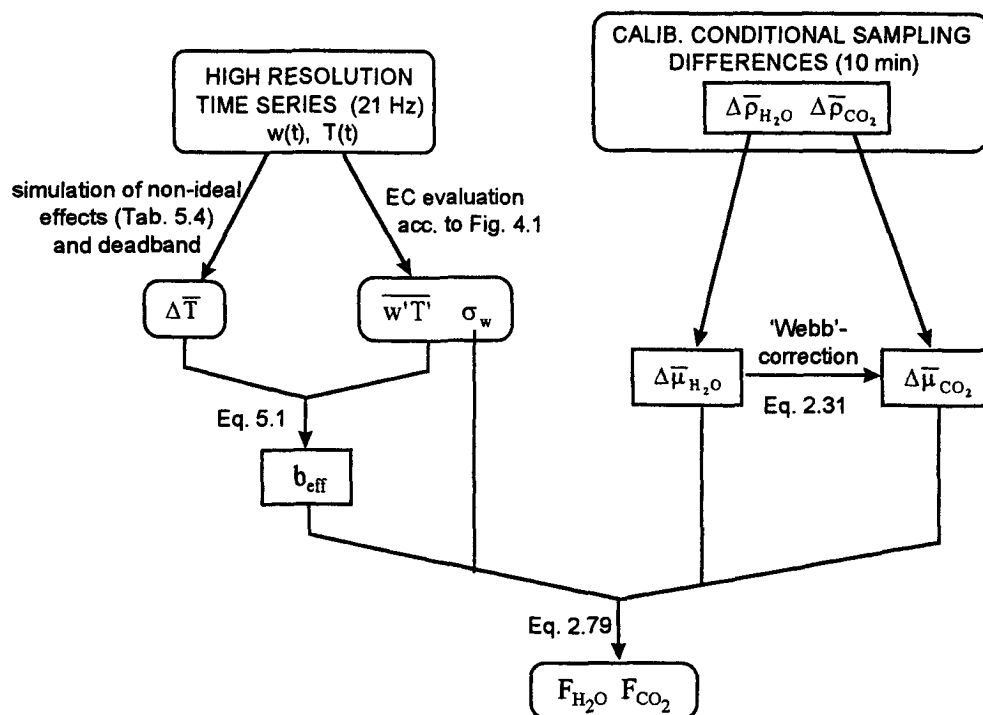


Fig. 5.24: Processing steps for the calculation of CO_2 and H_2O fluxes from REA measurements.

Like the eddy correlation and the profile method, the REA concept was derived in terms of the trace gas mixing ratio (cf. Eq. 2.79) which allows a simpler flux calculation than the absolute gas density. Thus the gas density difference measured by the REA system (cf. Section 3.4.2) first has to be converted to a difference of mixing ratio (relative to dry air). The influence of the correlated density effect of water vapour can be considered fully analogous to the profile method calculations (Eq. 4.31). However, this simple correction is only appropriate for REA systems in which the trace compound is analysed directly in the gas phase, like in the present case. If accumulation devices like cryo-traps or adsorbents are used, the correction gets generally more complex (cf. Pattey et al., 1992).

5.3.2 Data Rejection

The REA method shares the methodological and some instrumental problems of the eddy correlation method. They limit for example the accuracy of the w measurement and also the estimation of a representative b -factor. Therefore most of the rejection criteria for EC listed in Table 4.3 also apply for the REA measurements. Additionally, specific problems of the REA method have to be considered. For conditions with a small σ_w , the effective sampling time becomes very short due to the constant deadband of 5 cm s^{-1} . In order to avoid small samples and thus large statistical uncertainty of the conditional means, a minimum sampling time share of 1/3 of the whole interval is demanded for each line. For a Gaussian distribution of the vertical windspeed, this corresponds to a lower limit for the standard deviation of $\sigma_w = 2.5 \cdot w_d$ and thus $\sigma_w > 12.5 \text{ cm s}^{-1}$ for the present case. A survey of all applied criteria and the respective rejection percentage is given in Table 5.5. In total, over 40% of the measurements were discarded. The resulting final dataset of the evaluated REA fluxes with all rejection criteria applied is displayed in Appendix B together with the results of the common methods (evaluated in Chapter 4).

Tab. 5.5: Overview of rejection criteria for the evaluation of the REA field measurements.

critereon		quantity	rej. percentage
instrumental problem:	- logging failure (data gaps > 5 %)	all	4.4 %
methodological problems:	- extreme stability ($ z/L > 2$)	all	13.3 %
	- low wind eddy corr. ($r_{uw} > -0.1$)	all	19.5 %
	- low sampling time share ($\sigma_w < 12.5 \text{ cm s}^{-1}$)	all	31.9 %
total combined rejection:		all	42.5 %

In the REA test system, condensation of water vapour was likely to occur, similar to the closed path EC and profile systems, but its occurrence could not be clearly identified, because no absolute water vapour signal was available. Condensation water in the sampling tubes strongly affect the water vapour measurements, but the influence on CO₂ (through absorption/desorption effects) is assumed to be small, because the equilibrium CO₂ density in liquid water does not exceed the atmospheric CO₂ concentration.

5.3.3 Error Estimation

The relative error of the measured REA fluxes strongly depends on the mean concentration difference, that has to be detected by the analyser system. This should represent no major problem for the water vapour, but for the carbon dioxide, the fluxes and thus the differences to be resolved were generally small during the field campaign. Moreover, due to the strong damping effects (caused especially by the non-constant sampling flow), the concentration difference was up to 5 times lower than expected, which made the measurements much more sensitive to random as well as to systematic error sources. Figure 5.24 shows the range of the CO₂ and H₂O concentration difference detected by the REA test system during the Bellheim experiment. The values are mostly below 1 ppm for CO₂ and below 0.2 mmol mol⁻¹ for H₂O. Compared to the corresponding ambient air concentrations (cf. Fig. 4.41) this corresponds to a relative value of about 0.25 % and 1.3 % respectively.

Random Error Sources

As discussed in Section 4.3.2, a similar random error for the finite turbulence measurement has to be expected for all micrometeorological methods. It depends on the environmental conditions (cf. Fig. 4.27) but rarely exceeds 20%. The random instrumental noise of the REA gas analyser is basically the same as for the EC measurements, because identical instruments were used. However, in the REA system, the signal was averaged internally over 1 s and was sampled every 5 s. For the final 30 min means, 150 samples were averaged (for each analyser line configuration) resulting in an instrumental noise error of about 0.01 ppm for CO₂ and about 0.005 mmol mol⁻¹ for water vapour. In addition, the limited discretisation of the data logger has to be considered particularly for CO₂, because it corresponds to a noise effect of about 0.1 ppm which is significantly higher than the analyser noise effect. This value is within the range of the measured concentration differences displayed in Fig. 5.25. For typical (average) values, the total noise effect leads to relative errors of about 30% for CO₂ and 10% for H₂O respectively.

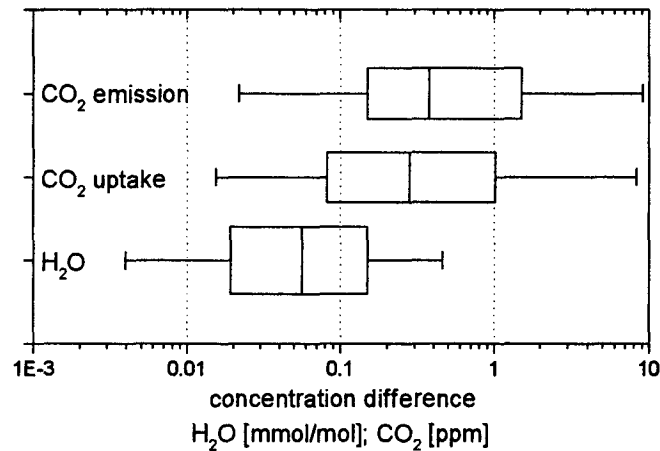


Fig. 5.25: Box-plots of the concentration differences for CO₂ and H₂O as observed by the REA test system during the Bellheim experiment (explanation of box-plot see Appendix C).

Systematic Error Sources

Small relative differences as observed in the REA measurements are also sensitive to systematic error effects, which might be neglected under normal conditions. A possible offset in the analyser characteristic was avoided by the regular switching of the analyser channels. Yet, a CO₂ difference in the order of the measured values (0.3 ppm) could also be produced by a very small pressure difference of only 1 mbar or a temperature difference of 0.3 K between both measurement cells! Such systematic differences were tried to be prevented by the specific setup with a venting of the analyser to ambient air. However, small pressure differences are difficult to identify (especially with two separate pressure sensors) and a measurement directly within the cells is not possible. Thus a systematic error effect due to a difference in the flowrate or the flow resistance can not be generally excluded.

Other systematic effects already mentioned before are the condensation of water vapour inside the sampling tubes and a non-appropriate estimation of the effective b-factor from the temperature time series (cf. Fig. 5.22). Both can be assumed to result in an underestimation of the trace gas fluxes.

6 DISCUSSION

The measurements and simulation results (presented in Chapter 4 and 5) will be discussed and compared to related findings of other studies in the following. First, the flux measurements of the different methods are compared and validated by several approaches. Then the applicability of the REA method in comparison to the common methods is discussed under various aspects. Beside the general theoretical validity of the REA concept, the importance of various practical problems are considered and possible technical solutions are discussed. Finally, the potential applicability of the REA method for typical trace gas flux studies is examined.

6.1 Comparison and Verification of Measured Fluxes

6.1.1 General Considerations

It was shown in the previous chapters, that micrometeorological flux measurements may be influenced by many different error sources not only due to instrumental problems but also due to non-ideal setup and environmental conditions. Since there exists no general calibration or absolute reference for trace gas fluxes, the overall performance of the measurement systems and the accuracy of the results may only be checked by indirect verification methods. A commonly applied verification method for turbulent energy fluxes (cf. Section 2.1.4) is the test of the surface energy budget closure. It is investigated for the eddy correlation and the profile method in Section 6.1.2. It represents a relatively straight check for the water vapour flux (latent heat flux), but it may also be regarded as an indirect partial test of other trace gas fluxes. They are often measured with the same setup (especially with the same windspeed sensors) at the same point and are thus subjected to the same (non-ideal) environmental conditions. However, trace gas specific problems are not covered by the energy balance test, and it is not directly applicable to the REA technique, because the sensible heat flux cannot be measured with that method.

Another more general approach is the simultaneous application and comparison of different measurement methods for the same trace gas flux. In principle, such a verification is more valuable if the measurement techniques rely on totally independent concepts, like the eddy correlation and porometer measurements compared in Section 6.1.3. However such an analysis can yield only rough results, because it requires several assumptions and upscaling calculations. The comparison among the micrometeorological methods in Section 6.1.4 is more direct but does not imply total independence, because all micrometeorological methods rely for example on the constant flux layer concept with homogeneous stationary conditions and $\bar{w} \neq 0$. Hence the agreement of different flux measurement techniques is not a sufficient criterion for their validity. However, the comparison of two (or more) methods can identify inconsistencies and potential error sources and thus helps to create confidence in the flux results. Often, this is the only way to assess the quality of trace gas flux measurements.

A comparison of different methods represents a mutual verification and it is not clear a priori, which method is responsible for a possible disagreement. However, the eddy correlation is often considered as a reference in practice because it requires the least semi-empirical assumptions and allows independent tests of consistency, because the EC time series contain much more information than just the integral

covariance flux. For example the variances or correlation coefficients and the spectral forms can be compared to common similarity functions (Section 4.1.6). Especially the eddy correlation is assumed to be less sensitive to inhomogeneous surface conditions than the profile method (cf. Section 2.6.1). Thus the following strategy was applied in the following sections: first the flux results (especially for the EC method) are verified and discussed under favourable large fetch conditions, and for the subsequent comparison of limited fetch conditions, the eddy correlation results are used as a reference for the profile and the REA method.

A direct comparison of flux measurements with results reported in the literature is of limited evidence and has to be interpreted with care. For the present study, a direct comparison with literature results is regarded to be most meaningful for the ozone deposition. It can be normalised for the ambient concentration and for the aerodynamic conditions (cf. Sections 2.1.3 and 4.4.4). Although a direct comparison of the surface resistance would be more evident, only deposition velocities are usually reported in literature. Ernst et al. (1991) and Sprung (1993) measured ozone fluxes over wheat and barley field at the same Bellheim site. Ernst et al. give a total range of observed deposition velocities of $0.05 - 1.2 \text{ cm s}^{-1}$ with highest values for daytime and lowest for night. This range is in good agreement with the findings of the present study displayed in Fig. 4.40. Sprung calculated monthly means of $0.2 - 0.4 \text{ cm s}^{-1}$ for daytime and about $0.1 - 0.25 \text{ cm s}^{-1}$ for night. His daytime values are significantly lower than the averages of the present study whereas the nighttime values agree well. A survey of various publications is given by Colbeck and Harrison (1985). The present results are comparable to the reported average deposition velocities for agriculture crops of $0.17 - 0.3 \text{ cm s}^{-1}$ for night and $0.6 - 0.8 \text{ cm s}^{-1}$ for daytime.

6.1.2 Closure of the Surface Energy Budget

As mentioned in Section 2.2.1, the mass change of a trace gas species in the soil-vegetation compartment is generally not measurable and thus can not serve as a reference for the local surface flux in practice. The change of the energy content, however, is much easier to determine because it is mainly connected to a temperature change (cf. Sections 3.5.2 and 3.5.3). Hence the closure of the surface energy budget (Eq. 2.9) can be used as an independent validation of the turbulent energy fluxes. The radiative energy transfer is also included in the budget equation. It is represented by the net radiation R_n which is easy to measure with a reasonable accuracy (cf. Section 3.5.1).

For the present field experiment, the closure of the energy budget can only be tested for the triticale field and thus for the SW wind sector. This is primarily because radiation and soil measurements are only available for this plot, and secondly because the fetch has to be large enough to provide turbulent measurements with a comparable source area (cf. Schmid, 1997). The determination of the non-turbulent energy fluxes was already discussed in Sections 3.5.1 - 3.5.3. The turbulent sensible and latent heat flux H and LE were calculated according to Eqs. 2.32 and 2.33 from the eddy correlation and profile measurements of water vapour and temperature. Figure 6.1 shows the various energy budget components in the course of one full day. The main part of the absorbed incoming radiation is transferred to the atmosphere by H and LE . They are of about similar importance in the present case with a predominance of LE during the first half and of H during the second half of the day. As illustrated in Fig. 4.36, the relative contribution of H and LE (i.e. the Bowen ratio) significantly changed during the field measurements due to the senescence development of the triticale plants.

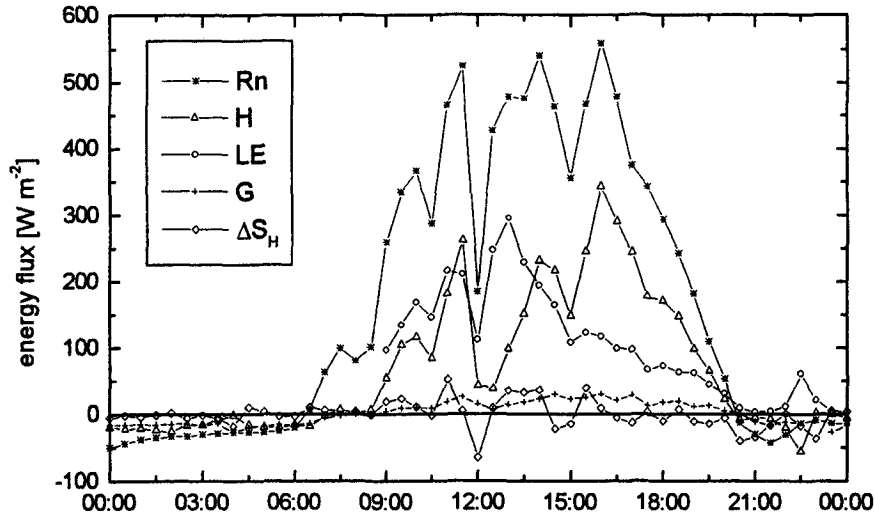


Fig. 6.1: Diel course of all energy budget components of the triticale field on 15 July 1995 with SW wind conditions; the displayed values for H and LE are a combination (average) of the eddy correlation and the profile measurements.

According to the comments in Section 3.5.2, the energy storage in the canopy layer consists of two terms. The assimilation energy ΔS_A is generally not displayed here, because it can be neglected for the triticale field compared to the other terms. With the observed CO_2 flux range of about $\pm 5 \mu\text{mol m}^{-2} \text{s}^{-1}$ (cf. Fig. 4.35, 180° - 260°), the corresponding energy flux (Eq. 3.14) is always smaller than $\pm 2.5 \text{ W m}^{-2}$. The heat storage change of the canopy ΔS_H (Eq. 3.13) as well as the soil heat flux G (Eq. 3.15) are also relatively small but can not be neglected. It can be noticed, that they behave differently in the course of the day, although both represent a heat storage within a solid body exposed to radiation. The difference becomes even clearer, if their general relation to the net radiation flux is analysed. For the soil heat flux G, a linear (proportional) dependence can be found (see Fig. 6.2). It amounts to 7.5 % of Rn during daytime and to about 70% during the night.

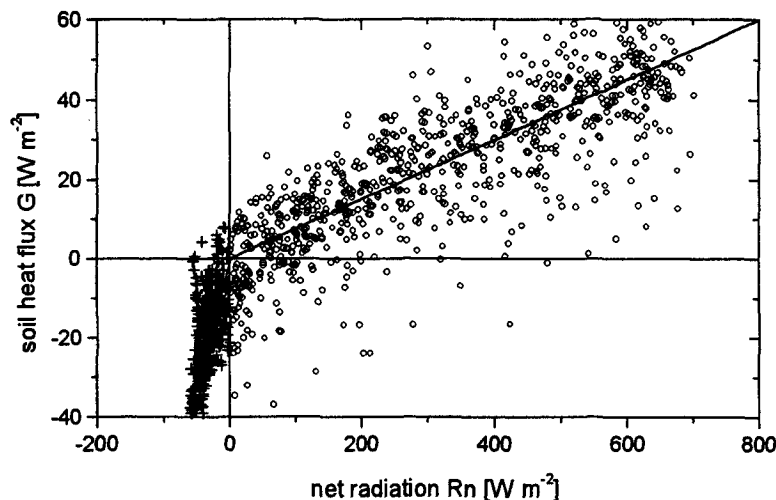


Fig. 6.2: Relationship between soil heat flux and net radiation for daytime (circles) and nighttime (crosses) for the entire field campaign; linear fits yield ratios of 0.075 and ca. 0.7 respectively.

The heat flux into the canopy biomass ΔS_H also exhibits a distinct diurnal variation (Fig. 6.3) but not proportional to Rn. It is highest in the late morning, goes back to zero in the afternoon and reaches the lowest negative values in the evening. This course is more or less proportional to the temporal derivative

of R_n and can be explained by the small heat capacity of the canopy. Consequently, it is always in a dynamic thermal equilibrium with R_n and the surrounding air. A change in the heat storage only occurs, if R_n and thus the equilibrium condition changes. The soil, in contrast, represents an almost infinite heat reservoir that is never in equilibrium with the environment, because the heat transfer within the soil is much slower than the environmental changes. The observed magnitude of G and ΔS_H relative to R_n is in good agreement with data given by Hicks and McMillen (1988) for corn.

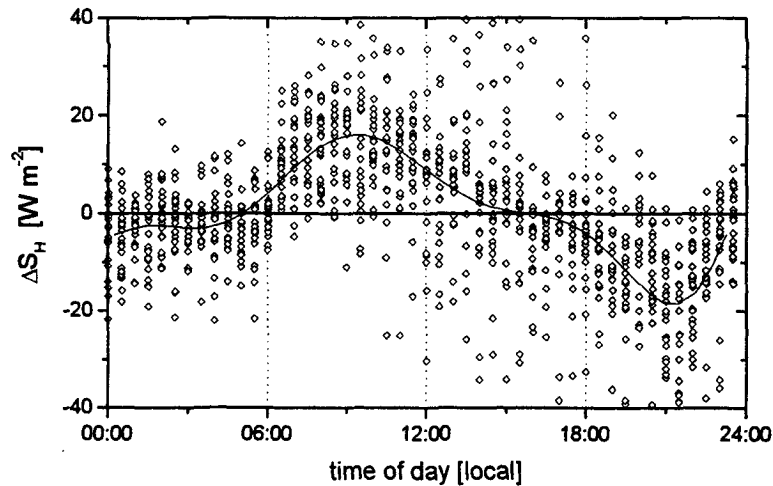


Fig. 6.3: Diurnal variation of canopy heat storage change for the triticale field; smooth curve was determined as polynomial regression of 9th order.

The closure of the energy budget for the triticale field is illustrated in Figure 6.4, where the sum of the turbulent energy fluxes is plotted against the summed non-turbulent fluxes. The agreement is generally good with a slight systematic difference of about 11% for both eddy correlation and profile methods (slopes of linear regression lines 0.89 and 0.88 respectively). The random scatter around the regression line is between 5 and 10 % for larger fluxes and at least 10 $W m^{-2}$ near zero (Fig. 6.4b) and thus well within the predicted uncertainty for finite turbulence measurements presented in the previous section (Fig. 4.27). However, the systematic residual in the energy budget can not be explained by random measurement errors. The excellent agreement between the eddy correlation and the profile measurements indicates either an unknown systematic error in the non-turbulent fluxes or a conceptual error in the assumptions for the budget closure. The second possibility is supported by Laubach (1996) who investigated many published energy budget measurements. He found a large scatter in the ratio of the turbulent and non-turbulent fluxes $(H+LE)/(R_n-G-\Delta S)$ with an average value of about 0.85 corresponding to a energy budget residual of 15 %.

He explains this phenomenon with the contribution of large scale convective structures leading to a mean vertical windspeed $\bar{w} \neq 0$. As shown in Fig. 4.38, the canopy temperature of the triticale field at the Bellheim site became very high during the senescence development leading to a probably hotter surface than for the surrounding fields still in the growing state. This could have produced a heat island effect during high radiation periods, which favoured the formation of a local coherent circulation (thermal) with a positive mean vertical windspeed. Panin et al. (1996) propose a method to correct the fluxes for such effects. They describe the inhomogeneity influence as non-detected low frequency contributions to the turbulence cospectrum. However a sound quantitative parameterisation for the flux correction was not presented up to now.

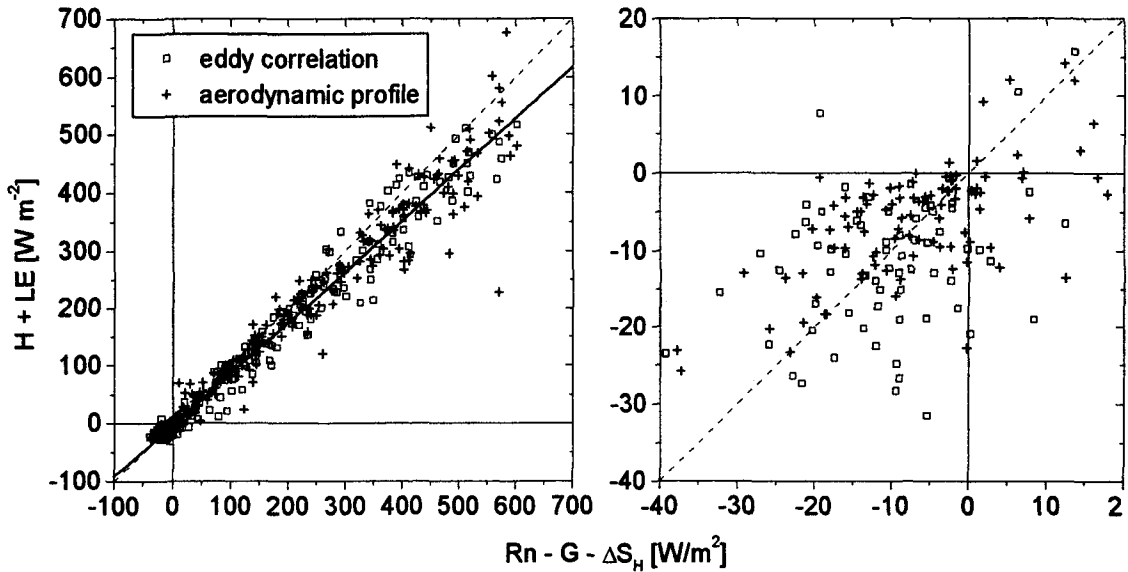


Fig. 6.4: Illustration of the energy budget closure for the triticale field: sum of turbulent energy fluxes determined by eddy correlation and aerodynamic profile method versus sum of physical energy fluxes (available energy); (a) all values, with linear regression curve; (b) small values, mainly nighttime cases.

The influence of fetch condition on the closure of the energy budget is illustrated in Figure 6.5. The residuals of the measured budget (using aerodynamic profile fluxes) are plotted together with the fetch length against the wind direction. Within the favourable SW wind sector analysed so far, the residuals are smallest with average values of about 20 W m^{-2} and maximum values (95% percentile) of about 100 W m^{-2} . For other wind directions, the residuals are much higher indicating, that the smaller fetch length is not sufficient for turbulent flux measurements representative for the triticale field alone. The corresponding results of the eddy correlation measurements (not shown here) are very similar to Fig. 6.5.

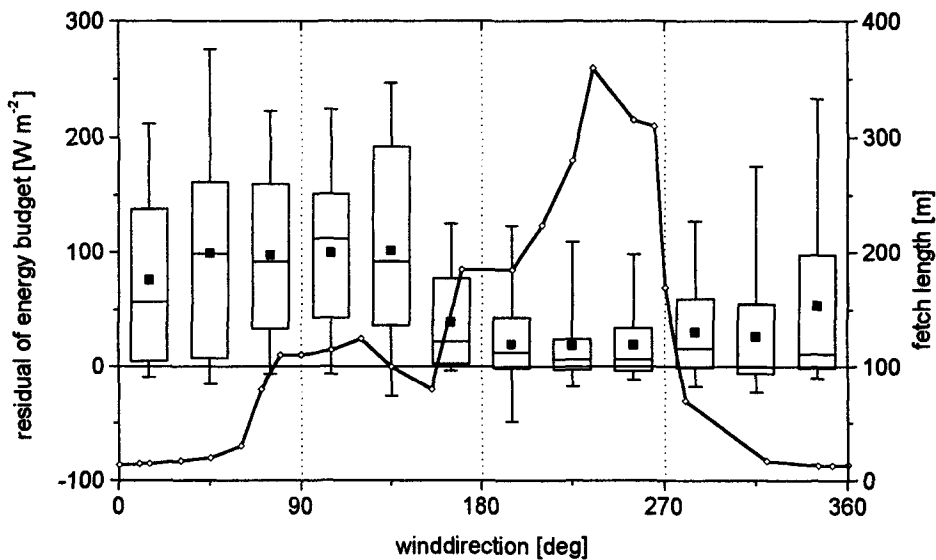


Fig. 6.5: Residuals of the surface energy budget including aerodynamic profile fluxes, displayed as boxplots for different wind sectors; additional indication of the triticale field fetch (solid line).

6.1.3 Comparison with Enclosure Measurements

As mentioned in Section 3.1.3, porometry measurements of the H₂O and CO₂ exchange were performed on the triticale leaves during the entire measurement campaign close to the micrometeorological towers. In principle, the respective results may also be used for a comparative verification of the micrometeorological flux measurements. However, due to the artificial environment produced in the chamber and due to the different scale of the source area, a comparison needs some assumptions and simplifications. While porometry, usually applied for plant physiology studies, addresses spatial scales of 10⁻² to 10⁻¹ m, the micrometeorological techniques integrate over source areas with a characteristic length scale of 10¹ to 10⁴ m (see Sections 2.6 and 4.4.2). In order to compare the measurements performed at different scales, porometer data have to be upscaled to the entire canopy level. Experiments related to this problem are reported for forests (Herbst, 1995; Lindroth and Cienciala, 1996; Guenther et al., 1996) as well as for low vegetation (Dugas et al., 1991; Pattey et al., 1991; Desjardins, 1992; Christensen, 1996).

Since a comparison of different measurement methods may lose its significance if complex model calculations are included, the most direct upscaling approach for the porometry results was applied for the present study. The leaf exchange rates $F_c(L_i)$ derived from the chamber measurements were multiplied with the respective partial leaf area index $LAI(L_i)$ and summed over the active leaf levels:

$$F_c(\text{canopy}) = \sum_{\substack{\text{active} \\ \text{leaf layers}}} LAI(L_i) \cdot F_c(L_i) . \quad (6.1)$$

The contribution of plant parts other than the leaves (stalk, leaf sheath, awns and bracts) to H₂O as well as to CO₂ exchange was ignored due to the state of senescence (cf. Section 4.4.3). The partial LAI values in Eq. 6.1 were estimated from the results of the scanner and optical method displayed in Fig. 3.3 to 0.9, 1.5, and 0.8 m² m⁻² for the important leaf levels L1, L2, and L3, respectively. This simple upscaling disregards the influence of the artificial environmental conditions within the porometric chamber. This problem was minimised by (a) use of a small and flat leaf-chamber, (b) appropriate choice of chamber materials, and (c) optimised operation characteristics. Especially, the high exchange rate (30 min⁻¹) of the chamber air prevents the building up of a large excess or deficit of temperature, humidity and CO₂ concentration compared to ambient air (Willert et al., 1995). However, the high flushing rate may also reduce the leaf boundary layer resistance and lead to an overestimation of the gas exchange (cf. Rochette et al., 1991). For a comparison with micrometeorological methods, also the contribution of the soil to the net trace gas flux of the ecosystem has to be considered. Unfortunately, no specific soil exchange measurements are available for the present field campaign. As far as water vapour is concerned, the soil evaporation is assumed to be small and thus primarily negligible compared to active plant transpiration (cf. Rutter, 1975:150). For the daytime CO₂ emission from the soil under a growing and senescent wheat canopy, Denmead (1976) observed values roughly proportional (ca. 25 %) to the total plant CO₂ uptake. Thus the daytime net ecosystem flux may be estimated as

$$F_{CO_2}(\text{ecosystem}) \approx 0.75 \cdot F_{CO_2}(\text{canopy}) . \quad (6.2)$$

The majority of porometry measurements addressed the diurnal (seasonal) behaviour of the flag leaf (L1) of the triticale plants. In the early senescence phase (20 June, 27-30 June), additional measurements on all other active leaves were performed (cf. Busch et al., 1997). During these days, micrometeorological flux measurements were unfortunately not suitable for a direct comparison due to the prevalence of winds from NW and NE. The only day with favourable fetch conditions (SW wind direction) and a more or less complete diurnal course of porometry and EC data is the 5 July. Although porometry

was performed only on flag leaves during this day, the upscaling to the entire canopy is possible due to special conditions. For the water vapour exchange, the following assumptions have been made: (a) only leaf levels 1 (flag leaf) and 2 were still active on 5 July, (b) the transpiration rates of leaf 1 and 2 were not significantly different at that time.

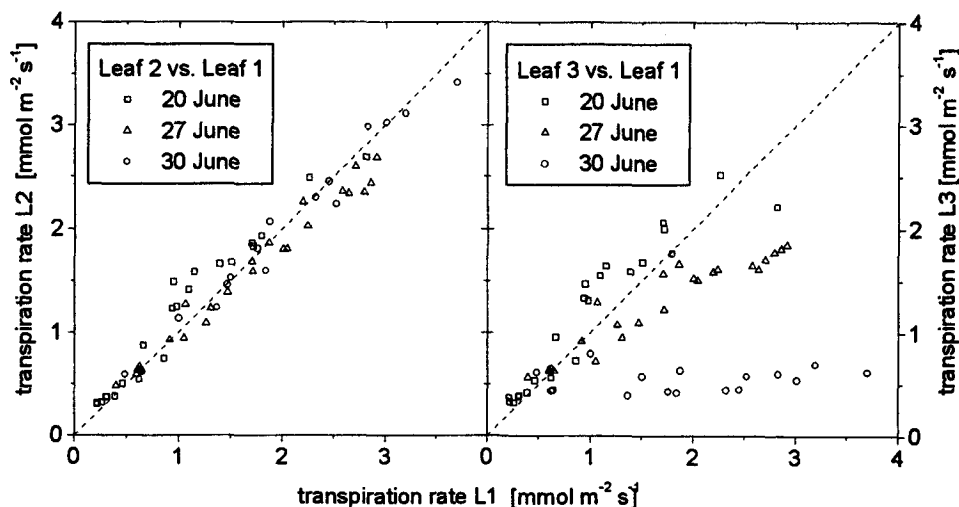


Fig. 6.6: Comparison of transpiration rate of different leaf levels at 20, 27 and 30 June: (a) Leaf 2 vs. Leaf 1; (b) Leaf 3 vs. Leaf 1.

The second assumption is based on the observations on those days, when porometry measurements were performed on the complete set of active leaves (dates see above). In Figure 6.6 the transpiration rates of leaves L2 and L3 are plotted against the values of the flag leaf. In the first case, the observations are almost equal during the whole observation period, whereas the transpiration activity of Leaf 3 was only similar at the beginning and decreased rapidly. Hence, upscaling of the porometrically determined fluxes to the entire canopy was calculated as the product of the observed flag leaf's transpiration rate and the sum of active LAI ($2.4 \text{ m}^2 \text{ m}^{-2}$; leaf area index of leaf 1 and 2, cf. Fig. 3.3). Figure 6.7 shows the daily course of the net H_2O flux as measured by the eddy correlation technique and upscaled from porometry. The agreement is reasonably good with somewhat higher porometric values (20-30%) in the afternoon. The distinct minima of both methods around 14:00h and 16:00h can be attributed to a substantial decrease of global radiation (Fig. 2a) due to a temporary cloud cover resulting in a reduction of the leaf temperature (stomatal saturation vapour pressure) as well as a higher stomatal resistance.

As far as CO_2 exchange is concerned, porometry measurements showed that, except for the flag leaf, all other leaves had terminated their activity already by about 30 June. The different behaviour of leaves 1 and 2 with respect to transpiration and photosynthetic activity can be explained by the progressed degradation of chlorophyll, indicated by the observed yellowing. Hence, for the upscaling of the leaf exchange rates to the entire ecosystem Equations 6.1 and 6.2 were evaluated with the flag leaf measurements only. The estimated net CO_2 flux is shown in Fig. 6.7 together with the corresponding eddy correlation measurements. As observed for water vapour, also the CO_2 fluxes show a sharp drop in early afternoon caused by the collapse of global radiation. The agreement of porometry and eddy correlation data is even better than for H_2O . The obvious differences after 18:00h is due to a change of the fetch of the eddy correlation measurements. The wind direction turned to the north-easterly sector resulting in a source area covering the neighbouring sugar beet rather than the triticale field. Therefore, the peak of the eddy correlation CO_2 flux is due to the sugar beets which were in full growing state, in contrast to the triticale plants.

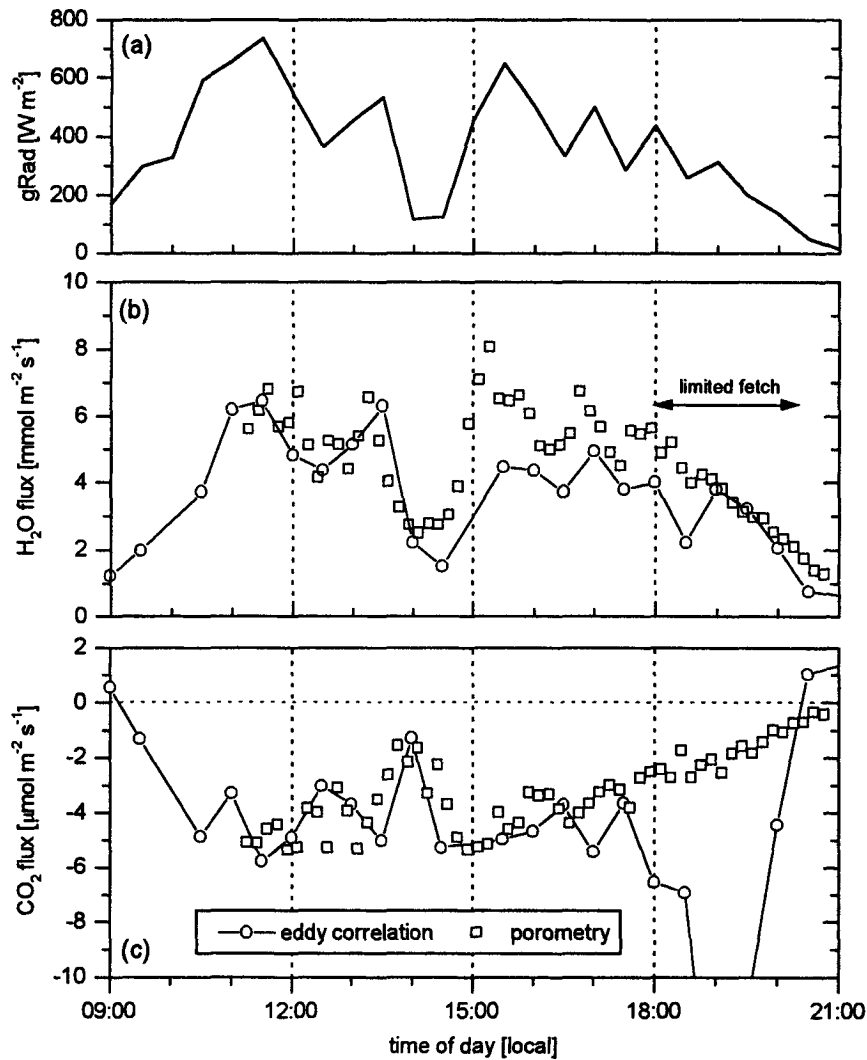


Fig. 6.7: Comparison of eddy correlation and upscaled porometry gas exchange fluxes of the triticale field on 5 July 1995: (a) global radiation; (b) water vapour flux; (c) carbon dioxide flux.

The presented comparison of independent methods, although based on a limited dataset, supports the validity of the measured fluxes. The micrometeorological method is also able to describe fast fluctuating (non-stationary) conditions in an appropriate way. Moreover, the agreement of fluxes determined on totally different scales indicates that the spatial variability (between individual plants) is relatively small and single leaf exchange measurements are on average representative for the entire field.

6.1.4 General Comparison of Micrometeorological Methods

In the foregoing sections, the quality of the eddy correlation measurements was verified with independent flux measurements (non-turbulent energy fluxes and enclosure measurements). Although a direct verification for inhomogeneous surface conditions was not possible, the eddy correlation method is assumed to be least sensitive to such situations in that it detects an effective average flux of the respective source area (cf. Section 6.1.2). Hence in the following comparison of the micrometeorological methods, the EC results will be generally used as a reference for the profile and REA measurements.

An exemplary four-days-period of H_2O and CO_2 flux results is displayed in Figure 6.8. It represents an extract of the complete dataset given in Appendix B and includes varying wind direction and radiation

conditions. The time series obtained by all three micrometeorological methods show roughly similar diurnal courses following the solar radiation. The REA method reveals on average a relatively good agreement with the EC method for CO_2 but tends to underestimate the water vapour flux (especially on the first day). In contrast, the profile method yields good agreement for H_2O but often poor results for the CO_2 flux (especially on the last day). Figure 6.8 also illustrates the effect of the various rejection criteria applied to the datasets (cf. Sections 4.3.1 and 5.3.2). There are often large gaps in the time series particularly during nighttime due to condensation problems or extreme stability conditions. Since the rejection procedure was not the same for all methods, a direct comparison of the flux results is not always possible. This fact has to be considered in the following overall verification by means of scatter-plots, which is first presented for the common profile method and afterwards for the REA technique.

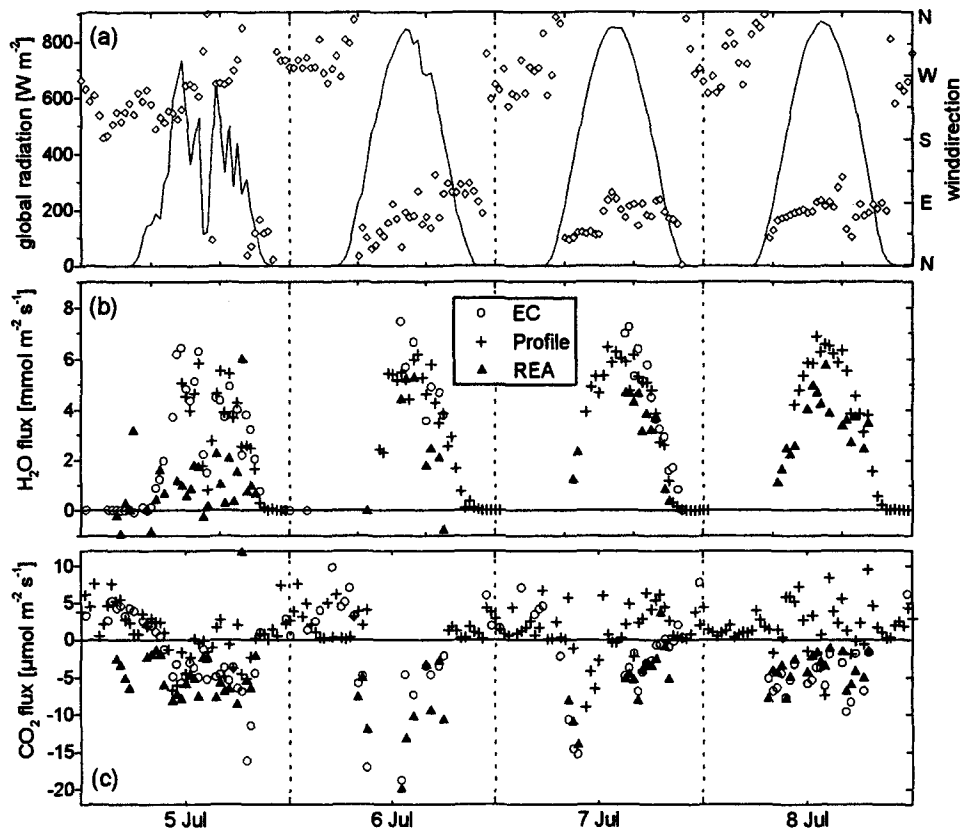


Fig. 6.8: Exemplary time series of (a) global radiation (solid line) and wind direction (diamonds), (b) H_2O flux, and (c) CO_2 flux obtained by three micrometeorological methods: EC (circles), REA (triangles), and aerodynamic profile method (crosses).

In Figure 6.9, the aerodynamic profile fluxes for the different trace gases are plotted against the respective eddy correlation values. Using two different symbols types, it is generally distinguished between cases with favourable fetch conditions and thus comparable source areas (fetch length > 200 m, SW sector) and cases with limited fetch conditions (other wind directions; cf. Fig. 4.34). Additionally the correlation coefficient (and the no. of samples) is displayed for a linear relationship through zero. For the water vapour flux (Fig. 6.9a), a very good agreement without systematic deviations is observed, as already indicated by the energy budget closure in Section 6.1.2. The agreement for limited fetch (open symbols) is only little worse than for good fetch conditions as indicated by the high value of the correlation coefficient.

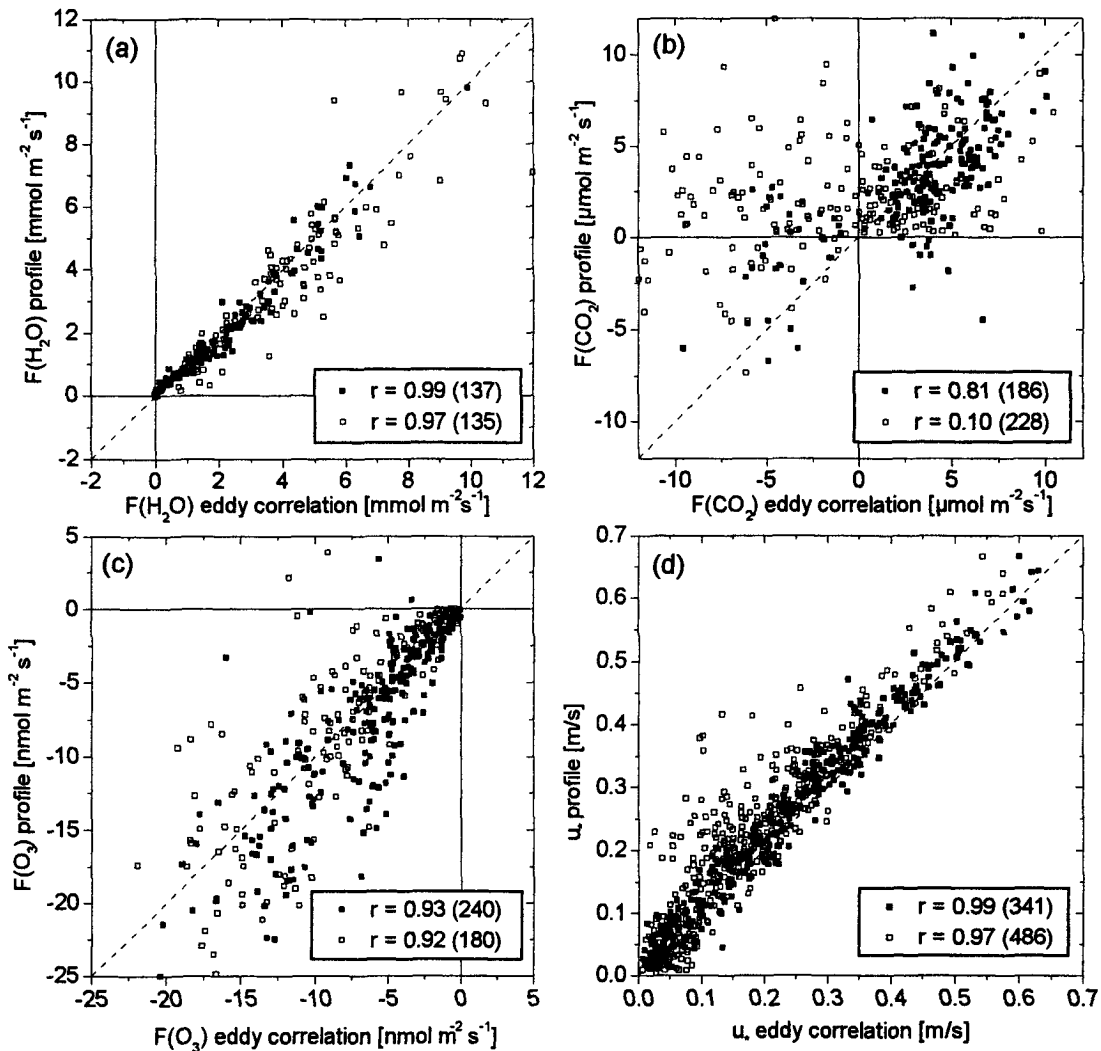


Fig. 6.9: Comparison of eddy correlation and aerodynamic profile measurements for the entire measurement campaign under favourable (solid squares: $180^\circ < \text{wdir} < 260^\circ$) and unfavourable fetch conditions (open squares: other wind directions): (a) H_2O flux; (b) CO_2 flux; (c) O_3 flux; (d) friction velocity; the displayed correlation coefficients (with number of samples) describe the linearity of the relationship through zero.

For the ozone flux (Fig. 6.9c), the variation is larger but also shows a mainly random characteristic without a significant dependence on the fetch condition. It may be attributed for the EC method to the uncertainty of the ozone sensor due to the very fast sensitivity drift (cf. Section 4.3.4), and for the profile method to sensor resolution problems as well as the influence of chemical reactions. No distinct systematic deviations between the two methods can be observed, in contrast to similar measurements e.g. by Sprung (1993) who found on average 30% lower values with the profile method.

The CO_2 flux results (Fig. 6.9b) reveal a clearly stronger dependence on the fetch conditions than the H_2O and O_3 fluxes. Although the scatter is generally large, a much better agreement is found for the SW sector ($r = 0.81$) than for the other wind directions ($r = 0.1$). In the latter group, a number of cases even show opposite signs of the profile and EC fluxes. The reasons for this behaviour may be on the one hand the larger variation of the CO_2 exchange between the neighbouring fields and on the other hand a generally larger sensitivity of the CO_2 concentration (relative to the profile differences) on surface inhomogeneities. The large scatter for the cases with favourable fetch can be attributed mainly to daytime profile measurements according to the effect displayed in Fig. 4.28. Because of the low resolution of the CO_2 profile sensor, relative deviations of 100% or more (different signs) have to be expected. For

nocturnal conditions, the random error of the profile measurements should be significantly smaller but also an error contribution from the EC fluxes has to be considered, because the correction effect of high frequency attenuation and detrending could amount up to 50%.

All micrometeorological flux techniques consist of mainly two parts: the wind and the trace gas measurements. The first component is equal for all scalar fluxes and thus an associated error would be observed in all trace gas fluxes. Due to the good agreement of the water vapour results, it can be concluded, that the error contribution of the wind measurements (profile or sonic) are very small and generally negligible compared to the errors in the respective trace gas measurements. The same information is obtained by comparing the friction velocity (momentum flux) determined by profile and EC methods, as displayed in Figure 6.9d. Their agreement is excellent for conditions with sufficient fetch with only a very small systematic difference and an almost constant absolute variability. For other wind directions, the scatter is only little larger, which supports the chosen evaluation method for the aerodynamic method with the application of the SW z_0 and d values for all wind directions (cf. Section 4.2.1).

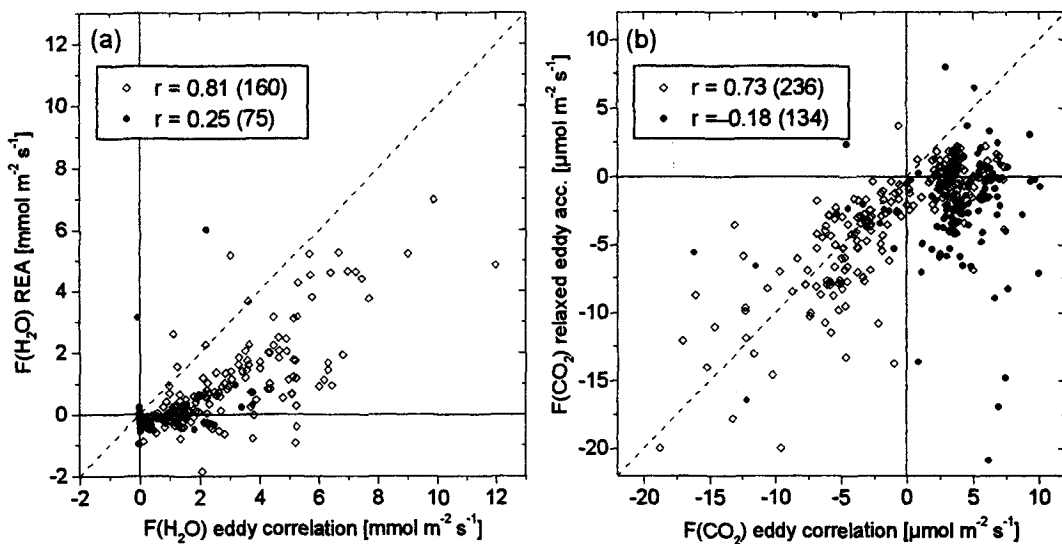


Fig. 6.10: Comparison of REA and eddy correlation measurements under unstable (open diamonds) and stable (solid circles) conditions: (a) H_2O flux; (b) CO_2 flux; the displayed correlation coefficients (with no. of samples) describe the linearity of the relationship through zero.

The flux measurements obtained by the REA test system for CO_2 and H_2O are plotted in Figure 6.10 against the corresponding eddy correlation results. For convenience, different symbols for stable and unstable cases are used (unlike in Fig. 6.9). Concerning water vapour, the agreement is poorer than for the profile method. The REA values are systematically lower than the EC results (ca. 50% for the unstable cases), often close to zero. This may be due to frequent occurrence of condensation water, which could be neither avoided nor detected with the current setup (cf. Section 5.3.2). Therefore an objective assessment and interpretation of the REA water vapour measurements is generally not possible.

For the carbon dioxide fluxes, a clear difference between deposition (assimilation) and emission (respiration) cases can be observed. The latter group comprises most of the stable nighttime cases showing a totally scatter around zero with frequent wrong signs ($r = -0.18$). The deposition fluxes mainly corresponds to daytime unstable cases, for which the agreement is generally better ($r = 0.73$). Although, the data points reveal a considerable scatter, no overall systematic deviation from the 1:1 line can be detected. The agreement between the REA and EC fluxes in the negative range is comparable to

the results obtained by Oncley et al. (1993) for a growing cotton field or Beverland et al. (1996a) for peatland, but not as good as the results by Pattey et al. (1993) for soybean and Hensen et al. (1996) for grassland. However, in contrast to the present investigation, all those studies presented limited datasets of only few days (mainly daytime cases).

The general underestimation of the REA emission fluxes might be an indication of a systematic negative offset in the concentration difference caused by instrumental problems (cf. Section 5.3.3). Another possible effect could be the sensitivity of the present REA setup on the eddy reversal frequency. The erf was generally low during unstable daytime periods and higher during near-neutral or stable conditions (Fig. 5.17a). However, no clear evidence could be found for that explanations and a plain interpretation is generally difficult due to the large non-ideal effects and uncertainties discussed in Sections 5.2 and 5.3. Thus the following detailed comparison of the different flux methods focuses on CO₂ deposition periods, which are supposed to be least affected by the instrumental problems of the REA test system.

6.1.5 Selected Diurnal Cycles of CO₂ Flux

After the overall comparison in the previous section, the micrometeorological flux results for CO₂ are compared and discussed in detail for some selected diurnal courses. Special attention is paid to the influence of varying fetch conditions on the flux measurements by the aerodynamic profile and REA method as well as on the individual measurement errors. The error bars for the profile and REA fluxes displayed in the following figures are mainly due to the discretisation error of the trace gas signal of about 0.7 ppm and 0.1 ppm respectively (Sections 4.3.3 and 5.3.3), combined with the finite sampling error of 5% - 20% (Section 5.3.2). The error bars for the reference EC values are omitted for the purpose of clarity. They mainly consist of the finite sampling error and are usually much smaller than for the other methods.

Case 1: 11 July 1995 (NE and SW wind direction)

Figure 6.11 shows an special diurnal cycle (11 July) including favourable as well as non-favourable fetch conditions. In the morning, the wind direction is in the north-easterly sector, but it begins to change before noon and almost continuously turns to the south-westerly sector. Thus the source areas for the flux measurements also strongly change in the course of the day (cf. Fig. 6.12). For SW wind directions, all 50% source areas are within the triticale field and a good agreement between all three flux methods can be observed. They show a small net CO₂ emission from the triticale field of about +2 μmol m⁻² s⁻¹. This value is assumed to be more or less representative of the triticale exchange for the entire day; it indicates that the triticale plants have almost terminated their senescence phase. In the morning hours (wind direction around 30 deg), the flux measurements are influenced by different vegetation types. The source area for EC, which is supposed to be also representative for REA, mainly covers the neighbouring sugarbeet field as indicated in Figure 6.12a. Accordingly, relative large negative CO₂ fluxes are observed with a good agreement between EC and REA. The scalar source areas of the two profile concentration measurements are plotted in Figure 6.12b. They are influenced to a different degree by both crop types. The source area of the lower level covers mainly the triticale field, whereas the upper level source area includes the sugarbeet field to a considerable part. Obviously, the flux results are controlled by the lower profile measurement in this case, since they are not very different from the afternoon results representative for the triticale field. The REA method also yields reasonable results during the non-stationary phase at midday, whereas the profile method indicates implausibly high emission exceeding the displayed range.

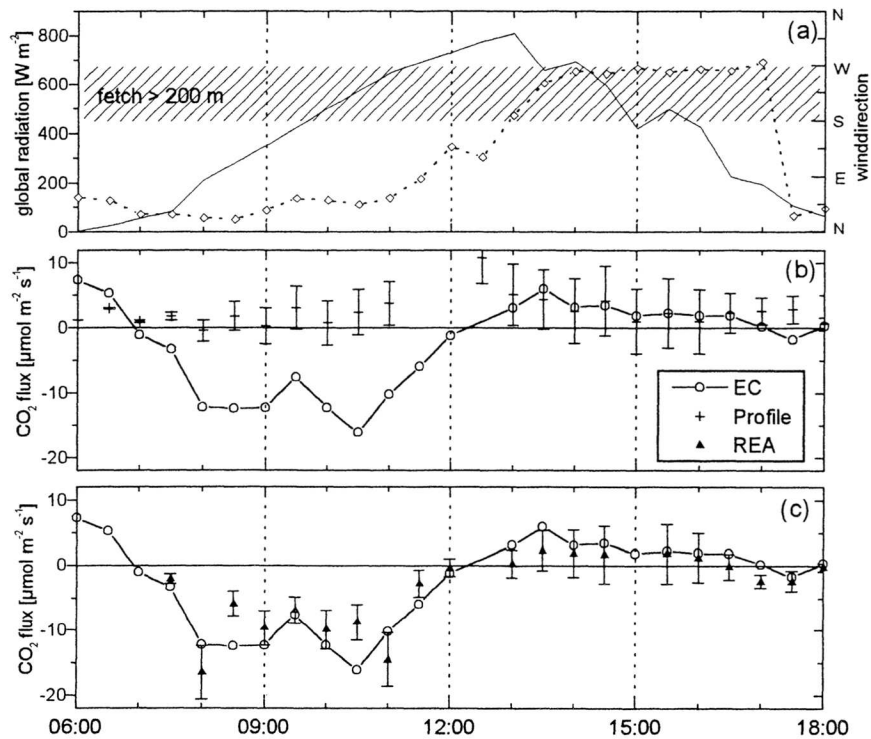


Fig. 6.11: Diurnal course of measured environmental parameters and CO_2 flux on 11 July 1995: (a) global radiation (solid line) and wind direction (diamonds); (b) CO_2 flux obtained by profile method (crosses) and eddy correlation (circles); (c) CO_2 flux obtained by REA (triangles) and eddy correlation (circles); error bars signify estimated 1σ measurement errors.

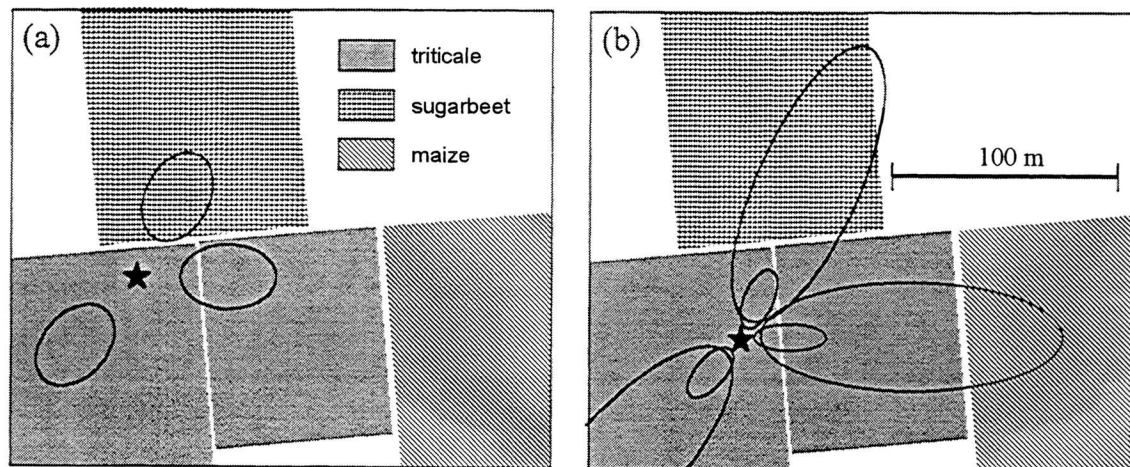


Fig. 6.12: Typical daytime 50% source areas for south-westerly, north-easterly, and easterly wind direction under moderately unstable conditions ($z/L = -0.2$) as typically observed on 8, 11, and 12 July 1995 during daytime: (a) for eddy correlation measurements; (b) for upper and lower profile measurements (with aerodynamic heights $z_4 = 3.35 \text{ m}$ and $z_1 = 0.75 \text{ m}$).

Case 2: 8 July 1995 (E wind direction)

The second case displayed in Figure 6.13 represents a more stationary situation than the first case with a relatively constant easterly wind direction (around 90°). In this sector, the fetch of the triticale field is about 100 m which is in the critical range for daytime unstable source areas (cf. Fig. 4.33). For the eddy correlation measurements, the fetch is well sufficient (cf. Fig. 6.12a), whereas the source area of

the upper profile level extends beyond the triticale and into the neighbouring maize field. The EC flux values mainly represent the assimilation of the triticale flag leaf (as observed for the 5 July in Section 6.1.3), which was already reduced due to the progressed senescence (see also Fig. 4.39). The short-term variations in the daily course cannot be assigned to the solar radiation, which shows an almost perfect undisturbed course. But on some occasions like in the morning or around 16:00h - 17:00h, the wind direction shifted to NE and therefore the influence of the sugarbeet field led to increased CO_2 fluxes. Overall there is a fairly good agreement between EC and REA mostly within the estimated error ranges. In contrast, the profile method shows predominantly positive values, yet with large error bars, which reflects on the one hand the poor resolution of the profile CO_2 analyser but also the systematic influence of the maize field adjoining to the east. It can be assumed, that the maize field in full growing state showed a even higher CO_2 uptake during this day than the senescent triticale field (represented by the EC flux results), and therefore the observed positive CO_2 fluxes are not representative for either of the fields. This behaviour may be explained by a lower CO_2 concentration over the maize field (due to higher assimilation) influencing mainly the upper profile level. The present example illustrates the specific fetch problem of the profile techniques, that depends on the deformation of the vertical scalar profiles by the surface inhomogeneity and does not generally provide a meaningful average flux value like the eddy methods. Differences in the roughness length of the agricultural plots also have to be considered. However, they are supposed to be of minor importance for the deviation of the profile results, because a fair agreement of the u^* values was found (cf. Fig. 6.9d).

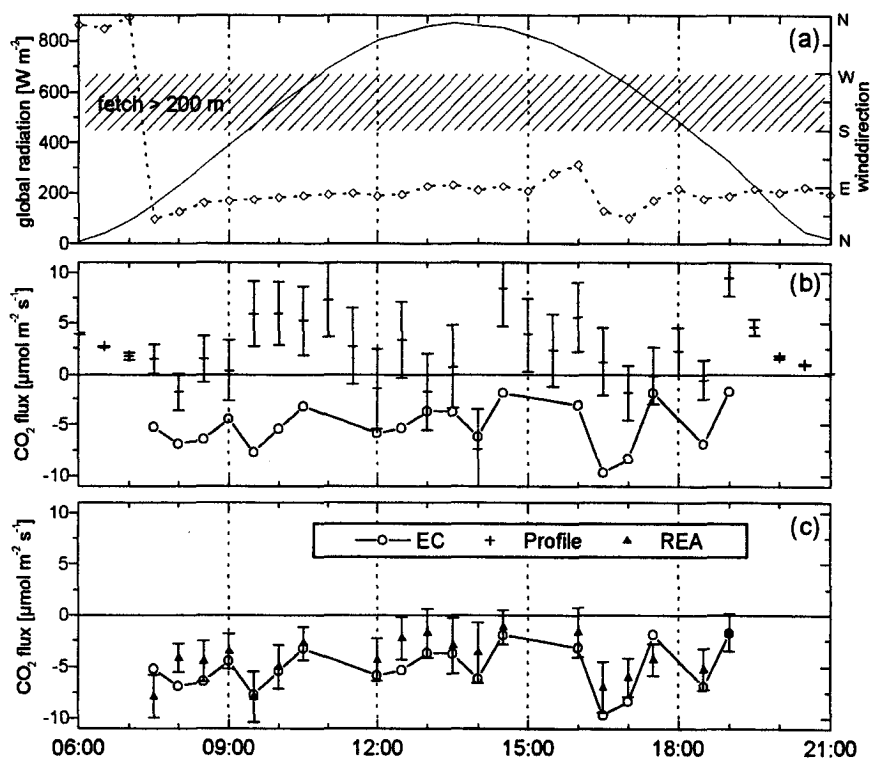


Fig. 6.13: Same as Fig. 6.11 but for 8 July.

In contrast to CO_2 , the ozone and water vapour fluxes derived by the profile method exhibited no significant dependence on the fetch conditions (cf. Fig. 6.9). This observation can be assigned on the one hand to the smaller difference in the O_3 uptake and evapotranspiration among the fields, but may also reflect differences in the specific gas exchange processes (see Sections 4.4.4 and 2.1.3).

Case 3: 12 July 1995 (SW and NW wind direction)

The third diurnal course presented in Fig. 6.14 shows predominantly favourable fetch conditions due to wind direction in the SW sector. Only in the late afternoon, the wind directions turned to NW for a few hours. According to the fetch conditions, the profile method shows good agreement with EC up to 15:00h, but deviates for the NW cases in a similar way like on 11 July (first case). The REA results follow much better the relatively fast variations of the EC data on late afternoon. However, between about 10:00h and 14:00h the REA fluxes show some systematic underestimation in the order of the error bar width corresponding to about 0.1 ppm in the measured concentration difference. As mentioned before, such a small difference may be easily produced by a small and in practice undetectable pressure or temperature difference within the differential analyser (cf. Section 5.3.3).

During the morning and evening hours, a more distinct deviation of the REA results is observed, which cannot be explained by the estimated random or systematic error effects. As discussed in the previous section, these cases are generally related to near neutral or stable conditions with a high eddy reversal frequency. In contrast to the REA method, the profile technique shows much smaller error ranges during stable conditions than for unstable conditions. This effect is related to the stability dependence of the vertical concentration gradients, which is discussed in Section 6.3.

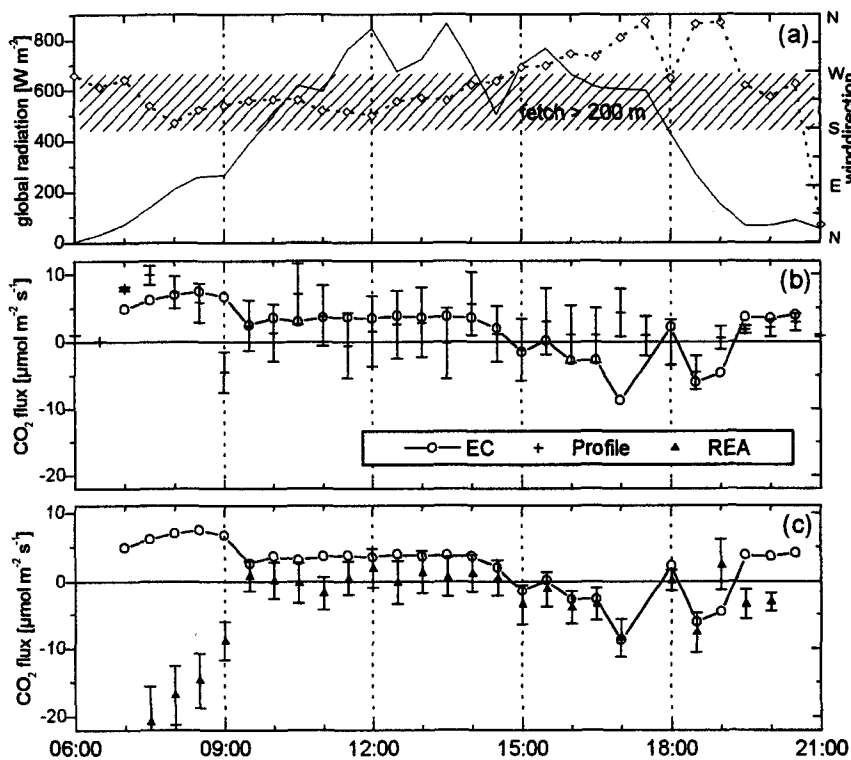


Fig. 6.14: Same as Fig. 6.11 but for 12 July.

The findings of this section, together with the results of Figure 5.4, indicate that the source area estimated for eddy correlation can be regarded as also representative for the REA method. The profile flux measurements have in general different source areas not only due to the slightly different measurement location (in the present experiment), but also due to the different physical principle (cf. Section 2.6.1). The latter can lead to large systematic deformations of the concentration profiles and hence erroneous flux results under specifically unfavourable fetch conditions (e.g. Fig. 6.13).

6.2 General Validity of the REA Concept

The flux validation in Section 6.1 revealed major problems in the REA system tested in the Bellheim field experiment. They often led to poor results, which are not necessarily representative for the REA method in general. However, it was also shown, that the eddy correlation fluxes and thus the measured high resolution time series are of good quality. They are thus suitable for the simulative analysis of the REA method performed in Section 5.1. In that way, the general applicability of the REA concept independent of practical shortcomings can be examined. The results are summarised and discussed in the following in comparison with literature values.

6.2.1 Ideal b-Factor

Up to now, no systematic variations of the b-factor with environmental conditions have been described in literature. Most authors give only an overall average value for observations predominantly under daytime conditions. Table 6.1 gives a survey of the reported values. They were derived from eddy correlation time series mainly of temperature but also of trace gases. All measurements were performed in the inertial sublayer (on towers) above various mostly homogeneous surfaces with different roughness lengths. The average b-factors obtained under unstable conditions range within 0.56...0.58 and are thus well comparable to the respective results of this study listed in Table 5.2. All studies indicate constant b-factors for unstable conditions, although individual values sometimes showed a considerable scatter with ranges from 0 to 1 (e.g. Oncley et al., 1993; Beverland et al., 1996a).

Tab. 6.1: Survey of average REA b-factors obtained by simulation studies with EC measurements in the surface layer (with $z/h_c > 2$).

Publication	scalar	average b-factor	stability range	surface type
Businger and Oncley (1990)	T, H ₂ O	0.6 ± 0.06 (n = ca.25)	stable and mod. unstable	?
Baker et al. (1992)	T	0.56 (n = 594)	all stabilities	bare soil, soybean
Pattey et al. (1993)	T, H ₂ O, CO ₂	0.57 ± 0.03 (n = 162)	unstable	soybean
Pattey et al. (1995)	T, CO ₂	0.56 ± 0.04	unstable	bare soil
		0.49 ± 0.13	stable	
Gao (1995)	T	0.58 ± 0.04 (n = 20)	mod. unstable	deciduous forest
Katul et al. (1996)	T, H ₂ O	0.58 (n = 36)	moderately unstable	short grass and corn
	O ₃ , CO ₂	0.56 (n = 36)		
Beverland et al. (1996a)	T	0.56 (n = 199)	neutral/unstable	peatland
this study (cf. Table 5.2)	T, H ₂ O, O ₃ , CO ₂	$0.56...0.57 \pm 0.05$ (n > 500)	unstable (-z/L < 2)	senescent triticale and sugarbeet
		≥ 0.57 (cf. Eq. 5.2) (n > 380)	stable (z/L < 2)	

Only very few observations under stable conditions are reported in literature. Obviously, they did not allow to investigate the influence of stability on the b-factor in detail, but were just incorporated into the overall mean (Baker et al., 1992) or averaged to a single mean value for the entire stable range (Pattey et al., 1995). The evaluations of the present dataset, covering a large range of conditions, indicate a systematic variation of the b-factor for stable conditions. It can be best described as a function of the dimensionless stability parameter z/L (cf. Eq. 5.2), as expected from surface layer similarity theory. The observed increase of the b-factor for stable conditions agrees with the individual data of Businger and Oncley (1990), but disagrees with the results of Pattey et al. (1995). They report a distinctively lower average b-factor for nighttime compared to daytime, yet with a large variability (Tab. 6.1). They explain their finding with large concentration changes at low frequencies and generally small fluxes. Such effects were minimised in the present evaluation by the use of restrictive rejection criteria (for small fluxes and for extreme stability conditions $|z/L| < 2$) and by an effective detrending on a 10 min basis.

From the similarity hypothesis for scalar transport it can be assumed, that the b-factor for trace gases is identical to that for temperature (sensible heat). Only few studies investigated this question up to now (Pattey et al., 1993; Katul et al., 1996). They found a relatively good agreement for temperature, H_2O and CO_2 under unstable conditions. The results of the present investigation on T, H_2O , CO_2 and O_3 data supports the general similarity of the b-factor for all scalar quantities. A small systematic deviation was observed for ozone, which yielded generally larger values in the stable range than T and CO_2 . However, this deviation is hardly significant from a statistical point of view, especially because the ozone fluxes during night were often close to zero with large relative errors. In contrast, the sensible heat and CO_2 fluxes under stable conditions had a much better error characteristic and showed a good agreement if medians instead of arithmetic averages were considered (cf. Fig. 5.3). The influence of instrumental limitations (high frequency damping) on the estimated b-factors can be excluded, because they only affected the CO_2 but not the temperature measurement.

According to these findings, a general parameterisation of the ideal REA b-factor as a function of z/L is suggested for all scalar quantities. It is based on the results given in Table 5.2, Eq. 5.2 and Table 6.1:

$$b = \begin{cases} 0.57 & -2 \leq z/L \leq +0.01 \\ 0.63 + 0.03 \cdot \log_{10}(z/L) & +0.01 \leq z/L \leq +2. \end{cases} \quad (6.3)$$

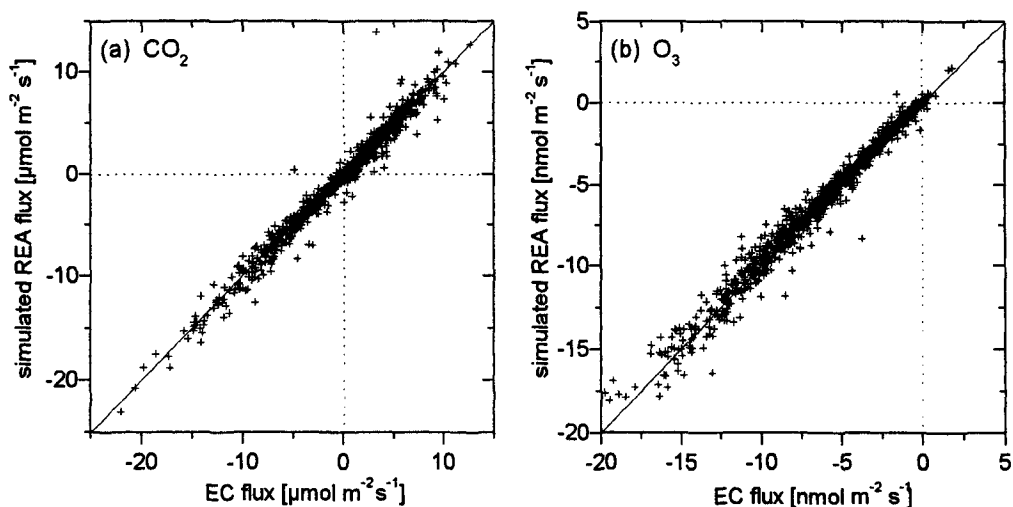


Fig. 6.15: Comparison of simulated REA and EC fluxes for (a) CO_2 and (b) O_3 ; REA fluxes calculated from EC time series by Eq. 2.79 with b-factor according to Eq. 6.3.

The general validity of this parameterisation is illustrated in Figure 6.15. It compares simulated REA fluxes (using Eq. 6.3) with the original eddy correlation fluxes for CO₂ and O₃. The agreement is excellent with correlation coefficients of about 0.99 (see Table 6.2) and very few outliers. This comparison includes all wind directions irrespective of the fetch condition. It thus confirms the result of Section 6.1.4 and Figure 5.4, that the sensitivity of the REA b-factor to inhomogeneous source areas is negligibly small and the REA method in principle yields the same averaged flux like the EC method.

It was suggested by some authors (e.g. Oncley et al., 1993; Pattey et al., 1993) not to use a prescribed b-factor for trace gas flux measurements, but to adopt the individual b(T)-factors derived from simultaneous EC measurements of temperature. This approach was evaluated too, and the corresponding correlation coefficients for the various trace gases are listed in Table 6.2. The correlation is high as well, but always lower than for the application of the prescribed b-factor (Eq. 6.3). It can be deduced, that there is no undetected systematic influence on the b-factor beside the described dependence on z/L . As already addressed in Fig. 5.5, the deviations from the functional relationship are purely random and uncorrelated for the different scalars. Thus the lower correlation results from the combined random errors in both the temperature and the trace gas measurements. The negative effect of using b(T) seems to be largest during stable conditions when the sensible heat flux is small, since the correlation coefficients for water vapour with only few nighttime cases shows the smallest difference. These findings lead to the conclusion, that Eq. 6.3 is more appropriate for the estimation of the REA b-factor than the calculation of individual values from simultaneous EC measurements. Nevertheless, it is highly recommendable for each field application, to investigate the individual b-factors in order to check the validity of the parameterisation or to detect measurement problems and failures.

Tab. 6.2: Correlation coefficients between EC and simulated REA fluxes using parameterised b-factors and simultaneously determined b(T)-factors.

method	T	CO ₂	H ₂ O	O ₃
parameterised b-factor (Eq. 6.3)	0.998	0.989	0.991	0.991
simultaneous b(T)	-	0.886	0.988	0.820

Equation 6.3 may be regarded as a similarity relationship according to the Monin-Obukhov-theory. Yet the relative variation is only about 10% and thus significantly smaller than for other semi-empirical relationships used in flux measurement techniques, i.e. the flux-profile relationships (stability correction functions, cf. Section 2.4.2) and the flux-variance relationships (correlation coefficient, cf. Section 2.4.4). Moreover, the random variability of individual b-values and the difference between the various scalar quantities is much smaller than for the correlation coefficients evaluated in Section 4.1.6. The direct comparison with profile similarity relationships is not possible in the present case due to the limited number of measurement levels.

It can be concluded, that the relaxed eddy accumulation method is based in fact on a self-standing and well defined concept. It is not as direct as the eddy correlation and the proportional eddy accumulation method, but the theoretical disadvantage due to empirical assumptions is relatively small because of the low systematic variability of the b-factor.

6.2.2 Deadband Effect

In many of the REA field applications reported so far (Pattey et al., 1993; Oncley et al., 1993; Guenther et al., 1996; Hensen et al., 1996, Valentini et al., 1997), a deadband around zero vertical velocity was used for the conditional sampling control. Some authors used a constant deadband like in the present study, others made an online adjustment relative to σ_w . It is thus of general interest to investigate the quantitative effect of a deadband as precisely as possible. In Section 5.1.4, the effective b-factor resulting from the increased conditional mean difference could be adequately described by functions of the general form given by Eq. 5.6. The effect of stability results in slightly varying numerical coefficients (cf. Tab. 5.3). In Figure 6.16, the functions are displayed in a combined form as a shaded area. It is limited by the extremely stable and unstable cases. For comparison the function derived from the ideal joint Gaussian distribution is also plotted; it is very similar to the empirical relationship for stable conditions. Similar evaluations, had already been performed by Businger and Oncley (1990) and Pattey et al. (1993), however based on limited datasets. The first examined only 25 individual cases with near neutral and stable conditions, whereas the second study was confined to unstable conditions. Businger and Oncley fitted a simplified form of Eq. 5.6 to their data with $b_\infty = 0$ and $a = 0.75$ while Pattey et al. presented a more complex functional relationship, which however also can be transformed into the form of Eq. 5.6 with $b_0 = 0.57$, $b_\infty = 0.32$ and $a = 1.96$.

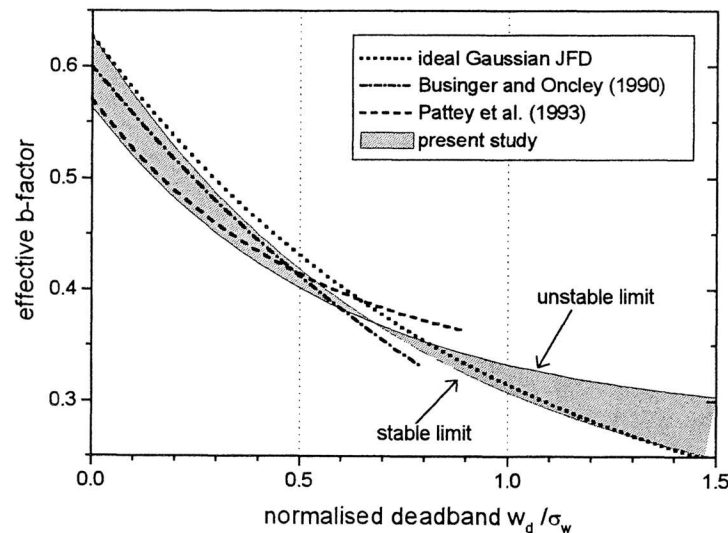


Fig. 6.16: Survey of functional relationships between b-factor and the normalised deadband width: results of present study compared to ideal Gaussian relationship and literature results.

Both functions are displayed in Figure 6.16. The result of Pattey et al. agrees fairly well with the unstable limit of the present study whereas the function proposed by Businger and Oncley follows the stable limit. Both models are confined to smaller deadband widths ($0 < w_d/\sigma_w < 0.8; 0.9$). All findings are fairly consistent and support the systematic dependence on stability observed in the present study. Like for the ideal b_0 -factor discussed in the foregoing section, no systematic difference in the deadband function for various scalar quantities could be found (see also Pattey et al., 1993). The relationship between the b-factors for variable deadband and the characteristics of the corresponding joint frequency distribution are discussed in the following section.

The question of interest in this context is, whether there is a net advantage in using a deadband for REA applications and, if yes, which deadband is optimal. The most obvious advantage of a deadband is the

increase in the conditional mean difference that has to be resolved by the analyser. Yet, the effect is always lower than 100% in respect to the zero-deadband value, as shown in Figure 6.17. On the other hand, a deadband also reduces the effective sampling time for the updraft and downdraft lines and thus the accuracy of the concentration measurements, which is proportional to the square root of the sampling time (cf. Section 4.3.2). According to Oncley et al. (1993), the combination of both effects results in an optimum of statistical accuracy at $w_d/\sigma_w = 0.6$. Their calculations rely on several idealised assumptions and use the deadband function of Businger and Oncley (1990), which represents mainly stable conditions. If a function representative for the more important unstable conditions is applied, the optimum is shifted to about 0.4 (cf. Fig. 6.17). However, it is in any case only weak and hardly relevant. Additionally, the uncertainty of the b-factor for different deadbands is not considered. This is particularly important, if the b-factor is determined from simultaneous EC measurements.

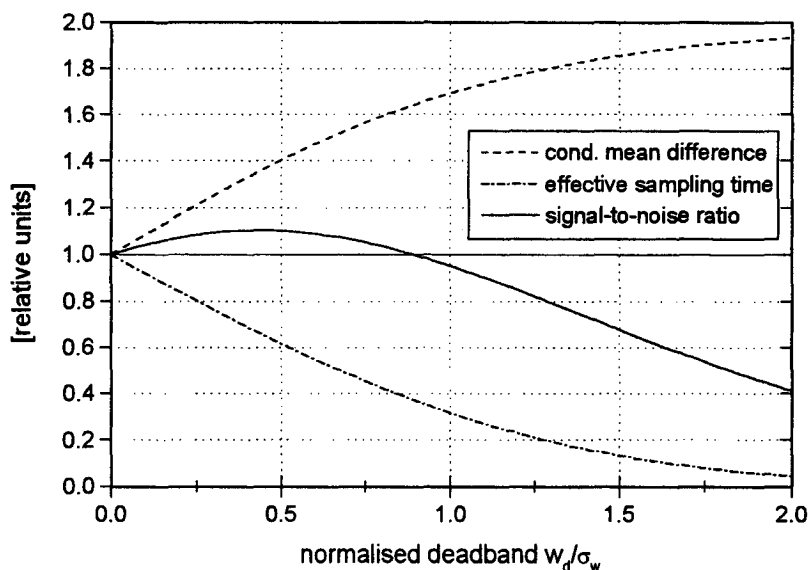


Fig. 6.17: Individual and combined uncertainty effects as a function of the normalised deadband width based on the fitted deadband function for unstable conditions (cf. Fig. 5.12a): conditional mean difference, effective sampling time and resulting signal to noise ratio of the REA flux; all quantities are given in relative units with respect to zero-deadband.

In principle, there is no significant disadvantage for any deadband value smaller than the standard deviation of the vertical windspeed ($w_d/\sigma_w < 1$). Above that value, an increased uncertainty of the b-factor is observed for unstable conditions (cf. Fig. 5.12a and Pattey et al., 1993). However, practical considerations like the delay time of the valve control or the use of online analysers with constant air-flow (see later Section 6.4) may favour low or zero deadbands producing longer open-state and shorter closed-state periods for the conditional sampling lines. If a deadband is applied, it may be either constant (e.g. Pattey et al., 1993; Hensen et al., 1997) or adjusted online to σ_w . (Guenther et al., 1996; Valentini et al., 1997). The first solution requires an individual calculation of the effective b-factor, the second one a more complicated online processing. For constant deadbands, it might be necessary to make at least a rough adjustment for stable and unstable cases as performed by Oncley et al. (1993). They switched the deadband width between 15 cm s^{-1} during day and 5 cm s^{-1} during night.

An intriguing feature represented in Fig. 6.16 is the minimum stability dependence of the effective b-factor at a normalised deadband width of about 0.7 ($b \approx 0.37$). It is caused by the crossing of the functions for different stabilities. Based on this behaviour, an online adjustment of the deadband to this specific value may be preferred (see Wesely and Hart, 1994; Valentini et al., 1997).

6.2.3 Dependence on Joint Frequency Distribution

The analysis in Section 5.1.3 shows, that the deviation of the b-factors from the ideal Gaussian value of 0.627 can be explained by a departure from the ideal linear relationship of the correlated contributions in the joint frequency distribution (cf. Fig. 5.10). Similar results were already observed by Baker et al. (1992) and Katul et al. (1996), however only for very small datasets limited to unstable daytime cases. The present results confirm and complete their findings for a broad range of conditions.

For unstable situations, the non-linearity in the JFD is fairly constant and thus completely insensitive to the strong variation in the two-dimensional asymmetry illustrated in Fig. 5.8. In contrast, the JFD's in the stable range are generally symmetric but nevertheless experience a variable departure in linearity as a function of z/L . This departure that determines the b-factor can generally be assigned to a positive kurtosis of the w -distribution (see also Katul et al., 1994), which is larger than for the scalar quantities. For this reason, the $b(w)$ -factor determined according to Eq. 5.4 from the vertical windspeed alone generally overestimates the scalar b-factor by 10% or more (cf. Fig. 5.9). Hence, as stated by Pattey et al. (1993) and Nie et al. (1995), it should not be applied for the evaluation of REA measurements (as done e.g. by Hall et al., 1997).

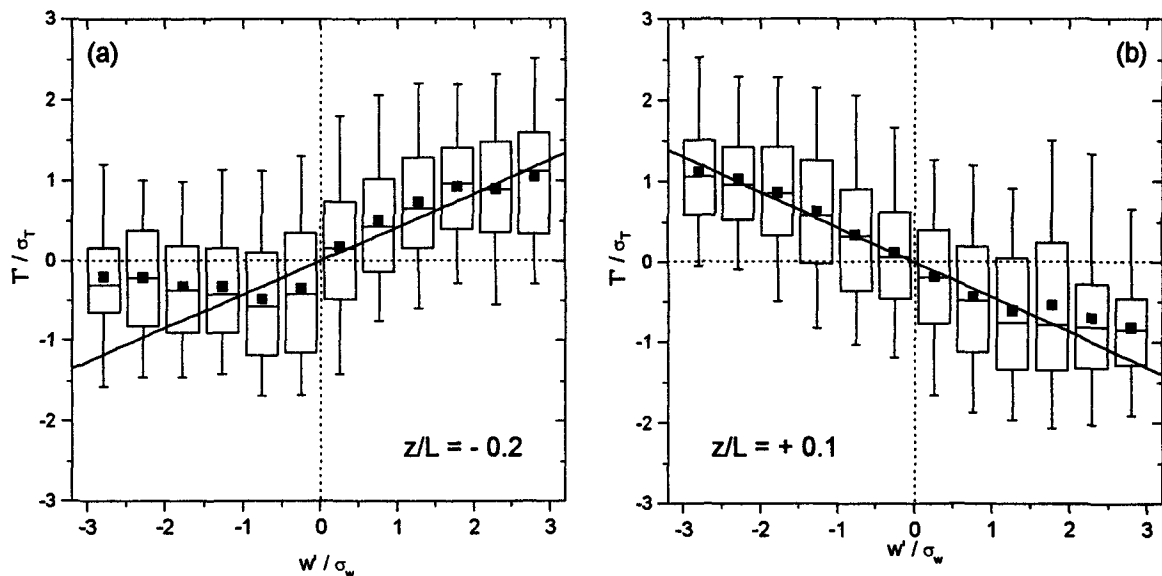


Fig. 6.18: Non-linearity of two exemplary JFD's illustrated by the conditional means of T' for equal size classes of w' : (a) same case as Fig. 5.7a; (b) same case as Fig. 5.7d.

The non-linearity of the experimental JFD's is difficult to identify in the contour plots of Fig. 5.7. Therefore the examples (a) and (d) are displayed in Figure 6.18 in a more appropriate way as a series of boxplots representing the distribution of T' in equally spaced classes of w' . Additionally the conditional arithmetic averages and the calculated linear regression lines are plotted. It has to be noted that the w' and T' axes are exchanged compared to Figure 5.7, because the linear regression is physically more meaningful with w used as independent variable on the horizontal axis. In the unstable case, the averages (and medians) deviate from the regression line in a pronounced S-shape, which is characteristic for two individual distributions with different kurtosis. On both tails, the T' values are smaller than predicted by the linear model. This deviation is more pronounced on the downdraft side as could be expected from Fig. 5.7a. However, also the stable case shows a small but distinct departure of the class averages from the linear regression line, which could not be recognised in the isoline plot of Fig. 5.7d.

Obviously it is still sufficient to cause a significant reduction of the b-factor compared to the ideal Gaussian value (about 0.60 instead of 0.63 at $z/L = +0.1$ according to Eq. 6.3).

Figure 6.18 may also help to explain the difference in the deadband functions for stable and unstable conditions displayed in Fig. 6.16. For the stable case, the deviations at the tails only get important for very large deadbands, because it has to be considered, that the central values have a much higher weight than the outer ones. For the same reason, the influence on the unstable deadband function is generally larger, because also the central values deviate significantly from the regression line. For a zero-deadband, the positive deviations in the centre produce a larger scalar mean difference and consequently a lower b-factor. But with increasing deadband, the central contributions are ignored and the negative deviations in the tail regions get more and more important. For large normalised deadbands above 0.7 they lead to a smaller scalar difference compared to the ideal JFD and thus to larger b-factors.

The presented results and considerations elucidate the relation between the joint frequency distribution and the REA b-factor, but they do not explain the reasons for the variable deviations from the ideal linear model. In order to investigate these questions, a combined application of frequency distribution and spectral analysis techniques may be necessary, as performed in an exemplary attempt by Katul et al. (1996). In this way, it might be possible to investigate the influence of the different integral time scales of the vertical windspeed and scalar fluctuations - depending on stability as well as on the boundary layer height - on the linearity of the joint frequency distribution.

6.2.4 Applicability Outside the Inertial Sublayer

The present study as well as the literature results reported so far are limited to the inertial sublayer. However, it is desirable and sometimes even necessary to perform micrometeorological flux measurements also below and above the inertial sublayer, i.e. in the roughness sublayer and in the mixed layer (or nocturnal boundary layer). The first is often inevitable for the measurement of fluxes over high and rough vegetation like forest, because the tower height is limiting. Additionally, an increasing number of studies recently performed flux measurements within the canopy in order to investigate the source sink distribution and the structure of the turbulent transport (Baldocchi and Meyers, 1991; Lee et al., 1994; Baldocchi and Vogel, 1996; Katul et al., 1997b). As shown by Maitani and Shaw (1990), the joint frequency distribution for vertical scalar transport in the roughness sublayer is significantly different from the inertial sublayer in that the flux contributions of sweeps and ejections is reversed. Thus a deviation of the b-factor may also be expected.

Gao (1995) investigated this question in detail. He determined the b-factor with EC datasets of temperature and humidity measured at six different heights in and above a deciduous forest. The uppermost height was at 2.4 times the canopy height and can be considered to represent the inertial sublayer (cf. Table 6.1). The observed b-values, averaged over three different experiments with varying LAI, are illustrated in Figure 6.19. One value obtained by Beverland et al. (1996c) at 1.5 times the canopy height above a spruce forest is also included. The values decrease from the inertial sublayer value of 0.58 to about 0.51 at the canopy top and increase again within the canopy up to 0.62. Gao explains the observed variation by the strongly coherent turbulence structure within the canopy but gives no quantitative characterisation. The b-factor for temperature and humidity agree well in the reported study, but there may be deviations for scalars with a significantly different vertical source-sink-distribution. Nevertheless, the results are encouraging, because the variability of the b-factor is significantly smaller than the variations observed for the flux-profile relationships observed within the roughness sublayer (cf.

Schween, 1993; and references therein). Further investigations are necessary to explain these results and to determine whether the observed height dependence is a general feature or depends on the canopy type and structure. Yet, the b-factor only describes the correspondence between the REA concept and the direct EC approach. To what extent point measurements in the roughness sublayer are spatially representative has to be examined independently.

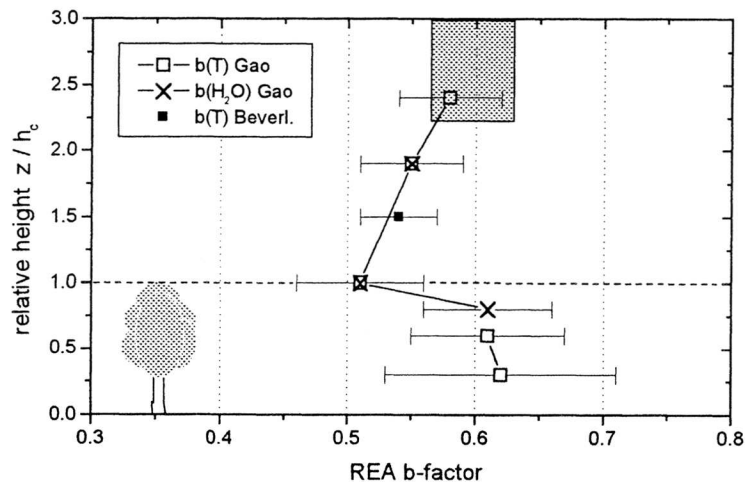


Fig. 6.19: Height dependence of REA b-factor for temperature and humidity in the roughness sublayer of a deciduous forest, after Gao (1995) and over a spruce forest after Beverland et al. (1996c); the horizontal bars indicate the observed variability (standard deviation), the gray area the observed range in the inertial sublayer (cf. Section 6.2.1).

The b-values above the surface layer are of special interest for airborne flux measurements on a regional scale (cf. Section 2.6.2), which can only be performed by eddy correlation or accumulation techniques. McPherson and Desjardins (1991) determined b-factors from airborne EC measurements in the convective boundary layer (mixed layer) and obtained average values for temperature, H_2O and CO_2 between 0.58 and 0.60. These values are not significantly different from the observations in the surface layer and also agree with the results of a large eddy simulation model (LES) presented by Wyngaard and Moeng (1992). They found a b-factor of about 0.6 throughout most of the CBL for a bottom up scalar diffusion, i.e. for a scalar which is exchanged at the surface but not through the top of the boundary layer.

In addition, Wyngaard and Moeng (1992) investigated the joint frequency distribution of the LES (see Fig. 6.20a) and found a form very similar to the JFD's for the unstable surface layer represented in Fig. 5.7. One should note that the horizontal and vertical axes are exchanged in Fig. 6.20. For a top-down scalar diffusion (exchange through CBL top by entrainment but no exchange at the surface) yielded a totally different JFD displayed in Figure 6.20b. It shows a much larger deviation from the ideal linear joint Gaussian JFD and results in a significantly lower b-factor of 0.47. Thus the application of the REA concept seems to be unproblematic for the airborne measurement of large scale surface exchange. A successful experimental application is reported by Zhu et al. (1997; 1998) for isoprene, methane, and agrochemicals.

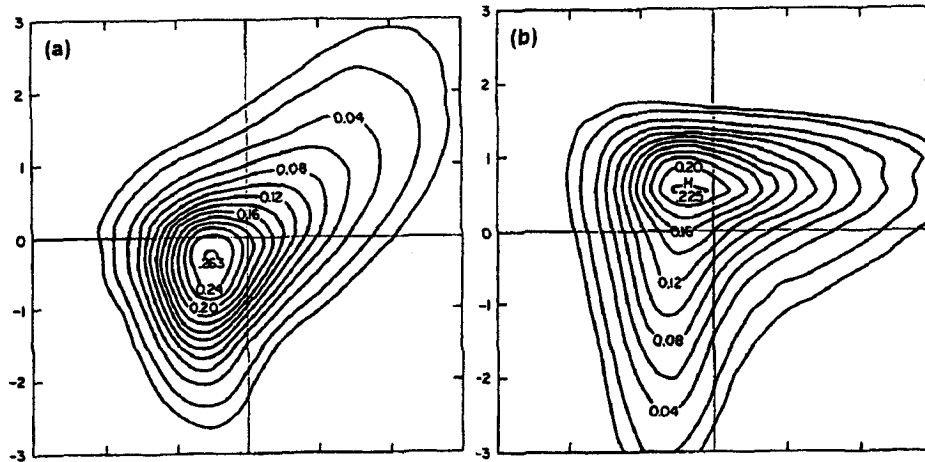


Fig. 6.20: Joint frequency distribution and corresponding b -values obtained by large eddy simulations for (a) bottom-up scalar diffusion (surface layer) and (b) top-down scalar diffusion after Wyngaard and Moeng (1992).

6.3 Analyser Resolution Requirements

A basic advantage of the micrometeorological flux measurement methods compared to enclosure techniques is the measurement under undisturbed natural conditions. However, this also implies the basic practical disadvantage, that the trace gases have to be detected at their natural ambient concentrations which are often very low, and that small temporal fluctuations or vertical gradients have to be resolved. Thus a crucial point for the applicability of flux measurement techniques is their requirement for the resolution of the trace gas sensors. The concentration difference or fluctuations to be resolved depends obviously on the magnitude of the flux, but also on the environmental conditions. In the following sections, this dependence is examined for typical measurement tasks and conditions, and the requirements of the different flux measurement methods are directly compared.

6.3.1 Comparison of Different Methods for Bellheim Field Conditions

In a first step, the dependence of the resolution requirements on the micrometeorological conditions experienced during the Bellheim field campaign are examined. The analysis follows the procedure proposed by Businger and Delany (1993). They presented the resolution requirements of the EC, REA and profile method in a general way as a two-dimensional function of the parameters u_* and z/L . In order to allow a more direct and clear comparison between the difference methods, the problem was reduced to a one-dimensional relationship. For typical daytime (unstable) and nighttime (stable) conditions in the Bellheim experiment, a relationship between the windspeed u and the stability z/L could be observed (see Fig. 6.21a). High windspeeds led to near neutral conditions, whereas low windspeeds resulted in either extremely stable or unstable conditions. The relationship was quantified by the composite linear function also represented in Figure 6.21. With this relationship and a known roughness length (for the Bellheim experiment cf. Section 4.2.1), the analyser resolution requirement for a given flux can be described as a function of the single parameter z/L . Additionally, the similarity functions of Section 2.4 and 6.2.1, which are partly different from the ones applied by Businger and Delany, are used for the calculations.

As first example, the requirements for a constant CO_2 flux of $\pm 5 \mu\text{mol m}^{-2} \text{s}^{-1}$ were determined. This value represents a typical magnitude of the CO_2 uptake observed during daytime in early senescence as well as of the CO_2 loss at daytime in late senescence and generally during the night. The ideal assumption of a constant flux also illustrates best the influence of the micrometeorological conditions on the resolution requirements. The results are displayed in Figure 6.21b, in double logarithmic plots. For the REA and profile method, the corresponding average concentration difference $\Delta\mu(\text{CO}_2)$ is indicated, as well as for porometry, which is included for comparison here. These values can be compared to each other in a direct quantitative way. For the EC method, the standard deviation $\sigma_\mu(\text{CO}_2)$ of the turbulent fluctuations is displayed, which is also representative for the variance similarity method (cf. Section 2.4.4). It is not directly comparable to the mean concentration differences due to different integration times. This problem is addressed in Section 6.3.2.

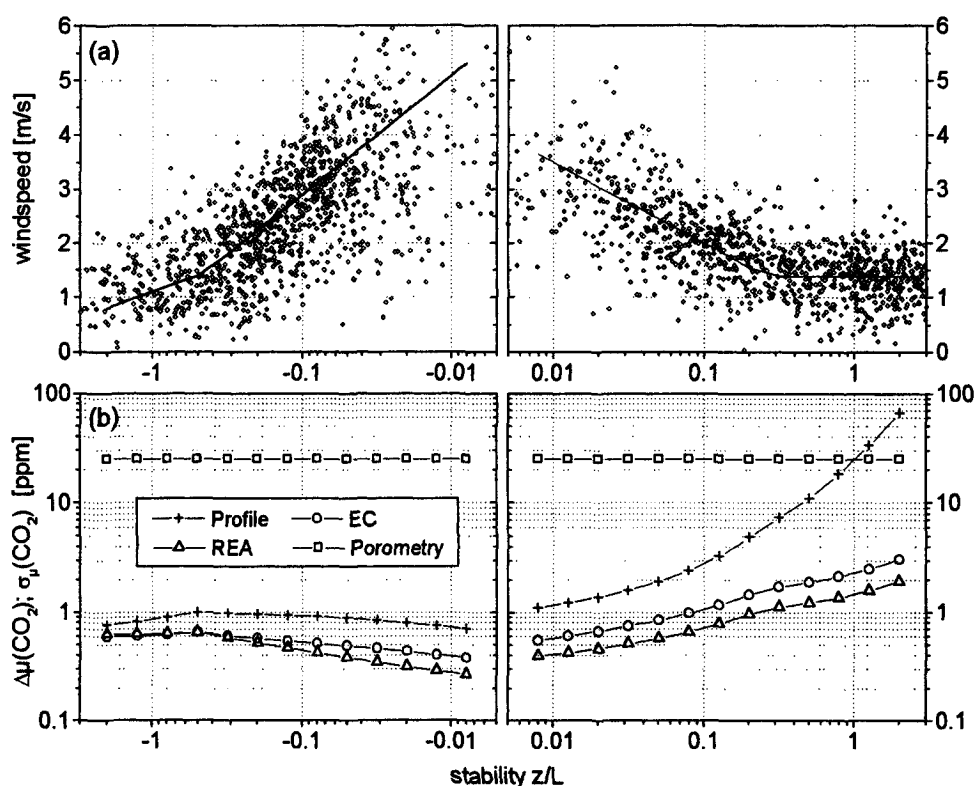


Fig. 6.21: (a) Relationship between mean windspeed u (4.25 m) and stability z/L during the Bellheim experiment; the solid line indicates the estimated functional relationship used for calculations of resolution requirements; (b) concentration difference (and std. deviation) to be resolved by the flux measurement techniques for a constant CO_2 flux of $5 \mu\text{mol m}^{-2} \text{s}^{-1}$ as a function of stability.

The analyser requirements for all micrometeorological methods are highest (most critical) at daytime near neutral conditions with very high windspeeds. The mechanical turbulence produces a well mixed boundary layer where the vertical gradients as well as the turbulent trace gas fluctuation are small. They increase only little for lower windspeeds and larger instability because the lower mechanic turbulence production is compensated by higher thermal convection. Thus the CO_2 concentration difference and standard deviation to be resolved is generally below 1 ppm for the given flux. In the stable range, the dependence on z/L is generally more pronounced because the intensity of turbulent mixing decreases quickly with increasing stability leading to very large concentration gradients well above 10 ppm for CO_2 . The larger gradients also favour larger fluctuations of the trace gas concentration. Yet the thermal stability and the weak turbulence have an opposite influence and the net effect for EC and REA is only

a small increase with z/L to only little higher than 1 ppm. The concentration difference between inlet and outlet of the porometric chamber is independent of the micrometeorological conditions and usually much higher than for the other methods, even though the airflow through the chamber was very high (cf. Ammann et al., 1997).

The concentration differences in this example are generally larger (and thus more favourable) for the profile method than for REA. However, the profile difference strongly depends on the ratio of the aerodynamic measurement height z_2/z_1 , which was equal to about 4.5 in the Bellheim experiment. The difference is roughly proportional to the height ratio, which has to be considered in the planning of a profile system. A ratio of 4 or higher may be achieved under most conditions, except over forest where the available tower height (and the large roughness length) are often limiting factors. For the 'eddy methods' (EC and REA) the measurement height is of secondary importance; the standard deviations of vertical windspeed and scalar quantities show only a weak dependence on height through the similarity relationship with the local stability z/L (cf. Section 2.4.4).

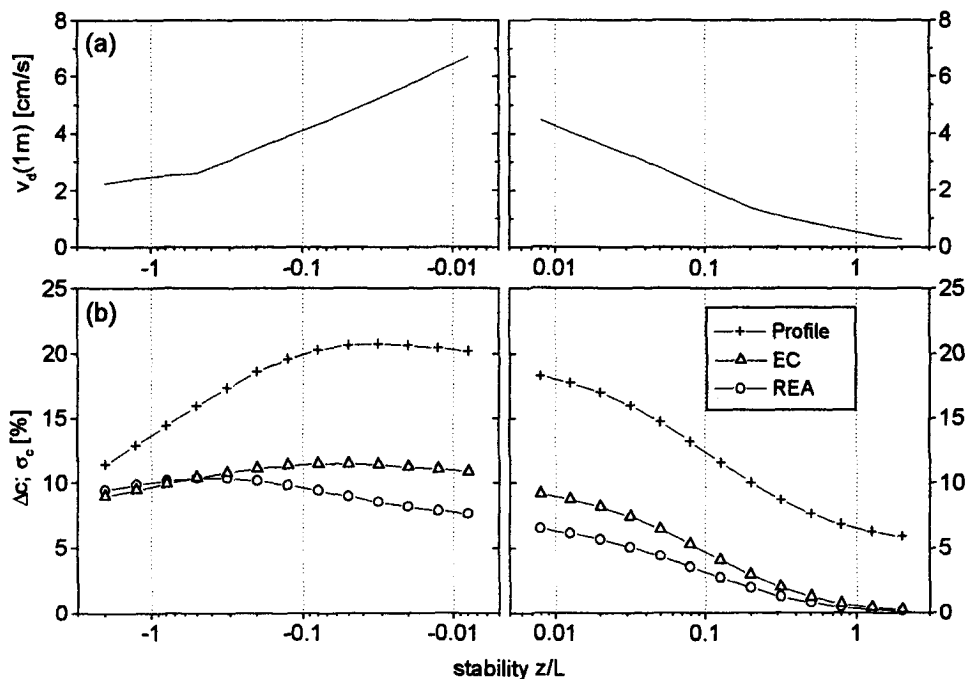


Fig. 6.22: (a) standard deposition velocity for an absolute deposition process with $R_c = 0$; (b) relative concentration difference (or standard deviation for EC, respectively) to be resolved by various flux measurement techniques for an absolutely depositing trace gas as a function of stability.

A constant flux for all stability conditions is not typical for most trace gases. Especially deposition processes are directly influenced by the stability (and windspeed) through the turbulent or aerodynamic resistance (cf. Section 2.1.3). In order to illustrate this effect, the extreme case of an absolute deposition with negligible surface resistance ($R_c = 0$) and without compensation point is analysed. It approximately describes the deposition of strong acids like HNO_3 or HCl on wet surfaces and represents the upper limit for the deposition velocities. For the following evaluation, it is assumed that the concentration above the surface layer (at a height of 50 m) remains constant. The resolution requirements are expressed in relative units (% of the ambient concentration) and are thus generally applicable for various trace gases and absolute concentrations.

Figure 6.22a shows the maximum deposition velocity v_a , which was derived according to Eq. 2.7 from R_a and R_b values typically observed in the Bellheim experiment, as a function of z/L . It is closely related to the windspeed and thus shows a similar form like the functional relationship obtained in Fig. 6.21a. The deposition velocity roughly describes the magnitude of the flux, which additionally depends on the concentration at the reference height (1 m). Thus in contrast to the previous example, the flux in this case varies considerably with z/L . This behaviour strongly affects the resolution requirements especially in the unstable range. For all micrometeorological methods, the relative differences and standard deviations are smallest for extremely stable situations due to the very small flux. The difference between the methods is not affected and is about the same as in Figure 6.21.

The cases discussed in Figs. 6.21 and 6.22 represent opposite extremes: on the one hand a constant flux, which is totally unaffected by the micrometeorological conditions, and on the other hand a variable deposition flux which is fully controlled by the turbulence intensity. The exchange of most trace gases is determined by a combination of micrometeorological and surface processes as described in Section 2.1, and thus the individual effect of the stability on the analyser resolution requirements is somewhere in between the presented extremes. The quantitative requirements for several particular trace gases of interest is discussed in the following section.

6.3.2 Requirements of REA Method for Specific Trace Gases

As mentioned already in the introductory chapter, the micrometeorological flux measurement techniques are of interest especially for trace gas species that play an important role in the greenhouse effect or in atmospheric chemistry, and for which the Earth's surface represents a major source or sink. The REA method, in particular, is of interest for trace gases that can not be measured by the eddy correlation technique due to the lack of fast online sensors. A selection of such trace gases is reviewed in this section. Based on typical flux and concentration values reported in the literature, the (relative) concentration difference to be resolved by available analysers are estimated.

The relative concentration difference measured by the REA technique is directly related to the respective flux-concentration ratio in the following way:

$$\frac{\Delta\mu_c(\text{REA})}{\mu_{c,\text{amb}}} = \frac{1}{\mu_{c,\text{amb}}} \cdot \frac{F_c}{\rho_a \sigma_w b} = (\sigma_w b)^{-1} \cdot \frac{F_c}{\rho_{c,\text{amb}}} \quad (6.4)$$

For deposition processes, the flux concentration ratio $F_c/\rho_{c,\text{amb}}$ represents the (negative) deposition velocity (Eq. 2.7), which can be expressed through the aerodynamic, laminar boundary layer and surface resistance. The first two are equal for all passive scalars and thus the surface resistance R_c determines the individual value of the deposition velocity and (according to Eq. 6.4) the resolution requirement for a particular trace gas. For emission processes, there is no general term and illustrative explanation for the flux-concentration ratio like the deposition velocity. However, under some simplifying assumptions, it is related to the residence time of the trace gas in the planetary boundary layer $\tau_{c,\text{PBL}}$:

$$\frac{F_c}{\rho_{c,\text{amb}}} = \frac{h_{\text{PBL}}}{\tau_{c,\text{PBL}}} \quad (6.5)$$

This relationship is valid, if the PBL is well mixed and if the surface represents either the only source or the only sink for the trace gas of interest. The boundary layer height h_{PBL} can vary considerably de-

pending on the surface and radiative conditions (cf. Section 2.1.2). For the following evaluation it was prescribed to 1 km, which is a typical value often used for the daytime convective boundary layer over land.

Figure 6.23a shows typical ranges of the flux-concentration ratio reported for various trace gases. The values do not cover all occurring conditions but reflect the exchange of the specific surface types which are currently investigated, because they represent a major source or sink for the respective trace gas (e.g. peatlands for methane emission, for more details see references in the legend of Fig. 6.23). Most of the displayed literature values were estimated directly from flux and ambient concentration values or deposition velocities. The ranges for isoprene and monoterpene emission (over forest) were estimated according to Eq. 6.5 from residence time values given by Guenther et al. (1995). They agree well with the flux-concentration ratios given by Pattey et al. (1997).

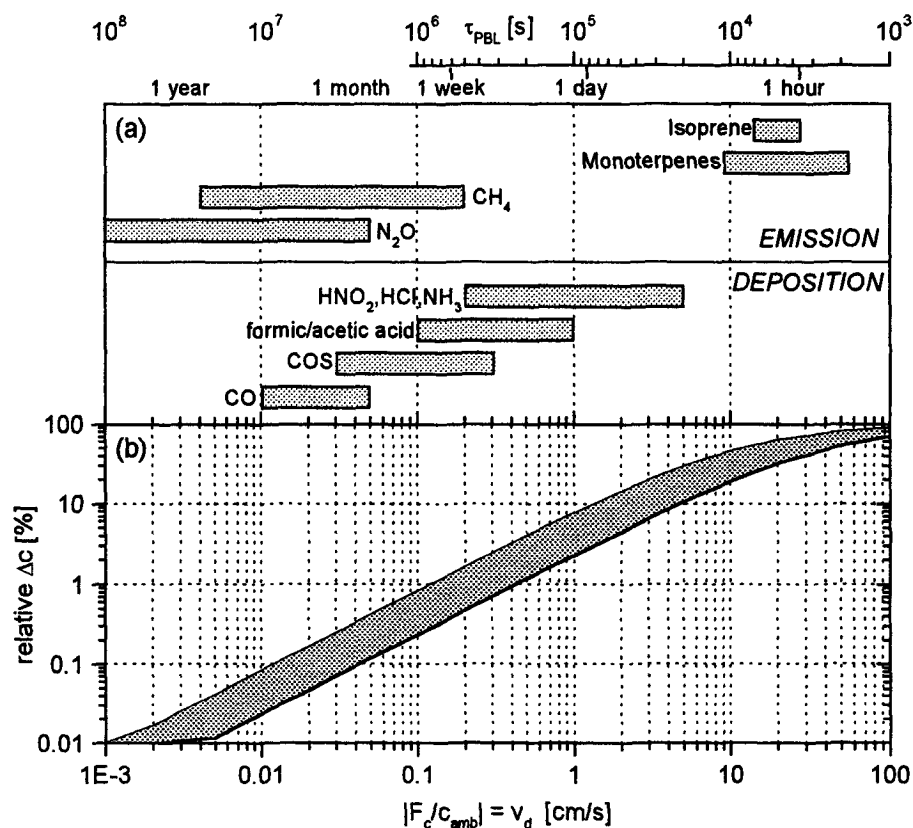


Fig. 6.23: (a) observed flux-concentration ratio for various trace gases: isoprene and monoterpenes after Guenther et al. (1995); CH_4 after Fowler et al. (1995) and Kormann (1997); N_2O after Wienhold et al. (1994) and Beverland et al. (1996b); $HNO_2/HCl/NH_3$ after Sutton (1990) and Duyzer (1995); formic/acetic acid after Hofmann et al. (1995) and Kesselmeier et al. (1998); COS after Kuhn et al. (1997); CO after Sanhueza et al. (1997); (b) relative concentration difference to be resolved by the REA method as a function of the flux-concentration ratio (deposition velocity).

In Figure 6.23b, the relative REA concentration difference (Eq. 6.4) as a function of the flux-concentration ratio is displayed. The linear relationship was displayed in a double logarithmic plot due to the large ranges (several orders of magnitude) used in both axes. The shaded area represents the typical variability of the b-factor (0.56 - 0.63) and of σ_w ($0.2 - 0.7 \text{ m s}^{-1}$). Among the trace gas species represented in Fig. 6.23a, the biogenic volatile organic compounds (monoterpenes and isoprene) have the best prerequisites for REA measurements. Their short lifetime in the boundary layer (fast removal through oxidation by ozone and other reactive species) leads to relative concentration differences of

20% and higher, which can be resolved even by relatively coarse analysing methods. Therefore, most applications of the REA method reported so far concentrate on the measurement of these species (Guenther et al., 1996; Beverland et al., 1996c; Pattey et al., 1997; Valentini et al., 1997; Geron et al., 1997). However, an appropriate validation of the flux results is generally difficult in this case, since comparisons with upscaled enclosure measurements (cf. Guenther et al., 1996; Geron et al., 1997) or with results of the profile methods (cf. Schween et al., 1997) are not very reliable.

For deposition fluxes, such high flux-concentration ratios as observed for volatile organic compounds are theoretically impossible. As discussed in Section 2.1.3, the flux is limited by the ambient concentration and the resistance of the air transfer (R_a and R_b) resulting in a maximum flux-concentration ratio or deposition velocity of about 5 cm s^{-1} (cf. Fig. 6.22). This value can be approached only by strong acids with almost zero surface resistance R_c like HNO_3 or HCl and sometimes by ammonia (Sutton, 1990; Duyzer, 1995). In this case, REA concentration differences of well above 1% can be observed that are resolvable by optimised wet denuder samplers and electric conductivity detectors (Blatter and Nefel, 1997, pers. communication). Weaker acids like formic or acetic acid and inert compounds like COS have a considerably higher surface resistance and thus show deposition velocities in the order of some millimetres per second (Hofmann et al., 1995; Kesselmeier et al., 1998; Kuhn et al., 1997). They result in concentration differences in the order of 1 %, which can not be resolved by the common techniques like cryo-trapping with ion or gas chromatographic analysis (Hofmann et al., 1992; Hofmann et al., 1997).

Methane (CH_4) and nitrous oxide (N_2O) and carbon monoxide (CO) show much lower flux-concentration ratios than the volatile organic compounds due to longer residence times. The resulting concentration differences are generally below 1% and thus difficult to resolve by common analysing techniques like gas chromatography. With the more sophisticated tunable diode laser (TDL) technique, Beverland et al. (1996a) were able to detect differences of N_2O well below 0.1% with sufficient accuracy. However, the practical advantage of REA measurements with TDL instruments is questionable, because they are usually fast enough to be used for eddy correlation measurements. In order to investigate this question, a simple statistical consideration of the instrumental resolution requirements for REA and EC is made in the following.

Let us assume, that an instrument is available (like e.g. a TDL) which can be operated with a temporal resolution of $\Delta t = 0.1 \text{ s}$ and a corresponding random noise level $\sigma_{c,\text{noise}}$. For an EC flux averaged over 30 min, the instrumental error can be estimated by Eq. 4.37 with the help of Eq. 2.66 and a typical correlation coefficient $r_{wc} = 0.4$:

$$\frac{\sigma(F_c)}{F_c} = \frac{\sigma_w \sigma_{c,\text{noise}}}{r_{wc} \sigma_w \sigma_c} \sqrt{\frac{\Delta t}{T_a}} = \frac{1}{0.4} \cdot \frac{\sigma_{c,\text{noise}}}{\sigma_c} \cdot \sqrt{5.6 \cdot 10^{-5}} \approx 0.02 \cdot \frac{\sigma_{c,\text{noise}}}{\sigma_c} \quad (6.6)$$

If the same instrument is used for the trace gas analysis in an operational REA system, only about one third of the averaging interval is available for each conditional mean concentration because it has to be switched between the updraft and downdraft air and some flushing time is also necessary. Thus the instrumental error of the mean updraft and downdraft concentration equals:

$$\sigma(\bar{\mu}_{c,U}) = \sigma(\bar{\mu}_{c,D}) = \sigma_{c,\text{noise}} \sqrt{\frac{\Delta t}{T_a}} = 0.0075 \cdot \sigma_{c,\text{noise}} \quad (6.7)$$

The relative error in the REA flux is equal to the relative error in the conditional mean difference:

$$\frac{\sigma(F_c)}{F_c} = \frac{\sigma(\Delta\mu_c)}{\Delta\mu_c} = \frac{\sqrt{2} \cdot 0.0075 \cdot \sigma_{c,\text{noise}}}{\Delta\mu_c} \approx 0.01 \cdot \frac{\sigma_{c,\text{noise}}}{\Delta\mu_c} \quad (6.8)$$

According to Figures 6.21 and 6.22, the REA concentration difference is generally about half of the turbulent standard deviation σ_c , and thus the resulting flux error in the REA measurement is about 4 times as high as for the EC method. This result favours the application of the eddy correlation technique, whenever a fast sensor (response time below 1 s) is available. However, systematic error sources like unstable sensitivity of the sensor (often met with TDL systems, cf. Kormann, 1997) may sometimes be more important than random errors and may affect the REA and EC technique to a different degree.

6.4 Design of Conditional Sampling Systems

In the previous sections, the characteristics and requirements of the REA method under the assumption of an ideal sampling system were discussed. However, the technical implementation also represents a crucial limiting factor. The considerable practical problems met for the REA test system in the present study (cf. Section 5.2) raise the question about the 'optimal' setup. Several different systems are proposed in the literature; they not only differ in the general sampling flow design as presented in Section 2.5.4, but also in details depending on particular trace gas and analyser characteristics. In the following sections, the discovered setup problems are discussed in comparison to alternative designs, and suggestions for possible improvements are given.

6.4.1 Sampling Flow System for Online Analysis

The crucial technical part of a REA system is the routing and control of the conditional sampling air-flow. As discovered in the present study, a constant flow during the open state of the valve is very important, but not always easy to achieve. The observed non-constant sampling flow was caused by a varying underpressure in the sampling lines (cf. Section 5.2.3) due to the continuous operation of the pumps in the closed state. Since this setup was proposed and tested by Baker et al. (1992), the question is raised, why they did not observe the same effect. There are several possibilities for differences in technical details: a different pressure-flow characteristic of the pumps or a different orifice size of the valves. However, these effects would reduce the problem only to a certain extent. Baker et al. also reported some systematic underestimation of the water vapour flux by the REA method, that they could not explain (they could not verify the CO_2 flux). Additionally, their correction for the delay time effect (7 - 40%) was much too high as shown in Sections 5.2.2 and 6.4.4. Thus it is likely, that the non-constant flow problem already occurred in the original setup, but was not recognised there.

The non-constant pressure and sampling flow is a general problem of REA systems with online analysers, because the interrupted conditional sampling flow has to be matched with a preferably constant analyser flow. A simple way to overcome this problem, is the separation of the conditional sampling and the analyser flow system. This can be achieved as illustrated in Figure 6.24. The conditional sampling lines are connected at the end and flushed by one single pump. In this way, pressure variations within the sampling lines are minimised, because the pump can flush one open line at any time. If a deadband is used, the setup can be extended by a third line and valve, which is opened during threshold windspeed values. The analyser flow, which may be either constant or switched, is branched off the main lines just

after the valves. In order to minimise the mutual disturbance of both flow systems, the analyser flow should be considerably smaller than the main sampling flow ($Q_2 \ll Q_1$). In this way, a possible back-flow to the analyser from the opposite sampling line is avoided. A buffer volume between the analyser branch-off and the main pump might also be helpful.

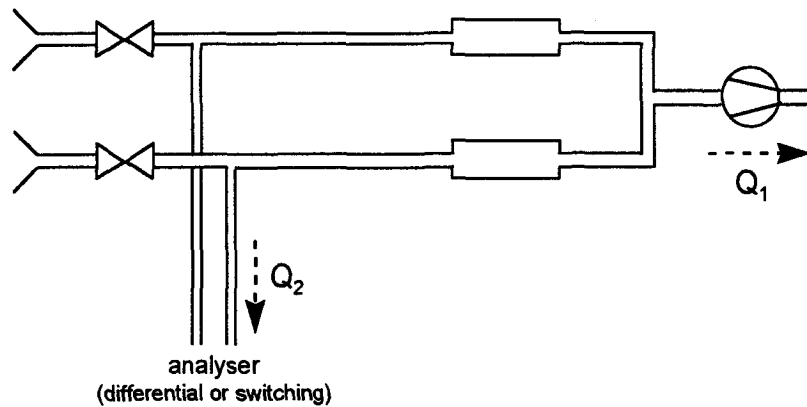


Fig. 6.24: Schematic online REA system with separate conditional sampling and analyser flow.

Some preliminary tests with this modified setup were performed under field conditions. The main pump produced a conditional sampling flow of 10 L min^{-1} and two constant analyser flows of 0.5 L min^{-1} each were branching off. Compared to the original setup in Fig. 3.18, the pressure variations in the sampling lines could be reduced by about one order of magnitude as displayed in Figure 6.25. No significant under-pressure is built up with this arrangement and thus the extreme 'oversampling' just after the opening of the valve is avoided. Another important advantage of the modified setup is, that it can be combined with various types of analysers using either pushing or sucking pumps and also with trapping and accumulation units described in the following section.

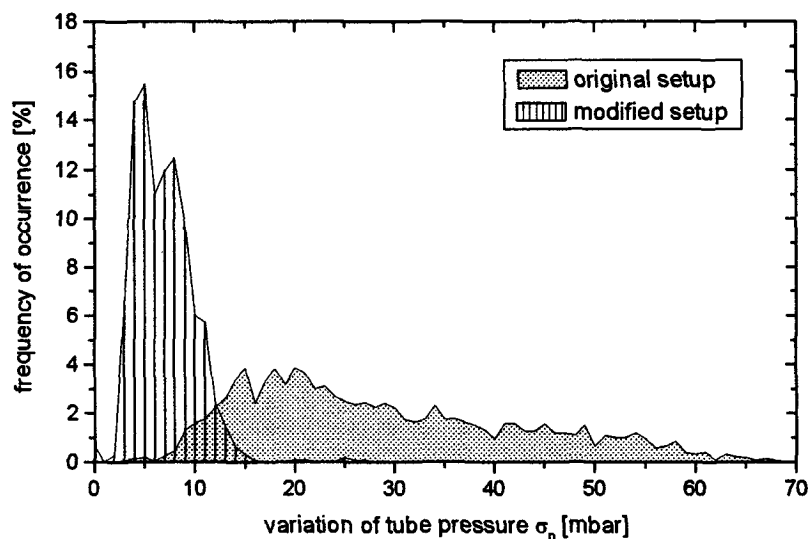


Fig. 6.25: Histogram of standard deviations of sampling line pressure in the original (Fig. 3.18) and the modified REA system (Fig. 6.24).

6.4.2 Alternative Accumulation and Analysing Methods

The optimal design of a REA system may be strongly influenced by the analyser type and the corresponding trace gas sampling method (cf. Delany et al., 1991). Beside the continuous online analysis applied in the present study (and similar test measurements e.g. by Beverland et al., 1996b), mainly two different sampling and accumulation techniques are reported in the literature: (a) mass accumulation of the trace gas in various kinds of scrubbers and traps with subsequent analysis, (b) collection of air in bags or canisters with subsequent analysis. The advantages and problems of these sampling methods are discussed in the following paragraphs.

Accumulation in Scrubbers and Traps

Trace gas species, which are not detectable at their actual air concentration, need to be scrubbed from the sampling air and accumulated over a certain period. Commonly applied accumulation techniques are for example cryogenic traps for sulphur compounds and acids (Hofmann et al., 1992; Hofmann et al., 1997), wet denuders for strong acids and ammonia (Keuken et al., 1990; Neftel et al., 1997), and adsorption cartridges for hydrocarbons and aldehydes (Kesselmeier et al., 1996; Kesselmeier et al., 1997b). The scrubbed compounds are usually deactivated in the frozen or adsorbed state and thus even reactive species may be stored for a longer time till the subsequent laboratory analysis.

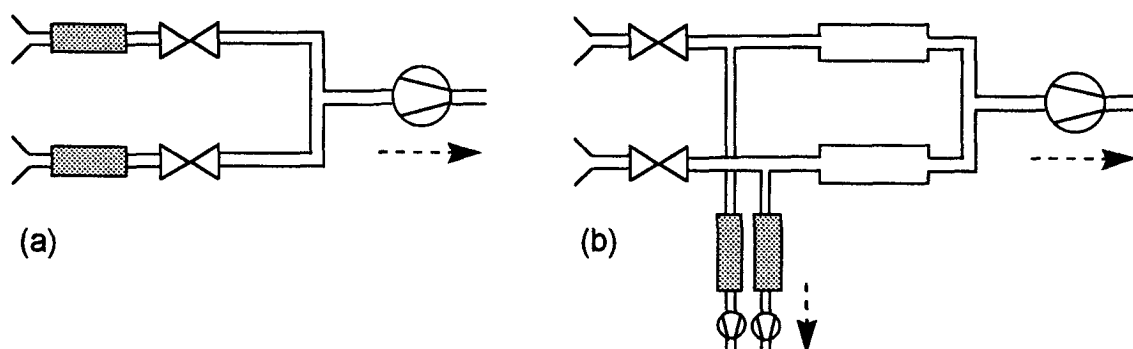


Fig. 6.26: Schematic REA designs for direct trap accumulation: (a) with interrupted air flow through traps (cf. Valentini et al., 1997); (b) with constant airflow through traps.

Adsorption cartridges (Majewski et al., 1993; Beverland et al., 1996c; Valentini et al., 1997) as well as denuders (Blatter and Neftel, personal communication) were already applied for REA measurements. In most cases, the accumulation devices were placed directly at the air inlets before the conditional sampling valves, as indicated in Fig. 6.26a. Hence the trace compounds of interest could be sampled without first passing long tubes, valves or pumps. However, with such an arrangement the accumulating units experience a fluctuating airflow. Since most trapping systems for trace gases were developed for a constant flow rate, the operation at a variable flow could be a problem and has to be tested carefully before the application in a REA system. If the contact with the conditional sampling valve does not affect the trace gas of interest, the setup proposed in Fig. 6.24 can be adapted (cf. Fig. 6.26b), and the accumulators may be flushed with a constant flow rate.

A crucial problem of the mass accumulation techniques is the determination of the sampled (and scrubbed) air volume. It was already discussed for the proportional eddy accumulation method in Section 2.5.1. The exact magnitude of the air volume is necessary for converting the accumulated mass to an average mixing ratio, which can be inserted into Eq. 2.79 for the final flux calculation. The uncertainty of the volume measurement affects the flux results in the same way as the error of the trace gas

analysis and thus has to satisfy the same resolution requirements (cf. Section 6.3). Only if the system is ideally symmetric in the updraft and downdraft intake lines, the relative difference in both sample volumes can be estimated directly from the corresponding sampling time, which is in general not equal for updrafts and downdrafts (cf. Section 5.1.3). An online measurement of the fluctuating conditional sampling flow is difficult because most common sensors do not have a sufficient accuracy and/or response time. The problem is relieved concerning the response time, if the setup proposed in Fig. 6.26b is applied, because the flow rate to the accumulator can be held more or less constant. However, no general easy solution can be given and the optimal technique has to be found for each individual REA setup.

Bag Sampling

The most versatile type of trace gas sampling is the collection of air in Teflon bags or canisters (cf. Fig. 2.20a). It can be combined with any subsequent analysing method under adjusted conditions concerning e.g. temperature and pressure conditions, analyser airflow, etc. It was applied so far for REA flux measurements of CO₂ and H₂O (by various authors mainly for test purposes), CH₄ and N₂O (Beverland et al., 1996a), and for isoprene (Guenther et al., 1996; Pattey et al., 1997; Zhu et al., 1997). The bag sampling does not represent a real accumulation, because the total mass or volume is only of secondary importance. It rather corresponds to an averaging of the concentration over the sampling interval through mixing inside the bag. For the subsequent analysis on site or in the laboratory, an arbitrary part of the sampled air volume can be used. The effective accuracy of the difference between the updraft and downdraft concentration depends on the precision of the analyser and on the number of measurements. Beverland et al. (1996a/b) applied the bag collection method for REA flux measurements of methane and analysed up to 60 individual samples from both bags in alternating sequence (see also de Wilde and Duyzer, 1995). In this way, they were able to resolve concentration differences smaller than 1% with a gas chromatography instrument. However, for operational flux measurements over a longer period, the analysis time should not exceed the corresponding sampling interval. For the application of a deadband, Oncley et al. (1993) suggest the use of a third bag, in which the air is collected during the threshold periods. The corresponding trace gas concentration may be useful for checking purposes.

For pushing the sample air into the different bags, usually one single pump is used according to the illustration in Fig. 2.20a. This arrangement implies a dead-volume consisting of the inner volume of the pump and the tubing volume before the air is switched to the appropriate updraft or downdraft line. The dead-volume produces a negative time lag, which is opposite to the delay effects discussed in Section 5.2.2. The lag effect either has to be kept small by minimising the dead-volume, or it can be compensated by a delayed control of the valves (cf. Pattey et al., 1993; Oncley et al., 1993).

The bag sampling can not be applied for very reactive trace gases, which either show homogenous reactions with other gases or which are adsorbed at the walls. Such species have to be deactivated by trapping (see above) or analysed online with a sufficiently short residence time before detection. The latter solution might be a promising method for flux measurements of NO and NO₂, which can not be trapped on adsorbing material, and for which slow online analysers are available (cf. Ludwig, 1994). However, it has to be tested, if the analyser precision is sufficient for typical conditions and to what extent the concentrations are affected by the gas phase reaction with ozone even during short residence times.

6.4.3 Windspeed Measurement and Valve Control

Compared to the sampling and analysing problems discussed in the previous sections, the measurement and processing of the vertical windspeed w and the control of the conditional sampling valves is generally less problematic but nevertheless requires some considerations. Mainly two aspects are important: the corrections for offset and tilt effects and the delay time between the w -measurement and the conditional air sampling.

Delay Time Effect

The effect of a non-zero delay time on the REA flux recovery rate was investigated and quantified in Section 5.2.2 as a function of the eddy reversal frequency erf (Fig. 5.18). A similar analysis with eddy correlation temperature datasets was performed by Beverland et al. (1996a,c) for two vegetation types: a peatland and a spruce forest. For a direct comparison, the findings of the present study were adjusted linearly to their delay time of 44 ms. The different parameterisation curves are plotted in Figure 6.27. They are limited to the erf -range actually observed in the respective field experiment (typically 1-3 Hz). The flux loss reported by Beverland et al. (1996c) for peatland shows a similar dependence on erf like the present results but is about 40% smaller. Over forest (Beverland et al., 1996a), a linear relationship was fitted. It agrees reasonably well with the curve derived in the present study between 2 and 3 Hz. However, for lower erf values, the flux recovery increases above one (100%), meaning that the flux result with the applied delay time was larger than without delay. This surprising behaviour could not be explained by the author. Hence it is not clear, whether it is a natural effect or caused by instrumental or methodological constraints. Beier and Weber (1992) made similar observations of a maximum covariance flux for $w'T'$ at a non-zero delay time under special micrometeorological conditions but also gave no physical interpretation.

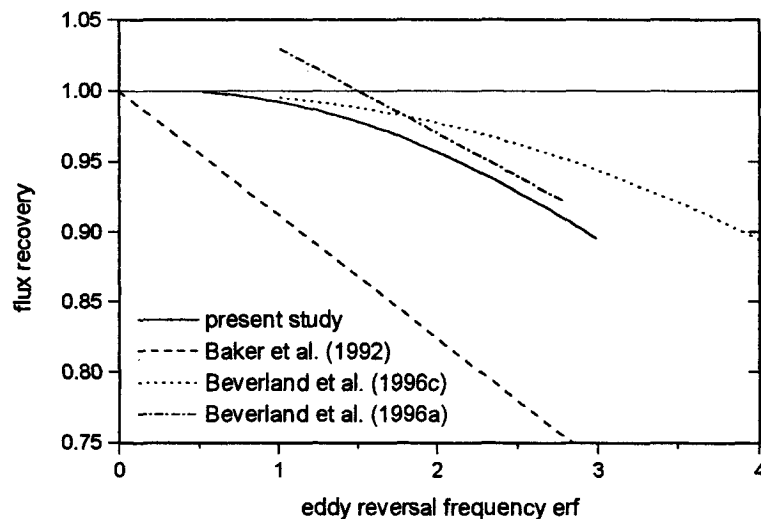


Fig. 6.27: Different parameterisation schemes of the flux recovery effect for a delay time of 44 ms.

All empirical parameterisation schemes displayed in Fig. 6.27 indicate a flux loss of generally below 10%. The model presented by Baker et al. (1992) was derived from theoretical considerations and was not validated with experimental datasets. The respective estimated flux loss (cf. Eq. 5.14) overestimates the empirical results by almost one order of magnitude. It thus has to be concluded, that the ideal assumptions used by these authors are generally not valid.

In principle, the parameterisation schemes in Figure 6.27 can be applied for an integral post-processing correction of the delay time effect. However, because of the observed variability and the uncertainties in the estimation of the effective delay time (see below), it is generally recommendable to minimise the delay time in the REA system as far as possible. An overview of the various contributions to the total delay time was already given in Section 5.2.2. The most intrinsic effect results from the discretisation of the windspeed measurement and valve control. The measurement interval $\Delta t = 48$ ms used in the present study is at the lower end of the values reported in the literature (typical range: 40 - 200 ms). Δt is primarily limited by the performance of the anemometer. Most modern research type sonic anemometers sample at a rate of 20 Hz or faster and thus the corresponding delay time contribution can be kept below 50 ms. The analog output provided by many instruments has at least the same resolution limitation like the digital output, because the analog signal has to be first converted from the original digital measurement values. Therefore, the application of an analog comparator device as presented by Beverland et al. (1997) provides only a minor improvement of the delay time. Additionally it is less flexible than a computer based valve control concerning the online processing of the w -signal (detrending, rotation, deadband etc.).

Compared to the discretisation effect, the valve response time is generally less crucial for the total delay time. Most common 2-position solenoid valves provide response times of 20 ms and below (cf. Baker et al., 1992; Pattey et al., 1993; Beverland et al., 1996b) and thus the respective contribution is usually much smaller than the measurement interval Δt . Hence, for the choice of the appropriate valve type, more attention can be paid for other important characteristics like the valve material (possible interaction with trace gases), life-time, and orifice size (flow resistance, pressure drop).

A variable delay time effect is caused by the horizontal separation between the sonic anemometer and the sampling line inlets. It depends on the windspeed and wind direction and is therefore difficult to correct in the online or post-processing. In principle it is recommended to locate the REA inlets as close to the sonic head as possible. If the wind direction is relatively stable within a known sector, the inlets should be put to the lee side of the sonic anemometer. In this way, not only the flow distortion effect is minimised, but also the delay time effect is reduced, because the air passes the inlets after the sonic. If the wind is blowing from various directions, a compromise has to be made between the sensor separation effect and the windfield distortion around the sonic head, depending on the specific measurement conditions.

Eddy Reversal Frequency

The eddy reversal frequency erf (Eq. 5.11) originally defined by Baker et al. (1992) was demonstrated to be an adequate parameter for the quantification of the delay time effect and other time related characteristics and problems of the REA technique. It was shown in Section 5.2.2, that the observed variability in erf can be described by a similarity function according to the Monin-Obukhov-theory (cf. Eq. 5.13 and Fig. 5.17). The relationship presented in Fig. 5.17 and Eq. 5.13 seems to be more concise than the dependence of erf on the turbulence intensity σ_w presented by Beverland et al. (1996a). However, the similarity function requires further validation for other relevant environmental conditions (surface types).

From theoretical considerations, it may be expected that the eddy reversal frequency is closely related to the integral time scale and the peak frequency of the w -spectrum. The latter quantity is relatively well defined for all stability conditions (KF94:44) and shows a monotonous decrease with highest values for extremely stable and lowest values for extremely unstable conditions. In Figure 6.28 both similarity relationships are directly compared in their normalised form which corresponds to a dimensionless

wavenumber. For convenience, the function for the spectral peak frequency is multiplied by a factor of four. It can be observed, that there is a close agreement (proportionality) throughout the stable range. Yet, in unstable conditions the peak frequency shows a totally different course than the eddy reversal frequency. This behaviour may be related to the asymmetry in the w -distribution (cf Fig. 5.8), which also shows an 'ideal behaviour' for stable conditions and an increasing deviation for unstable conditions. A skewed w -distribution favours the reversal of the sign by small (random-like) variations and thus may enhance the eddy reversal frequency.

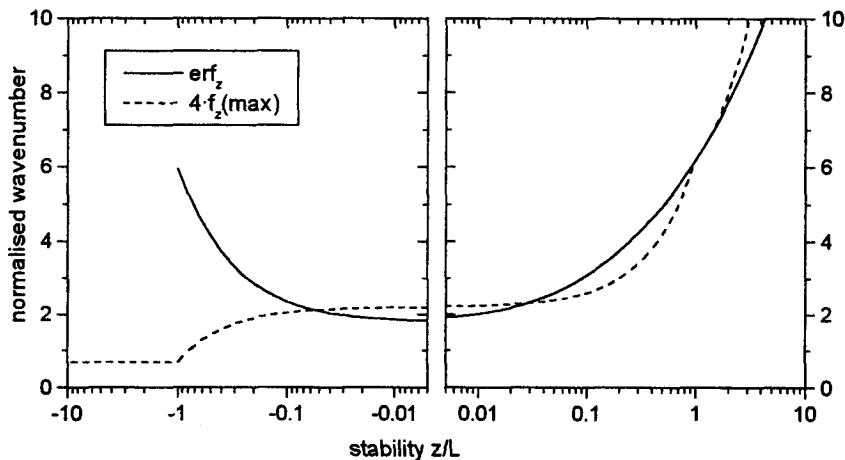


Fig. 6.28: Comparison of similarity functions for normalised eddy reversal frequency erf_z (Eq. 5.13) and the peak frequency of the w -spectrum $f_z(max)$ according to KF94:44.

Offset and Tilt Effect

It was shown in Section 5.2.1, that the online detrending of the w -signal applied in the present study still produced systematic flux errors up to 20% due to remaining offset and tilt effects. Some improvement can be achieved by the application of a high-pass filter with a higher cutoff frequency and a sharper cutoff characteristic (recursive and higher order filters). The cutoff frequency should not be chosen too high in order to avoid attenuation effects of the low-frequency part of the turbulent spectrum. However, Beverland et al. (1996a) found no significant flux loss between the filtering with 200 s and 600 s removal time, which is consistent with the results presented by McMillen (1988) for eddy correlation fluxes. Thus a 200 s moving average seems to be appropriate at least over low vegetation. An additional improvement may be obtained by the online rotation of the wind coordinate system to compensate tilt effects of the sonic sensor head (cf. Fig. 5.16). This procedure was also described and analysed in detail by McMillen (1988).

Even with an effective high-pass filter applied, there may still be remaining offsets due to strong trend effects and the necessary asymmetry of the filter. The corresponding flux error can be simulated and corrected in the post-processing as described in Section 5.2.1. For unstable conditions, a fairly linear relationship (Eq. 5.9) was found for the quantification of the offset effect. It is in good agreement with results presented by Pattey et al. (1993). Like for the deadband function, the deviation from the ideal Gaussian behaviour (Eq. 5.8) may be related to the non-linearity of the joint frequency distribution illustrated in Fig. 6.18a. In contrast, for stable conditions (Fig. 5.15a) the offset effect shows a totally random distribution which can not be quantified in a meaningful way. In this case, an integral flux correction is not recommended.

7 CONCLUSIONS

The general objective of this study was the comprehensive investigation of the relaxed eddy accumulation technique and its applicability for the flux measurement of various trace gases. In order to achieve this objective, several theoretical and experimental evaluations were performed and presented in the previous chapters. Flux measurement systems for eddy correlation (EC), relaxed eddy accumulation (REA), and aerodynamic profile method were built up and operated during a field experiment of several weeks.

In contrast to comparable studies, the Bellheim field experiment provided an comprehensive EC dataset of four different scalars for a wide range of environmental conditions (windspeed, radiation, surface conditions, flux magnitude, fetch), with a good representation also of stable cases. It was subjected to a careful evaluation, rejection and verification procedure and allowed extensive and representative simulation studies of the REA method. Beside air temperature, CO₂ turned out to be most suitable for simulation studies for all stability conditions, because in contrast to other trace gas fluxes (e.g. H₂O, O₃) the daytime and nighttime CO₂ fluxes were significantly different from zero. The EC results were also used as a reference for the validation of the REA test system and the accompanying profile measurements. In this way, the applicability of the REA and the profile method could be directly compared for various source area conditions.

7.1 Major Findings of the Present Study

REA b-factor

Based on the performed simulation studies, the REA b-factor as well as other REA related quantities (e.g. eddy reversal frequency) in the inertial sublayer were described (quantified) in a concise way within the framework of the Monin-Obukhov-similarity-theory. A general stability dependence of the REA b-factor was formulated. In good agreement with previous publications, a constant value between 0.56 and 0.57 was found for unstable and near-neutral conditions. For stable conditions, however, a significant increase with stability was identified which can be well described by a logarithmic relationship between b and z/L . These findings disagree with previous results of Pattey et al. (1995), who reported a lower b-factor for stable than for unstable conditions. It was also found, that the b-factor shows no significant difference for the four scalar quantities investigated.

Deadband Effect

The influence of a deadband on the b-factor was analysed for various stability conditions and numerical relationships between b and the normalised deadband width were determined. It was shown, that previous parameterisation schemes (Businger and Oncley, 1990; Pattey et al., 1993) mainly reflected the limited stability ranges covered by the respective database, and that they can be reconciled if the systematic stability dependence is considered.

Joint Frequency Distribution

The analysis of the joint frequency distributions (of the vertical windspeed w and the scalar quantities s) yielded useful information for the physical and statistical interpretation of the results. It showed, that there is no direct relationship between the b -factor and the asymmetry in the one-dimensional w -distribution nor with the asymmetry of the main quadrants (sweep-ejection-ratio). Though the systematic variation of the b -factor could be explained by the influence of the non-linearity of the bivariate distribution, which is connected to the different kurtosis of the w - and s - distributions.

General Implementation Problem

Through the evaluation of the REA field measurements and the detailed investigation of the conditional sampling system applied, several practical problems were identified. Simulation studies showed, that the offset error in the vertical windspeed measurement and the delay time due to valve switching is usually below 10%. Sensor tilt effects and the spatial separation of wind measurement and air sampling inlet can lead to systematic deviations of up to 25% and thus, need to be either avoided or corrected. The present analysis of systematic error effects of REA systems complements the findings of recent publications (e.g. Oncley et al., 1993; Pattey et al., 1993; Beverland et al., 1996a/c), which were mainly limited to homogenous terrain, unstable daytime conditions and a relatively small sample size.

Shortcomings of Specific REA design

The most crucial problem of the specific REA system applied in the present study (after Baker et al., 1992; Beverland et al., 1996a) turned out to be the non-constant conditional sampling flow (during valves open) due to pressure fluctuations in the sampling system. It seems to be an intrinsic characteristic of this setup, but it was obviously not recognised in previous applications (maybe due to compensating errors). The systematic error led to a reduction of the conditional mean concentration difference of often more than 50%, which partly could be compensated by the use of effective b -factors based on the EC temperature data. However, the effect may be generally avoided by a modification of the REA design, i.e. by decoupling the sampling and accumulation/analysing airflow.

Sensor Resolution Requirements

The most crucial limitation for the applicability of the REA method is the requirement and availability of analysers with sufficient resolution (precision). This is a problem for all micrometeorological methods that have to resolve small trace gas concentration differences under natural conditions. Estimations based on similarity relationships and the Bellheim field observations showed that the resolution requirements are generally highest under unstable and neutral conditions with only minor differences among the micrometeorological methods. Under stable conditions, the concentration difference to be resolved for a constant flux grows slightly for REA (by a factor ≤ 5) but much more for the profile method (up to two orders of magnitude). The concentration difference may be further increased for the REA method by the application of a deadband (up to ca. 60%) and for the profile method by larger vertical distance of the measurement levels. The requirements for the trace gas detection can be satisfied with reasonable instrumental effort mainly for trace gases with a large flux-concentration-ratio (deposition velocity). These species are typically short-lived (due to chemical destruction or fast dry deposition) like biogenic volatile organic compounds, strong acids and bases, or nitrogen oxides.

Sensitivity to Inhomogeneous Surface

The effect of inhomogeneous terrain on the applicability of the REA method was investigated (to the authors knowledge) for the first time by the present study. Simulations with eddy correlation datasets as

well as the comparison of measured REA and EC fluxes indicate, that the REA method has the same favourable sensitivity characteristics to inhomogenous surface conditions like the EC method. It can be assumed, that the source area models developed for EC also apply for REA. In contrast, the profile method shows a much stronger sensitivity to inhomogenous terrain, that may be described by differing scalar source areas for each profile level. Depending on the specific fetch conditions, cases with minor deviations from the reference EC fluxes but also cases with totally unrepresentative flux results were observed.

7.2 Recommendations and Outlook

Application of REA and other Methods

It was shown, that the measurement of the conditional mean concentrations in the REA method does not provide a statistical advantage compared to the covariance determination in the EC method. Since the EC technique is more direct and allows more detailed analysis and correction procedures, it should be preferred to the REA method whenever a trace gas analyser with a time resolution of about 1 Hz or faster (depending on vegetation type and measurement height) is available.

For the major part of trace species, for which no fast response measurement is possible, the relaxed eddy accumulation represents an excellent alternative to the profile method. Apart from the higher resolution requirements, it has substantial advantages especially in the sensitivity to inhomogenous terrain. Also the application within the roughness sublayer (over forest) seems to be less problematic. Thus, if only a limited homogenous surface is provided for the flux measurement (which is usually the case), the REA method is usually preferable to the profile method. However, for each individual application of the REA technique, a careful pre-analysis of the specific resolution requirements and available instrumental precision is highly recommended.

Operation of REA Systems

For the control of the conditional sampling valves, an online detrending and vector rotation of the wind signal is recommended. It minimises a priori the corresponding error effects, which can not be corrected entirely in the post-processing. The deadband width should be either set to zero or to a constant normalised value of ca. $0.7 \cdot \sigma_w$. The first solution is the most simple one because it requires no online adjustment of the deadband or estimation of effective b-factors. The second solution on the other hand is especially recommended if the analyser resolution is critical, because it enhances the conditional mean concentration difference by ca. 60% and shows a relatively constant effective b-factor of ca. 0.37. In any application, it is recommended to check the REA b-factors for the specific field condition by comparing simulation results from EC measurements of temperature (or other scalars) with parameterisation schemes as presented in this study.

Measurement Verification and Error Prevention

Whenever possible, a combined application of REA together with another method (profile or enclosure) is desirable for creating confidence in the flux results and for supporting their interpretation. Additionally, a preliminary online calculation is highly desirable for all flux measurement systems, because it allows a permanent check of the results and an early detection of possible problems and instrumental failures that can be fixed immediately. Unfortunately, no online flux calculation software was available in the present study, and therefore the problems and systematic error effects mentioned above could be checked only after the field campaign. Hence for future field experiments, the establishing of an online

flux calculation and display programs, preferably for a direct comparison of different methods, is recommended. The online calculation of the EC fluxes can be directly adopted from the evaluation procedure applied in this study.

Further Development of REA Method

Together with the findings of other publications, the results of the present study show that the relaxed eddy accumulation represents a self-standing theoretical concept relying only little on empirical assumptions. Due to the well defined b-factor and the much simpler sampling technique, the REA method has some practical advantages over the normal proportional eddy accumulation method (cf. Section 2.5.2), for which no successful experimental applications were reported in recent years. Thus, future activity should focus on the optimal adjustment of the REA design for various measurement tasks and trace gases of interest. The REA flux measurement for inert species and reactive gases that can be easily trapped and deactivated (e.g. VOC's) may be regarded as preliminarily established. However, the applicability and practical implementation of REA systems for reactive short-lived compounds (e.g. NO, NO₂, NH₃) that have to be detected by slow online gas analysers needs further development and testing.

Trace Gas Exchange of Senescent Triticale Field

The field experiment presented in this study also exhibits interesting information about the specific gas exchange behaviour of a cereal field during the senescence development. Issues such like the change in leaf area and stomatal control and the corresponding effect on the water and CO₂ exchange as well as the uptake of O₃ were outside the actual scope of the present study but deserve further evaluation. In addition, a more extended comparison (reconciliation) of flux measurements on different spatial scales (porometric chamber - micrometeorological surface layer methods - PBL budget methods) as well as the application of in-canopy diffusion models could provide further insight in the mechanisms of trace gas exchange and corresponding measurement problems.

APPENDICES

APPENDIX A: Spectral Analysis of Turbulence Time Series

Spectral analysis is a useful statistical tool to analyse and describe the temporal and spatial characteristics of complex physical phenomena such as turbulence. From spectra of measured high resolution time series it can be discovered how eddies of different time and space scales (frequencies, wavelengths) contribute to the overall turbulence state and processes. Additionally the proper operation of the measurement systems can be checked and errors can be identified. Some errors with a pronounced spectral characteristic (e.g. sensor separation, tube damping) can only be described and corrected appropriately in the spectral domain.

A.1 Harmonic Fourier Decomposition

The classical spectral representation of a time series with length T_a is obtained through a harmonic (Fourier) analysis. The time series are decomposed into a linear combination of harmonic sine and cosine functions. The term 'harmonic' means, that the trigonometric functions all have integer frequencies with respect to T_a and are therefore linearly independent. For simplicity, the frequencies in the following sections are not given in the time dependent form f with units Hz (s^{-1}), but in the dimensionless form $n = f \cdot T_a$ which denotes the (integer) number of fluctuation periods within the considered time interval T_a . The advantages of the *harmonic analysis* are its special mathematical characteristics that provide efficient calculation, simple manipulation and a good statistical interpretation of spectra. For this reason harmonic (Fourier) analysis is commonly used in turbulence studies. For convenience the discussion in the following section is limited to time series consisting of equally spaced data points with a sampling interval Δt . This is the normal case for micrometeorological measurements. The theory can be applied in the same way to spatial data sets. A time series $x(k)$ consisting of N equally spaced data points (indexed with $k = 0 \dots N-1$) can be decomposed into a linear combination of harmonic sine and cosine terms with frequencies $n = 0 \dots N/2$:

$$x(k) = A_x(0) + \sum_{n=1}^{N/2} A_x(n) \cdot \cos\left(2\pi \frac{n}{N} k\right) + \sum_{n=1}^{N/2} B_x(n) \cdot \sin\left(2\pi \frac{n}{N} k\right) \quad (\text{A.1a})$$

This decomposition can be written in a mathematically equivalent form as linear combination of only cosine terms but with variable phase angles $\Phi_x(n)$. Each of the two formulations may show some advantages under certain conditions.

$$x(k) = C_x(0) + \sum_{n=1}^{N/2} C_x(n) \cdot \cos\left(2\pi \frac{n}{N} k - \Phi_x(n)\right) \quad (\text{A.1b})$$

The Equations A1.a/b are called discrete Fourier series or periodogram representations (Chatfield, 1975: 133). The Fourier series represent an interpolation function through the N given data points. In order to reproduce N independent values, N independent parameters are necessary: the amplitudes of the sine and cosine functions (or the amplitudes and the phase shifts of cosine functions only). The first

parameter $A_x(0)$ represents the arithmetic mean of the data points and can be interpreted as the amplitude of a cosine with infinite period length and thus frequency 0. The amplitudes with $n = 1$ correspond to the functions with the fundamental frequency 1 over the whole data range. The higher terms in the Fourier series have integer frequencies referring to the fundamental period T_a . The highest frequency that can be resolved with a sampling interval Δt is the so-called Nyquist-frequency $n_f = N/2$. With N even, the sine term with $B_x(n_f)$ or phase shift $\Phi_x(n_f)$ equals zero, because the phase is directly coupled to the position of the sampling points.

A.2 Unresolvable High and Low Frequencies

The harmonic analysis only resolves and uses frequencies, that lie between the fundamental and the Nyquist frequency. If there are variations in the original time series with frequencies outside of this range (e.g. trend, high-frequency noise), they cannot be adequately represented and their effect on the data points will be reproduced by other (wrong) frequencies *inside* the resolvable range. The decomposition of a given time period into harmonic functions includes an implicit assumption about the course of the time series before and after the measurement period. All harmonic terms and also their superposition are periodic with the fundamental period. It is assumed that the finite data set represents exactly one period of a periodic infinite time series. This implies for example that $x(N) = x(0)$, $x(N+1) = x(1)$ and so on (see Fig. A.1).

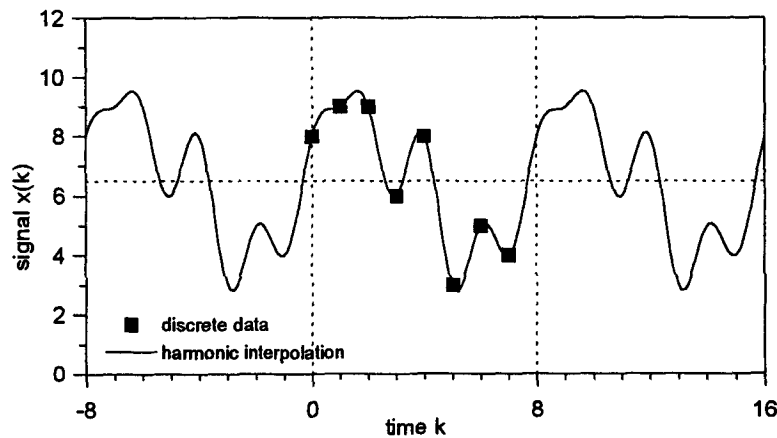


Fig. A.1: Illustrative example for the interpolation and implicit extrapolation of a limited discrete time series ($N = 8$) by a combination of harmonic Fourier series (Equation A.1a/b).

If there is a trend in the data set, which can often be observed in real environmental time series (e.g. from diurnal changes), a periodic component of roughly triangular form and with the fundamental period is introduced. In the harmonic decomposition it will be represented also through frequencies closely below the fundamental one. This effect (enhanced spectral amplitudes in the low frequency range) is called 'red noise'. The red noise can be eliminated or at least minimised through preconditioning procedures. One possibility is the *detrending* of the time series. Normally a fitted linear trend is subtracted from the data so that the end of the series shows about the same average value like the beginning. Another conditioning method is the *tapering*. It brings both ends of the time series to zero by subtracting the average and multiplying the dataset with a weighting function ('window') that is approximately equal to one in the middle part and goes to zero at both ends. The tapering window can

have different forms that are discussed for example by KF94:266 and St88:308. The tapering also reduces the variance of frequencies in the good range, which have to be corrected later.

The opposite problem to the red noise effect is the so-called 'aliasing' in the high frequency range. If data are sampled at intervals Δt , variations with a minimal period of $2 \cdot \Delta t$ (corresponds to the Nyquist frequency) can be resolved. If there are faster fluctuations in the original analogue time series, they appear in the discretely sampled data sets as variations with lower frequencies inside the resolvable range. Harmonic frequencies are just mirrored at the Nyquist frequency: e.g. n_f+i is represented through n_f-i (with the same amplitudes and phase shift except for sine terms with opposite phase shift). An illustrative example is given in Figure A.2.

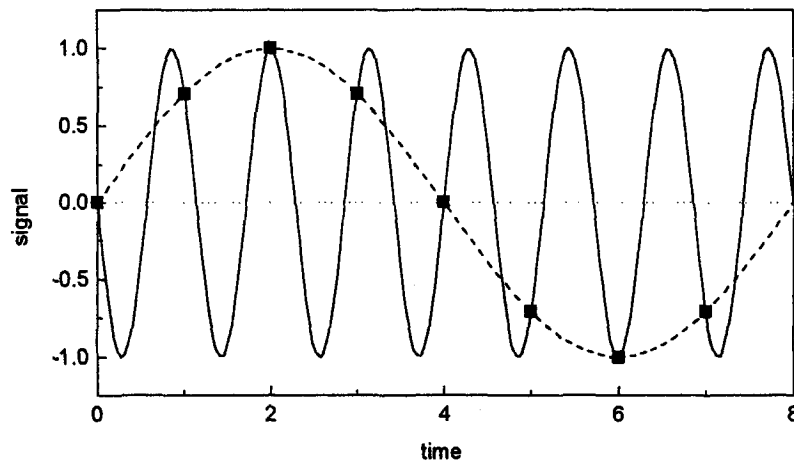


Fig. A.2: Illustrative example for the aliasing effect for a discrete time series with $N=8$: a signal with the frequency $n = 7$ (higher than the Nyquist frequency $n_f = N/2 = 4$) is interpreted as lower frequency signal with $n = 1$ (mirrored at the Nyquist frequency).

The aliasing is mainly a problem of the discrete digitalisation of continuous signals. There is no effect, if the respective sensor has a response time similar to Δt or if the output is smoothed or averaged to that time interval. Attention has to be given to high-frequency noise that can be caused by electronic devices or may be induced by external electromagnetic fields e.g. from power lines. If an aliasing problem occurs, the only way to get rid of it is a low-pass prefiltering of the continuous time series with a cutoff frequency close to n_f . This can be done either by an electronic analogue filter device or by digital pre-sampling at a higher rate and consecutive block average to the time interval Δt . The detailed effects of this procedures is discussed by KF94:262.

A.3 Calculation of Spectral Amplitudes

In order to get a spectral representation of a time series, the harmonic amplitudes and/or phase shifts in equation A.1a/b have to be calculated. This procedure needs a lot of computations and is carried out almost exclusively on computers. The mostly used algorithm is the Fast Fourier Transform (FFT). It has an optimised performance concerning the number of computer operations and thus minimises the computation time. The FFT is limited to equally-spaced data sets with no missing points allowed. If this condition is not given and cannot be simulated it may be necessary to use much more time consuming calculation methods like a least squares best fit of the different harmonic wave functions (St88:335).

The FFT algorithm is based on a general Fourier decomposition procedure for *complex* datasets and therefore yields the harmonic amplitudes for a real time series (Eq. A.1) not directly. The expected input for the FFT algorithm is a series $\hat{x}(k)$ consisting of N equally spaced complex data points. The corresponding discrete Fourier decomposition may be represented in the following form with complex coefficients:

$$\hat{x}(k) = \sum_{n=0}^{N-1} \hat{F}_x(n) \cdot \left(\cos\left(2\pi \frac{n}{N} k\right) + i \cdot \sin\left(2\pi \frac{n}{N} k\right) \right) \quad (\text{A.2})$$

Unlike in the real case (Eq. A.1), the complex Fourier series consists of N harmonics with complex amplitudes. The FFT algorithm yields the complex spectral coefficients as real and imaginary parts:

$$\hat{F}_x(n) = F_{\text{Re},x}(n) + i \cdot F_{\text{Im},x}(n) \quad (\text{A.3})$$

If a pure real time series $x(k)$ is fed into the FFT algorithm (all imaginary parts equal to zero), only the real terms in Equation A.2 remain:

$$x(k) = \sum_{n=0}^{N-1} \left(F_{\text{Re},x}(n) \cdot \cos\left(2\pi \frac{n}{N} k\right) - F_{\text{Im},x}(n) \cdot \sin\left(2\pi \frac{n}{N} k\right) \right) \quad (\text{A.4})$$

This has almost the same form as Equation A.1a except for the opposite sign of the sine terms and the doubled number of harmonic function (N instead of $N/2$). The general complex Fourier decomposition needs $2 \cdot N$ independent functions for the representation of N complex data points consisting of $2 \cdot N$ independent real values. For real time series, the components above the Nyquist frequency $n_f = N/2$ cannot be distinguished from the respective aliased frequencies below n_f (see above). In order to obtain the spectral Amplitudes $A_x(n)$ and $B_x(n)$, the high-frequency terms in Eq. A.4 have to be "folded back" i.e. be added to the respective lower frequencies. It turns out that for real time series, the complex Fourier transform divides the spectral amplitudes evenly between the lower (resolvable) and the upper (aliased) part of the Fourier series. The latter is just the mirrored complex conjugate of the first. Therefore the folded spectral amplitudes can be calculated from the FFT results according to Eq. A.5. The coefficients for $n = 0$ and $n = n_f$ (if N is even) are always real and can be taken directly (without factor 2).

$$\left. \begin{aligned} A_x(n) &= 2 \cdot F_{\text{Re},x}(n) \\ B_x(n) &= -2 \cdot F_{\text{Im},x}(n) \end{aligned} \right\} (0 < n < n_f) \quad (\text{A.5})$$

A.4 Variance and Covariance Spectra

A common type of question in spectral analysis is how much of the total variance of a given time series is associated with certain frequencies. Such statistical investigations are particularly easy to make with harmonic spectra following Parseval's theorem (Chatfield, 1975: 134). It states that with the superposition of harmonic functions the respective variances are just added. This means that the spectral contributions to the variance of a time series can be explained by the variances of the Fourier series components in Eq. A.1. The variance of a single cosine function with Amplitude C equals $0.5 \cdot C^2$. Therefore the spectral variance at frequency n can be calculated as

$$S_x(n) = \frac{1}{2} C_x^2(n) = \frac{1}{2} [A_x^2(n) + B_x^2(n)] \quad (\text{A.6})$$

The variance spectrum $S_x(n)$ is also called power-, energy-, or auto-spectrum. All spectra are represented here in the folded form, i.e. with all contributions folded below the Nyquist frequency, which is more meaningful than the unfolded spectra resulting directly from the FFT output. According to Parseval's theorem, the total variance of the time series equals the sum of all spectral components:

$$\sigma_x^2 = \sum_{n=1}^{n_f} S_x(n) \quad (\text{A.7})$$

If the power spectra of atmospheric turbulence data are plotted on a linear-linear graph, the plot is normally useless to view, because the most important lower frequencies crowd at one end (cf. St88: 315f.). One alternative is to display the frequency axis with a logarithmic scaling. In that case, it is of big advantage to multiply the spectral variance with the frequency n resulting in a plot $n \cdot S_x(n)$ vs. $\log(n)$. This representation has the desirable characteristic, that the area under any portion of the curve is proportional to the portion of variance explained by the corresponding frequency range and therefore:

$$\sigma_x^2 = \sum f \cdot S_x(n) \cdot \Delta(\log n) \quad (\text{A.8})$$

In analogy to Equation A.6, the spectral distribution of the covariance of two time series $x(k)$ and $y(k)$ can be obtained by calculating the covariance of the corresponding harmonic functions at each frequency. The resulting cospectrum $Co_{xy}(n)$ depends on the amplitudes as well as on the relative phase shift of the cosine functions.

$$Co_{xy}(n) = 1/2 C_x(n) C_y(n) \cdot \cos[\Phi_x(n) - \Phi_y(n)] \quad (\text{A.9a})$$

$$Co_{xy}(n) = 1/2 [A_x(n) A_y(n) + B_x(n) B_y(n)] \quad (\text{A.9b})$$

With the more general form of Parseval-theorem called power-theorem, relationships similar to Equations A.7 and A.8 are obtained.

$$\text{cov}(x, y) = \overline{x'y'} = \sum Co_{xy}(n) \quad (\text{A.10})$$

$$\overline{x'y'} = \sum f \cdot Co_{xy}(n) \cdot \Delta(\log n) \quad (\text{A.11})$$

Often, the cospectrum is normalised with the corresponding power spectra to form a correlation spectrum:

$$r_{xy}(n) = \frac{Co_{xy}(n)}{\sqrt{S_x(n) \cdot S_y(n)}} \quad (\text{A.12})$$

By forming the spectral covariance through multiplication of the Fourier coefficients, a part of the original information gets lost concerning e.g. variations which are out of phase. As a complement to the cospectrum, the quadrature spectrum $Q_{xy}(n)$ can be calculated. It corresponds to the spectral covariance of the two time series shifted for a quarter of the respective period ($\Delta t \cdot N/n$).

$$Q_{xy}(n) = 1/2 C_x(n) C_y(n) \cdot \sin[\Phi_x(n) - \Phi_y(n)] \quad (\text{A.13a})$$

$$Q_{xy}(n) = 1/2[A_x(n) B_y(n) - B_x(n) A_y(n)] \quad (\text{A.13b})$$

A.5 Spectral Averaging and Statistical Significance

Without averaging or smoothing processes, the procedure described above yields *raw spectra* for $N/2$ frequencies. The single values of these raw spectra are not of practical use because the spectral estimates show large scatter and are hardly statistically significant. This means that they can not be distinguished significantly from spectra of totally random time series ('white noise'). For that reason, averaging processes have to be applied, which correspond e.g. to a simple smoothing (band averaging) of the respective spectrum. The intensity (width) of spectral averaging depends on the individual requirements. If statistical significance of spectral data should be evaluated in a quantitative way, it is advisable to average a constant number of neighbouring harmonics. According to Chatfield (1975: 143f.), an averaging over m neighbouring frequencies creates $\nu = 2 \cdot m$ degrees of freedom, that determine the confidence interval for the smoothed spectral estimates (denoted by an overbar). Jenkins and Watts (1969: 254) give the $(1-\alpha)$ -confidence interval for a smoothed variance spectrum as:

$$\frac{\nu}{\chi^2_{\nu}(\alpha/2)} \cdot \bar{S}_x(\bar{n}) \leq \dots \leq \frac{\nu}{\chi^2_{\nu}(1-\alpha/2)} \cdot \bar{S}_x(\bar{n}) \quad (\text{A.14})$$

For the cospectrum, the confidence limits are more complicated to determine. They do not correspond to constant factors for a certain ν like in Eq. A.14, but rather depend additionally on the respective quadrature and power spectral values. According to Chatfield (1975: 184), it is more convenient and useful to investigate the spectral relationship between two time series with the help of the coherency spectrum. It is defined in the squared form as:

$$\overline{\text{Coh}}_{xy}^2(\bar{n}) = \frac{\overline{\text{Co}}_{xy}^2(\bar{n}) + \overline{Q}_{xy}^2(\bar{n})}{\bar{S}_x(\bar{n}) \cdot \bar{S}_y(\bar{n})} \quad (\text{A.15})$$

The coherency spectrum is only meaningful if determined from smoothed spectra (for raw spectra it is always equal to one!). It can be interpreted as maximal spectral correlation between the two time series x and y with an optimal phase adjustment. The squared coherency represents the fraction of the explained or linearly related variation of the two time series, either in phase (directly correlated) or out of phase (shift-correlated). It takes thus values between 0 and 1. The remaining, totally uncorrelated variance can be assigned to random white noise. In contrast to the coherency, the normal squared correlation as defined in Eq. A.15 gives only the fraction of directly (in phase) correlated variance. It is therefore always smaller than the coherency.

The value of the coherency depends on the spectral averaging width m (or on the no. of degrees of freedom respectively), since the phase adjustment is constant over the averaged frequency range. Confidence intervals show a particularly simple symmetric form, if the coherency is subjected to a z -transformation (Jenkins and Watts, 1969: 380):

$$\text{arctanh}[\overline{\text{Coh}}_{xy}] \pm \frac{z_{\alpha/2}}{\sqrt{\nu}} \quad (\text{A.16})$$

$z_{\alpha/2}$ stands for the limit of the standard normal distribution for the probability $\alpha/2$. For a two sided confidence level of $(1-\alpha) = 95\%$, $z_{0.025}$ equals 1.96. If the lower confidence limit lies below zero, the spectral coherency and thus the correlation between the two time series is not significantly different from zero in the corresponding frequency range. An alternative approach for testing non-zero coherency is also proposed by Jenkins and Watts (1969: 433). It is based on the uncertainty in the coherency of two uncorrelated white noise series. The following test quantity shows a F-distribution with degrees of freedom 2 and $(v-2)$:

$$\frac{(v-2) \cdot \overline{\text{Coh}}_{xy}^2}{2 \cdot (1 - \overline{\text{Coh}}_{xy}^2)} \sim F_{2, v-2} \quad (\text{A.17})$$

For an error level α , the significance limit for the coherency is thus:

$$\overline{\text{Coh}}_{xy} \geq \sqrt{\frac{2F_{2, v-2}(\alpha)}{2F_{2, v-2}(\alpha) + v - 2}} \quad (\text{A.18})$$

Vong & Kowalski (1995) for example applied the test with 100 degrees of freedom and an error level $\alpha = 5\%$. In this case, the significance limit equals about 0.25.

Another more quantitative testing procedure for covariance spectra is the calculation and visual inspection of the cumulative spectral distribution (Jenkins and Watts, 1969: 367f.), also called 'ogive'. It does not require a pre-averaging of the raw spectra, since it has a strong smoothing effect itself. For turbulence studies, cumulative cospectra were determined e.g. by PD84:210 and Beier and Weber (1992). They are usually calculated and plotted according to Equation A.8 on a logarithmic frequency scale. In the ideal case, the ogive shows a roughly monotone course except for small opposite contributions.

Statistical examination is not the only purpose of spectral averaging. For turbulence studies, an optimised display as well as a suitable data reduction are important aspects. KF94:269 suggest an increasing averaging bandwidth towards the high frequency end, where the harmonics are more and more crowded in a logarithmic scaled plot. A constant number (ca. 8) of spectral averages should be formed within each frequency decade. This results in about 30-40 equally spaced spectral estimates in the usual logarithmic plots. In such a spectral representation, the statistical uncertainty is largest at low frequencies and decreases towards higher frequencies.

A.6 Semi-empirical Form of Turbulence Spectra

In trace gas exchange studies, knowledge about the form of turbulence cospectra (Co_{wc}) and variance spectra (S_w and S_c) is of great interest. It is necessary in order to determine, which frequency response and averaging times are required for obtaining reliable flux estimates (Section 2.3.2). Furthermore, it may allow to test and correct measured fluxes for the inadequate response of an imperfect sensor (Section 4.1.6). Since turbulence in the atmospheric surface layer obeys Monin-Obukhov-similarity (cf. Section 2.4.1), one can expect, that the form of turbulence spectra and cospectra is clearly defined under given conditions and can be uniquely related to the respective key parameters, like other statistical properties of turbulent transport.

According to Taylor's hypothesis (Section 2.3.1), the spectra of time series measured by a fixed sensor are representative for the spatial turbulence structure. The integer frequency n (dimensionless, related to

the length of the time series T_a) or the equivalent frequency $f = n/T_a$ (with units $Hz = s^{-1}$) are related to the eddy size λ_{eddy} according to Equation 2.20. For convenience, a normalised eddy wavenumber, which results from the scaling of the eddy size with the height z , is generally used as frequency scale for turbulence spectra:

$$f_z = \frac{z}{\lambda_{\text{eddy}}} = f \cdot \frac{z}{u} \quad (\text{A.19})$$

According to Kaimal et al. (1972) the spectral density functions can be normalised in a way, that their form (and peak position) is only a function of the dimensionless frequency f_z and the stability parameter z/L . The relationships are defined in the frequency weighted form (cf. Eqs. A.8 and A.11), which provides area-proportionality:

$$f \cdot \frac{Co_{wc}(f)}{u_* \cdot \mu_{c*}} = K_{wc}(f_z, z/L) = K_{wT}(f_z, z/L) \quad (\text{A.20})$$

$$f \cdot \frac{S_w(f)}{u_*^2} = K_w(f_z, z/L) \quad (\text{A.21})$$

$$f \cdot \frac{S_c(f)}{\mu_{c*}^2} = K_c(f_z, z/L) = K_T(f_z, z/L) \quad (\text{A.22})$$

Kaimal et al. (1972; 1976) derived their model spectra from windspeed and temperature data collected during the Kansas and Minnesota experiments. Only few experimental results are available for spectra and cospectra of trace gas concentrations, but they provide evidence, that there is no significant difference between various scalar quantities (PD84:210; Anderson and Verma, 1985; Anderson et al., 1986). Therefore, the ‘Kaimal spectra’ for temperature are usually adopted for other scalars (Moore, 1986; Laubach and Teichmann, 1996).

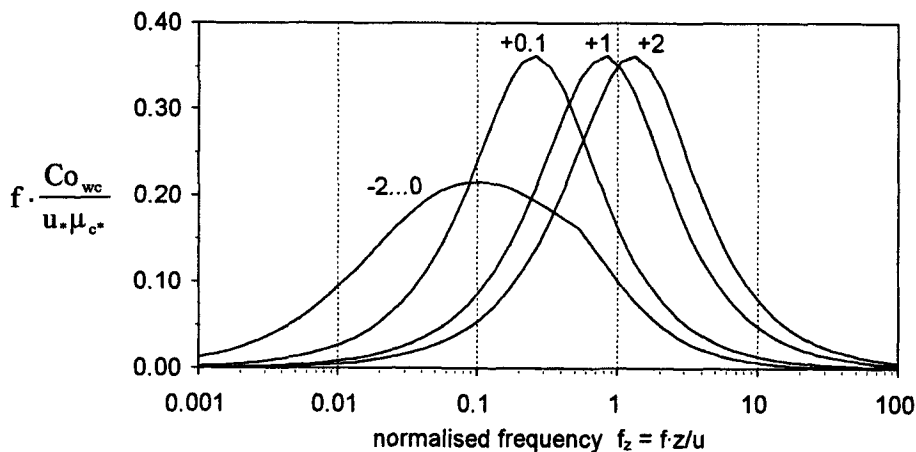


Fig. A.3: Normalised Kaimal cospectra for scalar fluxes under different stability conditions indicated as z/L values.

The Kaimal spectra used in this study are taken from Moore (1986), where they are given in a slightly modified form compared to the original (Kaimal et al., 1972). Only the cospectral relationship is rewritten explicitly in the following. Whereas in the stable range, a well defined dependence on the stabil-

ity z/L is found (Eq. A.23a), the unstable cospectra crowd into a narrow band that straddles the neutral cospectrum. Therefore the latter is generally used for neutral as well as unstable conditions (Eq. A.23b).

$$z/L > 0 : K_{wc} = f_z \cdot \left[0.284 \cdot (1 + 6.4 z/L)^{0.75} + 9.345 \cdot (1 + 6.4 z/L)^{-0.825} \cdot f_z^{2.1} \right]^{-1} \quad (\text{A.23a})$$

$$z/L \leq 0 : K_{wc} = \begin{cases} 12.92 \cdot f_z \cdot (1 + 26.7 f_z)^{-1.375} & f_z < 0.54 \\ 4.378 \cdot f_z \cdot (1 + 3.8 f_z)^{-2.4} & f_z \geq 0.54 \end{cases} \quad (\text{A.23b})$$

The Kaimal cospectra (Eq. A.23a/b) are displayed in Fig. A.3 for different stability values. With the logarithmic scaling of the horizontal frequency axis, the area under the curves is proportional to the covariance (vertical flux) explained by the corresponding frequency range. All functions are normalised with the total flux and have therefore the same integral area.

Through similarity theory, it could also be deduced, that the spectra and cospectra are falling off on both sides by certain power laws (KF94:38). This behaviour can be illustrated and tested in a spectral plot with double logarithmic scaling (see Fig. A.4). In the inertial subrange, the cospectra have a constant slope $-4/3$ (log. decades), indicating a power law relationship $f^{-4/3}$. It is usually much better defined than the f^{-1} power law in the low frequency range, which is often disturbed by longterm non-turbulent variations. For the variance spectra, the same behaviour is found for the low frequency side, whereas in the inertial subrange, a power law with $f^{-2/3}$ can be observed. It has to be kept in mind, that all these power laws are valid for the weighted cospectrum (multiplied with f). In the pure form, the powers are decreased by 1.

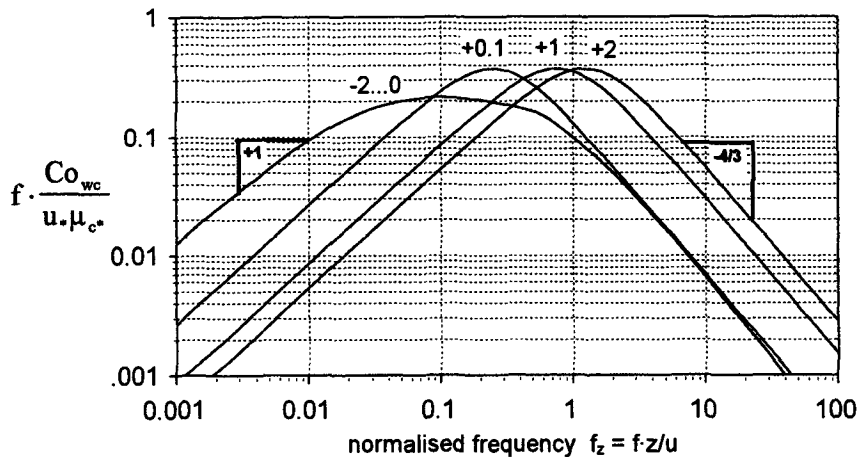


Fig. A.4: Normalised Kaimal cospectra for scalar fluxes in a log-log-plot under different stability conditions, with indication of the power laws: f^{-1} in the low frequency range and $f^{-4/3}$ in the inertial subrange.

A.7 Spectral Response of Turbulence Measurement Systems

Measured time series do not represent exactly the real behaviour of the investigated quantity since they are more or less affected by the response characteristics of the measurement system. Beside the limitations connected with the sampling rate (see Section A.2), the physical response behaviour of instruments may also have an attenuation effect on fluctuations within the resolvable frequency range. They often lead to an underestimation of the spectral intensity especially in the high-frequency range and also affect

the integral characteristics (variance or covariance) of the time series. The attenuation characteristics due to limited instrumental response can be quantified by spectral transfer functions $T(f)$ which represent the attenuation factor on the power spectrum for each frequency f .

$$S_x(f)_{\text{meas.}} = T(f) \cdot S_x(f)_{\text{true}} \quad (\text{A.24})$$

The total transfer function is usually a product of various effects which correspond to transfer functions of different forms. In the following sections, all damping effects are discussed, which have an influence on the turbulence (eddy correlation) measurements of the present study.

First Order Analog Filter

Many measurement systems do not react immediately to a change in the measured quantity, but have a certain memory effect. Their output signal $y(t)$ is not only a function of the actual (instantaneous) input of the measured quantity $x(t)$, but also depends on the preceding state. Mathematically such systems can often be described by a linear differential equation of first order:

$$\frac{dy(t)}{dt} = \frac{1}{\tau_R} [x(t) - y(t)] \quad (\text{A.25})$$

The approach of the output signal $y(t)$ to the true measurement value $x(t)$ is proportional to the actual deviation $[x(t) - y(t)]$. For an ideal step change of $x(t)$ between two constant values ($C \rightarrow 0$), the solution of the differential equation yields an exponential approach function:

$$y(t) = C \cdot \exp(-t/\tau_R) \quad (\text{A.26})$$

The parameter τ_R represents the time interval, that the output signal $y(t)$ needs to approach the true input value by the factor $e = 2.718$. It is called the 'response time' of the measurement system. According to Moore (1986) the spectral transfer function of a first order system (filter) takes the form:

$$T_R(f) = \frac{1}{1 + (2\pi f\tau_R)^2} = \frac{1}{1 + (f/f_0)^2} \quad (\text{A.27})$$

The parameter f_0 is the so-called 'cutoff frequency' or 'half-power frequency' and indicates the frequency, at which the power spectrum is damped to 50% (see Eq. A.28 and Fig. A.5). It is often used as a general characterisation parameter for transfer functions.

$$T(f_0) = \frac{S_x(f_0)_{\text{meas.}}}{S_x(f_0)_{\text{true}}} = 0.5 \quad (\text{A.28})$$

The memory effect of first order systems does not only produce an attenuation of the spectral variance but also a characteristic phase shift. According to Profos and Pfeiffer (1993) it can be described mathematically as:

$$\phi_R(f) = \arctan(-f/f_0) = \arctan(-2\pi f\tau_R) \quad (\text{A.29})$$

The phaseshift is largest (close to 90°) for high frequencies, which are also strongly damped in amplitude. For frequencies lower than f_0 , the delay time resulting from the phase shift approaches asymptotically the constant value τ_R .

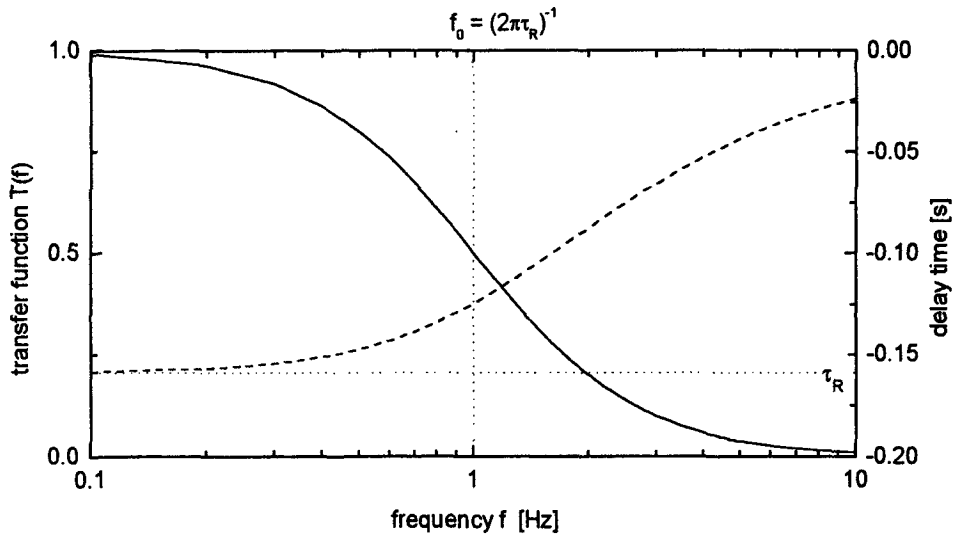


Fig. A.5: Spectral characteristics of a first order system with a cutoff frequency $f_0 = 1$ Hz: transfer function describing the attenuation factor for the variance spectrum (solid line); spectral delay time caused by the phase shift (dashed line).

Most passive sensors like e.g. thermocouples, thermistors, impedance humidity instruments or moving windspeed sensors (propeller or cup) represent first order systems and obey the described theory. Also the simplest electronic filter, a resistor-capacitor (RC) element, shows this response characteristic. Such an RC-filter is used in the Gill sonic instrument to prefilter the analog inputs of the external instruments (see Section 3.3.1). Its response time was determined to $\tau_R = 0.125$ s corresponding to a cutoff frequency of about 1.3 Hz.

Spatial Averaging

Most active measurements systems used for atmospheric turbulence studies (e.g. optical trace gas sensors, sonic anemometers etc.) do not have the memory effect and the time response problems of the first order systems. Instead, they usually make a spatial average over a certain pathlength (or area/volume), which has a similar spectral attenuation effect like temporal averaging, since temporal and spatial variations are strongly related (see Section 2.3.1). Moore (1986) gives approximated transfer functions for sensor line averaging over a pathlength ℓ . They are defined as functions of a specific frequency $f_\ell = f\ell/u$ normalised with the length scale ℓ and the windspeed u similar to Equation A.19. It has to be distinguished between sensors for scalar and vector quantities as well as for the orientation of the sensor path relative to the mean windvector. For scalar quantities (temperature, gas concentrations), the two limiting cases for angles of 0 and 90 deg between sensor path and windvector are given as:

$$T_{\ell,s0}(f_\ell) = \frac{\sin^2(\pi f_\ell)}{(\pi f_\ell)^2} \quad (\text{A.30})$$

$$T_{\ell,s90}(f_\ell) = \frac{1}{2\pi f_\ell} \left[3 + e^{-2\pi f_\ell} - \frac{4}{2\pi f_\ell} (1 - e^{-2\pi f_\ell}) \right] \quad (\text{A.31})$$

The influence of spatial averaging on the measurement of windvector components (sonic anemometer) is more complex than for scalar quantities. According to Moore (1986) a suitable generalised expression can be given only for a vertical orientation of the sensor path, i.e. for the direct sonic measurement of the vertical windspeed w with a single path. The resulting function A.32 has a similar form as Equation

A.31 but with slightly differing coefficients. The course of the three transfer functions A.30 - A.32 is drawn in Figure A.6

$$T_{\ell,w}(f_{\ell}) = \frac{1}{2\pi f_{\ell}} \left[4 + 2 e^{-2\pi f_{\ell}} - \frac{6}{2\pi f_{\ell}} (1 - e^{-2\pi f_{\ell}}) \right] \quad (\text{A.32})$$

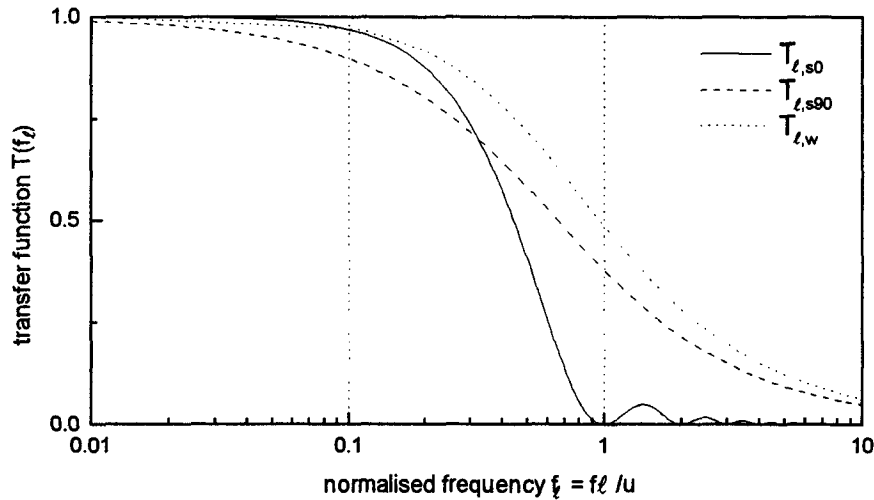


Fig. A.6: Spectral transfer functions describing the attenuation effect of line averaging on vertical wind and scalar measurements (with 0° and 90° orientation relative to the mean wind).

The Gill sonic anemometer used in the present study has three measurement paths of length $\ell = 0.15$ m. They have a non-orthogonal orientation with an angle of 45° relative to the horizontal (cf. Section 3.3.2). The sonic temperature is derived from a single path whereas the vertical windspeed (and the horizontal components) results from a combination of all three paths. Unfortunately, no transfer functions for this relatively complex geometric arrangement were presented in literature up to now. However, since the angle between the individual paths and the wind vector is always between 45° and 90° depending on the wind direction, the described transfer functions for a perpendicular wind attack $T_{\ell,s90}$ (A.31) and $T_{\ell,w}$ (A.32) seemed to be the best available information describing the attenuation of the sonic temperature as well as the vertical windspeed. They were therefore generally used for the correction of the path averaging effect.

Damping Effect of Tube Sampling

If air is measured in a closed-path system, it is usually sampled through a tube of a certain length. Small scale turbulence and molecular diffusion within the tube lead to an attenuation of small scale (high frequent) fluctuations in the air properties. Leuning and Moncrieff (1990), Lenschow and Raupach (1991) and Massman (1991) discuss the attenuation effects on the concentration of gas components, which have no interaction with the tube walls. The attenuation strongly depends on the flow type (laminar or turbulent) and thus on the Reynolds number Re .

$$Re = \frac{D \cdot u_t}{\nu} \quad (\text{A.33})$$

The parameter D denotes the inner diameter of the tube, ν the kinematic viscosity ($\nu = 1.46 \cdot 10^{-5} \text{ m}^2/\text{s}$ for standard atmospheric conditions), and u_t here is the mean flow speed inside the tube. The flow

regime is laminar for Reynolds numbers below a critical value $Re_{crit} \approx 2300$ and turbulent above that value. Lenschow and Raupach (1991) give spectral transfer functions for both flow types:

$$T_{t,lam}(f_t) = \exp(-0.82 \text{ Re Sc } f_t^2) \quad (\text{A.34})$$

$$T_{t,turb}(f_t) = \exp(-280 \cdot \text{Re}^{-1/8} \cdot f_t^2) \quad (\text{A.35})$$

Sc is the Schmidt number of the investigated gas and $f_t = f \cdot (0.5D \cdot X)^{0.5} / u_t$ is the frequency normalised with the characteristic tube length scale depending on tube diameter D and length X. The spectral attenuation effect strongly depends on the type of flow; it is much stronger for laminar than for turbulent conditions. It is therefore crucial for closed-path eddy correlation measurements, to maintain a turbulent flow in the sampling tube. It was shown in Section 3.3.3, that for both closed-path eddy correlation systems used in the present study ($\text{CO}_2/\text{H}_2\text{O}$ -analyser as well as O_3 -analyser) the sampling tube flow was turbulent. Thus the corresponding attenuation characteristic is appropriately described by the transfer function $T_{t,turb}$ (A.35).

A.8 Spectral Attenuation of Covariance Measurements

In the previous section, the possible attenuation effects of single measurement systems on the spectral variance was discussed. They also affect cospectra estimations between two measured quantities x and y. The influence can be described by partitioning the cospectrum according to Equation A.12:

$$Co_{xy}(f) = \sqrt{S_x(f)} \cdot \sqrt{S_y(f)} \cdot r_{xy}(f) \quad (\text{A.36})$$

Hence, both measurement systems attenuate the cospectrum by the square root of their transfer functions $T_x(f)$ and $T_y(f)$. However, in addition to this individual effects, there may also be an attenuation of the spectral correlation coefficient $r_{xy}(f)$, that results from the combination of two independent sensors. It can be described as analogous to Eq. A.24 by a transfer function $T_{xy}(f)$:

$$r_{xy}(f)_{\text{meas.}} = T_{xy}(f) \cdot r_{xy}(f)_{\text{true}} \quad (\text{A.37})$$

A specific attenuation of the correlation has to be connected with a spectral phase shift between the two time series, since $r_{xy}(f)$ only depends on the spectral phase difference; a combination of Equations A.6, A.9, and A.12 yields:

$$r_{xy}(f) = \cos(\Phi_x - \Phi_y) = \cos(\Delta\Phi) \quad (\text{A.38})$$

If a certain additional phase shift $\varphi(f)$ is introduced, the resulting transfer function for the correlation or cospectrum follows from Equations A.9a and A.13a (Moore, 1986):

$$T_{xy}(f) = \cos[\varphi(f)] + \sin[\varphi(f)] \frac{Q_{xy}(f)}{Co_{xy}(f)} \quad (\text{A.39})$$

The second term is difficult to quantify, since it depends on properties of the time series which can vary considerably. For atmospheric turbulence measurements, Moore (1986) suggests as a first approximation, that the second term may be neglected assuming that the quadrature spectrum is small compared to the cospectrum.

A common problem in covariance measurements is the synchronicity of the two sensors. This may lead to a constant time lag τ_L between the time series. If the covariance is not calculated online, the time lag can be determined in the postprocessing and the series can be adjusted by shifting against each other. If this is not possible, the resulting attenuation effect may be estimated from the first term of Eq. A.39:

$$T_L(f) \approx \cos[\varphi(f)] = \cos[2\pi f\tau_L] \quad (\text{A.40})$$

Mismatching Phase Shift of First Order Systems

A somewhat more complex effect than a time lag is caused by the spectral phase shift of first order systems described in Equation A.29. If the phase shift functions of the two sensors are different (because of different response times), the effect of the corresponding phase difference can be estimated again from Equation A.39. The resulting general transfer function is given by Zeller et al. (1989). In many situations, it can be simplified by the assumption, that one sensor is much faster than the other, and its response effect may be neglected. Thus the mismatching effect on the correlation is only a function of the response time τ_R of the slower sensor:

$$T_{\Delta R}(f) \approx \cos[\varphi_R] = \cos[\arctan(2\pi f\tau_R)] = \frac{1}{\sqrt{[1 + (2\pi f\tau_R)^2]}} \quad (\text{A.41a})$$

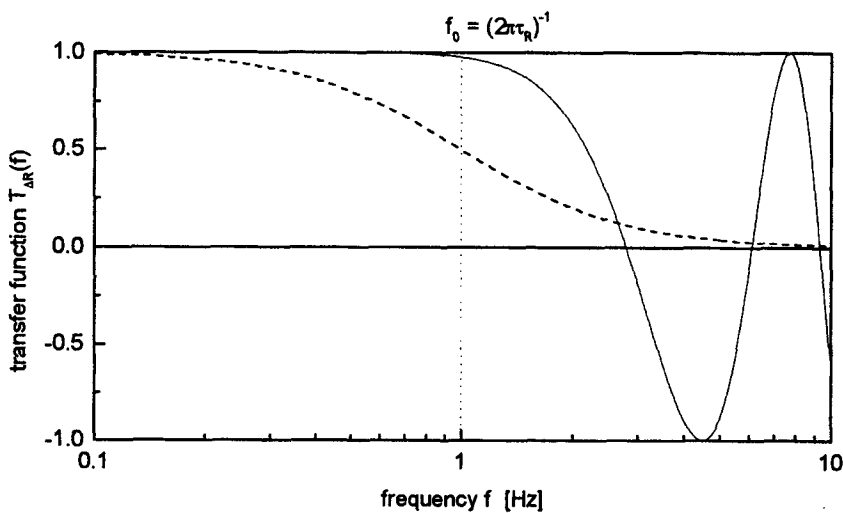


Fig. A.7: Spectral transfer functions describing the attenuation effect of phase shift mismatching with (solid line; Eq. A.41b) and without (dashed line; Eq. A.41a) a constant time shift adjustment.

The electronic prefilter of the Gill sonic anemometer, used for the recording of the trace gas signals (see Section 3.3.1), produced a spectral attenuation as well as a frequency dependent time shift of the logged signals. However, the time shift effect (Eq. A.41a) between the trace gas concentrations and the vertical windspeed could be considerably reduced through the individual delay time adjustment of the time series (Section 4.1.1.1). Ideally this corresponds to a constant time shift of length τ_R (see Fig. A.7):

$$T_{\Delta R}(f) \approx \cos[\arctan(2\pi f\tau_R) - 2\pi f\tau_R] \quad (\text{A.41b})$$

Sensor Separation

Another attenuation effect particularly important for cospectral measurements of atmospheric turbulence is the separation distance s between the two sensors. The sensors are usually installed at the same height with only a horizontal separation. Hence, it has to be distinguished between lateral (perpendicular to wind direction) and longitudinal (along wind direction) separation. For the latter case, the Taylor hypothesis (Section 2.3.1) suggests, that the two sensors measure the same turbulent properties but with a certain time lag depending on the mean windspeed u . The corresponding attenuation effect may be therefore estimated by Eq. A.40 with a time lag $\tau_L = s/u$. Defining again a normalised frequency $f_s = f \cdot s/u$ (analogous to Eq. A.19), the transfer function can be given as:

$$T_{s,\text{long}}(f_s) \approx \cos[2\pi f_s] \quad (\text{A.42})$$

For a lateral sensor separation, no time shift is involved, but the turbulent fluctuations are generally less correlated. For this case, Moore (1986) gives the fitted transfer function A.43, derived for isotropic turbulence. He also suggests this relationship for general use (lateral and longitudinal separation) as long as the separation distance s is relatively small.

$$T_{s,\text{lat}}(f_s) = \exp(-9.9 \cdot f_s^{1.5}) \quad (\text{A.43})$$

In the present eddy correlation setup, the inlets of the sampling tubes for the trace gas analysers were horizontally separated from the sonic head by $s = 0.12$ m for the $\text{CO}_2/\text{H}_2\text{O}$ -analyser and $s = 0.40$ m for the ozone-analyser. This led to a spectral attenuation of the covariance between the vertical windspeed and the concentration measurements. The effect has to be split into a longitudinal (along the mean wind) and a lateral (perpendicular to the mean wind) component, that can be quantified according to Equations A.38 and A.39. The longitudinal separation corresponds to a constant time lag, that was already corrected through the delay time adjustment between the two time series (see Section 4.1.1.1). Thus only the lateral separation with the transfer function $T_{s,\text{lat}}$ (A.39) has to be considered. The ozone inlet was positioned at an azimuth angle of about $\vartheta_s = 100$ deg of the sonic centre, the $\text{CO}_2/\text{H}_2\text{O}$ -inlet at $\vartheta_s = 75$ deg (both ca. east). For a given wind direction ϑ , the lateral sensor separation was estimated as:

$$s_{\text{lat}} = s \cdot \{ |\sin(\vartheta_s - \vartheta)| + [1 - |\sin(\vartheta_s - \vartheta)|] \cdot \sin(\Delta\vartheta) \} \quad (\text{A.44})$$

The second term accounts for the uncertainty in the azimuth angle of $\Delta\vartheta \approx 15$ deg. It does not affect the maximum separation but limits the minimum to $s/4$.

Combined Spectral Attenuation of Eddy Correlation Measurements

Combining the Equations A.24, A.36, and A.37, the total transfer function for a measured cospectrum can be written as:

$$Co_{xy}(f)_{\text{meas.}} = \sqrt{T_x(f)} \cdot \sqrt{T_y(f)} \cdot T_{xy}(f) \cdot Co_{xy}(f)_{\text{true}} \quad (\text{A.45})$$

$T_x(f)$, $T_y(f)$ and $T_{xy}(f)$ are themselves a combination of several individual effects. For the eddy correlation system used in the present study, all important attenuation effects were presented and quantified in the previous sections. Fig. A.8 gives an overview of the course of the individual transfer functions for the eddy correlation fluxes of trace gases. The path averaging and sensor separation effects are not constant but depend on the windspeed u . They are drawn for a typical low ($u = 1$ m/s) and high value ($u = 4$ m/s). The resulting total transfer functions are also indicated. They were determined according to

Equation A.45 as the product of the individual functions. Effects which act only on the fluctuations of a single quantity and not directly on the covariance, are represented by their square root:

$$T_{wc}(f) = \sqrt{T_{\ell,w}} \sqrt{T_R T_{t,turb}} \cdot T_{\Delta R} T_{s,lat} \tag{A.46}$$

At low windspeeds, the influence of the analog RC-filter is most important. It has a (constant) cutoff frequency of about 2 Hz. For higher windspeeds, the sensor separation (typical value for ozone: $s = 0.2$ m) becomes more and more dominant. At 4 m/s, it shows a relatively low cutoff frequency of about 0.8 Hz. In both cases the influence of the tube flow as well as the sonic path averaging are so small that they can be neglected.

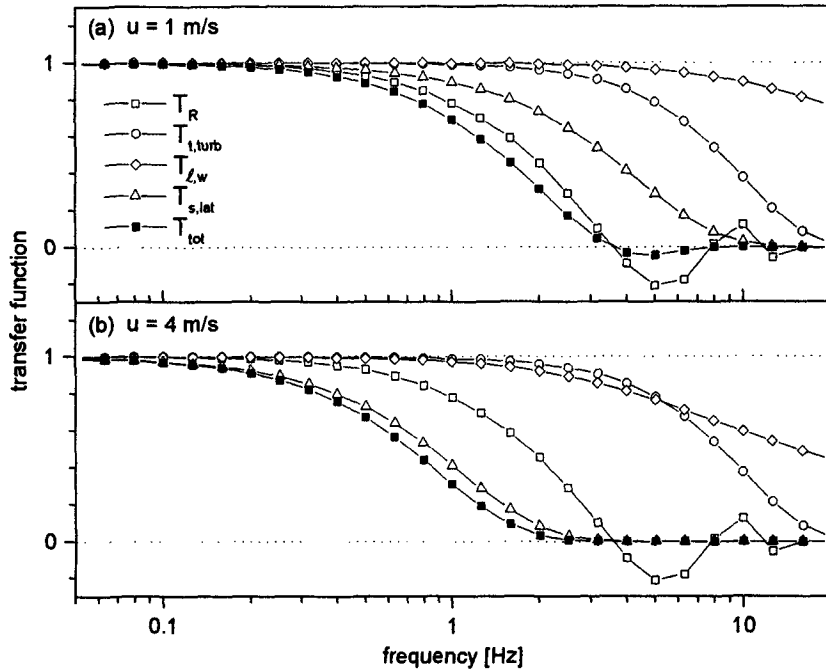


Fig. A.8: Individual and total spectral transfer functions for the trace gas fluxes measured by the eddy correlation systems for a lateral sensor separation $s = 0.2$ m and two different windspeeds: (a) $u = 1$ m/s and (b) $u = 4$ m/s.

Similar to Equation A.46, the total transfer function of the temperature covariance (sensible heat flux) is formed. In this case, only the path averaging effects have to be considered, since both quantities (temperature and vertical windspeed are determined by the same sensor. The two transfer functions are displayed in Figure A.6. The corresponding cutoff frequency is between 10 Hz and 30 Hz for typical windspeed values.

$$T_{wT}(f) = \sqrt{T_{\ell,w}} \sqrt{T_{\ell,s90}} \tag{A.47}$$

APPENDIX B: Compilation of Flux Results

The following pages give a survey of all trace gas flux results for CO₂, H₂O and O₃ obtained during the Bellheim field experiment by the eddy correlation, relaxed eddy accumulation and aerodynamic profile method. All values that passed the rejection criteria described in Table 4.3 and Table 5.5 are displayed, except for few values out of range. For a better understanding and interpretation of the flux results, some information about the micrometeorological conditions is also given. All quantities are displayed as half-hour averages. Table B.1 gives a list of all displayed quantities and the corresponding symbols and units, which are not indicated on each page.

Tab. B.1: Survey of quantities, symbols and units displayed in Figures B.1...B.6

layer	quantity	symbol/style	units
(a)	global radiation (gRad)	solid line	W m ⁻² (left axis)
	wind direction (wdir)	diamonds	N, E, S, W (right axis)
(b)	bulk Richardson number (Ri _{bulk})	solid line	(dimensionless)
(c)	CO ₂ flux:	eddy correlation	μmol m ⁻² s ⁻¹
		profile method	
		relaxed eddy accum.	
(d)	H ₂ O flux:	eddy correlation	mmol m ⁻² s ⁻¹
		profile method	
		relaxed eddy accum.	
(e)	O ₃ flux:	eddy correlation	nmol m ⁻² s ⁻¹
		profile method	
		relaxed eddy accum.	

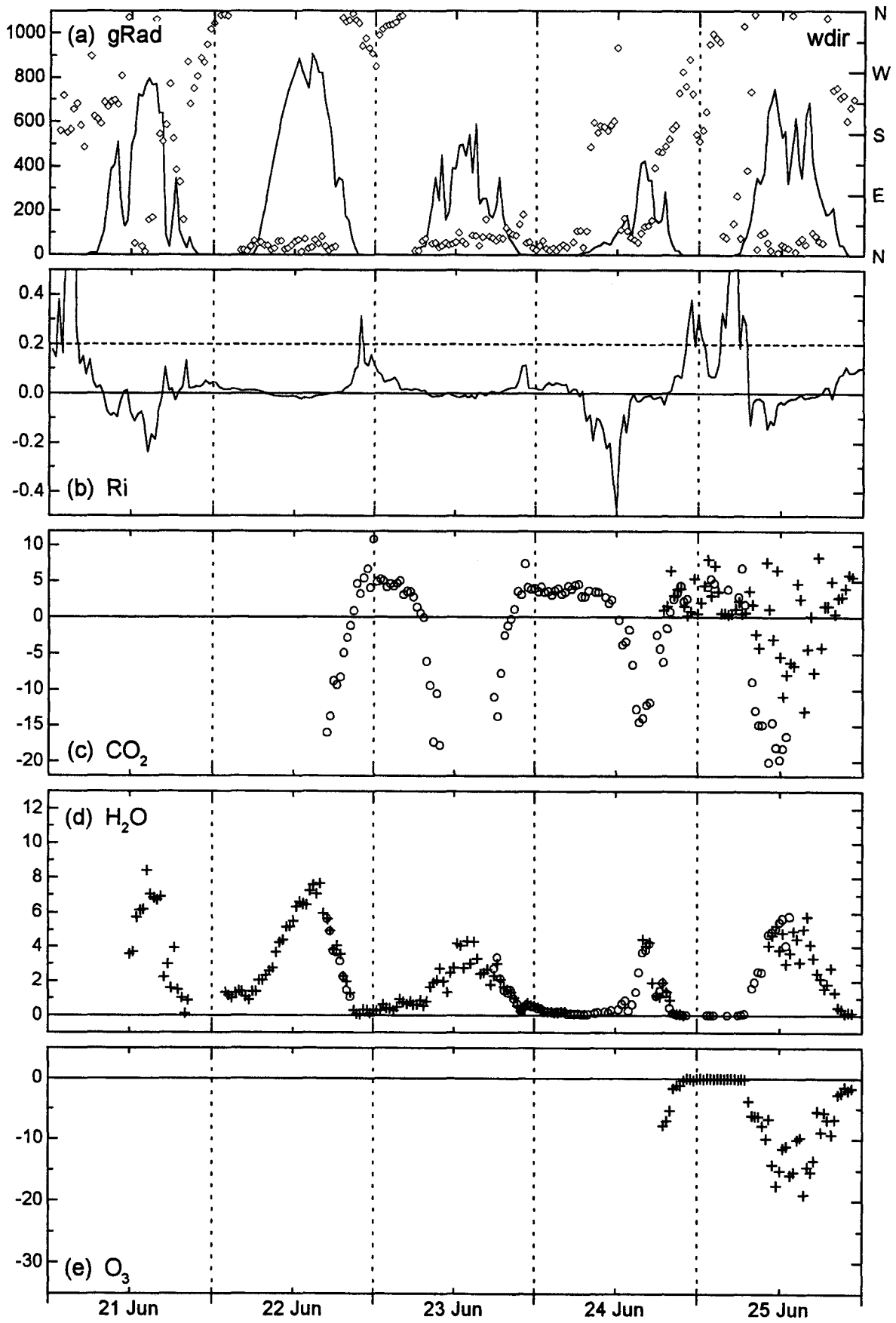


Fig. B.1: Survey of meteorological conditions and measured trace gas fluxes from 21 June to 25 June 1995. Scale units and symbols are defined in Table B.1.

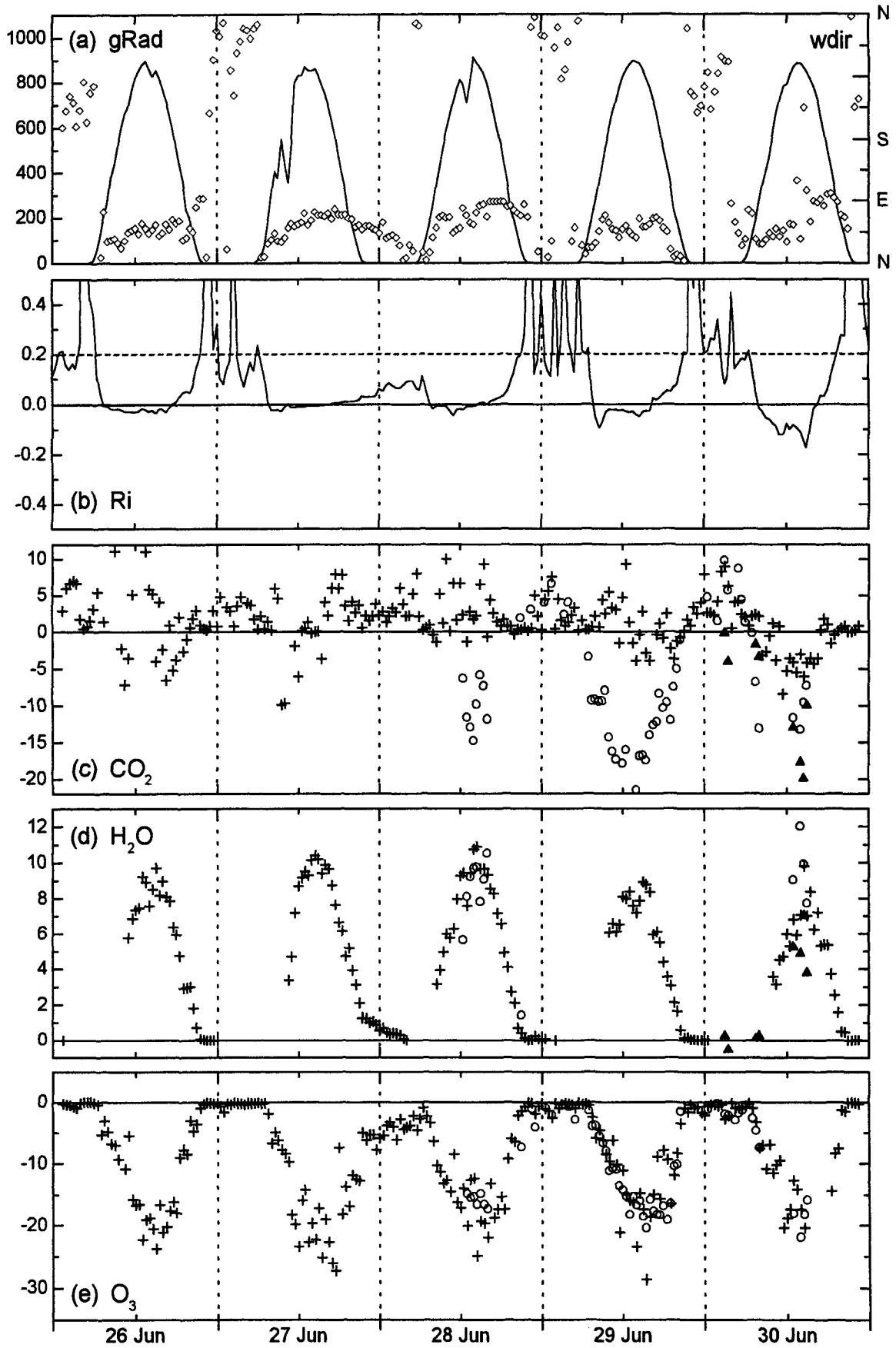


Fig. B.2: Same as Fig. B.1 but for 26 June to 30 June 1995.

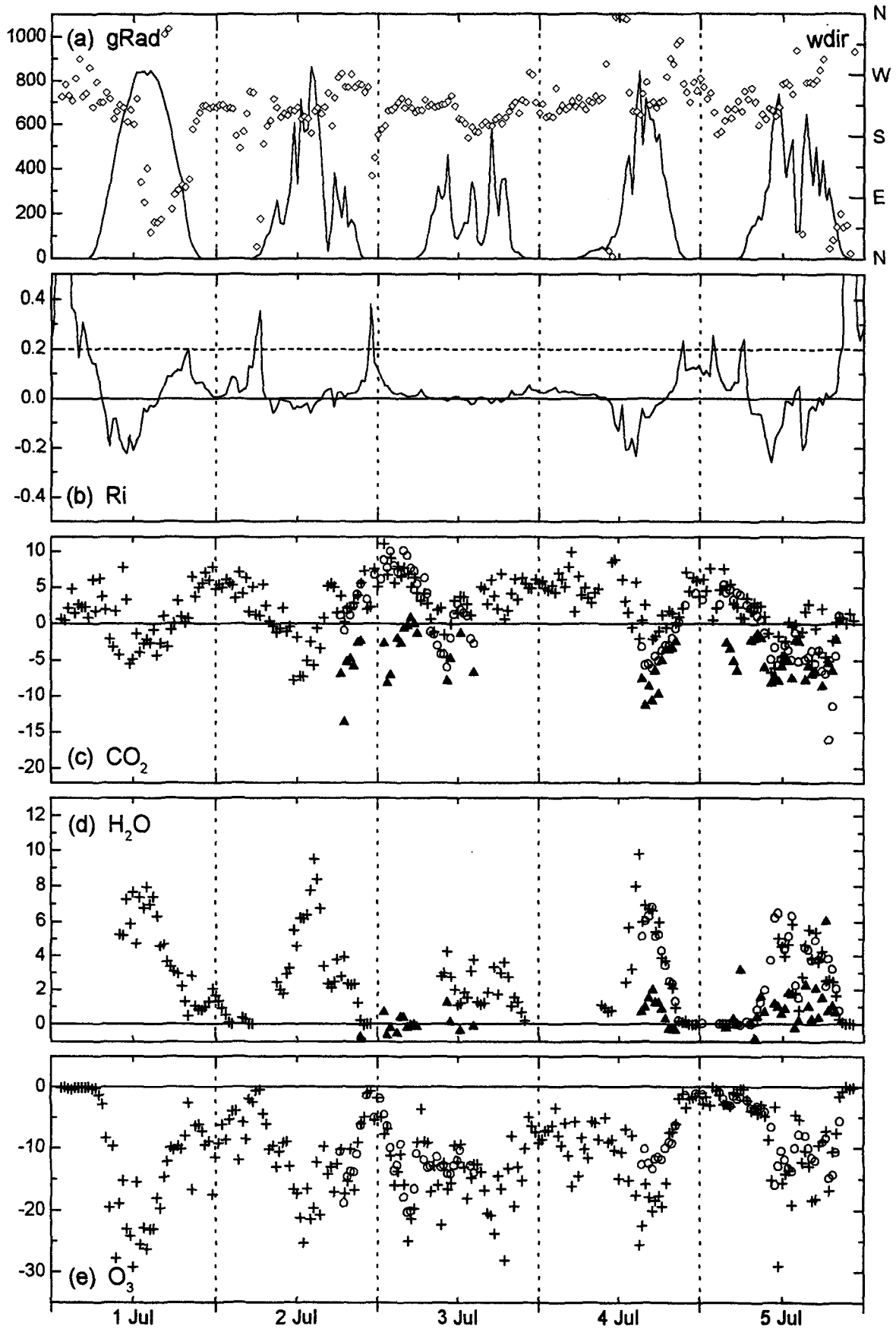


Fig. B.3: Same as Fig. B.1 but for 1 July to 5 July 1995.

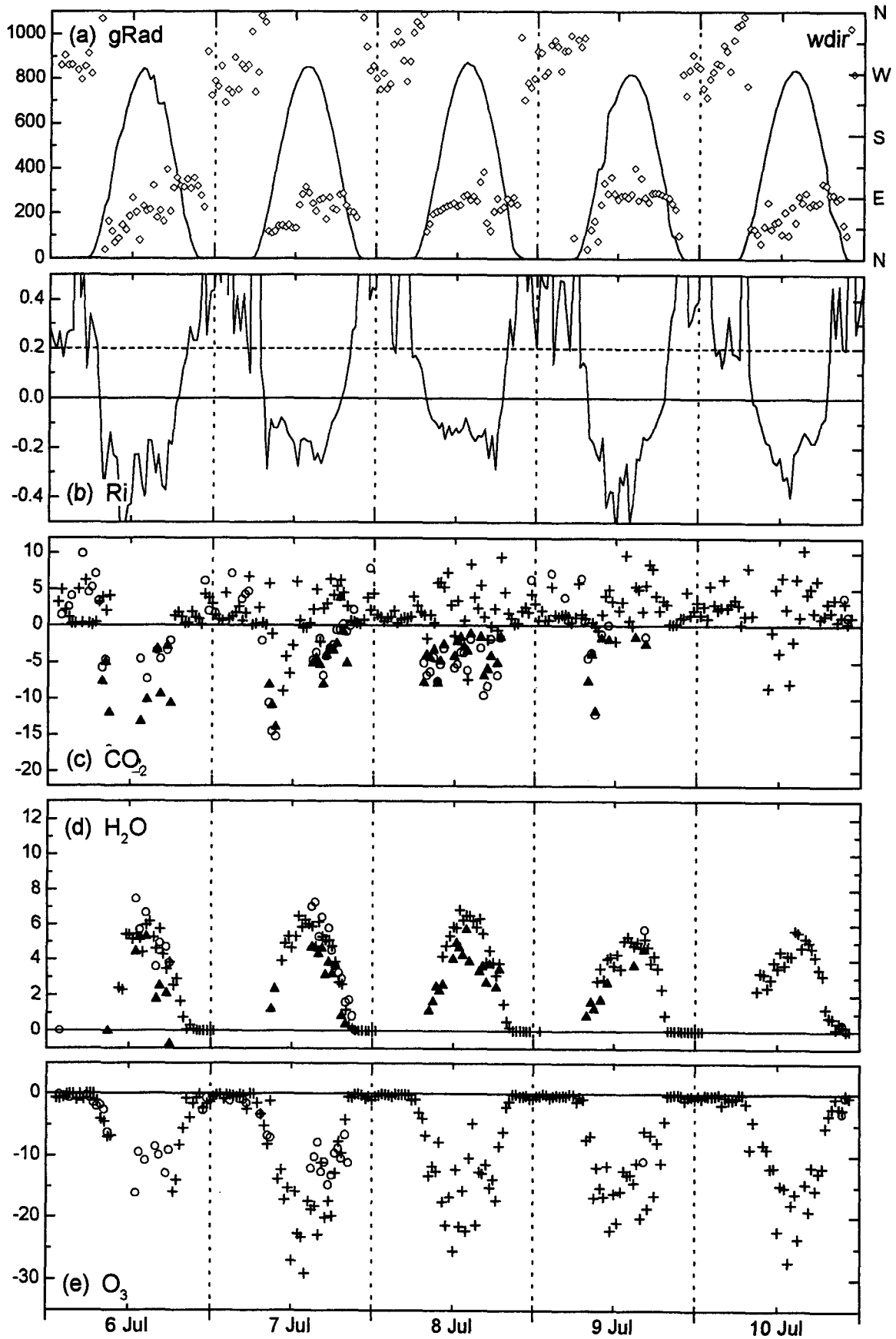


Fig. B.4: Same as Fig. B.1 but for 6 July to 10 July 1995.

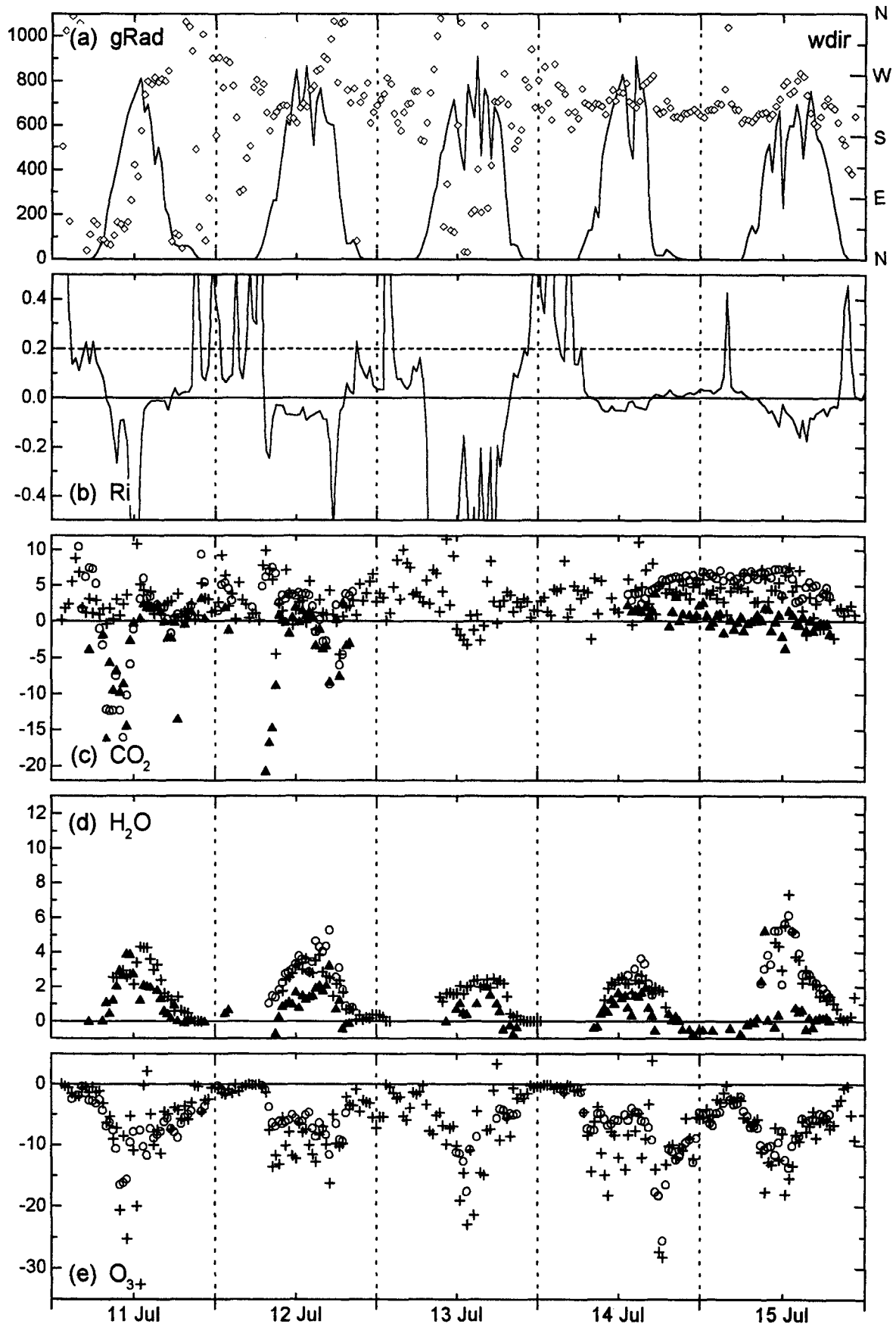


Fig. B.5: Same as Fig. B.1 but for 11 July to 15 July 1995.

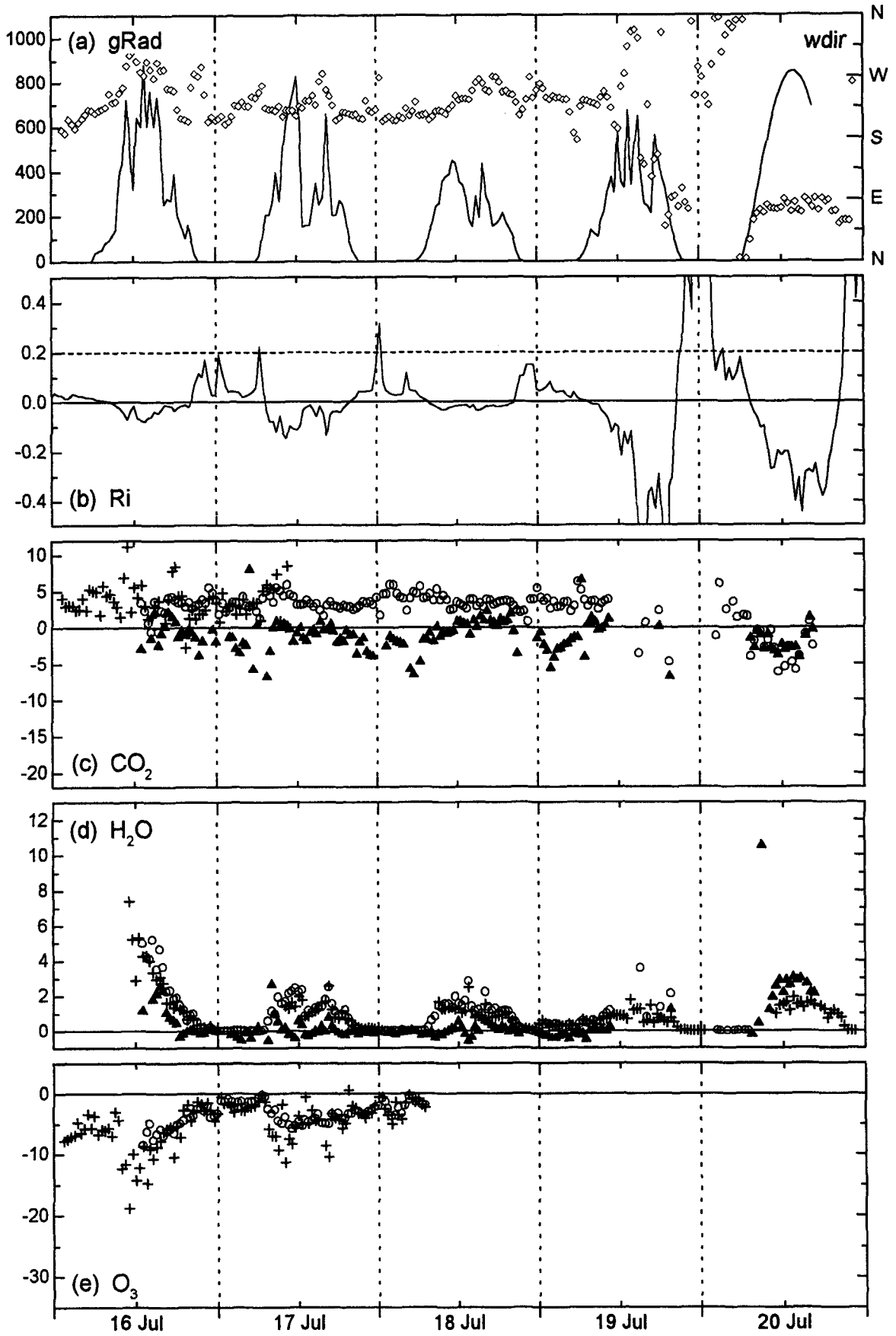


Fig. B.6: Same as Fig. B.1 but for 16 July to 20 July 1995.

APPENDIX C: Symbols and Abbreviations

General Comments on Concentration Quantities

In order to generalise and simplify the presented equations for the application with different trace gases, all mass/concentration quantities are based on the unit *mol* rather than on *kg*. The term 'concentration' is used throughout the text in a general sense not specifying certain quantities or units. For specific use, the terms 'absolute concentration' or 'relative concentration' are used. An absolute concentration ρ_c is volume related (mol m^{-3}) and equal to a 'gas density'; a relative concentration μ_c is equal to a molecular or volume 'mixing ratio' (usually relative to dry air) and given in mol mol^{-1} or *ppm*, *ppb*, *ppt* respectively.

Abbreviations

ADC	analog-to-digital-converter	MOST	Monin-Obukhov-similarity-theory
CBL	convective (daytime) boundary layer	NBL	(stable) nocturnal boundary layer
EA	eddy accumulation (non-relaxed)	PBL	planetary boundary layer
EC	eddy correlation	REA	relaxed eddy accumulation
IRGA	infra-red gas analyser	RL	residual layer
JFD	joint frequency distribution	SL	surface layer
LES	large eddy simulation		

Latin Symbols

A	[m ²]	area
b	[-]	relaxed eddy accumulation factor
c	[m s ⁻¹]	speed of sound
c _x	[J kg ⁻¹ K ⁻¹]	specific heat capacity of given material
c _v , c _p	[J kg ⁻¹ K ⁻¹]	specific heat capacity of air at constant volume or pressure
C _s	[J m ⁻³ K ⁻¹]	total volumetric soil heat capacity
Co _{xy}		cospectrum for time series x(t) and y(t)
d	[m]	(zero-plane) displacement height for the surface layer similarity relationships
D	[m]	tube diameter
erf	[Hz]	(average) eddy reversal frequency
E	[J mol ⁻¹]	total energy content of air
f	[Hz]	(time related) frequency
f	[-]	volume fraction
F _c	[mol m ⁻² s ⁻¹]	surface exchange flux of trace gas species c
g	[m s ⁻²]	gravity acceleration
g _i	[-]	weighing factor
gRad	[W m ⁻²]	global radiation
G	[W m ⁻²]	(conductive) soil heat flux
h	[m]	height above (solid) ground
H	[W m ⁻²]	sensible heat flux
k	= 0.4	von-Kàrmàn-constant
ℓ	[m]	sonic path length
L	[m]	Obukhov length
L [↑] , L [↓]	[W m ⁻²]	upward/downward longwave radiation flux

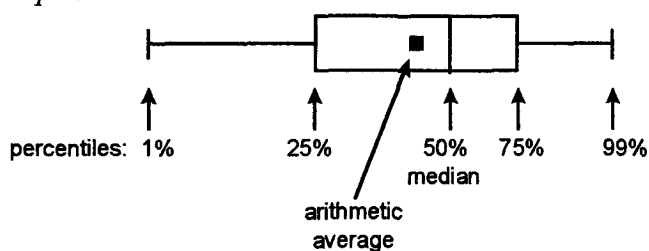
LE	[W m ⁻²]	latent heat flux
L _v	[J kg ⁻¹]	specific heat of vaporisation
m	[kg mol ⁻¹]	molecular mass
M	[mol]	amount of matter
n	[-]	dimensionless frequency
n _f	[-]	dimensionless Nyquist frequency
N	[-]	no. of discrete equidistant measurements within an averaging interval T _a
p	[hPa; mbar]	air pressure
p(.,.)	[-]	bivariate joint probability density function (normalised JFD)
Pr	[-]	Prantl number
Q	[L min ⁻¹]	air volume flow
Q _{xy}		quadrature spectrum for time series x(t) and y(t)
r, r _{xy}	[-]	correlation coefficient/function/spectrum between quantities x and y
R	[s m ⁻¹]	resistance for trace gas transfer
[R]		wind vector rotation matrix
Re	[-]	Reynolds number
Ri	[-]	gradient Richardson number
Rn	[W m ⁻²]	net radiation
s		arbitrary scalar quantity, raw signal
s	[m]	sensor separation distance
S _x		variance spectrum of time series x(t)
Sc	[-]	Schmidt number
ΔS	[W m ⁻²]	energy storage change in the canopy layer
t	[s]	time
T	[K]	(absolute) temperature
T(f)	[-]	spectral transfer function
T _a	[s]	time interval for Reynolds averaging
T*	[K]	MOST temperature scale
[T], [T _s]	[m ² s ⁻²]	Reynolds stress tensor (in micromet. coordinate system)
u, v, w	[m s ⁻¹]	components of the windvector (in micromet. coordinate system)
u _s , v _s , w _s	[m s ⁻¹]	components of the windvector (in sensor based coordinate system)
u*	[m s ⁻¹]	friction velocity; MOST velocity scale
v, v _n	[m s ⁻¹]	air velocity (normal to a reference surface)
v _{tr}	[m s ⁻¹]	transfer velocity
v _d	[m s ⁻¹]	deposition velocity
V	[m ³]	volume
V _c	[V]	analyser voltage signal
w _d	[m s ⁻¹]	deadband (threshold) half-width for REA measurements
x, y, z	[m]	components of the micromet. coordinate system
x(t), y(t)		time series of arbitrary atmospheric quantities
X	[m]	tube length
z	[m]	aerodynamic height above the surface (above zero-plane displacement level)
z _g	[m]	geometrical height above (or below) solid ground surface
z*	[m]	aerodynamic height of the roughness sublayer

Greek Symbols

$\alpha, \beta, \gamma, \delta$	[-]	numerical fitting parameters (coefficients)
α, β, γ	[deg]	angles of sonic wind vector rotation
β	[-]	Bowen-ratio
$\Delta(\dots)$		interval, difference
$\varphi_c, \varphi_T, \varphi_w$	[-]	variance similarity functions for trace gas, temperature and windspeed
Φ_c, Φ_T, Φ_u	[-]	differential profile similarity func. for trace gas, temperature and windspeed
η	[-]	recovery rate (attenuation factor) for eddy covariance measurements
λ	[-]	wavelength or diameter of turbulent eddies
μ_c	[mol mol ⁻¹]	mixing ratio relative to dry air
μ_{c^*}	[mol mol ⁻¹]	MOST trace gas concentration scale
ν	[m ² s ⁻¹]	kinematic viscosity
ν	[-]	no. of degrees of freedom
Π_i	[-]	dimensionless Pi-group
Ψ_c, Ψ_T, Ψ_u	[-]	integral profile similarity func. for trace gas, temperature and windspeed
ρ	[mol m ⁻³]	molar (gas) density
σ	[W m ⁻²]	Stefan-Boltzman-constant
ϑ	[deg]	angle, wind direction
θ	[K]	potential temperature
θ_w	[%]	volumetric water content
τ	[kg m ⁻¹ s ⁻²]	momentum flux, shear stress
τ, τ_L	[s]	lag time between two time series
$\tau_{c,PBL}$	[s]	residence time of trace gas c in the PBL
τ_R	[s]	response time of a first order system (sensor)
τ_w	[s]	integral time scale of turbulent variations in the vertical windspeed
ξ	[m ²]	proportionality factor between vertical windspeed and sampling flow in an eddy accumulation system

Supplementary Symbols

$(\dots)_a$	characteristic of (wet) air
$(\dots)_{ad}$	characteristic of dry air
$(\dots)_c$	characteristic of an arbitrary trace gas compound c
$(\dots)_U, (\dots)_D$	conditionally sampled quantity for upward/downward airmotion
$\overline{(\dots)}$	Reynolds average (over all turbulent fluctuations, time interval T_a)
$(\dots)'$	instantaneous (turbulent) deviation from Reynolds average
$\sigma(\dots)$	standard deviation (standard error)
$\langle \dots \rangle_x$	average over x

Boxplots

REFERENCES

- Ammann, C., 1992: Berechnung von Energiebilanzen aus Profildaten. Diplomarbeit, Geographisches Institut ETH, Zürich, 83 pp.
- Ammann, C., Meixner, F.X., Busch, J., Lösch, R., 1997: CO₂ and H₂O gas exchange of a triticale field: II. Micrometeorological flux studies and comparison with upscaling from porometry. *Physics and Chemistry of the Earth*, 21(3): 151-155.
- Andersen, H.V., Hovmand, M.F., Hummelshoj, P. and Jensen, N.O., 1993: Measurements of Ammonia Flux to a Spruce Stand in Denmark. *Atmospheric Environment*, 27A(2): 189-202.
- Anderson, D.E. and Verma, S.B., 1985: Turbulence spectra of CO₂, water vapor, temperature and wind velocity fluctuations over a crop surface. *Boundary-Layer Meteorology*, 33: 1-14.
- Anderson, D.E., Verma, S.B., Clement, R.J., Baldocchi, D.D. and Matt, D.R., 1986: Turbulence spectra of CO₂, water vapor, temperature and velocity over a deciduous forest. *Agricultural and Forest Meteorology*, 38: 81-99.
- Arya, S.P., 1988: Introduction to micrometeorology. Academic Press, San Diego, California, 230 pp.
- Auble, D.L. and Meyers, T.P., 1992: An open path, fast response infrared absorption gas analyzer for H₂O and CO₂. *Boundary-Layer Meteorology*, 59: 243-256.
- Baker, J.M., Norman, J.M. and Bland, W.L., 1992: Field-scale application of flux measurements by conditional sampling. *Agricultural and Forest Meteorology*, 62: 31-52.
- Baldocchi, D., 1988: A multi-layer model for estimating sulphur deposition to a deciduous oak forest canopy. *Atmospheric Environment*, 22: 869-884.
- Baldocchi, D.D. and Meyers, T.P., 1991: Trace gas exchange above the floor of a deciduous forest: 1. Evaporation and CO₂ flux. *Journal of Geophysical Research*, 96: 7271-7285.
- Baldocchi, D. and Vogel, C.A., 1996: Energy and CO₂ flux densities above and below a temperate broad-leaved forest and boreal pine forest. *Tree Physiology*, 16: 5-16.
- Baldocchi, D.D., Hicks, B.B. and Meyers, T.P., 1988: Measuring biosphere-atmosphere exchanges of biologically related gases with micrometeorological methods. *Ecology*, 69(5): 1331-1340.
- Baumbach, G., 1996: Air Quality Control. Springer, Berlin, 490 pp.
- Beier, N., 1991: Measuring fluxes of chemical components by eddy accumulation. Proc. of the 7th AMS Symposium on Meteorological Observations and Instrumentation, New Orleans, Louisiana, pp. 1-5.
- Beier, N. and Schneewind, R., 1991: Chemical reactions of gases in tubes of probing systems and their influence on measured concentrations. *Annales Geophysicae*, 9: 702-707.
- Beier, N. and Weber, M., 1992: Turbulente Austauschprozesse in der Grenzschicht, Meteorologisches Institut der Ludwig-Maximilians-Universität, München, 181 pp.
- Beljaars, A.C.M. and Holtlag, A.A.M., 1991: Flux parametrization over land surfaces for atmospheric models. *Journal of Applied Meteorology*, 30: 327-341.
- Berkowicz, R. and Prahm, L.P., 1982: Evaluation of the profile method for estimation of surface fluxes of momentum and heat. *Atmospheric Environment*, 16: 2809-2819.
- Betts, A.K., Desjardins, R.L. and MacPherson, J.I., 1992: Budget analysis of the boundary layer grid flights during FIFE 1987. *Journal of Geophysical Research*, 97(D17): 18533-18546.
- Beverland, I.J., Moncrieff, J.B., O'Neill, D.H., Hargreaves, K.J. and Milne, R., 1996a. Measurement of methane and carbon dioxide fluxes from peatland ecosystems by the conditional-sampling technique. *Quarterly Journal of the Royal Meteorological Society*, 122: 819-838.
- Beverland, I.J., O'Neill, D.H., Scott, S.L. and Moncrieff, J.B., 1996b. Design, construction and operation of flux measurement systems using the conditional sampling technique. *Atmospheric Environment*, 30(18): 3209-3220.

- Beverland, I.J., Milne, R., Boissard, C., O'Neill, D.H., Moncrieff, J.B., Hewitt, C.N., 1996c. Measurements of carbon dioxide and hydrocarbon fluxes from a sitka spruce using micrometeorological techniques. *Journal of Geophysical Research*, 101(D17): 22807-22815.
- Beverland, I.J., Scott, S.L., O'Neill, D.H., Moncrieff, J.B. and Hargreaves, K.J., 1997: Simple battery powered device for flux measurements by conditional sampling. *Atmospheric Environment*, 31(2): 277-281.
- Bieder, U., Ludwig, J., Meixner, F.X. and Schatz, A., 1992: On the deposition of air pollutants to wet vegetation surfaces. In: G. Angeletti, S. Beilke and J. Slanina (Editors), *Field measurements and interpretation of species related to photooxidants and acid deposition*. CEC, Brussels, pp. 179-187.
- Blatter, A. and Nefel, A., 1997: Personal communication. Institut für Umweltschutz und Landwirtschaft IUL, Liebefeld-Bern, Switzerland
- Bort, J., Febrero, A., Amaro, T. and Araus, J.L., 1994: Role of awns in ear water-use efficiency and grain weight in barley. *Agronomie*, 2: 133-139.
- Bowen, I.S., 1926: The ratio of heat losses by conduction and by evaporation from any water surface. *Physical Review*, 27: 779-787.
- Brutsaert, W., 1982: *Evaporation into the atmosphere*. Environmental Fluid Mechanics. Volume 1. D. Reidel Publishing Company, Dordrecht, 299 pp.
- Buckley, D.J., Desjardins, R.L., Lalonde, J.L.M. and Brunke, R., 1988: A linearized, fast response gas sampling apparatus for eddy accumulation studies. *Computers and Electronics in Agriculture*, 2: 243-250.
- Busch, N.E., 1973: On the mechanics of atmospheric turbulence. In: D.A. Haugen (Editor), *Workshop on Micrometeorology*. American Meteorological Society, Boston, pp. 1-65.
- Busch, N.E. and Kristensen, L., 1976: Cup anemometer overspeeding. *Journal of Applied Meteorology*, 15: 1328-1332.
- Busch, J., Lösch, R., Meixner, F.X. and Ammann, C., 1997: CO₂ and H₂O gas exchange of a triticale field: I. Leaf level porometry. *Physics and Chemistry of the Earth*, 21(3): 151-155.
- Businger, J.A., 1986: Evaluation of the accuracy with which dry deposition can be measured with current micrometeorological techniques. *Journal of Climate and Applied Meteorology*, 25: 1100-1124.
- Businger, J.A. and Delany, A.C., 1990: Chemical sensor resolution required for measuring surface fluxes by three common micrometeorological techniques. *Journal of Atmospheric Chemistry*, 10: 399-410.
- Businger, J.A. and Oncley, S.P., 1990: Flux measurement with conditional sampling. *Journal of Atmospheric and Oceanic Technology*, 7: 349-352.
- Businger, J.A., Wyngaard, J.C., Izumi, Y. and Bradley, E.F., 1971: Flux-profile relationships in the atmospheric surface layer. *Journal of the Atmospheric Sciences*, 28: 181-189.
- Campbell Scientific, 1991: CSI Bowen ratio instrumentation. Instruction manual. Campbell Scientific Ltd, Shepshed, Leicestershire, UK
- Castro, M.S. and Galloway, J.N., 1991: A comparison of sulfur-free and ambient air enclosure techniques for measuring the exchange of reduced sulfur gases between soils and the atmosphere. *Journal of Geophysical Research*, 96(D8): 15427-15437.
- Ceulemans, R. and Mousseau, M., 1993: Effect of elevated atmospheric CO₂ on woody plants. *Tansley Review no. 71. New Phytologist*, 127: 425-446.
- Chahuneau, F., Desjardins, R.L., Brach, E. and Verdon, R., 1989: A micrometeorological facility for eddy flux measurements of CO₂ and H₂O. *Journal of Atmospheric and Oceanic Technology*, 6: 193-200.
- Chatfield, C., 1975: *The spectral analysis of time series: theory and practice*. Monographs on applied probability and statistics. Halsted Press, John Wiley & Sons Inc., New York, 263 pp.
- Choularton, T.W., Gallagher, M. W., Bower, K. N., Fowler, D., Zahniser, M., Kaye, A., 1995: Trace gas flux measurements at the landscape scale using boundary-layer budgets. *Philosophical Transactions of the Royal Society London A*, 351: 357-369.
- Christensen, S. and many others, 1996: Nitrous oxide emission from an agricultural field: comparison between measurements by flux chamber and micrometeorological techniques. *Atmospheric Environment*, 30(24): 4183-4190.
- Colbeck, I. and Harrison, R.M., 1985: Dry deposition of ozone: some measurements of deposition velocity and of vertical profiles to 100 meters. *Atmospheric Environment*, 19: 1807-1818.

- Conrad, R., 1994: Compensation concentration as a critical variable for regulating the flux of trace gases between soil and atmosphere. *Biogeochemistry*, 27: 155-170.
- Conrad, R., 1995: Soil microbial processes and the cycling of atmospheric trace gases. *Philosophical Transactions of the Royal Society London A*, 351: 219-230.
- De Wilde, H.P.J. and Duyzer, J., 1995: Methane emission off the Dutch coast: air-sea concentration differences versus atmospheric gradients. In: B. Jähne and E.C. Monahan (Editors), *Third International Symposium on Air-Water Gas Transfer*. AEON Verlag & Studio, Heidelberg University, pp. 763-773.
- Delage, Y., 1988: A parametrization of the stable atmospheric boundary layer. *Boundary-Layer Meteorology*, 43: 365-381.
- Delany, A.C., 1993: Fast-response chemical sensors used for eddy correlation flux measurements. In: *Measurement challenges in atmospheric chemistry*. American Chemical Society, pp. 91-100.
- Delany, A.C., Oncley, S.P. and Businger, J.A., 1991: Adapting the conditional sampling concept for a range of different chemical species. *Proc. of the 7th AMS Symposium on Meteorological Observations and Instrumentation*, New Orleans, Louisiana, pp. 7-10.
- Denmead, O.T., 1976: Temperate cereals. In: J.L. Monteith (Editor), *Vegetation and the atmosphere*. Academic Press, London, pp. 1-32.
- Denmead, O.T., 1995: Novel meteorological methods for measuring trace gas fluxes. *Philosophical Transactions of the Royal Society London A*, 351: 383-396.
- Desjardins, R.L., 1972: A Study of Carbon Dioxide and Sensible Heat Fluxes using the Eddy Correlation Technique. Ph.D. Thesis, Cornell University, Ithaca, 189 pp.
- Desjardins, R.L., 1977: Energy budget by an eddy correlation method. *Journal of Applied Meteorology*, 16: 248-250.
- Desjardins, R.L., 1992: Review of techniques to measure CO₂ flux densities from surface and airborne sensors. In: G. Stanhill (Editor), *Advances in Bioclimatology*. Springer-Verlag, Berlin, pp. 1-23.
- Desjardins, R.L., MacPherson, J.I., Schuepp, P.H. and Karanja, F., 1989: An evaluation of aircraft flux measurements of CO₂, water vapor, and sensible heat. *Boundary-Layer Meteorology*, 47: 55-69.
- Desjardins, R.L., MacPherson, J.I., Neumann, H., Den Hartog, G. and Schuepp, P.H., 1995: Flux estimates of sensible and latent heat, carbon dioxide, and ozone using an aircraft-tower combination. *Atmospheric Environment*, 29(21): 3147-3158
- Dillmann, M., 1991: Untersuchungen zur Genauigkeit bei der Bestimmung turbulenter Flüsse mit der Eddy-Korrelationsmethode. Diplomarbeit, Meteorologisches Institut der Ludwig-Maximilians-Universität, München, 112 pp.
- Dugas, W.A., Fritschen, L.J., Gay, L.W., Held, A.A., Matthias, A.D., Reicosky, D.C., Steduto, P., Steiner, J.L., 1991: Bowen ratio, eddy correlation, and portable chamber measurements of sensible and latent heat flux over irrigated spring wheat. *Agricultural and Forest Meteorology*, 56: 1-20.
- Duyzer, J.H., 1985: Measurement of dry deposition of gases and particulates in the Netherlands using eddy correlation and gradient methods. Report No. P85/048, TNO Division of Technology for Society, Delft, 17 pp.
- Duyzer, J., 1995: Dry deposition of nitrogen compounds to semi-natural ecosystems. Doctoral Thesis, University of Utrecht, 163 pp.
- Dyer, A.J., 1974: A review of flux-profile relationships. *Boundary-Layer Meteorology*, 7: 363-372.
- Dyer, A.J. and Hicks, B.B., 1972: The spatial variability of eddy fluxes in the constant flux layer. *Quarterly Journal of the Royal Meteorological Society*, 98: 206-212.
- Ehleringer, J.R., Field, B., 1993: Scaling physiological processes, leaf to globe. *Physiological Ecology*. Academic Press, Inc., San Diego, 388 pp.
- Erisman, J.-W. and Duyzer, J., 1990: A micrometeorological investigation of surface exchange parameters. Report No. 723001005, RIVM, Bilthoven, Netherlands, 15 pp.
- Erisman, J.W., Van Pul, A. and Wyers, P., 1994: Parametrization of surface resistance for the quantification of atmospheric deposition of acidifying pollutants and ozone. *Atmospheric Environment*, 28(16): 2595-2607.
- Ernst, N., Güsten, H., Heinrich, G., Mönnich, E. and Weppner, J., 1991: Measurements of the dry deposition velocity of ozone on to agricultural land. In: P. Borrell (Editor), *EUROTRAC Symposium '90*. SPB Academic Publishing, Den Haag, Netherlands, pp. 127-129.

- Eugster, W., 1994: Mikrometeorologische Bestimmung des NO₂-Flusses an der Grenzfläche Boden/Luft. Dissertation, Geographisches Institut der Universität Bern, 164 pp.
- Fairall, C.W., 1984: Interpretation of eddy-correlation measurements of particulate deposition and aerosol flux. *Atmospheric Environment*, 18(7): 1329-1337.
- Fiedler, F., 1992: Das Regio-Klima Projekt: Wie regeln die natürlichen Energieumsetzungen das Klima in der Region? *KfK Nachrichten*, 24(3), Forschungszentrum Karlsruhe, pp. 125-131.
- Field, C.B., Chapin III, F.S., Matson, P.A. and Mooney, H.A., 1992: Responses of terrestrial ecosystems to the changing atmosphere. *Annual Review of Ecology and Systematics*, 23: 210-235.
- Finn, D., Lamb, B., Leclerc, M.Y. and Horst, T.W., 1996: Experimental evaluation of analytical and lagrangian surface-layer flux footprint models. *Boundary-Layer Meteorology*, 80: 283-308.
- Fowler, D., Hargreaves, K. J., Skiba, U., Milne, R., Zahniser, M. S., Moncrieff, J. B., Beverland, I. J., Gallagher, M. W., 1995: Measurements of CH₄ and N₂O fluxes at the landscape scale using micrometeorological methods. *Philosophical Transactions of the Royal Society London A*, 351: 339-356.
- Fritsch, J., 1994: Etude et mise au point d'un prototype de mesure de flux par échantillonnage conditionnel. Diplôme d'Etude Approfondi (D.E.A.), Université Paul Sabatier / Institut Polytechnique de Toulouse.
- Ga92: cf. Garrat (1992)
- Gabriel, R., Schäfer, L., Helas, G. and Kesselmeier, J., 1996: Relationship between apoplastic concentration of organic acids and their diurnal exchange pattern between leaves of *Quercus Ilex* (Holm oak) and the atmosphere. In: M.E.A. Borrell (Editor), EUROTRAC Symposium '96, Transport and transformation of pollutants in the troposphere. Computational Mechanics Publications, Garmisch-Partenkirchen, Germany, pp. 397-402.
- Gallagher, M.W., Choularton, T. W., Bower, K. N., Stromberg, M., Beswick, K. M., Fowler, D., Hargreaves, K. J., 1994: Measurements of methane fluxes on the landscape scale from a wetland area in north Scotland. *Atmospheric Environment*, 28: 2421-2430.
- Gallagher, M., Fontan, J., Wyers, P., Ruijgrok, W., Duyzer, J., Hummelshoj, P., Pilegaard, K., Fowler, D., 1997: Atmospheric particles and their interactions with natural surfaces. In: S. Slanina (Editor), Biosphere-atmosphere exchange of pollutants and trace substances. Transport and chemical transformation of pollutants in the troposphere. Springer, Berlin, pp. 45-92.
- Gao, W., 1995: The vertical change of coefficient b, used in the relaxed eddy accumulation method for flux measurement above and within a forest canopy. *Atmospheric Environment*, 29(17): 2339-2347.
- Garratt, J.R., 1978: Flux profile relations above tall vegetation. *Quarterly Journal of the Royal Meteorological Society*, 104: 199-211.
- Garratt, J.R., 1992: The atmospheric boundary layer. Cambridge atmospheric and space series, 4. Cambridge University Press, Cambridge, 316 pp.
- Gash, J.H.C. and Culf, A.D., 1996: Applying a linear detrend to eddy correlation data in real time. *Boundary-Layer Meteorology*, 79: 301-306.
- Geron, C.D., Nie, D., Arnts, R.R., Sharkey, T.D., Singsaas, E.L., Vanderveer, P.J., Guenther, A., Sickles II, J.E., Kleindienst, T.E., 1997: Biogenic isoprene emission: Model evaluation in a southeastern United States bottomland deciduous forest. *Journal of Geophysical Research*, 102(D15): 18889-18901.
- Gill Instruments, 1992: Solent research ultrasonic anemometer 4.1 product specification. Gill Instruments Ltd., Lymington, Hampshire, UK, 46 pp.
- Goulden, M.L., Munger, J.W., Fan, S.-M., Daube, B.C. and Wofsy, S.C., 1996: Measurement of carbon sequestration by long-term eddy covariance: methods and a critical evaluation of accuracy. *Global Change Biology*, 2: 169-182.
- Goutorbe, J.-P. and many others, 1994: HAPEX-Sahel: A large-scale study of land-atmosphere interactions in the semi-arid tropics. *Annales Geophysicae*, 12: 53-64.
- Gower, S.T. and Norman, J.M., 1991: Rapid estimation of leaf area index in conifer and broadleaf plantations. *Ecology*, 72(5): 1896-1900.
- Grace, J., Lloyd, J., McIntire, J., Miranda, A.C., Meir, P., Miranda, H.S., 1996: Carbon dioxide flux over Amazonian rain forest in Rondonia. In: J.H.C. Gash, C.A. Nobre, J.M. Roberts and R.L. Victoria (Editors), Amazonian deforestation and climate. John Wiley & Sons, Chichester, pp. 611.
- Graedel, T.E. and Crutzen, P.J., 1993: Atmospheric change: An earth system perspective. Freeman & Co., New York, 446 pp.

- Grelle, A. and Lindroth, A., 1994: Flow distortion by a solent sonic anemometer: Wind tunnel calibration ant its assessment for flux measurements over forest and field. *Journal of Atmospheric and Oceanic Technology*, 11: 1529-1542.
- Grossman, R.L., 1984: Bivariate conditional sampling of moisture flux over a tropical ocean. *Journal of the Atmospheric Sciences*, 41(22): 3238-3253.
- Guenther, A.B. and many others, 1995: A global model of natural volatile organic compound emissions. *Journal of Geophysical Research*, 100: 8873-8892.
- Guenther, A. and many others, 1996: Isoprene fluxes measured by enclosure, relaxed eddy accumulation, surface layer gradient, mixed layer gradient, and mixed layer mass balance techniques. *Journal of Geophysical Research*, 101: 18555-18567.
- Güsten, H. and Heinrich, G., 1996: On-line measurements of ozone surface fluxes: Part I. Methodology and instrumentation. *Atmospheric Environment*, 30(6): 897-909.
- Güsten, H., Heinrich, G., Schmidt, R.W.H. and Schurath, U., 1992: A novel ozone sensor for direct eddy flux measurements. *Journal of Atmospheric Chemistry*, 14: 73-84.
- Hall, B., Lamb, B., Westberg, H., Baldocchi, D., Guenther, A., Harley, P., Klinger, L., Zimmerman, P., Pierce, T., Geron, C., 1997: Isoprene flux measurements , modeling, and associated uncertainties at the canopy scale, Workshop on biogenic hydrocarbons in the atmospheric boundary layer. American Meteorological Society, Charlottesville, pp. 44-47.
- Halldin, S. and Lindroth, A., 1992: Errors in net radiometry: Comparison and evaluation of six radiometer designs. *Journal of Atmospheric and Oceanic Technology*, 9: 762-782.
- Hargreaves, K., Fowler, D., Storeton-West, R. and Duyzer, J., 1992: The exchange of nitric oxide, nitrogen dioxide and ozone between pasture and the atmosphere. *Environmental Pollution*, 75: 53-59.
- Haugen, D.A., Kaimal, J.C. and Bradley, E.F., 1971: An experimental study of Reynolds stress and heat flux in the atmospheric surface layer. *Quarterly Journal of the Royal Meteorological Society*, 97: 168-180.
- Heck, W.W. and many others, 1982: Assessment of crop loss from ozone. *Journal of the Air Pollution Control Association*, 32(4): 353-361.
- Hensen, A., Vermeulen, A.T., Wyers, G.P. and Zhang, Y., 1996: Eddy correlation and relaxed eddy accumulation measurements of CO₂-fluxes over grassland. *Physics and Chemistry of the Earth*, 21(5-6): 383-388.
- Herbst, M., 1995: Stomatal behaviour in a beech canopy: An analysis of Bowen ratio measurements compared with porometer data. *Plant, Cell and Environment*, 18: 1010-1018.
- Hicks, B.B., 1981: An examination of turbulence statistics in the surface boundary layer. *Boundary-Layer Meteorology*, 21: 389-402.
- Hicks, B.B. and McMillen, R.T., 1984: A simulation of the eddy accumulation method for measuring pollutant fluxes. *Journal of Climate and Applied Meteorology*, 23: 637-643.
- Hicks, B.B. and McMillen, R.T., 1988: On the measurement of dry deposition using imperfect sensors and in non-ideal terrain. *Boundary-Layer Meteorology*, 42: 79-94.
- Hicks, B.B. and Wesely, M.L., 1978: An examination of some micrometeorological methods for measuring dry deposition. EPA 600/7-78-116, U.S. Environmental Protection Agency, Environmental Sciences Research Laboratory, Research Triangle Park, North Carolina, 18 pp.
- Hicks, B.B., Wesely, M.L. and Durham, J.L., 1980: Critique of methods to measure dry deposition. EPA-600/9-80-050, PB81 126443, U.S. Environmental Protection Agency, Environmental Sciences Research Laboratory, Research Triangle Park, North Carolina, 70 pp.
- Hicks, B.B., Hosker Jr., R.P. and Ma, G.-J., 1986: A prototype concentration accumulation apparatus for determining time-averaged dry deposition of gaseous pollutants, *Fifth Annual National Symposium on Recent advances in pollutant monitoring of ambient air and stationary sources*. EPA/600/9-85/029, pp. 16-22.
- Hicks, B.B., Baldocchi, D.D., Meyers, T.P., Hosker JR., R.P. and Matt, D.R., 1987: A priliminary multiple resistance routine for deriving dry deposition velocities from measured quantities. *Water, Air and Soil Pollution*, 36: 311-330.
- Hillel, D., 1980: *Fundamentals of soil physics*. Academic Press, San Diego, 413 pp.
- Hipps, L. and Zehr, D.F., 1995: Determination of evaporation from integrated profiles of humidity and temperature over an inhomogeneous surface. *Boundary-Layer Meteorology*, 75: 287-299.

- Hofmann, U., Hofmann, R. and Kesselmeier, J., 1992: Cryogenic trapping of reduced sulfur compounds under the influence of a NAFION dryer and cotton wadding as and oxidant scavenger. *Atmospheric Environment*, 26: 2445-2449.
- Hofmann, U., Weller, D., Ammann, C., Nathaus, F., Meixner, F.X., Kesselmeier, J., 1995: Organic acids in the atmosphere over an agricultural site, EGS General Assembly, Hamburg. *Annales Geophysicae*, 13: C404.
- Hofmann, U., Weller, D., Ammann, C., Jork, E. and Kesselmeier, J., 1997: Cryogenic trapping of atmospheric organic acids under laboratory and field conditions. *Atmospheric Environment*, 31(9): 1275-1284.
- Holtstag, A.A.M. and Nieuwstadt, F.T.M., 1986: Scaling the atmospheric boundary layer. *Boundary-Layer Meteorology*, 36: 201-209.
- Horst, T.W. and Weil, J.C., 1992: Footprint estimation for scalar flux measurements in the atmospheric surface layer. *Boundary-Layer Meteorology*, 59: 279-296.
- Horst, T.W. and Weil, J.C., 1994: How far is far enough?: The fetch requirements for micrometeorological measurement of scalar fluxes. *Journal of Atmospheric and Oceanic Technology*, 11: 1018-1025.
- Horst, T.W., 1997: A simple formula for attenuation of eddy fluxes measured with first-order-response scalar sensors. *Boundary-Layer Meteorology*, 82: 219-233.
- Houghton, J.T., Jenkins, G.J. and Ephraums, J.J., 1990: *Climate change: The IPCC scientific assessment*. Intergovernmental Panel on Climatic Change. Cambridge Press, New York.
- Högström, U., 1988: Non-dimensional wind and temperature profiles in the atmospheric surface layer: A re-evaluation. *Boundary-Layer Meteorology*, 42: 55-78.
- Iribarne, J.V. and Godson, W.L., 1981: *Atmospheric thermodynamics*. Geophysics and Astrophysics Monographs, 6. D. Reidel Publishing Company, Dordrecht, 259 pp.
- Jarvis, P.G. and McNaughton, K.G., 1986: Stomatal control of transpiration: scaling up from leaf to region. *Advances in Ecological Research*, 15: 1-49.
- Jenkins, G.M. and Watts, D.G., 1969: *Spectral analysis and its applications*. Holden-Day Series in Time series analysis. Holden-Day, San Francisco, Cambridge, London, Amsterdam, 525 pp.
- Johnson, D.L., 1990: New grains and pseudograins. In: J. Janick and J.E. Simon (Editors), *Advances in new crops - Proceedings of the first national symposium New Crops: Research, development, economics*. Timber Press, Portland, Oregon, Indianapolis, pp. 122-127.
- Jones, H.G., 1994: *Plants and microclimate*. University Press, Cambridge, 428 pp.
- Kaimal, J.C. and Gaynor, J.E., 1991: Another look at sonic anemometry. *Boundary-Layer Meteorology*, 56: 401-410.
- Kaimal, J.C. and Finnigan, J.J., 1994: *Atmospheric boundary layer flows*. Oxford University Press, New York, Oxford, 280 pp.
- Kaimal, J.C., Wyngaard, J.C., Izumi, Y. and Coté, O.R., 1972: Spectral characteristics of surface-layer turbulence. *Quarterly Journal of the Royal Meteorological Society*, 98: 563-589.
- Kaimal, J.C., Wyngaard, J. C., Haugen, D. A., Coté, O. R., Izumi, Y., Caughey, S. J., Readings, C. J., 1976: Turbulence structure in the convective boundary layer. *Journal of the Atmospheric Sciences*, 33: 2152-2169.
- Kalthoff, N. and Vogel, B., 1992: Counter-current and channelling effect under stable stratification in the area of Karlsruhe. *Theoretical and Applied Climatology*, 45: 113-126.
- Katul, G.G. and Parlange, M.B., 1992: On the active role of temperature in surface layer turbulence. *Journal of the Atmospheric Sciences*, 51: 2181-2195.
- Katul, G., Albertson, J., Chu, C.-R., Parlange, M., Stricker, H., Tyler, S., 1994: Sensible and latent heat flux predictions using conditional sampling methods. *Water Resources Research*, 30(11): 3053-3059.
- Katul, G., Goltz, S. M., Hsieh, C.-I., Cheng, Y. Mowry, F., Sigmon, J., 1995: Estimation of surface heat and momentum fluxes using the flux-variance method above uniform and non-uniform terrain. *Boundary-Layer Meteorology*, 74: 237-260.
- Katul, G.G., Finkelstein, P.L., Clarke, J.F., Ellestad, T.G., 1996: An investigation of the conditional sampling method used to estimate fluxes of active, reactive, and passive scalars. *Journal of Applied Meteorology*, 35: 1835-1845.
- Katul, G., Kuhn, G., Schieldge, J. and Hsieh, C., 1997a: The ejection-sweep character of scalar fluxes in the unstable surface layer. *Boundary-Layer Meteorology*, 83: 1-26.

- Katul, G., Hsieh, C., Kuhn, G., Ellsworth, D. and Nie, D., 1997b: Turbulent eddy motion at the forest-atmosphere interface. *Journal of Geophysical Research*, 102(D12): 13409-13421.
- Kesselmeier, J., 1991: Plant physiology and the exchange of trace gases between vegetation and the atmosphere, 5th IPSASEP Conference, Richland, pp. 949-966.
- Kesselmeier, J. and many others, 1996: Emissions of monoterpenes and isoprene from a Mediterranean oak species *Quercus Ilex L.* measured within the BEMA project. *Atmospheric Environment*, 30: 1841-1850.
- Kesselmeier, J., Bode, K., Schjorring, J.K. and Conrad, R., 1997a: Biological mechanisms involved in the exchange of trace gases. In: S. Slanina (Editor), *Biosphere-atmosphere exchange of pollutants and trace substances. Transport and chemical transformation of pollutants in the troposphere*. Springer, Berlin, pp. 117-133.
- Kesselmeier, J. and many others, 1997b. Emission of short chained organic acids, aldehydes and monoterpenes from *Quercus Ilex L.* and *Pinus Pinea L.* in relation to physiological activities, carbon budget and emission algorithms. *Atmospheric Environment*, 31(SI): 119-133.
- Kesselmeier, J., Bode, K., Gerlach, C. and Jork, E.M., 1998: Exchange of atmospheric formic and acetic acid with trees and crop plants under controlled chamber and purified air conditions. Submitted to *Atmospheric Environment*.
- Keuken, M.P., Otjes, R.P. and Slanina, S., 1990: Simultaneously sampling of NH_3 , HNO_3 , HNO_2 , HCl , SO_2 and H_2O_2 in ambient air by a wet annular denuder system. In: G. Restelli, G. Angeletti, (Editors), *Physico-chemical behaviour of atmospheric*. Kluwer Academic Publishers, Dordrecht, pp. 92-97
- KF94: cf. Kaimal and Finnigan (1994)
- Kley, D., 1997: Tropospheric chemistry and transport. *Science*, 276: 1043-1045.
- Kneubühl, F.K., 1988: *Repetitorium der Physik*. Teubner Studienbücher. B. G. Teubner, Stuttgart, 544 pp.
- Kondo, J. and Watanabe, T., 1992: Studies of the bulk transfer coefficients over a vegetated surface with a multilayer energy budget model. *Journal of the Atmospheric Sciences*, 49(23): 2183-2199.
- Kondo, J., Kanechika, O. and Yasuda, N., 1978: Heat and momentum transfers under strong stability in the atmospheric surface layer. *Journal of the Atmospheric Sciences*, 35: 1012-1021.
- Kormann, R., 1997: *Entwicklung eines frequenzmodulierten Diodenlaserspektrometers zur Bestimmung von Spurengasflüssen in der Atmosphäre*. Dissertation, Fraunhofer Institut für Atmosphärische Umweltforschung, Garmisch-Partenkirchen, 175 pp.
- Kramm, G., 1989: The estimation of the surface layer parameters from wind velocity, temperature and humidity profiles by least squares methods. *Boundary-Layer Meteorology*, 48: 315-327.
- Kroon, L.J.M. and Bink, N.J., 1996: Conditional statistics of vertical heat fluxes in local advection conditions. *Boundary-Layer Meteorology*, 80: 49-78.
- Kuhn, U., Ammann, C., Wolf, A., Meixner, F.X., Andreae, M.O. and Kesselmeier, J., 1997: Carbonyl sulfide exchange on an ecosystem scale: Soil represents a dominant sink for atmospheric COS. *Atmospheric Environment* (in press).
- Larsen, S.E., Edson, J.B., Fairall, C.W. and Mestayer, P.G., 1993: Measurement of temperature spectra by a sonic anemometer. *Journal of Atmospheric and Oceanic Technology*, 10: 345-354.
- Laubach, J., 1996: *Charakterisierung des turbulenten Austausches von Wärme, Wasserdampf und Kohlendioxid über niedriger Vegetation anhand von Eddy-Korrelationsmessungen*. Dissertation, Institut für Meteorologie der Universität Leipzig, 140 pp.
- Laubach, J. and Teichmann, U., 1996: Measuring energy budget components by eddy correlation: Data corrections and application over low vegetation. *Contributions to the Physics of the Atmosphere*, 69(2): 307-320.
- Leclerc, M.Y. and Thurtell, G.W., 1990: Footprint prediction of scalar fluxes using a Markovian analysis. *Boundary-Layer Meteorology*, 52: 247-258.
- Lee, X., Black, A. and Novak, M.D., 1993: Comparison of flux measurements with open- and closed-path gas analyzers above an agricultural field and a forest floor. *Boundary-Layer Meteorology*, 67: 195-202.
- Lenschow, D., 1995: Micrometeorological techniques for measuring biosphere-atmosphere trace gas exchange. In: P.A. Matson and R.C. Harris (Editors), *Biogenic trace gases: Measuring emissions from soil and water*. Blackwell Science Ltd., Oxford, pp. 126-163.
- Lenschow, D.H. and Delany, A.C., 1987: An analytical formulation for NO and NO_2 flux profiles in the atmospheric surface layer. *Journal of Atmospheric Chemistry*, 5: 301-309.

- Lenschow, D.H. and Kristensen, L., 1985: Uncorrelated noise in turbulence measurements. *Journal of Atmospheric and Oceanic Technology*, 2: 68-81.
- Lenschow, D.H. and Raupach, M.R., 1991: The attenuation of fluctuations in scalar concentrations through sampling tubes: *Journal of Geophysical Research*, 96(D8): 15259-15268.
- Lenschow, D.H., Mann, J. and Kristensen, L., 1994: How long is long enough when measuring fluxes and other turbulent statistics?. *Journal of Atmospheric and Oceanic Technology*, 11: 661-673.
- Leuning, R., 1983: Transport of gases into leaves. *Plant, Cell and Environment*, 6: 181-194.
- Leuning, R. and Judd, M.J., 1996: The relative merits of open- and closed-path analysers for measurement of eddy fluxes. *Global Change Biology*, 2: 241-253
- Leuning, R. and Moncrieff, J., 1990: Eddy-covariance CO₂ flux measurements using open- and closed-path CO₂ analysers: Corrections for analyser water vapour sensitivity and damping of fluctuations in air sampling tubes. *Boundary-Layer Meteorology*, 53: 63-76.
- Leuning, R., Neumann, H.H. and Thurtell, G.W., 1979: Ozone uptake by corn (*Zea Mays L.*): A general approach. *Agricultural Meteorology*, 20: 115-135.
- Lindberg, S.E., Lovett, G.M., Richter, D.D. and Johnson, D.W., 1986: Atmospheric deposition and canopy interactions of major ions in a forest. *Science*, 231: 141-145.
- Lindroth, A. and Cienciala, E., 1996: Water-use efficiency of short-rotation *Salix viminalis* at leaf, tree and stand scales. *Tree Physiology*, 16: 257-262.
- Livingston, G.P. and Hutchinson, G.L., 1995: Enclosure-based measurements of trace gas exchange: applications and sources of error. In: P.A. Matson and R.C. Harriss (Editors), *Biogenic trace gases: Measuring emissions from soil and water*. Blackwell Science Ltd., Oxford, pp. 394.
- Lo, A.K.-F., 1995: Determination of zero-plane displacement and roughness length of a forest canopy using profiles of limited height. *Boundary-Layer Meteorology*, 75: 381-402.
- Lohse, H., Apel, U., Claussen, M., Müller, A. and Siewers, H., 1990: Ein Messsystem für turbulente Flüsse in der bodennahen Grenzschicht. GKSS 90/E/37, GKSS-Forschungszentrum, Geesthacht, 90 pp.
- Louis, J.-F., 1979: A parametric model of vertical eddy fluxes in the atmosphere. *Boundary-Layer Meteorology*, 17: 187-202.
- Lovett, G.M. and Lindberg, S.E., 1993: Atmospheric deposition and canopy interactions of nitrogen in forests. *Canadian Journal of Forest Research*, 23: 1603-1616.
- Ludwig, J., 1994: Untersuchungen zum Austausch von NO und NO₂ zwischen Atmosphäre und Biosphäre. Dissertation, Fakultät für Biologie, Chemie und Geowissenschaften der Universität Bayreuth, 251 pp.
- MacPherson, J.I. and Desjardins, R.L., 1991: Airborne tests of flux measurement by relaxed eddy accumulation technique, 7th Symposium on Meteorological Observations and Instrumentation. American Meteorological Society, New Orleans, LA, pp. 6-11.
- Maitani, T. and Shaw, R.H., 1990: Joint probability analysis of momentum and heat fluxes at a deciduous forest. *Boundary-Layer Meteorology*, 52: 283-300.
- Majewski, M., Desjardins, R., Rochette, P., Pattey, E., Seiber, J., Glotfelty, D., 1993: Field comparison of an eddy accumulation and an aerodynamic-gradient system for measuring pesticide volatilization fluxes. *Environmental Science and Technology*, 27(1): 121-128.
- Massman, W.J., 1991: The attenuation of concentration fluctuations in turbulent flow through a tube. *Journal of Geophysical Research*, 96 (D8): 15269-15274.
- Massman, W.J., 1993: Errors associated with the combination method for estimating soil heat flux. *Soil Science Society of America Journal*, 57: 1198-1202.
- Matson, P.A. and Harris, R.C., 1995: *Biogenic trace gases: Measuring emissions from soil and water*. Methods in ecology. Blackwell science, 393 pp.
- Mazzoni, R., 1996: Turbulenzstruktur im gestörten Nachlauf einer künstlichen Oberflächenmodifikation. Dissertation, Zürcher Geographische Schriften Nr. 60, Geographisches Institut ETH, Zürich, 136 pp.
- McDermitt, D.K., Welles, J.M. and Eckles, R.D., 1993: Effects of temperature, pressure and water vapor on gas phase infrared absorption by CO₂, LI-COR Inc., Lincoln, NE, 18 pp.
- McMillen, R.T., 1988: An eddy correlation technique with extended applicability to non-simple terrain. *Boundary-Layer Meteorology*, 43: 231-245.

- Meixner, F.X., 1993: Surface exchange of ammonia: Three different micrometeorological procedures applied. In: Angeletti, G. and Rastelli, G. (Editors), *Physico-chemical behaviour of atmospheric pollutants*, Proc. of the 6th European Symposium, Report EUR 15609, Office for Official Publications of the European Communities, Luxembourg, pp. 749-754.
- Meixner, F.X., 1994: Surface exchange of odd nitrogen oxides. *Nova Acta Leopoldina*, 70(288): 299-348.
- Meixner, F.X. and Eugster, W., 1998: Effects of landscape pattern and topography on emissions and transport. to be published in report of Dahlem Workshop 1998 on Integrating hydrology, ecosystem dynamics, and biogeochemistry in complex landscapes.
- Meixner, F.X., Wyers, P.G. and Neftel, A., 1996: Bi-directional exchange of ammonia over cereals. In: M.E.A. Borrell (Editor), *EUROTRAC Symposium '96, Transport and transformation of pollutants in the troposphere*. Computational Mechanics Publications, Garmisch-Partenkirchen, Germany, pp. 129-136.
- Meixner, F.X., Fickinger, T., Marufu, L., Mukurumbira, L., Makina, E., Nathaus, F. J., Serca, D., Andreae, M. O., 1997: Preliminary results on nitric oxide emission from a southern African savanna ecosystem. *Nutrient Cycling in Agroecosystems*, 48: 123-138.
- Meyers, T.P., Hall, M.E., Lindberg, S.E. and Kim, K., 1996: Use of the modified Bowen-ratio technique to measure fluxes of trace gases. *Atmospheric Environment*, 30(19): 3321-3329.
- Mihalopoulos, N., Bonsang, B., Nguyen, B.C., Kanakidou, M. and Belviso, S., 1989: Field observation of carbonyl sulfide deficit near the ground: Possible implication of vegetation. *Atmospheric Environment*, 23(10): 2159-2166.
- Moncrieff, J.B., Malhi, Y. and Leuning, R., 1996: The propagation of errors in long-term measurements of land-atmosphere fluxes of carbon and water. *Global Change Biology*, 2: 231-240.
- Moncrieff, J., Valentini, R., Greco, S., Seufert, G. and Ciccioli, P., 1997: Trace gas exchange over terrestrial ecosystems: methods and perspectives in micrometeorology. *Journal of Experimental Botany*, 48(310): 1133-1142.
- Monin, A.S. and Obukhov, A.M.O., 1958: *Fundamentale Gesetzmäßigkeiten der turbulenten Vermischung in der bodennahen Schicht der Atmosphäre*. In: H. Goering (Editor), *Sammelband zur statistischen Theorie der Turbulenz*. Deutsche Akademie der Wissenschaften zu Berlin, Berlin, pp. 199-226.
- Monteith, J.L. and Unsworth, M.H., 1990: *Principles of environmental physics*. Edward Arnold, London, 291 pp.
- Moore, C.J., 1986: Frequency response correction for eddy correlation systems. *Boundary-Layer Meteorology*, 37: 17-35.
- Moortgat, G.K., Veyret, B. and Lesclaux, R., 1989: Kinetics of the reaction of HO₂ with CH₂C(O)O₂ in the temperature range 253-368 K. *Chemical Physical Letters*, 160: 443-447.
- Mortensen, N.G., 1994: Wind measurements for wind energy applications - a review, Proc. of the 16th British Wind Energy Association conference, Stirling, Scotland, pp. 353-360.
- Mortensen, N.G. and Hojstrup, J., 1995: The solent sonic - response and associated errors, Ninth Symposium on Meteorological Observations and Instrumentation, Charlotte, NC, pp. 14.10.
- Müller, H., Kramm, G., Meixner, F.X., Dollard, G.J., Fowler, D. and Possanzini, M., 1993: Determination of HNO₃ dry deposition by modified bowen ratio and aerodynamic profile techniques. *Tellus*, 45B: 346-367.
- Nappo, C.J., 1991: Sporadic breakdowns of stability in the PBL over simple and complex terrain. *Boundary-Layer Meteorology*, 54: 69-87.
- Neeb, P., 1995: *Laboruntersuchungen zur Ozonolyse einfacher Alkene in der Gasphase*. Dissertation, Johannes Gutenberg Universität, Mainz.
- Neftel, A., Moor, E., Oeschger, H. and Stauffer, B., 1985: Evidence from polar ice cores for the increase in atmospheric CO₂ in the past two centuries. *Nature*, 315: 45-47.
- Neftel, A., Blatter, A., Gut, A., Högger, D., Meixner, F.X., Ammann, C., and Nathaus, F.J., 1997: NH₃ soil and soil surface gas measurements in a triticale wheat field. *Atmospheric Environment*, 32(3): 499-505
- Neumann, H.H., Hartog, G.d. and Guise-Bagley, L.F., 1989: Evaluation of a digital-valve eddy accumulator using water vapor flux measurements and numerical simulations of its performance. *Atmospheric Environment*, 6: 1305-1313.
- Nie, D., Kleindienst, T.E., Arnts, R.R. and Sickles II, J.E., 1995: The design and testing of a relaxed eddy accumulation system. *Journal of Geophysical Research*, 100(D6): 11415-11423.

- Nieuwstadt, F., 1978: The computation of the friction velocity u^* and the temperature scale T^* from temperature and wind velocity profiles by least-square methods. *Boundary-Layer Meteorology*, 14: 235-246.
- Nobre, C.A. and many others, 1996: The large scale biosphere-atmosphere experiment in Amazonia (LBA), Concise Experimental Plan, SC-DLO Wageningen, The Netherlands.
- O'Brien, E.E., 1985: A Monte Carlo simulation of the eddy accumulation method for measuring scalar fluxes. *Journal of Climate and Applied Meteorology*, 24: 281-286.
- Obukhov, A. M., 1971: Turbulence in an atmosphere with a non-uniform temperature. *Boundary-Layer Meteorology*, 2: 7-29.
- Ohmura, A., 1982: Objective criteria for rejecting data for Bowen ratio calculations. *Journal of Applied Meteorology*, 21: 595-598.
- Ohmura, A. and Schrott, K., 1983: Physical characteristics of the Davos-type pyrrometer for short- and long-wave radiation. *Archives for Meteorology, Geophysics, and Bioclimatology*, ser. B 33: 57-76.
- Ohmura, A. and Rotach, M.W., 1986: Mikroklimatologie. *Berichte und Skripten*, Nr. 28. Geographisches Institut ETH, Zürich, 140 pp.
- Oke, T.R., 1987: *Boundary layer climates*. Routledge, London and New York, 435 pp.
- Oncley, S.P., Delany, A.C., Horst, T.W. and Tans, P.P., 1993: Verification of flux measurement using relaxed eddy accumulation. *Atmospheric Environment*, 27A(15): 2417-2426.
- Padro, J., 1993: An investigation of flux-variance methods and universal functions applied to three land-use types in unstable conditions. *Boundary-Layer Meteorology*, 66: 413-425.
- Panin, G.N., Tetzlaff, G., Raabe, A., Schonfeldt, H.-J. and Nasanov, A.E., 1996: Inhomogeneity of the land surface and the parameterisation of surface fluxes - a discussion. In: A. Raabe and J. Heintzenberg (Editors), *Meteorologische Arbeiten aus Leipzig (II)*. Wissenschaftliche Mitteilungen. Universität Leipzig, pp. 204-215.
- Panofsky, H.A. and Dutton, J.A., 1984: *Atmospheric turbulence, models and methods for engineering applications*. John Wiley & Sons, New York, 397 pp.
- Pattey, E., Rochette, P., Desjardins, R.L. and Dubé, P.A., 1991: Estimation of the net CO₂ assimilation rate of a maize (*Zea mays* L.) canopy from leaf chamber measurements. *Agricultural and Forest Meteorology*, 55: 37-57
- Pattey, E., Desjardins, R.L. and Rochette, P., 1993: Accuracy of the relaxed eddy-accumulation technique, evaluated using CO₂ flux measurements. *Boundary-Layer Meteorology*, 66: 341-355.
- Pattey, E., Cessna, A.J., Desjardins, R.L., Kerr, L.A., Rochette, P., St-Amour, G., Zhu, T. and Headrick, K., 1995: Herbicides volatilization measured by the relaxed eddy-accumulation technique using two trapping media. *Agricultural and Forest Meteorology*, 76: 201-220.
- Pattey, E., Desjardins, R.L., Westberg, H., Lamb, B. and Zhu, T., 1997: Isoprene emission over a black spruce stand, during BOREAS, measured by a tower-based relaxed eddy-accumulation system, AMS Workshop on Biogenic hydrocarbons in the atmospheric boundary layer, Charlottesville, pp. 66-68.
- Paulson, C.A., 1970: The mathematical representation of wind speed and temperature profiles in the unstable atmospheric surface layer. *Journal of Applied Meteorology*, 9: 857-861.
- PD84: cf. Panofsky and Dutton (1984)
- Profos, P. and Pfeiffer, T., 1993: *Grundlagen der Messtechnik*. Oldenbourg Verlag, München, 367 pp.
- Rasmussen, R.A. and Khalil, M.A.K., 1986: Atmospheric trace gases: Trends and distributions over the last decade. *Science*, 232: 1623-1624.
- Raupach, M.R., 1981: Conditional statistics of Reynolds stress in rough-wall and smooth-wall turbulent boundary layers. *Journal of Fluid Mechanics*, 108: 363-382.
- Raupach, M.R., 1989: Stand overstorey processes. *Philosophical Transactions of the Royal Society London*, B 324: 175-190.
- Raupach, M.R., Coppin, P.A. and Legg, B.J., 1986: Experiments on scalar dispersion within a model canopy. I. The turbulence structure. *Boundary-Layer Meteorology*, 35: 21-52.
- Raupach, M.R. and many others, 1994: OASIS (Observations at several interacting scales). Technical Report No. 68, CSIRO Centre for Environmental Mechanics, Canberra, 19 pp.

- Rayment, R. and Readings, C.J., 1971: The importance of instrumental tilt on measurements of atmospheric turbulence. *Quarterly Journal of the Royal Meteorological Society*, 97: 124-130.
- Raynaud, D., Chappellaz, J., Barnola, J.-M., Korotkevitch, Y.S. and Lorius, C., 1988: Climate and CH₄ cycle implications of glacial-interglacial CH₄ change in the Vostok ice core. *Nature*, 333: 655-657.
- Reid, W.S., Desjardins, R.L., Fagan, W. and Ginsburg, A., 1984: An open-loop fast response gas sampling valve with current control. *Journal of Physics E: Scientific Instruments*, 17: 323-327.
- Richardson, L.F., 1938: The supply of energy from and to atmospheric eddies. *Proceedings of the Royal Society London*: 354-373.
- Rochette, P., Pattey, E., Desjardins, R.L., Dwyer, L.M., Stewart, D. W. and Dubé, P.A., 1991: Estimation of maize (*Zea mays* L.) canopy conductance by scaling up leaf stomatal conductance. *Agricultural and Forest Meteorology*, 54: 341-261
- Rosswall, T. and many others, 1989: What regulates production and consumption of trace gases in ecosystems: biology or physicochemistry? (Group report). In: M.O. Andreae and D.S. Schimel (Editors), *Exchange of trace gases between terrestrial ecosystems and the atmosphere*. John Wiley & Sons, New York, pp. 73-95.
- Rotach, M.W., 1991: Turbulence within and above an urban canopy. Dissertation, Zürcher Geographische Schriften Nr. 45, Geographisches Institut ETH, Zürich, 245 pp.
- Rotach, M.W., 1994: Determination of the zero-plane displacement in an urban environment. *Boundary-Layer Meteorology*, 67: 187-193.
- Rotach, M.W., 1997: BAT Budget of atmospheric trace gases - Biosphere atmosphere transfer, Geographisches Institut ETH, Zürich, 20 pp.
- Rudolph, J., 1994: Umsetzung und Transport von Stickstoffmonoxid (NO) in Böden. Dissertation, Universität Konstanz.
- Rutter, A.J., 1975: The hydrological cycle in vegetation. In: J.L. Monteith (Editor), *Vegetation and the atmosphere*. Academic Press, London, pp. 111-154.
- Sachs, L., 1984: *Angewandte Statistik*. Springer-Verlag, Berlin, 552 pp.
- Sanhueza, E., Dong, Y., Scharffe, D., Lobert, J.M. and Crutzen, P.J., 1997: Carbon monoxide uptake by temperate forest soils: the effects of leaves and humus layers. *Tellus* (submitted).
- Schmid, H.P. and Oke, T.R., 1990: A model to estimate the source area contributing to turbulent exchange in the surface layer over patchy terrain. *Quarterly Journal of the Royal Meteorological Society*, 116: 965-988.
- Schmid, H.P., 1994: Source areas for scalars and scalar fluxes. *Boundary-Layer Meteorology*, 67: 293-318.
- Schmid, H.P., 1997: Experimental design for flux measurements: Matching scales for observation and fluxes. *Agricultural and Forest Meteorology* (in press).
- Schotanus, P., Nieuwstadt, F.T.M. and DeBruin, H.A.R., 1983: Temperature measurement with a sonic anemometer and its application to heat and moisture fluxes. *Boundary-Layer Meteorology*, 26: 81-93.
- Schuepp, P.H., Leclerc, M.Y., MacPherson, J.I. and Desjardins, R.L., 1990: Footprint prediction of scalar fluxes from analytical solutions of the diffusion equation. *Boundary-Layer Meteorology*, 50: 355-373.
- Schween, J., 1993: Herleitung ortsspezifischer Stabilitätsfunktionen für den Bestand 'Schachtenau' im Nationalpark Bayerischer Wald. Diplomarbeit, Meteorologisches Institut der Ludwig-Maximilians-Universität, München, 99 pp.
- Schween, J.H., Dlugi, R., Hewitt, C.N. and Foster, P., 1997: Determination and accuracy of VOC-fluxes above the pine/oak forest at Castelporziano. *Atmospheric Environment*, 31(SI): 199-215.
- Sellers, P. and many others, 1991: Charting the boreal forest's role in global change. *EOS*, 72 (4): 33-40.
- Sellers, P.J., Hall, F.G., Asrar, G., Strebel, D.E. and Murphy, R.E., 1992: An overview of the first international satellite land surface climatology (ISLSCP) field experiment (FIFE). *Journal of Geophysical Research*, 97: 18345-18371.
- Speer, R.E., Peterson, K.A., Ellestad, T.G. and Durham, J.L., 1985: Test of a prototype eddy accumulator for measuring atmospheric vertical fluxes of water vapor and particulate sulfate. *Journal of Geophysical Research*, 90(D1): 2119-2122.
- Sprung, D., 1993: Kontinuierliche Bestimmung der turbulenten Ozonflüsse in der bodennahen Grenzschicht mittels Eddy-Korrelationstechnik. Diplomarbeit, Institut für Meteorologie und Klimaforschung, Universität Karlsruhe, 100 pp.

- Sprung, D., Baumann, M., Güsten, H., Ammann, C. and Meixner, F.X., 1996: Vertical profiles of CO₂ and O₃ in the nocturnal boundary layer over an agricultural field. *Annales Geophysicae*, 14 (Supplement II): C 470.
- St88: cf. Stull (1988)
- Stace, C.A., 1987: Triticale: a case of nomenclatural mistreatment. *Taxon*, 36: 445-452.
- Stewart, T. and many others, 1989: Extrapolation of flux measurements to regional and global scales (Group report). In: M.O. Andreae and D.S. Schimel (Editors), *Exchange of trace gases between terrestrial ecosystems and the atmosphere*. John Wiley & Sons Ltd., pp. 155-174.
- Stull, R.B., 1988: *An introduction to boundary layer meteorology*. Kluwer Academic Publishers, Dordrecht, 666 pp.
- Sutton, M.A., 1990: Surface-atmosphere exchange of ammonia. PhD Thesis, University of Edinburgh, 194 pp.
- Sutton, M.A., Schjorring, J.K. and Wyers, G.P., 1995: Plant-atmosphere exchange of ammonia. *Philosophical Transactions of the Royal Society London A*, 351: 261-278.
- Sutton, M.A. and many others, 1996: Exchange of atmospheric ammonia with European ecosystems (EXAMINE). EV5V-CT97-0426, NERC Institute of Terrestrial Ecology (ITE), Penicuik, Midlothian.
- Suyker, A.E. and Verma, S.B., 1993: Eddy correlation measurements of CO₂ flux using a closed-path sensor: Theory and field tests against open-path sensor. *Boundary-Layer Meteorology*, 64: 391-407.
- Taylor, G.I., 1938: The spectrum of turbulence. *Philosophical Transactions of the Royal Society London A*, 164: 476-490.
- Thom, A.S., 1971: Momentum absorption by vegetation. *Quarterly Journal of the Royal Meteorological Society*, 97: 414-428.
- Thom, A.S., 1975: Momentum, mass and heat exchange. In: J.L. Monteith (Editor), *Vegetation and the atmosphere*. Academic Press, London, pp. 57-109.
- Thompson, A.M., 1992: The oxidizing capacity of the earth's atmosphere: Probable past and future changes. *Science*, 256: 1157-1165.
- Valentini, R., Greco, S., Seufert, G., Cieslik, S. and Ciccioli, P., 1995: Application of a modified eddy accumulation system (TEREA Trap Enriched Relaxed Eddy Accumulation) to study biogenic emissions: Preliminary observations. Report on the 1st BEMA measuring campaign at Castelporziano, EUR 16293 EN, Joint Research Centre of the European Commission, Ispra, pp. 53-60.
- Valentini, R., Greco, S., Seufert, G., Bertin, G., Ciccioli, P., Cecinato, A., Brancaleoni, E. and Frattoni, M., 1997: Fluxes of biogenic VOC from mediterranean vegetation by trap enrichment relaxed eddy accumulation. *Atmospheric Environment*, 31(SI): 229-238.
- Van Hove, L.W.A., Adema, E.A., Vredenberg, W.J. and Pieters, G.A., 1989: A study of the adsorption of NH₃ and SO₂ on leaf surfaces. *Atmospheric Environment*, 23(7): 1479-1486.
- Vila-Guerau de Arellano, J. and Duynkerke, P.G., 1992: Influence of chemistry on the flux-gradient relationships for the NO-O₃-NO₂ system. *Boundary-Layer Meteorology*, 61: 375-387.
- Vong, R.J. and Kowalsky, A.S., 1995: Eddy correlation measurements of size-dependent cloud droplet turbulent fluxes to complex terrain. *Tellus*, 47B: 331-352.
- Webb, E.K., Pearman, G.I. and Leuning, R., 1980: Correction of flux measurements for density effects due to heat and water vapour transfer. *Quarterly Journal of the Royal Meteorological Society*, 106: 85-100.
- Wellburn, A.R., 1990: Why are atmospheric oxides of nitrogen usually phytotoxic and not alternative fertilizers? *New Phytologist*, 115: 395-429.
- Welles, J.M. and Norman, J.M., 1991: Instrument for indirect measurement of canopy architecture. *Agronomy Journal*, 83: 818-825.
- Wesely, M.L., 1988: Use of variance techniques to measure dry air-surface exchange rates. *Boundary-Layer Meteorology*, 44: 13-31.
- Wesely, M.L., 1989: Parameterization of surface resistances to gaseous dry deposition in regional-scale numerical models. *Atmospheric Environment*, 23(6): 1293-1304.
- Wesely, M.L. and Hart, R.L., 1994: On eddy accumulation with limited conditional sampling to measure air-surface exchange. *Proceedings of the AMS Conference on Atmospheric Chemistry, Nashville, Tennessee*, pp. 233-236.
- Westgarth, G., 1996: Personal communication. Gill Instruments Ltd., Lymington, Hampshire, UK

- Wichura, B. and Foken, T., 1995: Anwendung integraler Turbulenzcharakteristiken zur Bestimmung von Energie- und Stoffflüssen in der Bodenschicht der Atmosphäre. 29, Deutscher Wetterdienst, Abteilung Forschung, Offenbach am Main, 51 pp.
- Wienhold, F.G., Frahm, H. and Harris, G.W., 1994: Measurements of N₂O fluxes from fertilized grassland using a fast response tunable diode laser spectroscopy. *Journal of Geophysical Research*, 99(D8): 16557-16567.
- Wienhold, F.G., Welling, M. and Harris, G.W., 1995: Micrometeorological measurement and source region analysis of nitrous oxide fluxes from an agricultural soil. *Atmospheric Environment*, 29(17): 2219-2227.
- Wieringa, J., 1989: Shapes of annual frequency distributions of wind speed observed on high meteorological masts. *Boundary-Layer Meteorology*, 47: 85-110.
- Wieringa, J., 1993: Representative roughness parameters for homogeneous terrain. *Boundary-Layer Meteorology*, 63: 323-363.
- Wilczak, J.M. and Businger, J.A., 1983: Thermally indirect motions in the convective atmospheric boundary layer. *Journal of the Atmospheric Sciences*, 40: 343-358.
- Willert, D.J., Matyssek, R. and Herppich, W., 1995: *Experimentelle Pflanzenökologie*. Georg Thieme Verlag, Stuttgart, 344 pp.
- Wilson, J.D. and Shum, W.K.N., 1992: A re-examination of the integrated horizontal flux method for estimating volatilisation from circular plots. *Agricultural and Forest Meteorology*, 57: 281-295.
- Wyngaard, J.C., 1973: On surface-layer turbulence. In: D.A. Haugen (Editor), *Workshop on Micrometeorology*. American Meteorological Society, Boston, pp. 101-149.
- Wyngaard, J.C., 1988: Flow-distortion effects on scalar flux measurements in the surface layer : Implications for sensor design. *Boundary-Layer Meteorology*, 42: 19-26.
- Wyngaard, J.C. and Moeng, C.-H., 1992: Parameterizing turbulent diffusion through the joint probability density. *Boundary-Layer Meteorology*, 60: 1-13.
- Wyngaard, J.C. and Zhang, S.-F., 1985: Transducer-shadow effects on turbulence spectra measured by sonic anemometers. *Journal of Atmospheric and Oceanic Technology*, 2: 548-559.
- Yang, P.C., Black, T.A., Chen, W.J., Blanken, P.D., Neumann, H.H., Novak, M.D., Nestic, Z. and Lee, X., 1997: Effect of turbulence on nocturnal CO₂ fluxes above a boreal aspen forest, 12th Symposium on Boundary layers and turbulence. American Meteorological Society, Vancouver, pp. 395-396.
- Zeller, K., Massmann, W., Stocker, D., Fox, D.G., Stedman, D. and Hazlett, D., 1989: Initial results from the Pawnee eddy correlation system for dry acid deposition research. Report No. RM-282, United States Department of Agriculture, Forest Service, Fort Collins CO, 30 pp.
- Zhu, T., Wang, D., Desjardins, R.L., MacPherson, J.I. and Pattey, E., 1997: Aircraft-based biogenic hydrocarbons fluxes measurement with relaxed eddy accumulation, Workshop on Biogenic hydrocarbons in the atmospheric boundary layer. American Meteorological Society, Charlottesville, pp. 61-64.
- Zhu, T., Desjardins, R.L., MacPherson, J.I., Pattey, E. and St. Amour, G., 1998: Aircraft measurements of the concentration and flux of agrochemicals. *Environmental Science and Technology*, 32: 1032-1038

Curriculum Vitae

- 22 December 1965 born in Kirchberg (SG), son of Wilhelm Ammann and Martha Ammann, with maiden name Bürge
- 1972 - 1978 primary school in Gähwil (SG)
- 1978 - 1985 Gymnasium Friedberg in Gossau (SG), finished with Matura type B
- 1985 - 1986 study of physics at the ETH Zürich
- 1986 - 1992 study of environmental physics at the ETH Zürich with specialisation in atmospheric physics, finished with the degree of Dipl. Natw. ETH
- Apr. - Oct. 1992 scientific co-worker at the Institute of Geography of the ETH Zürich (Microclimatology group)
- 1993 - 1998 doctoral thesis for the ETH Zürich, at the Max Planck Institute for Chemistry in Mainz, Germany